Numerical modelling of micro and macro cracking in plain and fibre-reinforced cementitious composites

Amrit Bains

School of Engineering

Cardiff University

Thesis submitted for the degree of Doctor of Philosophy

November 2021

Abstract

A micromechanical constitutive model for plain concrete and other quasi-brittle materials was formulated using a micromechanical damage approach. The model improved upon predecessors via the inclusion of a mechanism which simulated the transition from diffuse directional microcracking to localised macrocracking at the constitutive level. The mechanism was formulated using observations from non-destructive testing and numerical experiments carried out via lattice simulations. Lattice model simulations were used to gain insight into the crack localisation process. Modelling the transition to localised cracking was found to give more realistic results, especially under tensile loading paths where the post-peak response was too ductile with only diffuse microcrack growth. Also, by simulating the development of macrocracks, the model was able to capture tensile-splitting.

The constitutive model was extended to simulate the behaviour of fibre-reinforced cementitious composites by incorporating micromechanical solutions for the crack-bridging mechanism of short fibres. Comparison of the behaviour predicted by the model with experimental results showed that the model gave realistic results.

Next, a plastic-damage approach was used to formulate a micromechanical constitutive model for quasi-brittle materials where crack-planes were represented by local plastic yield surfaces and separate hardening parameters were used to capture isotropic and directional effects. The new model built on the previous micromechanical damage constitutive model for plain concrete by allowing for permanent deformations. Comparing numerical simulations to experimental data showed that the model matched the expected characteristic behaviour well. Suggestions were made on how the predictions could be improved further in the future.

The micromechanical plastic-damage model was implemented in the LUSAS finite element software package and regularised using the crack band method. Initial assessments of the performance of the implemented model were made by simulating a direct fracture test and a four-point bending test. Localised cracking behaviour was successfully predicted.

Acknowledgements

First and foremost, I would like to thank my supervisors Iulia Mihai and Tony Jefferson for their unwavering enthusiasm, positivity and faith. I can sincerely say that I enjoyed every single one of our meetings over the last three years. I would also like to thank Peter Grassl without whom my research would not have been possible.

Thank you to Carlos Azua-Gonzalez, Brubeck Freeman, Louis Barber, Sina Sayadi Moghadam, Evan Ricketts, Rob Davies, Diane Gardner and all of the other members in the research group for providing me with a stimulating working environment.

Finally, I would like to thank my parents, family and friends. You have always supported me and encouraged me through thick and thin.

Contents

List of Figures

List of Tables

Chapter 1

Introduction

Whilst there is some debate around the topic, the oldest concrete discovered was found in the floor of an Isreali hut and dated back to 7000 BC (Singh 2017). The addition of fibres to a material to improve its tensile behaviour is also not a new concept. Some 3500 years ago in ancient Mesopotamia (modern day Iraq), the 57m tall stepped temple tower "Aqar Quf" was built with sun-baked bricks reinforced with straw (Swamy 1980).

The Romans were the first civilization to extensively use volcanic earth to make hydraulic cement (Delatte 2001) and they made significant advances in concrete technology. Concrete structures used in Roman seaports along the coast of Italy remain intact to this day despite having being immersed in seawater for 2000 years (Jackson et al. 2013). According to Jahren & Sui (2018), the large advances in concrete technology made by the Romans can be attributed to systematic documentation of methods, the recognition of the greater durability of pozzolan cement over other materials, the diversity in the use of concrete and the diverse challenges faced across a large empire and the ability to spread technology. Unfortunately, the fall of the Roman Empire led to limited use and development of concrete for over 1000 years (Camões & Ferreira 2010, Jahren & Sui 2018).

After the long period of disuse of concrete, modern cement, known as Portland cement, was patented in 1824 by a builder from Leeds, England called Joseph Aspdin (Neville & Brooks 2010). A few decades later, French gardener Joseph Monier pioneered the use of plant pots made from reinforced concrete to replace those made from ceramics and wood (Camões & Ferreira 2010, Wang 2013). Following his success, Joseph Monier filed a patent for reinforced concrete in 1866 (Camões & Ferreira 2010). The initial development of modern fibre-reinforced concrete would follow a century later in the 1960s (Naaman 2011).

In the present age, concrete is second only to water as the most consumed material in the world (Gagg 2014) and the cement industry contributes as much as 8% of the total global CO_2 emissions (Andrew 2018). In light of environmental and industrial concerns, major work has been carried out to improve the sustainability of concrete. The current avenues of research range from experimental and numerical work on self-healing concrete technologies (Freeman et al. 2020, Davies et al. 2021, Balzano et al. 2021) and engineered cementitious composites (Huang et al. 2021, Zhu et al. 2021) to hybrid fibre-reinforced cementitious composites (Bhosale & Prakash 2020, Chella Gifta & Gopal 2021) and concrete with recycled or man-made aggregates (Belmokaddem et al. 2020, Thomas et al. 2020, Duan et al. 2021).

Numerical modelling and experimental work must be considered in unison to progress science and engineering (Van Mier 2013). In experimental studies, directly observing fracture in concrete is difficult because of the small scale of microstructural events during the fracture process (Skarżyński & Tejchman 2013). Though non-destructive testing and imaging techniques exist which enable study of these events, there are limitations in capturing the entirety of the cracking process. Numerical modelling is one method of gaining an insight into the fracture process. Experimental work is also valuable as analysing experimental results can lead to improved theories (Van Mier 2013).

Despite the decades of effort, there still no well-accepted, robust and accurate material model that is able to predict the characteristic mechanical behaviour of concrete and the evolution of cracking in the material. Constitutive models for plain concrete suffer from instability during the non-linear solution procedure as there is a lack of steel reinforcement which typically provides numerical stability (Markou & Roeloffze 2021). Additionally, the complex heterogeneous material structure causes highly complex material behaviour. In fact, the complexity of the behaviour means that there are no standard laboratory tests for concrete subject to multiaxial stresses (Mehta & Monteiro 2006).

The issue becomes further complicated with the addition of fibres to cementitious composites. For example, it is possible for addition of fibres to alter the mechanical behaviour to such an extent that the failure mode changes and the response is more akin to that of a ductile material (Li 2019). In order to engineer these significant changes in composite behaviour, composites must be optimised and theoretical models are necessary to avoid having to empirically investigate infinite combinations of different fibre, matrix and interface properties (Li 2019).

It is well accepted that the macroscopic behaviour of cementitious materials is controlled by the heterogeneous structure at the micro and meso-scales. Based on this understanding, a series of micromechanical constitutive models were developed for plain and fibre-reinforced concrete by Jefferson, Mihai and co-workers e.g. Jefferson & Bennett (2007), Mihai & Jefferson (2011, 2017). These models are the predecessors to the work contained in this thesis. The models successfully simulate the characteristic mechanical behaviour of concrete and fibre-reinforced concrete; however they do not simulate the entirety of the cracking processes that occur. Namely, the development of macrocracks and the transition from diffuse microcracking to localised macrocracking is not covered. The models must incorporate the crack localisation mechanism, which is the mechanism by which concrete fails (Zhao et al. 2018), to be able to simulate the characteristic cracking behaviour.

1.1 Overall aims and objectives

The main aims of the present thesis are listed below.

- Develop a full 3D micromechanics based constitutive models for quasi-brittle cementitious materials which improves upon its predecessors and to which prescribed stresses and strains can be applied.
- Extend the constitutive model to include the effects of the addition of short fibres to a cementitious composite on the mechanical and cracking behaviour.
- Simulate the characteristic mechanical and cracking behaviour of conventional concrete and fibre-reinforced concrete at the constitutive level.
- Validate and assess the predictions from the constitutive models using data from relevant literature.
- Implement a constitutive model for fibre-reinforced cementitious composites in a commercial finite element software package and validate the results using data from experiments.

1.2 Outline of thesis

The present thesis is divided into 8 chapters which detail the development and implementation of different constitutive models for cementitious composites.

In chapter 2, a review is presented of the current understanding of the cracking behaviour of plain and fibre-reinforced concrete. The review relies on experimental findings from literature. Chapter 3 focuses on presenting methods for mod-

elling cementitious composite behaviour. Together, these two chapters provide the background information necessary for developing numerical material models that improve upon their predecessors at matching the characteristic cracking behaviour of concrete observed in experiments.

Chapter 4 describes the development of a micromechanics and continuum damage based constitutive model for quasi-brittle cementitious composites. The model used different micromechanical solutions to incorporate homogenised elastic properties and directional microcracking. However, the novel feature of the model was the ability to capture the transition from diffuse microcracking to cracking localised to macrocracks. The work was supported by the understanding gained from numerical experiments carried out via lattice simulations in addition to observations from non-destructive testing in the literature. The chapter describes improvements in predicted material behaviour as a result of including the transition to localised cracking and also describes comparisons of numerical predictions from the model with experimental data.

Chapter 5 details the extension of the aforementioned constitutive model to capture the behaviour of fibre-reinforced cementitious composites. The model used micromechanical formulations to implement the underlying crack-bridging mechanism of short fibres. Assessments of the model made by comparing numerical simulations to data are given in the chapter.

In chapter 6, a new micromechanical plastic-damage constitutive model for quasi-brittle cementitious composites is proposed. The plastic-damage framework of the model addressed the inherent issue of not being able to capture permanent deformations using the damage based approach in the previous models. The model featured crack planes represented by local plastic yield surfaces and two plastic hardening parameters to capture directional and isotropic effects. The chapter also presents a series of validations carried out by comparing the results of simulating various loading paths to experimental data.

Chapter 7 covers implementation of the micromechanical plastic-damage model in the commercial finite element package LUSAS. This is followed by details of regularisation of the model performed using the crack band method to deal with the computational issues related to strain-softening behaviour. Next, the chapter describes finite element simulations carried out as an initial assessment of the implemented model.

Finally, in chapter 8 the conclusions of the main body of research and recommendations for future work to be carried out are given.

1.3 List of publications

A journal paper has been drafted by the author:

- Bains, A., Mihai, I. C., Jefferson, A. D., Grassl, P. 2021. Micromechanical constitutive model for crack localisation in quasi-brittle materials. *International Journal of Solids and Structures.* Submission imminent.

The author presented at the following national conference as first author:

- Bains, A., Mihai, I. C., Jefferson, A. D., Grassl, P. 2021. Micromechanical constitutive model for crack localisation in quasi-brittle materials. *UKACM 2021 Conference, Loughborough, UK.*

The author was also accepted to present at the following international conference as first author however attendance was not possible due to complications arising from the ongoing global Covid-19 pandemic:

- Bains, A., Mihai, I. C., Jefferson, A. D., Grassl, P. 2021. Micromechanical constitutive model for crack localisation in quasi-brittle materials. *XVI International Conference on Computational Plasticity (COMPLAS XVI), Barcelona, Spain.*

Chapter 2

Review of cracking mechanisms in cementitious materials

2.1 Introduction

This section describes the current understanding of cracking behaviour in concrete and fibre-reinforced concrete. Cracking in concrete and fibre-reinforced concrete can be divided into two main stages, namely microcracking and macrocracking. The following sections use experimental evidence from the literature to describe the evolution of cracking in plain concrete followed by the details of underlying mechanisms of fibre-reinforced concrete and effects of the addition of fibres on the cracking behaviour.

2.2 Plain concrete

2.2.1 Microcracking

Microcracks prior to application of loading

Microcracks are present in concrete before loading is applied and are concentrated at the matrix and aggregate interface (Slate & Hover 1984). The interfacial transition zone (ITZ) microcracks can be caused by drying shrinkage, the hydration process and chemical shrinkage (Van Mier 1997). Early observation of these microcracks were made by Slate & Olsefski (1963) using X-ray and microscopic methods. The ITZ microcracks, which were caused by drying shrinkage, were seen to be concentrated around the largest aggregate particles. Also, during investigations of microcracking in concrete cylinders under uniaxial and triaxial compression, Nemati & Monteiro (1997) and Nemati et al. (1998) saw that microcracks existed in specimens to which no load had been applied. The obser-

vations were made using a metal alloy porosimetry method and scanning electron microscope.

Types of microcracks

Early work that successfully observed the microcracking process was carried out by Hsu et al. (1963) for concrete cylinders under uniaxial compression, with a microscope and X-ray photographs. Hsu et al. (1963) identified 3 different types of microcracks which were later verified by Derucher (1977) using scanning electron microscopy:

- Bond microcracks exist between the cementitious matrix and aggregate particles prior to the application of loading.
- Matrix microcracks are bond microcracks that have propagated into the cementitious matrix.
- Aggregate microcracks occur just before failure is reached.

Microcracking process

The microcracking process was also observed by Nemati & Monteiro (1997) and Nemati et al. (1998). According to Nemati & Monteiro (1997) and Nemati et al. (1998), microcracks form as a result of local tensile stresses that are tangential to the the boundary of pores in the ITZ, as illustrated in Figure 2.1. From the pore boundaries the microcracks propagate into the matrix and then join with microcracks that are initiated in the matrix. The process is similar under tensile loads. If an applied tensile load is increased past the initiation threshold, existing microcracks propagate and further microcracks are progressively initiated in the ITZ of smaller aggregate particles (Karihaloo 1995). Microcrack initiation and propagation cause the pre-peak non-linearity that is seen in typical tensile stress-strain diagrams.

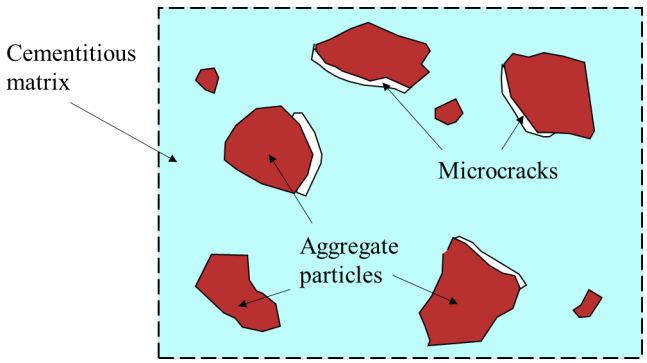

Figure 2.1: Diagram of microcracks at the interface between the cementitious matrix and aggregate particles. Adapted from Hearn (1999).

Influence of the ITZ

Crack initiation in concrete is related to the ITZ which acts as a weak zone. Kaplan (1963) cited by Karihaloo (1995) measured the strain at the initiation of microcracking in concrete under different tensile tests. It was found that the onset of microcracking only depended on the volume fraction of coarse aggregate in the concrete. This suggests that the onset of microcracking is based on the availability of matrix-aggregate interfaces where cracking can initiate. Note that although Kaplan (1963) suggests that the initiation of microcracking only depends on the the availability of matrix-aggregate interfaces, the relative properties of the cementitious matrix and aggregates, as well as the porosity of the matrix would also have an influence.

2.2.2 Crack localisation

Introduction

For concrete, fibre-reinforced concrete and other quasi-brittle materials, crack localisation is the formation of localised macrocracks via the coalescence of microcracks. Localisation of diffuse microcracks to localised macrocracks leads to failure in quasi-britle materials. However, there has been limited experimental work on studying localisation.

Tensile loading

Localised concrete behaviour was first measured by Evans & Marathe (1968) under uniaxial tension by ensuring that the localised macrocrack develops within the gauge length. The gauges around this localised zone measured a strain softening stress-deformation behaviour that early studies were not able to measure. If the gauges had been placed outside the localised zone then unloading of the specimen would have been measured (Van Mier 1997).

The onset of localised cracking has been studied with quantitative acoustic emission (AE) techniques. Quantitative AE was applied to concrete under uniaxial tension by Li & Shah (1994), Li (1996) and to mortar under three point bending by Landis & Shah (1995). AE events were concentrated at the localised zone between approximately 80% of the pre-peak load and 80% of the post peak load in the tests by Li & Shah (1994), Li (1996). AE events were concentrated at the localised zone at aproximately 75% of the peak load in the tests by Landis & Shah (1995). The peak load is illustrated in Figure 2.2.

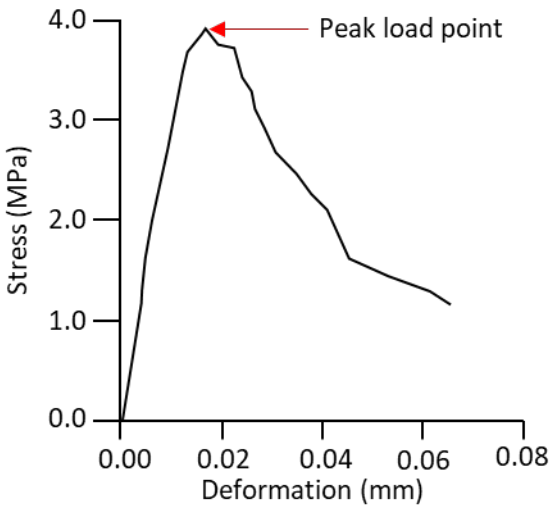

Figure 2.2: Diagram illustrating the peak load point during a uniaxial tension test by Li & Shah (1994). Reproduced from Li & Shah (1994).

Compressive loading

The failure of concrete under compressive loads is also a localisation phenomena. Van Mier (1984) tested prismatic concrete specimens of different heights under uniaxial compressive loading. The post peak stress-strain response of the different specimens depended on the specimen height. However, when the post-peak stress-displacement curves of the specimens are compared, it is clear that the same deformation is required to cause fracture. Localisation of cracking explains why the stress-strain responses of the specimens were not similar even though the stress-displacement responses were similar. Localisation of cracking means that cracking is concentrated to a cross-section which would be of different size for the specimens hence why the post-peak stress-strain response is different.

The onset of localisation in compression has been studied. Vonk (1992) found that localisation occured at peak stress. The same result was also suggested by Torrenti et al. (1991), Vonk (1992), Torrenti et al. (1993), Puri & Weiss (2006). Torrenti et al. (1991) and Torrenti et al. (1993) tested prismatic concrete specimens under uniaxial compression. Torrenti et al. (1993) varied boundary conditions by altering whether platen rotation was allowed and whether an antifriction system was used. Cracking patterns were analysed with strerophotogrammetry in both studies and localisation was found to occur at peak stress. Vonk (1992) carried out uniaxial compression tests of prismatic concrete speciments. Cracking in the specimens was analysed fluorescent epoxy resing vacuum impregnation method. Vonk (1992) found that the crack growth became unstable and localised at peak stress. Puri & Weiss (2006) tested concrete cylinders under uniaxial compression.

Microcracking of the specimens was analysed using an acoustic emission method. Puri & Weiss (2006) suggests that crack localisation occurs at peak loading based on their analysis.

Jansen & Shah (1997) tested concrete cylinders under uniaxial compression. Visible cracks and the development of a localised failure zone were observed post peak stress. Longitudinal cracks extended from the failure zone resulting in single shear or cone-type failure. According to Jansen & Shah (1997), compression tests of concrete cylinders were carried out by Shah & Sankar (1987). The crack patterns were analysed using a petrographic method. Localisation was found to occur just prior to the peak stress.

Unstable crack growth

According to Shah et al. (1995), the growth of a macrocrack which begins to form in the pre-peak regime is stable i.e. the crack only propagates with increasing load. In the post-peak regime, unstable localised macrocracking occurs with unloading of the material outside of the localised region. Microcracks starting to coalesce to a macrocrack coincides with a distinct jump in the rate of dissipated acoustic energy as was observed by Li & Shah (1994), Li (1996) and Landis & Shah (1995) - detailed above. During uniaxial tension tests on plain mortar and mortar with pre-arranged aggregates, Maji & Shah (1988) also observed a sharp increase in AE events prior to the peak load. However, the highest rate of AE events occurred just after the peak load. This is consistent with the notion that unstable macrocrack growth occurs after the peak load.

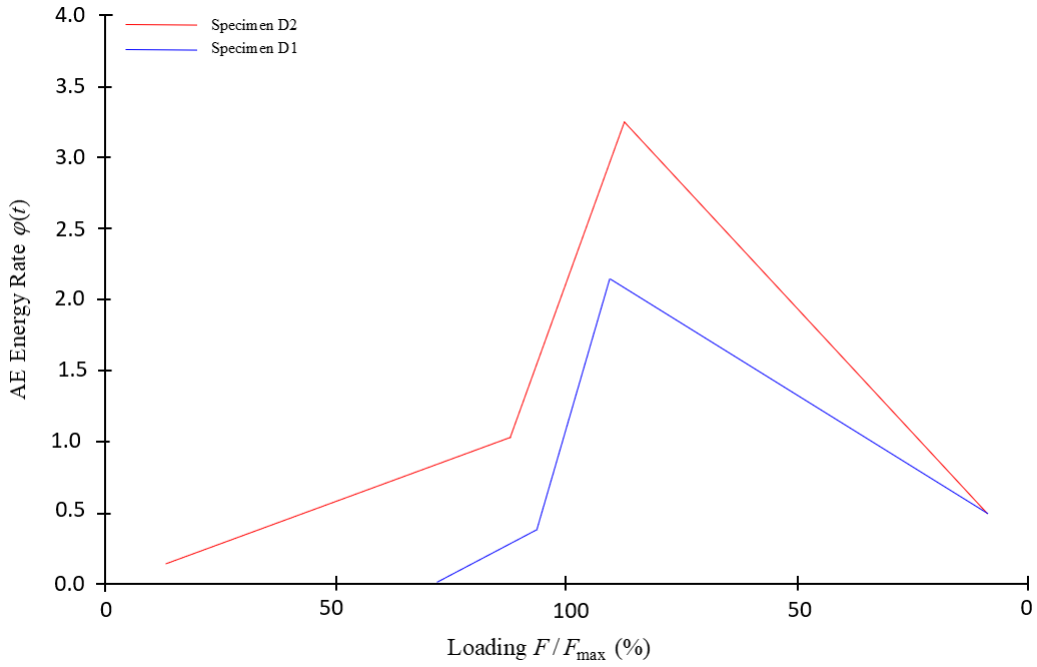

Figure 2.3: Diagram showing the evolution of the acoustic energy release rate where F_{max} is the peak load and F is the applied load. The AE energy rate was calculated by measuring the AE energy (J) over the time interval corresponding to a crack mouth opening displacement of 1μm. Reproduced from Alam & Loukili (2017).

The jump in the AE rate has also been seen under other loading cases e.g. the work of Puri & Weiss (2006), Alam et al. (2014), Alam & Loukili (2017). Alam & Loukili (2017) used a combination of acoustic emission techniques and DIC to study the fracture of concrete beams under three point bending. From 90% of the pre-peak load to 80% of the post-peak load, Alam & Loukili (2017) observed a distinct jump in the acoustic energy release rate - see Figure 2.3. The phase of increased energy release rate coincided with the transition from diffuse microcracking to discrete cracking. Performing the same test and analyses on concrete beams, Alam et al. (2014) also showed a similar jump in the acoustic energy release rate. Microcracks were observed by Alam et al. (2014) to coalesce to form localised cracks in the post-peak phase with higher acoustic energy release rate.

Puri & Weiss (2006) report that for concrete cylinders under compression, the rate of acoustic energy dissipated jumps at the peak stress. The jump in acoustic energy rate coincided with the formation of a localised compression damage zone and continues untill 60% of the post-peak stress.

2.2.3 Macrocracking

Fracture process zone

The growth of a macrocrack in concrete under tension derives from the fracture process zone (FPZ). In early literature, the existence of the fracture process zone was debated and measurement methods were not uniform (Mindess 1991). Mindess (1991) described the confusion as *"... the old story of a group of blind men trying to describe an elephant."* Current literature defines the FPZ as the localised zone of microcracking in front of a macrocrack (Zhou et al. 2021). Existence of the fracture process zone and the cause of of the tension softening behaviour has been confirmed through experiments as described below.

The initiation of microcracks near the tip of a macrocrack begins the development of the FPZ. The microcracks develop around the tip of the macrocrack because of a high state of stress (Shah et al. 1995). This process is known as microcrack shielding. According to Otsuka & Date (2000), it is possible to detect microcrack shielding with optical microscopy, electron microscopy, acoustic emission methods and laser speckle methods. X-ray, laser interferometry and laser holography methods have also been used to detect microcrack shielding (Li & Maalej 1996). Early work includes Cedolin (1987), Struble et al. (1989). Cedolin (1987) detected microcracked zones ahead of macrocrack tips with laster interferometry in concrete under tension. Struble et al. (1989) detected microcracking zones ahead of the tips of macrocracks in hardened cement paste with a scanning electron microscope. Otsuka & Date (2000) observed that the microcracking zones ahead of notches in concrete specimens grow as the applied load increases.

Crack bridging

Aggregates and unbroken material ligaments bridge cracks such that they are able to transfer stress across the crack until the aggregate or ligament is fractured or pulled out. Studies have shown that the bridging of cracks causes the strain softening behaviour of concrete (Li & Maalej 1996). Bridging prevents the stress transfered by concrete from dropping to zero immediately on the formation of macrocracks. Struble et al. (1989) detected bridging of cracks by unfractured material ligaments in hardened cement paste with scanning electron microscopy. Van Mier (1991) tested concrete plates under uniaxial tension. Using a vacuum impregnation method, bridging of cracks by material ligaments was observed. As will be discussed in later sections, fibres-reinforcement in concrete also bridges cracks.

Macrocrack paths

The path that macrocracks follow depends on the strength of the aggregates. Bentur & Mindess (1986) studied the crack patterns of wedge loaded conventional concrete, lightweight concrete and high strength concrete cantilever beams and studied the crack patterns with a microscope. For the conventional concrete beam, Bentur & Mindess (1986) saw that macrocracks went around aggregates and were tortuous. For the high strength concrete beam at the normal loading rate, the observed cracking patterns were similar. A difference in cracking pattern was observed for the lightweight concrete beam with the crack path going through the aggregate. When the loading rate was increased, the cracks in the high strength concrete beam also went though the aggregates. The crack paths were discontinuous.

2.3 Fibre-reinforced concrete

2.3.1 Introduction - the crack-bridging mechanism

Significant research has been devoted to improving the low cracking resistance of concrete over the last six decades. One of the main avenues for this research is the addition of randomly distributed short fibres into a cementitious matrix.

The underlying mechanisms behind the improvements in material behaviour due to the addition of fibres is crack-bridging by the fibres. As cracks widen, fibres that cross the cracks become debonded from the cementitious matrix and slip until they are pulled out. During the process, the fibres apply closure tractions to the crack faces which leads to stabilisation of crack growth (Lin & Li 1997). Conventional fibre-reinforced concrete (FRC) uses low volume fractions of fibres and has an increased fracture toughness compared to plain concrete though the post-peak behaviour does not differ considerably (Fantilli et al. 2009). The effects of the crack-bridging mechanism on the cracking process are given in the sections that follow.

When sufficiently high volume fractions of short fibres are used, sufficient load can be transferred after first cracking to allow the material to exhibit strain-hardening and multiple cracking behaviour (Lin & Li 1997). Strain-hardening behaviour for cementiitous composites reinforced with short steel fibres was first observed by Li (1998). Such composites are referred to as high performance fibre-reinforced cementitious composites (HPFRCCs). In the context of fibre-reinforced concrete, the “high performance” definition refers to the post-cracking strength being greater than the cracking strength (Naaman 2011). Section 2.3.3

will discuss this phenomena in greater detail.

2.3.2 Prevention of unstable microcrack widening and unstable microcrack growth

The addition of fibres to concrete reduces crack widths. For example, Lakavath et al. (2020) carried out three-point bending tests on concrete beams with varying volume fractions of hooked-end steel fibres. Using digital image correlation (DIC) it was concluded that crack widths decrease with increasing fibre volume fraction. More recent studies focusing on hybrid or multiscale fibre-reinforced composites also show that fibres delay microcrack opening. Lawler et al. (2003) carried out uniaxial tension tests of mortar specimens reinforced with PVA and steel microfibres and steel macrofibres. Cracking was analysed with a DIC method. The microfibres were observed to be more effective than macrofibres at delaying microcrack propagation because the smaller spacing between fibres meant that there was greater chance of bridging microcracks.

Much work has been carried out by Li and co-workers over the last few decades on using the ability of fibre-reinforcement to delay unstable microcrack growth. This led to the creation of a new class of fibre-reinforced concrete called "engineering cementitious composites" or ECCs (Lin & Li 1997, Wang & Li 2007, Li 2019). ECCs are designed so that the interactions between fibres, the fibre/matrix interface and the matrix give controlled crack widths and multiple cracking. Multiple cracking leads to toughening of the composite subsequently increasing the tensile strain capacity to typically 200 times greater than conventional FRC. In addition to the volume fraction of fibres, the parameters which control whether strain-hardening behaviour is achieved include the fibre aspect ratio, fibre mechanical properties, the matrix properties and interfacial properties such as chemical and frictional bonds.

An example of tests in which multiple cracking was observed is Moreno et al. (2014) who tested prismatic hybrid fibre-reinforced concrete specimens. Steel macrofibres, PVA-microfibres and a steel reinforcing bar were used in the specimens. The fibres were able to delay unstable microcrack propagation leading to multiple cracking behaviour. See section 2.3.3 for more details about the multiple cracking behaviour in fibre-reinforced composites.

2.3.3 Crack localisation

The localisation behaviour of fibre-reinforced cementitious composites under tension depends on whether the composite is strain softening or strain-hardening.

In strain softening composites, the formation of the first through crack or percolating crack coincides with crack localisation (Naaman 2008). Whereas in strain-hardening composites, the formation of the first through crack coincides with multiple cracking (Naaman 2008) and localisation coincides with fibre pull-out after the peak stress point. According to Choi et al. (2016), fibres support most of the load once a cracked plane has developed in the matrix. The tensile behaviour is then controlled by the pull-out of fibres from the matrix. The typical behaviour of fibre-reinforced cementations composites is shown in Figure 2.4.

Generally, using sufficiently high volume fractions of fibre reinforcement prevents crack localisation from occurring. As described in section 2.3.2, the addition of fibres to a cementitious composite can delay unstable microcrack propagation leading to multiple cracking behaviour. Some other examples of experiments where multiple cracking behaviour has been observed include Mobasher et al. (1990), Wille et al. (2011), Kwon et al. (2014), Magalhães et al. (2014). Mobasher et al. (1990) reinforced dog bone cement specimens with 8% and 12% volume fractions of polypropylene fibres. The dog bone specimens were loaded with uniaxial tension and the resulting cracks were analysed with reflective holographic interferometry and quantitative image analysis. Mobasher et al. (1990) observed that the fibres prevented unstable microcrack propagation and so localisation did not occur. Wille et al. (2011) carried out uniaxial tension tests of ultra-high-performance concrete reinforced with 1% steel fibres. The response of the composite was strain-hardening and multiple cracking was visually observed. Kwon et al. (2014) observed multiple cracking during the uniaxial testing of hybrid fibre-reinforced concrete dog bone specimens.

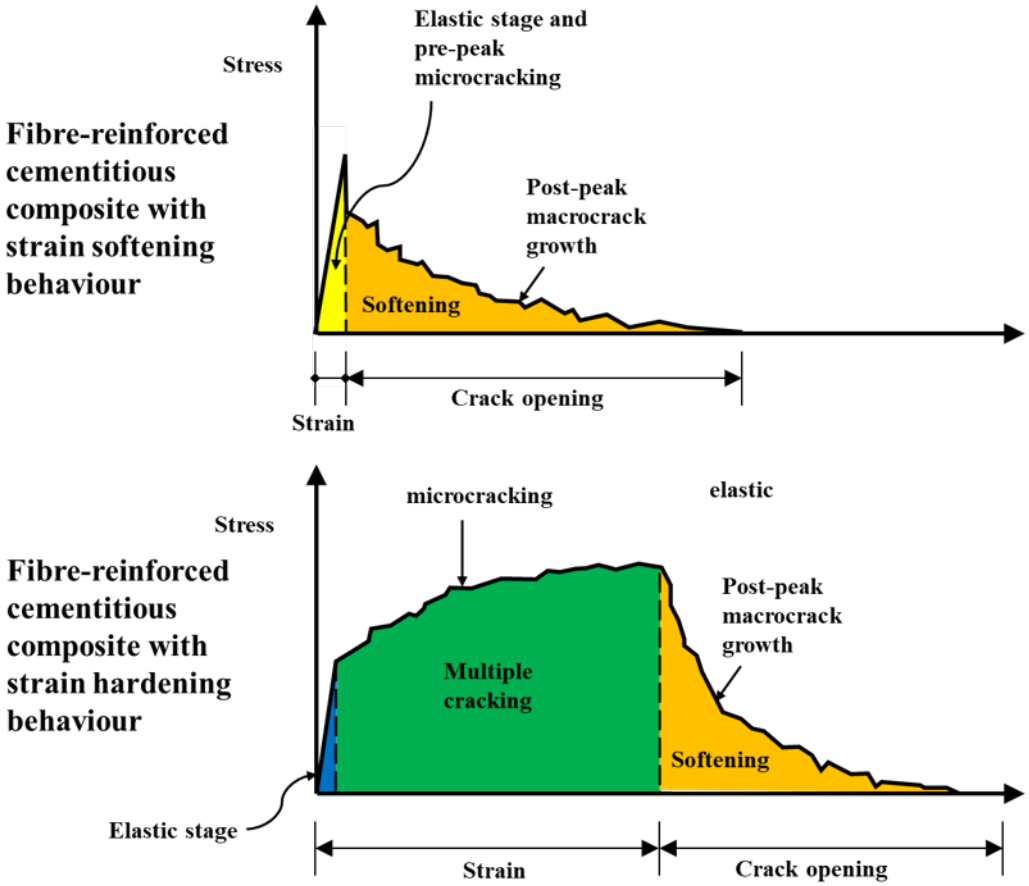

Figure 2.4: Diagram of the typical behaviour of fibre-reinforced cementious composites. Adapted from Naaman (2008).

Studies have been carried out confirming that localisation in fibre-reinforced strain-hardening cementiious composites occurs after the peak stress. For example, a comparative study of crack formation in strain-hardening cementitous composites has been published by van Zijl et al. (2016). As part of the comparative study, Magalhães et al. (2014) tested PVA fibre-reinforced strain-hardening cementitious composites under uniaxial tension. Multiple cracking followed by localised cracking at peak stress was reported.

2.3.4 Macrocracking

Delay in macrocrack growth

Fibres strongly bonded to the matrix can delay the development of the FPZ ahead of macrocracks. Nelson et al. (2002) carried out fracture toughness tests of fibre-reinforced concrete. With a microscope and AE, polyvinyl fibres were seen to delay the formation of microcracks in the FPZ. Polypropylene fibres were seen to not be able to provide the same effect. According to (Nelson et al. 2002), the Polypropylene fibres were not able to delay microcrack formation because the

chemical and frictional interfacial bond to the matrix was too weak.

Macrofibres are more effective than microfibres at bridging macrocracks. Lawler et al. (2003) carried out uniaxial tension and flexural tests of hybrid fibre-reinforced mortar specimens. Macrofibres were seen to increasingly carry greater load as cracks widened. Flexural tests of microfibre-reinforced concrete and macrofibre-reinforced concrete were carried out by Marković (2006). The macrofibres were seen to more effectively bridge cracks during the flexural tests, leading to enhanced ductility of the specimens.

Toughening

The pull-out of fibres from the cementitious matrix is a major toughening mechanism. Trainor et al. (2013) tested fibre-reinforced reactive powder concrete beams under 3-point bending. The beams were loaded to just past the maximum load and then X-ray computed tomography imaging was used to measure the internal energy dissipation. Trainor et al. (2013) manually measured the distance of fibre pull-out from the digital scans. It was shown that approximately half of the internal energy was dissipated by cracking of the matrix (including increased matrix cracking induced by fibres bridging cracks) and the remaining energy was dissipated by fibre pull-out. About 90% of the internal energy dissipation was accounted for. Later, The work of Trainor et al. (2013) was extended by Landis et al. (2019) to include split-cylinder fracture of ultra-high performance concrete with fibre reinforcement. Fibre pull-out was shown to be the main internal energy dissipation mechanism albeit only 60% of the total energy dissipation was accounted for.

Change in failure mechanism

The inclusion of effective fibre-reinforcement in concrete changes the failure mechanism. Grzymski et al. (2019) carried out compression, splitting tension and bending tests on plain concrete and fibre-reinforced concrete. Both typical hooked-end steel fibres and recycled steel fibres without anchorage were considered. The compression and splitting tests were carried out on cubic specimens and the bending tests were carried out on beams. There was little difference between the failed specimens containing recycled fibres, which were concluded to be ineffective, and the plain concrete specimens. However, the conventional fibre-reinforcement significantly improved structural integrity. The fibres enabled the cubic specimens to retain their shape during compression tests in contrast to the plain concrete specimens which would form an hourglass shape. During the splitting tests, the fibres prevented the cubes from being completely split. The plain concrete beams

would suddenly fail with a crack running vertically through the section. But, the failure of the fibre-reinforced beams was much more ductile and cracks running through the entire section were not able to form.

2.4 Conclusions

In this chapter it was shown that fracture process in cementitious composites is highly complex and involves cracking at multiple scales. Numerical models which aim to capture the entire fracture process should account for the initiation of microcracking, the formation of macrocracks and the transition from microcracking to macrocracking. Chapter 3 will discuss different modelling methods that have been used in the literature to simulate the mechanical and cracking behaviours of cementitious composites discussed in this chapter.

Chapter 3

Review of modelling methods

3.1 Introduction

This section details the current methods for modelling the behaviour of concrete and fibre-reinforced concrete. There is a particular focus on micromechanics based approaches. First, a background is given of classical modelling approaches that have been applied to modelling the behaviours of the above-mentioned materials. Micromechanical models are discussed followed by discussion of the issues related to strain-softening and approaches to overcome these.

3.2 Classical constitutive modelling approaches for plain cementitious composites

3.2.1 Fracture mechanics

Fracture mechanics theory describes the progressive failure of structures caused by initiation and propagation of cracks (Shah et al. 1995). The first fracture mechanics theories were proposed by Griffith (1921) and Griffith (1924). These theories were applicable to brittle materials such as glass. The theories were then developed further to be applicable to elastic-brittle materials such as certain metals (Shah et al. 1995).

Applications of the early linear elastic fracture mechanics (LEFM) theory to concrete were unsuccessful (Karihaloo 1995). LEFM requires that the size of the fracture process zone adjacent to the fracture front is small compared to the cross-section of the structure, however the large size of aggregate particles in concrete leads to the fracture process zone being relatively large (Bažant & Oh 1983). The non-linear behaviour of the fracture process zone in concrete is not accounted for

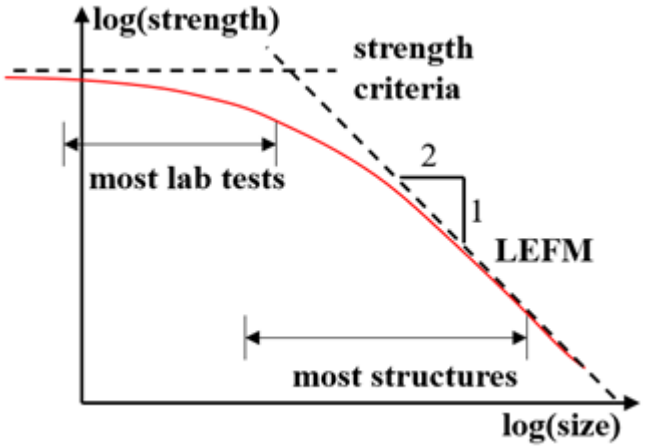

Figure 3.1: Size effect on the strength of concrete structures. Adapted from (Bažant & Planas 1997).

by the brittle description of material behaviour given by LEFM.

Plotting the strength of materials against their size based on strength limits or failure surfaces in terms of stress or strain gives a horizontal line as shown in Figure 3.1. Deviation of material strength from this horizontal line is known as the size effect (Bažant & Planas 1997). The strength criteria of small concrete structures follows the horizontal line (Bažant & Planas 1997). LEFM predicts failure along an inclined line with slope -1/2 i.e. geometrically similar structures exhibit an inverse square root size effect (Bažant & Planas 1997). Bažant & Planas (1997) analytically derived the inverse square root size effect by setting up general expressions for fracture energy and stress intensity factors and considering the implications of limit analysis on the size effect. For large concrete structures, such as dams, the size of the fracture process zone is relatively very small so failure follows LEFM (Karihaloo 1995). The behaviour of most concrete structures fall within a transitional range between the predictions of strength criteria and LEFM.

Within LEFM, the general stress state can be reduced to a combination of three states (Karihaloo 1995):

- Mode I, or the opening mode, where there is a planar symmetric stress state with stresses normal to the plane of the crack.
- Mode II, or the sliding mode, where there is a planar antisymmetric stress state causing relative displacement of the crack faces in their own plane.
- Mode III, or the tearing mode, where a shear stress causes an out of plane deformation of the crack faces.

Non-linear fracture mechanics based models have been developed that describe the behaviour of concrete. For example, see section 3.3.5 for an example of a model that combine fracture mechanics and micromechanics.

3.2.2 Total stress-strain

Early modelling efforts focused on using total stress-strain models which describe algebraic relationships between the total stresses and strains. The algebraic relationships are generally based on curve fitting and can be simple to implement. However, a single explicit algebraic form cannot capture the complexity of the full mechanical behaviour and therefore the simplicity of these approaches tends to be lost when aiming to simulate the behaviour more broadly (Bažant & Tsubaki 1980).

The total stress-strain approach has been applied to concrete e.g. by Cedolin et al. (1977), Kotsovos & Newman (1979), Palaniswamy & Shah (1974), Bažant & Tsubaki (1980), He et al. (2006). Application of the approach has also been made to reinforced concrete by Hofmeyer & Van den Bos (2008).

3.2.3 Plasticity

Plasticity models are widely used for the modelling of non-linear material behaviour (Kaneko 1995, Hartmaier 2020) including the behaviour of cementitious materials (William & Warnke 1975, Dragon & Mróz 1979). Plasticity models divide strains into an elastic part and a plastic part and make use of a yield function, flow rule and hardening function.

Yield functions define a surface that bounds the elastic domain in the stress space. For stress states inside the yield surface, strains are elastic. For stress states on the yield surface, plastic strains occur. Stress states outside of the yield surface are not permissible. The condition for yield is typically expressed as:

$$f(\boldsymbol{\sigma}, \kappa) \leq 0 \tag{3.1}$$

where $\boldsymbol{\sigma}$ is the stress tensor and κ is the hardening variable. The state of the material is such that $f > 0$ is not admissible and so either $f = 0$ or $f < 0$. According to de Souza Neto et al. (2008), the most used yield functions include the Tresca criteria (Tresca 1868) and the von Mises criteria (von Mises 1913) which describe plastic yielding in metals and the Mohr-Coulomb criteria and Drucker-Prager criteria (Drucker & Prager 1952) which describe plastic yielding for pressure sensitive materials such as soils, rocks and concrete.

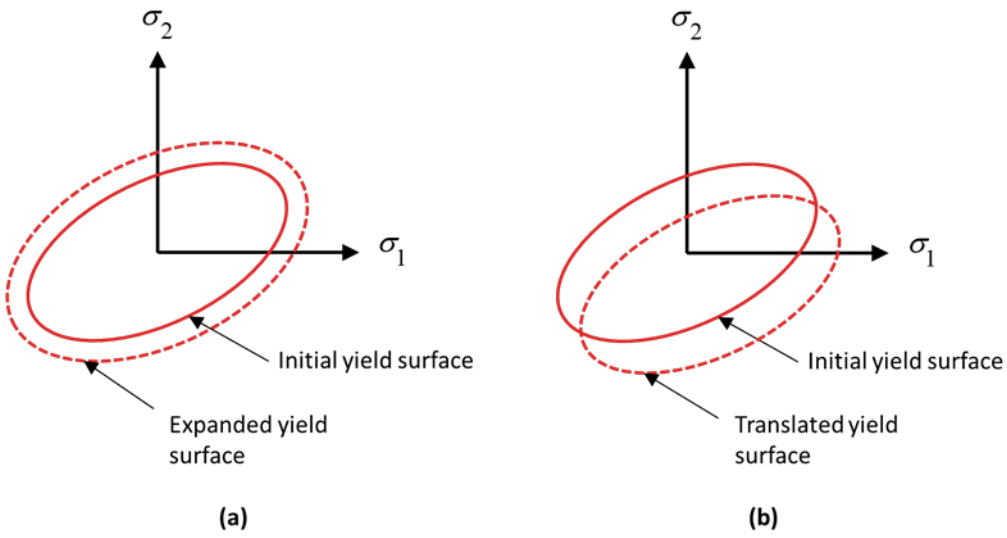

Figure 3.2: (a) Isotopically hardening yield surface, (b) kinematically hardening yield surface.

Evolution of the yield surface is based on a hardening function. The two basic types of hardening functions are isotropic hardening and kinematic hardening. For isotropically hardening materials, as the plastic deformation increases, the yield surface remains centred and expands uniformly in all directions as shown in Figure 3.2a. Alternatively, for kinematically hardening materials, the yield surface translates in the stress space with plastic deformation but does not expand (see Figure 3.2b).

The evolution of the plastic strains is controlled by the flow rule. A general flow rule is shown below:

$$\boldsymbol{\delta\varepsilon_p} = \lambda \frac{\boldsymbol{\partial\psi}}{\boldsymbol{\partial\sigma}} \tag{3.2}$$

$\boldsymbol{\delta\varepsilon_p}$ is the incremental change in the plastic strain and λ is the incremental plasticity multiplier. The plasticity multiplier is a positive scalar variable which describes the magnitude of plastic deformation. ψ is the plastic potential which is used to define the flow vector $\frac{\boldsymbol{\partial\psi}}{\boldsymbol{\partial\sigma}}$. The flow vector describes the direction of plastic deformation. When the yield function is chosen as the plastic potential, the flow rule is called an associative flow rule and plastic straining occurs in a direction that is normal to the yield surface. Flow rules based on plastic potentials other than the yield function are called non-associative flow rules.

Plasticity models have been applied to concrete e.g. by (William & Warnke 1975, Dragon & Mróz 1979, Feenstra & De Borst 1995, Imran & Pantazopoulou 2001, Grassl et al. 2002, Mihai & Jefferson 2013*a*, Piscesa et al. 2017, Durand & da Silva

2019). Although these models are able to describe the non-linear behaviour of concrete, the models are not able to describe the state of microcracking and the related degradation of material stiffness. This issue is addressed by the damage approach described in the next section.

3.2.4 Damage

Kachanov (1958) was the first to introduce the concept of damage, however the term continuum damage mechanics was first coined by Hult and used in his paper (Janson & Hult 1977). The concept of damage models is to represent the progressive degradation of material stiffness due to the propagation of microcracks with damage variables. The total stress-strain relation is given as (De Borst & Verhoosel 2017) as:

$$\boldsymbol{\sigma} = \boldsymbol{D}(\omega, \boldsymbol{\omega}, \boldsymbol{\Omega}) : \boldsymbol{\varepsilon} \tag{3.3}$$

where $\boldsymbol{\sigma}$ is the stress tensor, $\boldsymbol{\varepsilon}$ is the strain tensor and $\boldsymbol{D}$ is the secant stiffness tensor. $\boldsymbol{D}$ depends on internal variables such as scalars ω , second order tensors $\boldsymbol{\omega}$, and fourth-order tensors $\boldsymbol{\Omega}$ that describe the degradation of stiffness due to cracking.

The simplest damage models are based on isotropic damage. Scalar damage variables are used to represent degradation of the initial elastic stiffness $\boldsymbol{D_{el}}$:

$$\boldsymbol{\sigma} = (1 - \omega)\boldsymbol{D_{el}} : \boldsymbol{\varepsilon} \tag{3.4}$$

As ω increases from 0 to 1, the material stiffness decreases until a state of complete damage is achieved and no more stress can be carried by the material. The initiation of damage and change in damage is controlled by damage evolution laws that are typically written in terms of strains, stresses or energy.

Early applications of isotropic damage modelling to describing concrete behaviour was carried out by Mazars (1986) and Mazars & Pijaudier-Cabot (1989). The behaviour of concrete is very different when under tensile and compressive loading. To account for the difference in behaviour, Mazars (1986) and Mazars & Pijaudier-Cabot (1989) separate the damage parameter into two scalar parameters ω_c and ω_t. ω_c is controlled by an evolution law for compressive damage whereas ω_t is controlled by an evolution law for tensile damage.

Other models where the damage parameter is separated in tensile and compressive components include Lubarda et al. (1994), Comi & Perego (2001), Faria et al.

(1998), Marfia et al. (2004), Lee & Fenves (1998), Cicekli et al. (2007), Voyiadjis et al. (2008).

The deterioration of stiffness due to the cracking of concrete is an anisotropic process (Van Mier 1997) and therefore anisotropic damage models that employ direction dependent damage variables are able to better represent the behaviour of concrete than isotropic damage models. For the general representation of anisotropic behaviour, models typically employ a fourth-order tensor as the damage variable (Leckie & Onat 1981, Ortiz 1985, Lubarda et al. 1994). Anisotropic damage models for concrete are also formulated with second-order tensors as damage variables (e.g. Desmorat et al. (2007)) although second-order tensors are limited to describing orthotropic behaviour. Whilst anisotropic damage better represents the behaviour of concrete, these models have been avoided as they are complex when coupling to plasticity and application to structural analysis is not straightforward (Voyiadjis et al. 2008).

3.2.5 Plastic-damage

Plastic-damage models combine the damage and plastic approach. Whilst damage models can describe stiffness degradation, they are not suitable for describing inelastic deformation and inelastic volume expansion in compression (Grassl & Jirásek 2006). On the other hand, models formulated using a plasticity framework can capture inelastic deformations and volume expansion but cannot describe stiffness degradation. Plastic-damage models couple damage to plasticity so that damage and degradation of stiffness is related to deformation (De Borst et al. 2012). As concrete fracture is characterised by both plastic deformations and stiffness degradation (Lubliner et al. 1989), plastic-damage models are better able to capture the entirety of the characteristic behaviour.

The stress-strain relation used in these models is typically expressed as:

$$\boldsymbol{\sigma} = (1 - \omega)\boldsymbol{D_{el}} : (\boldsymbol{\varepsilon} - \boldsymbol{\varepsilon_p}) \tag{3.5}$$

where $\boldsymbol{\varepsilon_p}$ is the plastic strain. Examples of plastic-damage models applied to concrete include Lubliner et al. (1989), Grassl & Jirásek (2006), Cicekli et al. (2007), Voyiadjis et al. (2008), Xenos & Grassl (2016), Jefferson et al. (2016), Poliotti & Bairán (2019).

Plastic-damage models for concrete tend to be based on sound thermodynamic principles, however due to the difficulties in defining a damage dissipation potential some models make use of empirically defined damage criteria in place of

thermodynamics-based dynamics criteria (Jiao et al. 2019).

3.2.6 Microplane

Microplane models are based on the hardening plasticity model approach proposed by Taylor (1938).These models expressed the material stress-strain relation based on stress and strain vectors acting on planes of arbitrary orientation (Caner & Bažant 2013). The beforementioned planes are termed microplanes (Bažant & Gambarova 1984). Local constitutive relationships are described independently on microplanes by making use of either a static constraint where the microplane stresses are resolved components of the macroscopic stress or a kinematic constraint where the microplane strains are the resolved components of the macroscopic strain. In the basic formulation of Bažant & Prat (1988), which used a kinematic constraint, the principle of virtual work was used to calculate the overall macroscopic stress from the microplane stresses.

Other early microplane models for concrete include Carol et al. (1992) and Hasegawa & Bažant (1993). More recently, a series of microplane models for models for concrete have been developed from an early M1 version by Bažant & Oh (1985) to a M7 version Caner & Bažant (2013). The models are progressively labelled M1, M2, ..., M7.

An issue with microplane models is that they are difficult to calibrate as they make use of a large number of phenomenological material parameters. For example, according to Qiu (1999), no clear guidance is given by Hasegawa & Bažant (1993) on how to calibrate the 39 parameters of their proposed model.

3.2.7 Conclusion

The classical constitutive modelling approaches described above are phenomenological. Predictions of behaviour are prescribed directly such as through functions for the stress envelope, uniaxial tension and uniaxial compression. The models are fit to experimental data using parameters that typically have no physical meaning.

3.3 Micromechanics modelling approach for plain cementitious composites

3.3.1 Introduction

In contrast to the phenomenological approach, described in section 3.2, micromechanical approaches are mechanistic and use parameters with physical meaning. Micromechanics involves deriving an overall, macroscopic response or properties based on knowledge of the response or properties at the micro-scale. To predict macroscopic behaviour, micromechanical constitutive models combine mechanisms that simulate behaviour at the micro-scale.

Phenomenological models use input parameters that tend to be used to calibrate the overall material response against the experimental data for a particular composite. Typically for micromechanical models the properties of individual material phases, determined from experiments, are used as inputs to the model. This provides motivation for the development of micromechanical models as virtual testing can be carried out using micromechical models by varying the experimentally determined input parameters for individual material phases.

Examples of the application of micromechanics to the prediction of overall properties include the work of Bernard et al. (2003), Pichler et al. (2009) that focuses on estimating the early-age stiffness and strength evolution of cement paste. Micromechanics has also been recently used to upscale the properties of calcium-silicate-hydrate (C-S-H) to predict the elastic and poro-elastic properties of cement paste (Königsberger et al. 2020) and to upscale a failure criterion at the hydrate level to predict the strength of cement paste, mortar and concrete (Königsberger et al. 2018). Some other applications of micromechanics include modelling autogenous shrinkage of hydrating cement paste (Do et al. 2020), modelling the influence of the ITZ on elastic properties of concrete (Sharma & Bishnoi 2020) and predicting the elastic properties and strength of fibre-reinforced concrete (Dutra et al. 2010, 2013).

Much work has also been done on developing micromechanical formulations outside the field of cementitious composites. Micromechanics based solutions have been developed for matrix metal composites (Park & Kwon 2013, Ju & Sun 2001, Sun & Ju 2001), bones (Massarwa et al. 2017, Fritsch & Hellmich 2007, Hellmich et al. 2004), wood (Qing & Mishnaevsky 2010, Sedighi-Gilani & Navi 2006, Hofstetter et al. 2005) and rock (Zhu & Shao 2015, Hazzard et al. 2000).

The following sections detail micromechanical constitutive models for cementitious composites and fibre reinforced cementitious composites.

3.3.2 Rows and arrays of microcracks

Studies were carried out where the localised deformation of concrete and quasi-brittle materials was modelled based on the problems of a row (Horri 1989, Ortiz 1988) or array (Huang & Karihaloo 1992) of micro-cracks. The models were able to predict tensile post-localisation (Horri 1989) behaviour. Transition between pre-localisation and post-localisation behaviours was not predicted, besides when assumptions were made that localisation occurs at peak load.

Early work by Horri (1989) and Ortiz (1988) predicted the tension softening of concrete by applying linear fracture mechanics to the problem of an infinite row of collinear cracks along the eventual failure plane – see Figure 3.3. The 2D model predicted the steep slope of the tension softening curve in the post-peak regime near the peak stress. As the deflection of adjacent straight cracks from each other's plane was not accounted for, cracks ruptured unstably hence the characteristic long tail that is observed in experiments was not simulated. Instead, the inelastic deformation decreases with decreasing stress after a certain maximum value of the inelastic deformation is achieved. Also, Horri (1989) and Ortiz (1988) did not predict the onset of localisation and the model required values of crack density and size at the onset of localisation. As mentioned in section 2.2.3, the path of macrocracks is tortuous with cracks passing around aggregates. Representing well the underlying mechanisms of macrocracking would better capture the overall characteristic behaviour of concrete.

Inclusion of the characteristic long tail in predictions was achieved by Li & Huang (1990) via a 3D tension softening model that considered the problem of an infinite row of penny-shaped microcracks separated by the largest aggregate. Further development of the 3D tension softening model to allow for interactions between neighbouring cracks was carried out by Huang & Karihaloo (1992). In their model, macrocracks were modelled as either an infinite row or doubly periodic array of penny-shaped cracks.

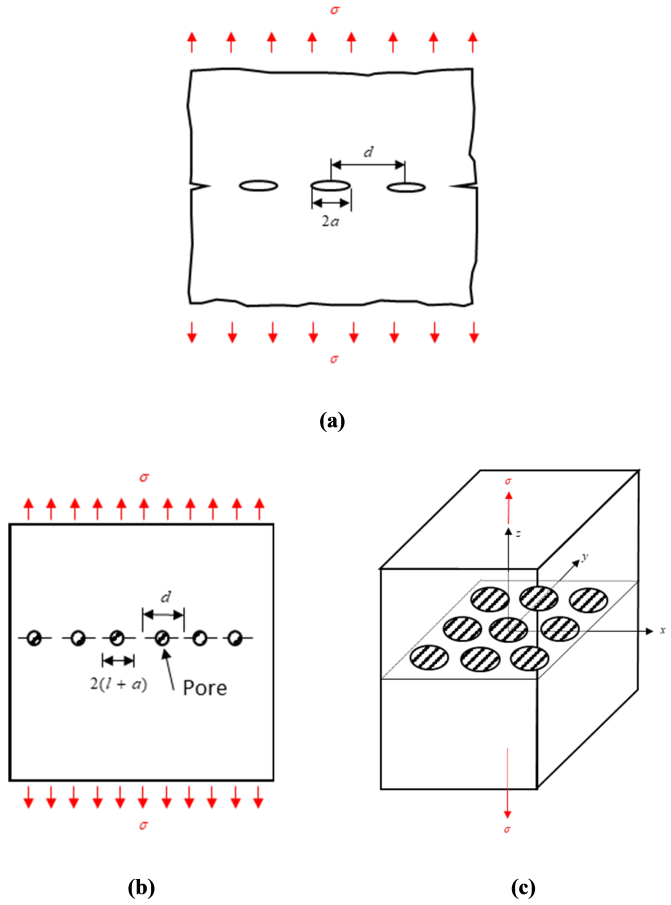

Figure 3.3: Models of (a) Horri (1989), (b) Karihaloo et al. (1991) and (c) Huang & Karihaloo (1992). Adapted from the respective papers.

Later, Karihaloo et al. (1991) expanded on the work of Li & Huang (1990) by allowing interaction between neighbouring cracks in a 2D model. An infinite row of cracks separated by circular holes and unbroken ligaments was modelled in a combined damage mechanics and fracture mechanics approach. The initial damage at the onset of crack localisation was based on experimental values from Karihaloo & Fu (1989).

3.3.3 Continuum micromechanics

Micromechanical solutions have been implemented within the context of continuum based constitutive models. The following sections give a general theoretical background for continuum micromechanics and also a review of various models employing these solutions.

Eshelby matrix-inhomogeniety problem

According to Böhm (2021), a large proportion of the mean-field homogenization methods that are used in continuum models are based on the work of Eshelby (1957). Hence, the matrix-inhomogeniety problem presented in Eshelby (1957) is briefly covered below.

Consider an infinite homogeneous elastic matrix and an elastic inclusion constrained within the matrix shown in Figure 3.4. When the inclusion is "cut" from the matrix and allowed to relax to a state of zero stress, the resulting strain is denoted as the "transformation strain" ε_t. The inclusion is returned to its original shape by applying a surface traction to the inclusion surface. Next the inclusion is returned to the matrix and the surface tractions are removed by applying a cancelling body force. Finally, the resulting strain field of the constrained inclusion, is denoted as the "constrained strain" ε_c.

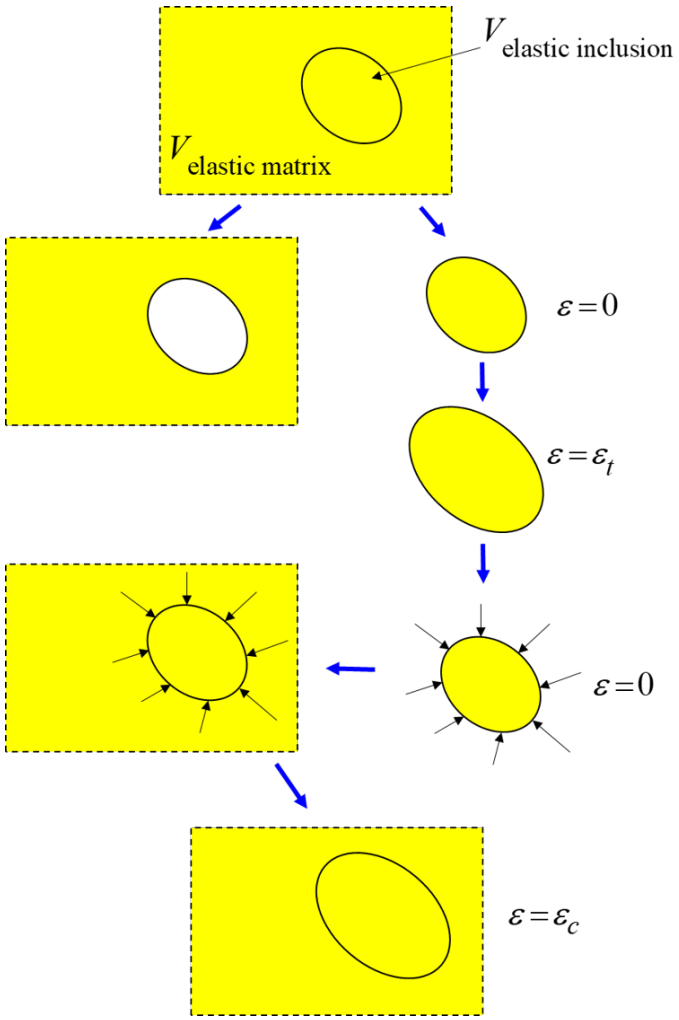

Figure 3.4: The Eshelby solution for determining the strain field of an elastic inclusion in an infinite elastic matrix. Adapted from Withers et al. (1989).

Eshelby (1957) showed that for inclusions that are ellipsoidal, the strain field within the inclusions is uniform and given by

$$\varepsilon_c = \boldsymbol{S}\varepsilon_t \tag{3.6}$$

where $\boldsymbol{S}$ is the interior point Eshelby tensor. Based on this result, it is possible to define an equivalent homogeneous composite for a matrix with an inclusion of a different material constrained within the matrix. This approach has been used to homogenise the elastic properties of a cementitious matrix embedded with aggregate particles (Jefferson & Bennett 2010, Mihai & Jefferson 2017) and also to homogenise cracking (Pensée et al. 2002, Zhu et al. 2008).

Homogenization schemes

As mentioned earlier, a large proportion of the mean-field homogenization methods used in continuum models are based on Eshelby (1957). For example, the non-interacting, or dilute Eshelby, scheme is a mean field method that can be used to homogenise a small volume fraction of spherical inhomogenieties in an elastic matrix (Hill 1965, Benveniste 1987). The Mori-Tanaka scheme is another example of a mean-field homogenization model. Using the scheme, the elastic modulii of ellipsoidal inclusions embedded in an unbounded matrix can be derived (Nemat-Nasser & Hori 1999). Whilst the Mori-Tanaka scheme accounts for the matrix-inclusion interactions, the scheme does not account for the interaction between inclusions (Zhu et al. 2008). Other multiphase schemes for ellipsoidal and spherical inclusions are covered in textbooks such as Nemat-Nasser & Hori (1999).

Averaging schemes do not necessarily consider only spherical or ellipsoidal shaped inclusions. The scheme of Castañeda & Willis (1995) uses tensors to describe the shape of inclusions and their spatial distribution separately and, unlike the previously described Mori-Tanaka scheme, is able to model interactions between inclusions.

For other homogenization schemes such as variational bounding methods and those based on studying discrete micro-geometries, the reader may refer to Böhm (2021).

Solutions for microcracking

Another classical solution used by many continuum micromechanics models is the crack density parameter of Budiansky & O'Connell (1976). The solution is used to describe effects of the development of microcracks on the material state. For

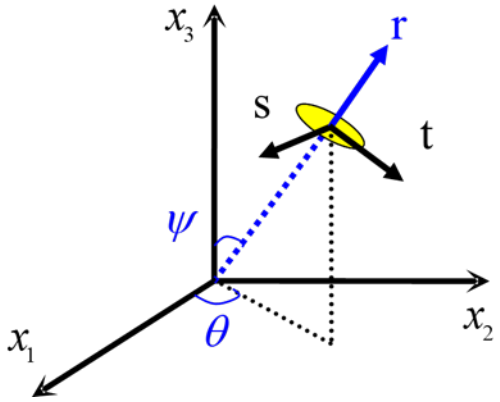

Figure 3.5: Local coordinate system of cracks. Reproduced from Mihai & Jefferson (2017).

example, the added strain tensor $\boldsymbol{\varepsilon}_\alpha$ from a series of penny-shaped microcracks with the same orientation is given by (Nemat-Nasser & Hori 1999, Budiansky & O'Connell 1976):

$$\boldsymbol{\varepsilon}_\alpha = f(\theta_1, \theta_2)\boldsymbol{C}_{\alpha c} : \boldsymbol{\sigma}_L \tag{3.7}$$

where $f(\theta_1, \theta_2)$ is the crack density parameter, $\boldsymbol{C}_{\alpha c}$ is the additional compliance tensor due to the cracks (see below) and ψ and θ are angles that represent the orientation of the cracks as shown in Figure 3.5. $\boldsymbol{\sigma}_L$ is the crack plane stress tensor.

$$\boldsymbol{C}_{\alpha c} = \frac{16(1-{\nu_m}^2)}{3E_m}\begin{bmatrix} 1 & 0 & 0 \\ 0 & \frac{4}{2-\nu_m} & 0 \\ 0 & 0 & \frac{4}{2-\nu_m} \end{bmatrix} \tag{3.8}$$

Models

A generalised anisotropic damage model for brittle materials was presented by Pensée et al. (2002). The model extended a 2D model by Andrieux et al. (1986) to 3D and uses continuum damage mechanics. The model considered a dilute distribution of non-interacting microcracks. Homogenised properties were derived using two equivalent approaches: an Eshelby type approach and an approach based on the free energy of microcracked material (Andrieux et al. 1986). Recovery of stiffness due to the close of microcracks was modelled based on frictionless crack surfaces. The crack density parameter of Budiansky & O'Connell (1976) was used as a scalar damage variable, the evolution of which was formulated based on the free energy of the damaged material. Predictions from the model

were compared to data from uniaxial compressions test for sandstone. The predictions agree qualitatively with the experimental data, but lateral strain was underestimated (Pensée et al. 2002).

Continuing the work of Pensée et al. (2002), an investigation comparing stress-based and strain-based approaches for anisotropic damage models for brittle materials was conducted by Pensée & Kondo (2003). The expressions for free energy from Pensée et al. (2002) were re-established in terms of stress using the Legendre transformation. Both approaches were compared to experimental data for uniaxial compression of sandstone. The stress-based formulation was not able to predict a stress peak hence strain-based formulations are suggested for use in future work.

The next investigation, carried out by Zhu et al. (2008), continued the work by comparing different schemes for homogenising microcracking. The dilute scheme, Mori-Tanaka scheme and the scheme of Castañeda & Willis (1995) were considered. It was shown that only the homogenisation scheme of Castañeda & Willis (1995) took into account the effects of microcrack spatial distribution. The homogenisation scheme of Castañeda & Willis (1995) was later implemented in an anisotropic damage model by Zhu et al. (2009).

Another group of models based on Budiansky and O'Connell's solution for a body with penny shaped microcracks, are those developed by Jefferson, Mihai and co-workers. Initially, Jefferson & Bennett (2007) used a sub-model to simulate the contact that occurs between the rough surfaces. The crack contact model allowed for cracks surfaces to regain contact under shear stresses in addition to normal stresses and so improved upon the work of Pensée et al. (2002) and Pensée & Kondo (2003) where crack surfaces were assumed to be frictionless. Also, a damage rule based on local strains is used instead of an energy-based rule. The Mori-Tanaka averaging scheme was used by Jefferson & Bennett (2010) to derive homogenised elastic properties assuming that the material is composite consisting of a matrix (i.e. the cementitious matrix in concrete) embedded with spherical inclusions (i.e. the aggregate particles in concrete).

The other main developments of the models include the use of the exterior point Eshelby solution such that microcrack initiation is based on the stresses in the ITZ (i.e. the zone between the embedded inclusions and the matrix) (Mihai & Jefferson 2011). Crack bridging by fibres was added to constitutive model by Mihai & Jefferson (2017) based on the work of Lin & Li (1997) and Li et al. (1991) – see section 3.4.2. Some work has also been carried out on enhancing the

robustness of the rough crack closure model (Mihai & Jefferson 2013*b*, 2015).

The micromechanical sub-models used by Jefferson, Mihai and co-workers have also been used in the context of plasticity based model (Mihai & Jefferson 2013*a*) and plastic-damage models (Jefferson et al. 2016, Mihai et al. 2016).

Recently Dutta & Kishen (2019) formulated a 2D continuum micromechanics based constitutive model. Using the Eshelby solution and the Mori-Tanaka averaging scheme, the homogenised elastic properties based on the assumption of a two-phase composite consisting of a matrix phase with embedded ellipsoidal inclusions. Budiansky and O'Connell's crack density parameter was used as the damage variable and the evolution of the damage variable was driven by the strain energy release rate. Although predictions from the model agreed well with experimental data from uniaxial tension tests of plain concrete, other load cases were not analysed.

3.3.4 Crack contact

Approaches where the frictional sliding of cracks is modelled have been used to model the behaviour of brittle and quasi-brittle materials. The models described below were mostly compared against experimental data for compressive stress states.

By considering sets of dilute flat non-interacting microcracks with different orientations and the criteria for their growth and frictional sliding, Gambarotta & Lagomarsino (1993) formulated an anisotropic damage model for brittle and quasi-brittle materials. The model used a scalar damage parameter to represent the relative crack size of an orientation. The predicted cyclic compressive behaviour for concrete was found to be characteristic for the material.

The above model was simplified by Brencich & Gambarotta (2001) by assuming isotropic damage and by only using a single scalar damage variable that represents the overall size of microcracks. Conditions for crack opening and crack closure were defined using two second order tensors that represent the average compressive stress on closed cracks and frictional tractions that limit sliding respectively. Biaxial strength envelopes were seen to agree well with the experimental results for plain concrete and high-strength concrete. However, the triaxial behaviour predictions underestimated material strength.

The next step in the development of the model, carried out by Gambarotta (2004), was to couple the frictional sliding and damage mechanisms such that in the triaxial tensile stress state (i.e. when all cracks are open), only the evolution of

damage occurs. Limit conditions and flow rules were defined on which damage and sliding evolution laws were formed.

As described in the previous section, Pensée et al. (2002) and Pensée & Kondo (2003) developed constitutive models where the normal component of stiffness could be recovered when microcracks close i.e. smooth crack surfaces were simulated. The micromechanical models developed by Jefferson, Mihai and co-workers differ from those of Pensée et al. (2002) and Pensée & Kondo (2003) as they are able to simulate rough crack surfaces regaining contact under both normal and shear stresses (Jefferson & Bennett 2007, 2010, Mihai & Jefferson 2013*b*, 2015).

3.3.5 Fracture process zone and cohesive zone

A combined fracture mechanics (see section 3.2.1) and continuum micromechanics approach can be used to model the fracture process zone. Pichler et al. (2007) developed a 2D model to describe the tension softening inside the fracture process zone ahead of a macrocrack. Linear elastic fracture mechanics was used to derive a criterion for the propagation of a single penny shaped microcrack. The microcrack propagation criteria was combined with micromechanical estimates for material stiffness to form a damage evolution law. Budiansky and O'Connell's crack density parameter was used as a scalar damage variable. Both the dilute homogenisation scheme (with non-interacting microcracks) and the Mori-Tanaka homogenisation scheme (with interacting microcracks) was considered. Neglecting crack interactions was found to predict unrealistic material behaviour.

3.4 Constitutive modelling approaches for fibre-reinforced cementitious composites

3.4.1 Classical constitutive modelling approaches

The classical constitutive modelling approaches described in section 3.2 are also applicable to fibre-reinforced cementitious composites. For example, the plasticity approach has been applied to fibre-reinforced concrete slabs by Barros & Figueiras (2001) and hybrid-fibre-reinforced concrete by Chi et al. (2014). In the two models, the effects of fibre-reinforcement were captured by using functions that were calibrated to match experimental data for fibre-reinforced concrete.

Damage models have been formulated to describe the behaviour of fibre-reinforced concrete and hybrid fibre-reinforced concrete. Such models include Fanella & Krajcinovic (1985), Li & Li (2001), Peng & Meyer (2000). Fanella & Krajcinovic (1985) use an an approach based on the parallel bar model which assumes that

the matrix is brittle and unable to transfer loads once the tensile strength has been exceeded. Then, fibres alone transfer loads. Li & Li (2001) extended the work of Fanella & Krajcinovic (1985) by accounting for the quasi-brittle nature of cementitious composites. However, the model requires the calibration of many parameters using experimental data. Similarly, the model of Peng & Meyer (2000) relies on calibration of material parameters with experimental data such that predictions fit experimental data.

Plastic-damage models have also been applied to fibre-reinforced concrete, for example by Hameed et al. (2013). Hameed et al. (2013) model the effective stress transferred across a crack via sliding fibres by fitting a constitutive law to experimental data for fibre-reinforced composites.

Cedolin & Di Luzio (2004), Beghini et al. (2007), Caner & Bažant (2011), Caner et al. (2013) extended the M4 - M7 microplane models to fibre-reinforced concrete. For terminology refer back to section 3.2.6. The microplane models use a simplified form of an equation from Kholmyansky (2002) to model the bridging stress resulting from fibres bridging an opened crack.

As for the plain concrete models in section 3.2, use of classical constitutive modelling approaches for fibre-reinforced composites has the drawback of not linking to parameters with physical meaning.

3.4.2 Micromechanics modelling approach for fibre-reinforced plain cementitious composites

Rows and arrays of microcracks

Using the same approach of modelling cracks via rows and arrays of microcracks covered in section 3.3.2, works were carried out to model localised deformation in fibre-reinforced cementitious composites. Similarly to the previous models, localisation of cracking is also assumed to occur at peak loading.

A 2D model for the tensile response of short-fibre-reinforced cementitious composites was developed by Karihaloo et al. (1996). To model pre-peak strain softening, an infinite doubly periodic array of cracks subjected to bridging forces was decomposed using a superposition approach. Using the superposition approach eliminated the divergence associated with a double infinite series encountered in previous studies of solids containing 2D multiple crack arrays. The predicted tensile response was found to agree with experimental results for a conventional FRC and cement densified with small particles (DSP cement). However, the tensile response was only studied prior to the coalescence of cracks.

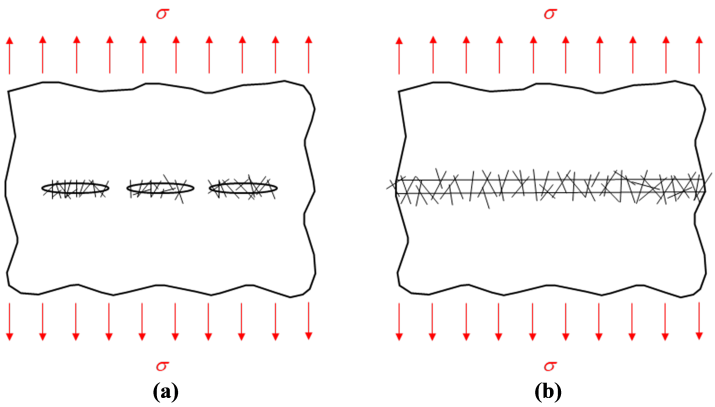

Figure 3.6: Cracks (a) prior to coalescence and (b) after coalescence in the model of Lange-Kornbak & Karihaloo (1997). Adapted from Lange-Kornbak & Karihaloo (1997).

To allow for crack coalescence, Lange-Kornbak & Karihaloo (1997) combined the tension softening model of Karihaloo et al. (1996) with the statistical tension softening model for a continuous macroflaw by Li et al. (1991) – see Figure 3.6. The predicted uniaxial tensile strength agreed with results from the rule of mixtures.

Crack bridging by fibres

Micromechanics has been used to model the pull-out of fibres from cementitious composite. For example, Wang et al. (1988) developed a model to predict the load-crack opening curve from tests of fibre pull-out from a cement matrix. The mechanism of two-sided fibre pull-out was modelled assuming that fibres behaved linear elastically and did not rupture. The distinctive feature of the model was that it allowed for variation of the frictional bond strength with slippage distance thus interface slip-hardening (for synthetic fibres) or slip-weakening (for steel fibres) behaviour could be allowed for. The effects of the fibre elastic bond were considered to be negligible.

The two-sided fibre pull-out model was incorporated into a tension-softening curve model for randomly distributed short fibres in a brittle matrix composite by Li et al. (1991). Statistics were used to account for random fibre embedment depth and orientation so that only fibres crossing the crack plane were considered. Snubbing effects caused by fibre inclination were accounted for using a snubbing friction coefficient. Examples of more recent micromechanical constitutive models incorporating the two-sided fibre-pull out model include Mihai et al. (2016) for fibre-reinforced concrete, Zhang et al. (2019) for hybrid fibre-reinforced cementitious composites under uniaxial compression and Yan et al. (2019) for hybrid

fibre-reinforced cementitious composites under uniaxial tension.

Later, a phenomenological slip-hardening model (Bao & Song 1993) was added to the tension-softening curve model by Lin & Li (1997). The model used two parameters: τ_0 , which is frictional sliding shear stress at the tip of the debonding zone before any slip has occurred, and β a non-dimensional hardening parameter. The linear slip-hardening model constitutive relation was:

$$\tau = \tau_0 \left(1 + \beta \frac{S}{d_f}\right) \tag{3.9}$$

where τ is the interfacial shear stress, S is the interfacial slip and d_f is the fibre diameter.

Further developments in this line of research by Li et al. (1993) and Yang et al. (2008) include micromechanical formulations for aggregate bridging, the Cook-Gordon effect, fibre pre-stress and micro-spalling of the matrix.

3.5 Constitutive modelling of the transition to localised cracking

This section describes works related to developing a constitutive model that is able to capture the transition from microcracking to localised macrocracking.

3.5.1 Combined fracture mechanics and continuum micromechanics model of Jin (2018)

A combined fracture mechanics and continuum micromechanics approach was used to couple a cohesive zone model (CZM) with continuum damage mechanics model by Jin (2018). A non-local (see section 3.6.1) micromechanical damage model was used to describe microcracking behaviour. A potential based cohesive model by Park et al. (2009) was used to describe pure mode I macrocracking. The transition from microcracking to localised cracking was initiated when damage reached a threshold value. The threshold value was set to be the value of damage at which the damaged Young's modulus from the micromechanical model of Kachanov (1987), which allows for crack-interactions, and the non-local micromechanical damage model, which does not allow for crack-interactions, differed. See Figure 3.7.

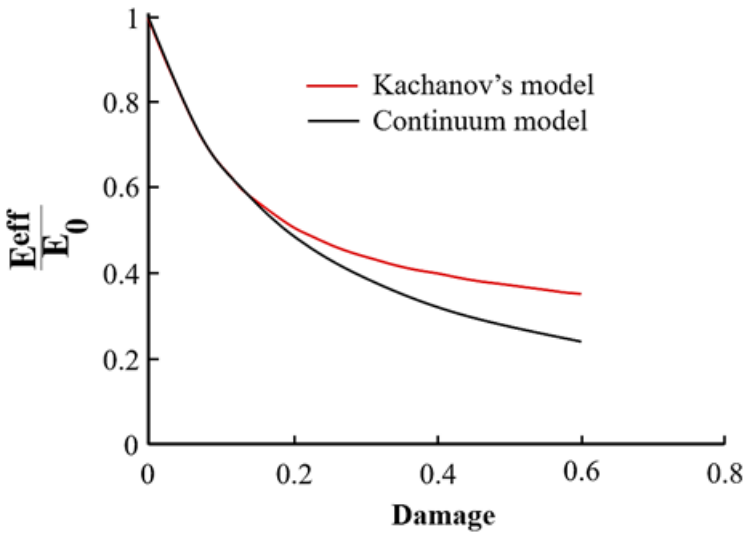

Figure 3.7: Calculation of the damaged Young's modulus from Kachanov's model and the continuum model. Reproduced from Jin (2018).

3.5.2 Micromechanics frictional sliding model of Zhao et al. (2018).

Newer developments in micromechanics based frictional sliding models for quasi-brittle materials, by Zhao et al. (2018), focus on modelling the transition from diffuse microcracking to localised macrocracking. An isotropic micromechanical friction-damage model based on Zhu & Shao (2015) and Zhu et al. (2016) was used to represent the diffuse microcracking behaviour. The transition to localised cracking based on the damage parameter reaching a critical value at which the material resistance to propagation of microcracks is at the maximum (see Figure 3.8). A traction-based friction-damage model was used to describe propagation of a localised crack after the coalescence of microcracks.

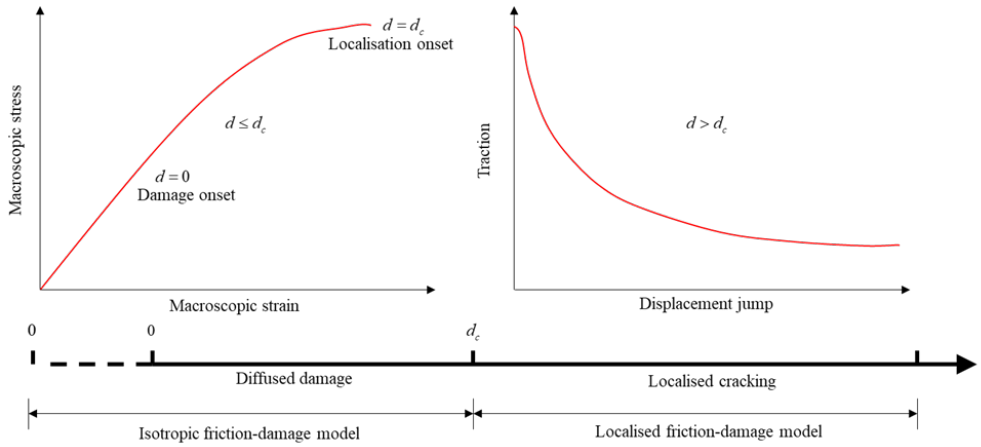

Figure 3.8: The transition from diffuse microcracking to localised macrocracking in the model of Zhao et al. (2018). Adapted from Zhao et al. (2018).

3.5.3 Rows and arrays of microcracks approach for FRC

To enable simulation of the transition from non-localised to localised behaviour, studies by Karihaloo & Wang (2000) and Wang & Karihaloo (2000) focused on investigating conditions for localisation in fibre-reinforced cementitious composites (FRCCs) and short-fibre-reinforced quasi-brittle composite.

Karihaloo & Wang (2000) investigated crack localisation in FRCCs as an instability process caused by perturbations in microcrack size and bridging stiffness. The superposition procedure and solution techniques of Karihaloo et al. (1996) were applied to the problem of five dissimilar rows of bridged cracks which represent the damage zone. It was shown that as the central crack propagates unstably, the applied load reduces and the cracks in the neighbouring rows close. This agreed with experimental observations. A small reduction in bridging stiffness of a row of cracks (caused by reducing the volume fraction of fibres as little as 4%) was found to cause localisation of damage to that row.

Using the procedures of Karihaloo et al. (1996), Lange-Kornbak & Karihaloo (1997), Wang et al. (2000*a*,*b*), Wang & Karihaloo (2000) developed an analytical model for the tensile response of short-fibre-reinforced quasi-brittle composite containing multiple parallel bridged micro-cracks. The classical bifurcation criterion was to examine conditions for localisation in the model.

The findings were as following (Wang & Karihaloo 2000):

- Localisation cannot occur when there is no material damage.
- If fibres remain bonded to the matrix (fibre bridging stiffness > 0) whilst damage has occurred, crack localisation cannot occur even if a continuous crack has formed.
- Loss of the fibre-bridging stiffness due to fibre pull-out, both when a through-crack has formed and when a through-crack has not formed, coincides with crack localisation.

As expected from the discussions in section 2.3.3, the above findings show localisation is related to the crack bridging and fibre pull-out mechanisms of fibre-reinforcement.

3.5.4 Conclusion

From the above sections, it can be seen the the latest constitutive models which include crack localisation use approaches which are based on parameters, such as damage, reaching threshold values. These approaches do not explicitly represent

the fracture process, discussed in chapter 2, that occur during the transition to localised cracking. Also, numerical investigations, in the context of fibre-reinforced cementitious composites, have further reinforced the link between the underlying mechanisms that occur and the crack localisation process.

Sections 3.6, 3.7 and 3.8 which follow will cover computational issues and discrete modelling methods which explicitly represent the crack localisation process.

3.6 Computational issues

Spurious mesh sensitivity is an issue in strain softening models (Pijaudier-Cabot et al. 1988, Brekelmans & De Vree 1995). Strain softening leads to loss of ellipticity of the governing equations and ill-posed mathematical descriptions (Peerlings et al. 1996). Bažant (1976) carried out finite element simulations of concrete with tension softening damage and observed that results depended on the finite element mesh with damage localising to a narrow region. Pijaudier-Cabot & Bažant (1987) showed mesh refinement would lead to localisation of damage into a single element and zero dissipated energy at failure.

Approaches were developed to deal with the issues caused by strain softening. These approaches include the crack band theory (Bažant & Oh 1983), integral type non-local theories e.g. Pijaudier-Cabot & Bažant (1987), Grassl & Jirásek (2006), Bobiński & Tejchman (2016) and gradient enhanced type non-local theories e.g. Peerlings et al. (1996), Addessi et al. (2002), Simone et al. (2003).

3.6.1 Regularisation methods

Crack band theory

The crack band theory was developed by Bažant & Oh (1983) to model mode I fracture in concrete. The theory is based on localisation of damage to a smeared crack band represented by finite elements. To achieve objectivity of the results, fracture energy is maintained for different widths of the crack band. For different band widths, the strength limit is adjusted so that the fracture energy is kept constant. This also subsequently changes the peak load. Alternatively, fracture energy is kept constant for different widths of the crack bank by adjusting the softening curve. The minimum width of the band is commonly believed to be one-element wide; however Jirásek & Bauer (2012) showed using higher-order elements that localisation can occur at a sub-element level.

When using the crack bank method, finite element packages commonly estimate the width of the crack band as the square root of the element area for 2D element

or as the cube root of the element volume for 3D elements. This is disadvantageous as the simplified estimation of the band width introduces mesh sensitivity of elements with large aspect ratios (Mathern & Yang 2021). Also, models can suffer from mesh orientation dependency if the localised band is not aligned with the mesh lines (Slobbe et al. 2013).

The crack band theory has been applied by many models for concrete behaviour and to fibre-reinforced concrete behaviour e.g. Xenos & Grassl (2016), Cunha et al. (2011).

Non-local theory

Pijaudier-Cabot & Bažant (1987) presented the non-local theory in the context of addressing the numerical issues caused by strain localisation. The non-local approach consists of replacing a variable with a weighted spatial average of that variable (Jirásek 2007). The spatial neighbourhood over which an average is taken is defined by introducing a characteristic length. The characteristic length l_{ch} controls the width of zone into which localisation can occur; hence non-local models are described as being localisation limiters. The averaging operations described above can be expressed as (Jirásek 2007):

$$\bar{f}(\xi) = \int_V \alpha(x,\xi) f(\xi) d\xi \tag{3.10}$$

where $\alpha(x,\xi)$ is a weight function depending on the distance between a source point ξ and a target point x. $f(\xi)$ and $\bar{f}(\xi)$ represent the local and non-local fields of a volume V respectively. Models that use the above type of formulation are described as integral type non-local models. A disadvantage of the integral type non-local approach is that it is difficult to implement (Seupel et al. 2018).

Weakly non-local models or gradient-enhanced non-local models involve enhancing the local equivalent strain with the Laplacian of the local strain (Jirásek 2007):

$$\bar{\varepsilon}_{eq} = \varepsilon_{eq} + {l_{ch}}^2 \nabla^2 \varepsilon_{eq} \tag{3.11}$$

where ε_{eq} and $\bar{\varepsilon}_{eq}$ represent the local and non-local equivalent strain. A drawback of the above explicit gradient approach is that it requires calculation of the third-order derivates of the displacements and therefore shape functions must have ${l_{ch}}^2$ continuity (De Borst et al. 2012). An implicit gradient-enhanced approach can be derived by differentiating equation 3.11 twice and substituting the result into

equation 3.11 (De Borst et al. 2012):

$$\bar{\varepsilon}_{eq} - {l_{ch}}^2 \nabla^2 \bar{\varepsilon}_{eq} = \varepsilon_{eq} \tag{3.12}$$

Integral type and gradient-enhanced models have been applied to concrete and fibre-reinforced concrete. For example, see Grassl & Jirásek (2006), Peerlings et al. (1998), Cedolin & Di Luzio (2004), Ahmed et al. (2021).

3.7 Discrete modelling of cracks

3.7.1 Introduction

The work of Ngo & Scordelis (1967) was on of the first to propose a discrete approach for modelling cracks in concrete. Discrete modelling of cracks involves representation of cracks as geometric entities (De Borst & Verhoosel 2017). Early discrete finite element models constrained crack surfaces to the faces of existing elements leading to mesh bias (Ingraffea & de Borst 2017). For example, Ngo & Scordelis (1967) modelled cracking by spitting the existing elements through which a crack passed.

3.7.2 Interface elements

Interface elements with cohesive zone (fracture mechanics) models can be inserted into the mesh to represent cracking if the path is known in advance (De Borst & Verhoosel 2017). This avoids the computationally expensive remeshing that is required if the crack path is not known (Ingraffea & Saouma 1985).

When the crack path is not known a priori, it is possible to consider all element boundaries as potential paths (Carol et al. 2001). Such an approach was used by Xu & Needleman (1994). In addition to avoiding remeshing, another advantage is that results are objective with respect to the mesh size (Carol et al. 2001). López et al. (2008) have applied this approach to concrete.

An alternate method used by Camacho & Ortiz (1996) is to adaptively insert the interfacial elements as required. Zhan & Meschke (2017) applied an adaptive method for modelling concrete and fibre-reinforced concrete where degenerated solid interfacial elements are inserted into the mesh.

3.7.3 Extended Finite Element Method (XFEM)

The extended finite element method (XFEM) is based on enhancing finite elements using the partition of unity concept (Belytschko & Black 1999). Regular finite elements consist of smooth continuous fields in the interior of elements

hence jumps in fields and the derivatives are restricted to the boundaries of the elements (Moës et al. 2017). The XFEM models discontinuities within the elements by introducing enhanced basis terms and additional degrees of freedom for nodes.

As shape functions form a partition of unity, a displacement field u can be interpolated as (De Borst & Verhoosel 2017):

$$u(\boldsymbol{x}) = \sum_{i=1}^{n} \left(N_i(\boldsymbol{x}) \left(\bar{a}_i + \sum_{j=1}^{m} \tilde{N}_j(\boldsymbol{x}) \tilde{a}_{ij} \right) \right) \tag{3.13}$$

where n is the total number of discrete nodes, N_i is the shape function at node i, $\tilde{N}_j$ is the enhanced basis term, $\bar{a}_i$ is the regular nodal degrees of freedom and $\tilde{a}_{ij}$ is the additional degrees of freedom.

3.7.4 Embedded discontinuities

The use of elements embedded with discontinuities is another approach to representing the fracture process in quasi-brittle materials. The approach is based on enriching finite elements with additional degrees of freedom so that discontinuities across cracks can be represented (Feist & Hofstetter 2006).

The discontinuities are the jumps in the strain field (weak discontinuities) or the displacement field (strong discontinuities). In other words, weak discontinuities involve jumps in the gradient of the displacement field with the displacement field remaining continuous whereas strong discontinuities involve jumps across the displacement field itself (Simo et al. 1993). See Figure 3.9 below. Models for concrete cracking based on embedded discontinuities tend to use a strong discontinuity approach e.g. Feist & Hofstetter (2006).

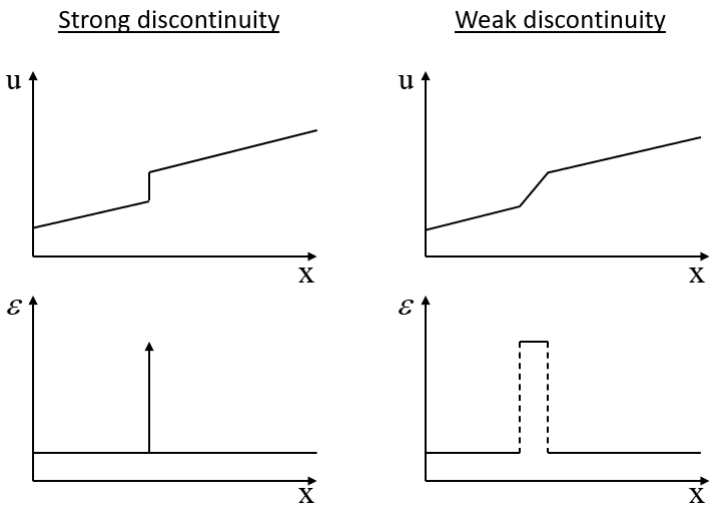

Figure 3.9: Strain localisation with a strong discontinuity and a weak discontinuity. Adapted from Cervera et al. (2004).

Unlike XFEM methods where additional degrees of freedom are attached to the nodes of elements which cross the discontinuity path, the additional degrees of freedom are attached to the elements crossed by the discontinuity path (Oliver et al. 2005). Whilst XFEM methods tend to be more stable, element enrichment via embedded discontinuities is easier to implement and is less computationally expensive (Oliver et al. 2005).

3.8 Multi-scale modelling

3.8.1 Introduction

The multi-scale approach is based on feeding results from smaller scales to larger scales with an aim to improve computational costs and reliability compared to single-scale models (Van Mier 2013). The approach involves simultaneous modelling and coupling two different scales of the material. A homogeneous description is used at the higher scale whereas the lower scale is described heterogeneously using representative volume elements (RVEs) (Gitman 2006). The RVE must be solved at every integration point of the higher level and for every time step for non-linear analysis and so multi-scale models suffer from high computational costs (Otero et al. 2015).

A RVE can only exist for statistically homogeneous materials, hence for materials which show softening and subsequently localised behaviour a RVE does not exist (Gitman et al. 2007). For strain softening materials, reference is made to representative material elements (RMEs) instead of representative volume elements. The RME represents the smallest region of a specimen which captures

the entirety of material strength variation (Joseph 2008).

For concrete, the smallest size-scale, the micro-scale, operates at the level of the cement paste, the intermediate size-scale, the meso-scale, the level of the aggregate structure and the largest size-scale, the macro-scale, the scale of buildings or structures (Van Mier 2013).

Examples of applications of the multi-scale approach to concrete include Eckardt & Könke (2008), Unger & Eckardt (2011), Nguyen et al. (2012), Toro et al. (2016). Application of the approach to fibre-reinforced concrete has been carried out e.g. by Zhan & Meschke (2017). An alternative adaptive multi-scale method has been developed by Rodrigues et al. (2018) where, for an initially homogeneous material, critical regions identified at the macro-scale are enhanced with detailed meso-scale information.

3.8.2 Lattice modelling

Lattice models involve either spatially mapping material properties to a network of lattice elements or by representing the interaction of two aggregates via a single element (Grassl et al. 2012). The elements are typically truss bars or beams (Nikolić et al. 2018). When modelling concrete, these materials are typically aggregate particles, cement and the ITZ.

Some examples of applications of lattice modelling to concrete include Cusatis et al. (2011), Schlangen & Van Mier (1992), Arslan et al. (2002), Kozicki & Tejchman (2008), Spagnoli (2009), Grassl & Jirásek (2010), Grassl et al. (2012), Grassl & Antonelli (2019), Karavelić et al. (2019).

Compared to other discontinuous models it is more simple to implement material heterogeneity in lattice models (Kozicki & Tejchman 2008). This is important because, as discussed in chapter 2, the fracture process in concrete is linked to the material heterogeneities such as aggregate particles and the interfacial transition zone.

In highly non-linear materials, the use of conventional boundary conditions at the edge of a specimen are known to cause stress concentrations at the boundaries subsequently introducing bias into fracture patterns (Grassl & Jirásek 2010).

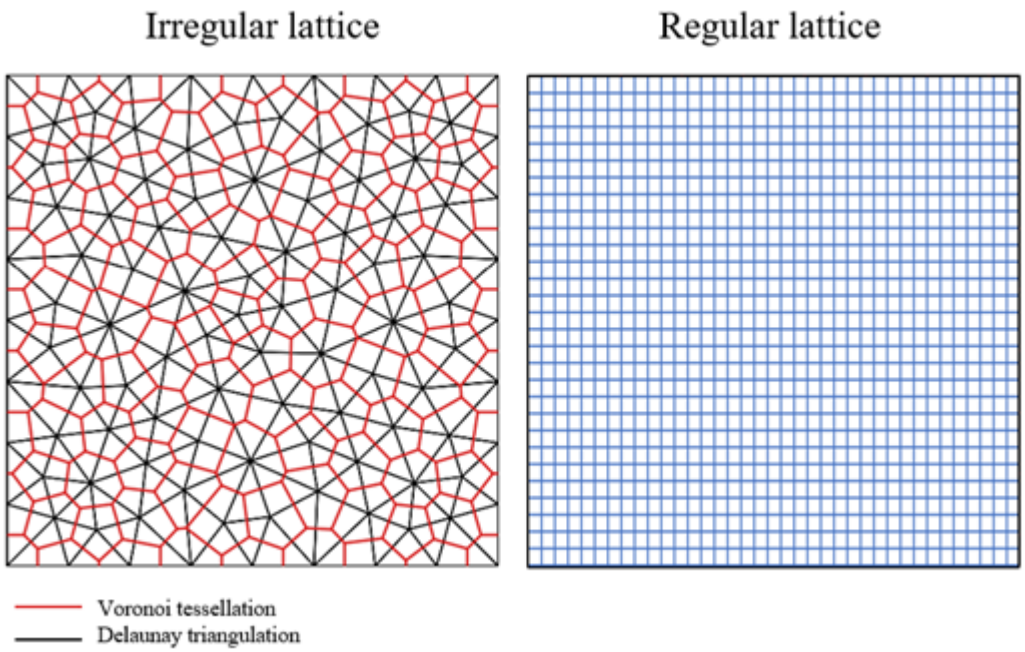

Figure 3.10: 2D irregular lattice and regular lattice. Adapted from Nikolić et al. (2018).

Another issue arises when considering the regularity of the lattice. Figure 3.10 above shows the two different types of lattice regularity: irregular and regular. The use of regular lattices allows for uniform elasticity under uniform straining however, the structured geometry can introduce bias into the directions of crack propagation (Nikolić et al. 2018). On the other hand, irregular lattices reduce the bias in the directions of crack propagation but suffer in terms of producing uniform straining (Nikolić et al. 2018).

Dual Delaunay and Voronoi tessellation is an approach used for generating an irregular lattice to reduce the bias in the directions of crack propagation whilst maintaining a homogeneous response under uniform straining. In this approach, random points placed are used to construct the tessellations. Lattice elements are placed along the Delaunay edges and the element properties are based on the associated Voronoi edges (or cells in 3D) that define the element mid-cross-sections (Grassl & Antonelli 2019). See Figure 3.11.

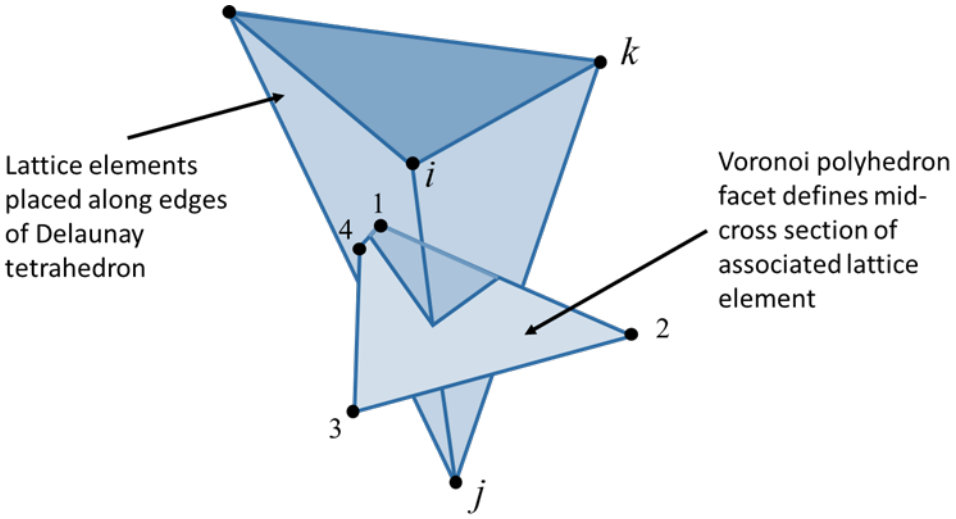

Figure 3.11: Example dual Delaunay and Voronoi tessellation. Adapted from Grassl & Antonelli (2019).

Discrete modelling methods are computationally expensive because of the high number of degrees of freedom involved when accurately representing the heterogeneous nature of the material directly. As discussed previously in section 3.6, when models describe strain softening behaviour, there is a loss of the ellipticity of the governing equations and mathematical descriptions become ill-posed further slowing computations down. To overcome this computational issue, a length scale representing the width of the localised band or zone is introduced using a regularisation method. For example, Berton & Bolander (2006) used the approach of the crack bank method, which involved conserving fracture energy as discussed in section 3.6.1, to formulate a regularised lattice model. A high discretisation resolution is needed to model the localised region as the embedded width of the localised zone is typically very small compared to the domain (Nguyen & Bui 2019).

The introduction of fibres in a lattice model exacerbates the problem of computational expense. Fibres can be modelled by adding elements that are connected to the background lattice (i.e. the elements representing the cementitious matrix and ITZ in the case of fibre-reinforced concrete) via linking elements (Yip et al. 2005). This approach can significantly increase the number of degrees of freedom involved, especially when modelling high volume fractions of fibres. It is possible to model fibres without increasing the number of degrees of freedom by using an alternative approach. Bolander et al. (2008) add the stiffness contributions of fibres crossing Voronoi facets in parallel to the corresponding lattice elements that represent the cementitious matrix phase.

3.9 Conclusions

This chapter detailed various modelling methods used to represent the behaviour of concrete and fibre-reinforced concrete. The advantages of using a micromechanics based modelling approach over a classical phenomenological one were highlighted. Namely, the parameters used in micromechanical models have physical meaning and the mechanistic approach used is in line the current understanding that the macroscopic behaviour of cementitious materials is controlled by the behaviour at the micro-scale. Unlike phenomenological models, micromechanical models rely on experimentally determined input parameters corresponding to the material properties of individual phases. Rather than having to completely re-calibrate the model for changes in the composition of a composite (e.g. volume fraction of material phases) like in phenomenological models, changes are modelled by adjusting the corresponding material properties and there is reduced calibration. Also, examples were given of micromechanical models in this chapter.

Discrete models, whilst having disadvantages such as high computational costs, are able to explicitly represent the mechanism of localised cracks developing. Lattice models in particular are able to represent well the heterogeneous nature of cementitious composites that is known to control the fracture process. As will be shown in the next chapter, these discrete models are valuable in providing an insight into the crack mechanisms that occur during the localisation process.

The state of the art constitutive models which focus on the crack localisation process in cementitious composite were seen to be based on approaches where localisation is triggered once certain parameters reach threshold values - the mechanics of the localisation process were not explicitly accounted for. The models derived and presented later in this thesis address the lack of mechanistic approaches detailed in the literature.

Chapter 4

Micromechanical constitutive model for crack localisation in quasi-brittle materials

4.1 Introduction

Directly observing fracture in concrete is challenging due to the microscopic scale of the events within the fracture process. The development of non-destructive testing and imaging techniques has facilitated the study of crack initiation and propagation in cementitious composites with some very valuable insights into the fracture process. However, even these techniques have limitations in capturing all facets of the crack development process.

One method of gaining an insight into the fracture process is lattice modelling. Lattice modelling is a discrete method that has been used to model the transition to localised cracking in concrete (Grassl & Jirásek 2010, Cusatis et al. 2011, Grassl et al. 2012, Grassl & Bolander 2016, Rezakhani et al. 2017, Karavelić et al. 2019). In lattice models, material properties are mapped to a network of lattice elements or the interaction of aggregate particles is represented by a single element (Grassl et al. 2012). An advantage of using lattice models is that they capture the influence of the meso-structure on macro-scale behaviour by describing the spatial distribution and properties of the material phases. The failure process of concrete at the macro-scale is influenced by the material heterogeneity at the meso-scale e.g. microcracks initiate in the ITZ. Although lattice models represent the intricate meso-structure and complex macroscopic behaviour well, lattice models are computationally expensive because of the high number of de-

grees of freedom involved when accurately representing the heterogeneous nature of the material directly. Also, a high discretisation resolution is needed to model the localised region as the embedded width of the localised zone is typically very small compared to the domain (Nguyen & Bui 2019).

The focus of the work in this chapter is to develop a constitutive model for concrete and other quasi-brittle materials that captures crack localisation. The macroscopic behaviour of such materials is controlled by the heterogeneous structure at the micro and meso-scales. Based on this understanding, this work uses a micromechanics approach where physical mechanisms at the micro-scale, meso-scale and macro-scale are combined to give the overall behaviour.

To guide the modelling of the crack localisation mechanisms, numerical experiments are carried out via a lattice model (Grassl & Antonelli 2019). The results from these discrete analyses are used to verify that the constitutive model gives the expected localised behaviour.

This work builds on a series of micromechanics based constitutive models developed by Jefferson, Mihai and co-authors e.g. Jefferson & Bennett (2007), Mihai & Jefferson (2011, 2017). The two-phase, 3D micromechanical models capture anisotropic effects via modelling the directional microcracking mechanism. Implementation of this constitutive model in finite element simulations is planned for future work. To regularise the model, the smeared crack approach with a non-orthogonal crack band will be used.

The structure of this chapter is as follows: in section 4.2 lattice simulations are used to describe the transition to localised cracking. Section 4.3 details the components of the constitutive model and section 4.4 describes the implementation of the constitutive model via a staggered solution algorithm. In sections 4.5 to 4.6 the results of simulations are presented and discussed, including comparisons with experimental data results from lattice model simulations. Finally, section 4.7 summarises the work and gives concluding remarks.

4.2 Lattice simulation of the transition from diffuse to localised cracking

4.2.1 Lattice model

Concrete is a highly heterogeneous material with an intricate meso-structure and a complex macroscopic behaviour. The failure process of concrete at the macro-scale is influenced by the material heterogeneity at the meso-scale. For example,

the ITZ between the mortar and aggregate particles is a weak zone which plays a role in the localisation of tensile stresses and subsequently crack initiation (Sun et al. 2019). Meso-scale models (e.g. lattice models) are able to capture the influence of the meso-structure on the macro-scale behaviour by describing the spatial distribution and properties of the material phases

The lattice based meso-scale model of Grassl & Antonelli (2019) was employed to carry out a series of simulations in order to study the transition from diffuse microcracking to localised macrocracking. The model describes the meso-structure of concrete by the inclusion of 3 material phases: mortar matrix; coarse aggregate particles and interfacial transition zone (ITZ). A full description of the model is given in Grassl & Antonelli (2019) but a summary of the key model components is given in the following sections for completeness.

4.2.2 Periodic meso-structure generation and network modelling

A representative cell is used to model the meso-structure of concrete. The cell is an idealised representation of the spatial distribution of the meso-structure constituents (see Figure 4.1) and the macroscopic behaviour of concrete is assumed to be represented by the behaviour of the cell. Inside the representative cell, the meso-structure of concrete is modelled as coarse aggregate particles, idealised as ellipsoids, embedded in a mortar matrix with an ITZ between the aggregate particles and the matrix. Fuller's grading curve (Fuller & Thompson 1907) is used to determine the size distribution of aggregate particles of a given volume fraction.

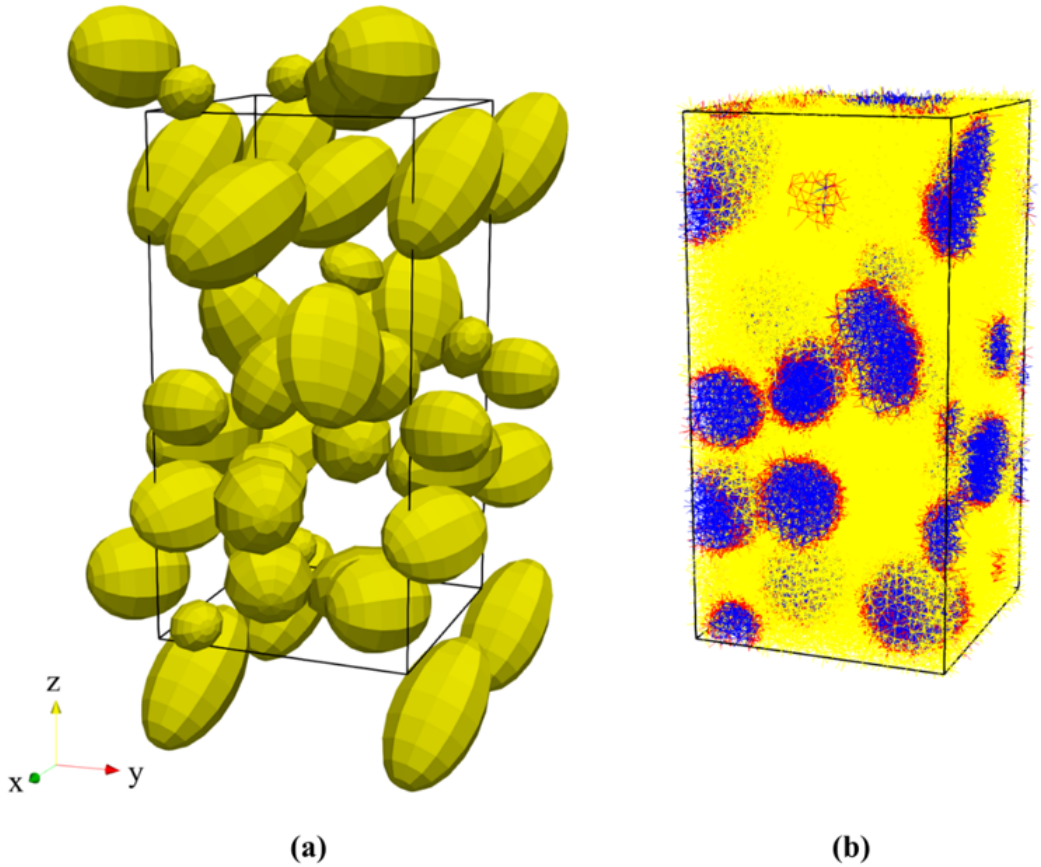

Figure 4.1: a) Periodic meso-structure for aggregate particles. b) Structural element network representing the mortar matrix (yellow), coarse aggregate particles (blue) and ITZ (red) material phases.

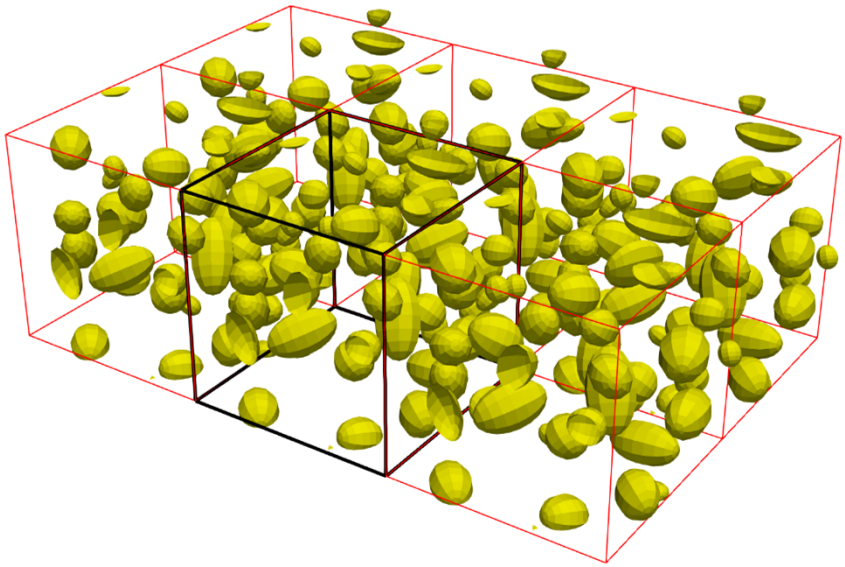

Figure 4.2: Periodic generation of coarse aggregate particles meso-structure. 5 out of a total of 26 adjacent cells containing periodic mirror images of the aggregate particles are shown.

The representative cell is generated by periodically arranging the coarse aggregate particles in the cell as shown in Figure 4.2. The centres of the ellipsoids are placed in the periodic cell using a random sequential addition approach. Overlapping is checked for every placed ellipsoid by considering the inner and outer bounding spheres. If the outer bounding spheres overlap with a previously placed ellipsoid, the ellipsoids do not overlap and 26 mirror images of the ellipsoid are generated in the adjacent cells. If the inner bounding spheres overlap, the ellipsoids do overlap and a new random position and orientation is generated. When the outer bounding spheres overlap and the inner bounding spheres do overlap, an algebraic system of equations from Wang et al. (2001) is used to check for overlapping. For highly non-linear material behaviour, boundary conditions at the boundary of the representative cell are known to cause stress concentrations near the boundary which then cause bias in the pattern of localised cracking (Grassl & Jirásek 2010). Periodicity replaces the boundary conditions and eliminates the undesired bias in the localisation pattern.

To generate a network of lattice elements within the representative/periodic cell, points are randomly placed in the cell and used for dual Delaunay (Delaunay et al. 1934) and Voronoi tessellations (Green & Sibson 1978). Discrete lattice elements are placed along the edges of the resulting tetrahedra with the mid-cross-sections set to be common facets of the Voronoi cells associated with the nodes of the elements (see Figure 3.11). The lattice elements that cross the boundaries of the cell are used to calculate the response of the periodic cell. For the aforementioned boundary elements, only the response of the nodes inside the periodic cell is determined. The response of the nodes outside of the periodic cell is based on the periodic mirror nodes inside the cell and average strain components that are applied to the cell.

The spatial arrangement of aggregate particles is mapped onto the network of structural elements. Elements are given the elastic properties of the matrix, aggregate particles or ITZ depending on their position – see Figure 4.1b. Elements with both nodes within an aggregate particle are given elastic properties representing aggregate particles. Elements with both nodes in the matrix are given properties representing the matrix. Elements with one node in an aggregate particle and the other in the matrix are given properties representing the ITZ. The stiffness of the ITZ is determined as the harmonic mean of the stiffnesses of the matrix and aggregate particles i.e. the stiffness is calculated by considering two springs in series. The use of the harmonic mean captures well the effects of any extremes in the stiffnesses of the matrix and aggregate particles.

4.2.3 Constitutive relationships for the lattice model

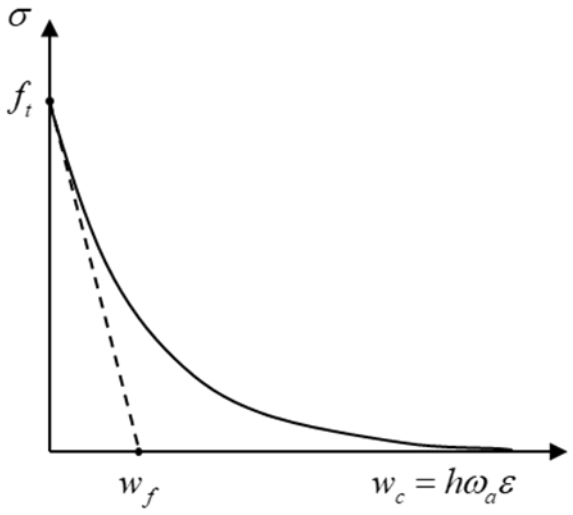

Figure 4.3: Stress-crack opening curve. Reproduced from Grassl & Antonelli (2019).

Aggregate particles are considered to have linear elastic behaviour, whereas the mechanical behaviour of both the matrix and the ITZ is modelled using a scalar damage model:

$$\boldsymbol{\sigma} = (1 - \omega_a)\, \boldsymbol{D}_e \boldsymbol{\varepsilon} \tag{4.1}$$

where $\boldsymbol{\sigma}$ is the stress vector, $\boldsymbol{\varepsilon}$ is the strain vector, $\boldsymbol{D}_e$ is the elastic stiffness matrix and ω_a is a scalar damage variable which increases from 0 at no damage to 1 at complete damage.

Damage onset is determined by an equivalent strain variable κ_d governed by a damage surface based on an ellipsoidal strength envelope in the stress space and standard loading/unloading conditions (Grassl & Bolander 2016). The ellipsoidal strength envelope makes use of three input parameters: tensile strength f_t, shear strength f_q and compressive strength f_c. Based on typical values for concrete, the shear strength and compressive strength are estimated as $f_q = 2f_t$ and $f_c = 10f_t$ (Grassl & Antonelli 2019).

The evolution of the damage variable ω_a is based on the exponential stress-crack opening curve shown in Figure 4.3. w_f is a parameter that controls the slope of the softening curve, w_c is the crack opening and h is the length of the element. The fracture energy $G_f = \int_0^{w_c} \sigma dw$ is the area under the stress-crack opening curve. The exponential stress-crack law for pure tension, shown in Figure 4.3, is ex-

pressed as:

$$\sigma_n = f_t e^{\left(-\frac{w_n}{w_f}\right)} \tag{4.2}$$

where $w_n = \omega_a h \varepsilon_n$ is the crack opening under monotonic tension and ε_n is the tensile strain. As the normal stress can also be expressed using the stress-strain law 4.1, a non-linear equation can be formed and used to determine ω_a iteratively:

$$(1 - \omega_a) E \kappa_d = f_t e^{\left(-\frac{\omega_a h \kappa_d}{w_f}\right)} \tag{4.3}$$

where E is the Young's modulus and ε_n has been replaced with κ_d (a monotonically increasing tensile strain has been assumed). The approach used means that the resulting load-displacement curves will not be dependent on element lengths even if inelastic displacements become localised in element length dependent zones.

4.2.4 Lattice element size for convergence

The lattice elements are placed in a random manner and so the spatial arrangement of the elements may influence the crack paths predicted by the lattice model. However, by ensuring that the lattice elements used are smaller than the size of the heterogeneities of the meso-structure, the influence of the element spatial arrangement is not significant (Grassl & Jirásek 2010).

The overall crack patterns should be independent of the background lattice. To ensure that this is the case, a series of uniaxial tension analyses were carried out. In all cases, the meso-structure (i.e. the arrangement of the aggregate particles) was fixed. Different lattice element sizes were trialled. For each lattice element size, a series of analysis with varying discretisation (i.e. the randomly generated network of lattice elements) was carried out.

Prismatic periodic cells with dimensions of 50 mm in the x and y directions and 100 mm in the z direction were generated (see the coordinate system in Figure 4.1) and the aggregate particles were distributed in the cells with a fixed random arrangement. As the aim of the convergence study was to find the dimensions of the lattice elements that do not cause bias in the overall crack pattern rather than to replicate the characteristic meso-structure of concrete, a high degree of heterogeneity was introduced by using 80% total volume fraction of coarse aggregate.

Table 4.1: Material parameters used for the lattice simulations.

E_m (MPa)	E_{itz} (MPa)	E_Ω (MPa)	$f_{t,m}$ (MPa)	$f_{t,itz}$ (MPa)	$G_{f,m}$ (J/m^2)	$G_{f,itz}$ (J/m^2)
30,000	45,000	90,000	3	1.5	120	60

Table 4.2: The different element sizes and heterogeneity ratios considered.

Heterogeneity/element size ratio	Element size (mm)	Range of aggregate particle diameters (mm)
2.7	3	8 - 16
4.0	2	8 - 16
5.0	1.6	8 - 16
6.25	1.6	10 - 20

The material properties used for the mortar, aggregate particles and ITZ are shown in Table 4.1. The stiffness of the ITZ was calculated as the harmonic mean of the mortar and aggregate particle stiffness. The material properties used are in the typical range for meso-scale analyses of concrete (Grassl et al. 2012).

The ratio of the heterogeneity size (i.e. diameter of smallest aggregate) to the element size was increased starting from approximately 3 until the crack patterns were independent of the background lattice and the stress-displacement response was converged. See Table 4.2 for the different cases considered. Note that reducing the lattice element size below 1.6 mm significantly increased the degrees of freedom of the resulting lattice. Hence for expediency requirements, a higher heterogeneity to element size ratio was achieved by increasing the size of the smallest heterogeneity. The resulting crack patterns and stress-displacement plots are shown in figures 4.4 to 4.7. The analyses for an approximate heterogeneity to element size ratio of 5 were terminated early for expediency reasons as it was clear that a converged response had not been achieved.

Note that to better compare the results alternative analyses, e.g. where a notch is used to control the location where localised cracks form, could have been carried out. This is an option to consider for future work.

Specimens generated with 1.6mm lattice elements and aggregate particle diameters ranging from 10mm to 20mm, giving a heterogeneity to element ratio of approximately 6, were found to give mesh convergence. Three of the resulting crack patterns are shown in Figure 4.8. The selected element sizes were found

to be adequate as there was no significant difference in the overall crack patterns and the overall stress-strain curve from analyses where the meso-structure is fixed but different background lattices are used.

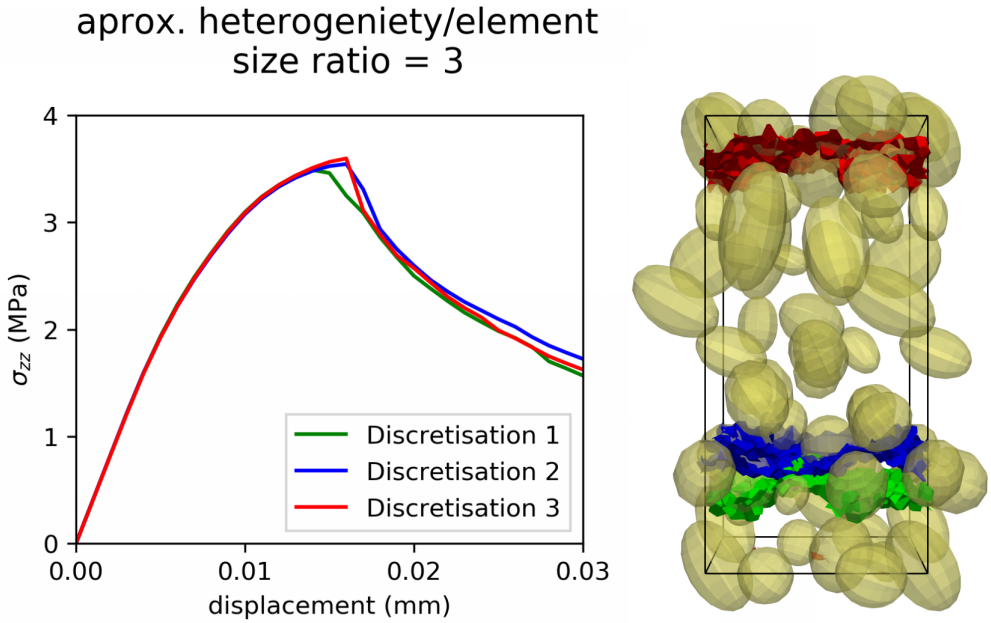

Figure 4.4: Comparison of stress-displacement curves and crack patterns from analyses with fixed mesostructure and element sizes (heterogeneity/element ratio = 3) but varying discretisation (tension $+ve$). Three crack patterns, corresponding to three discretisations, are shown via highlighting mid-cross-sections with active cracks in green, blue and red.

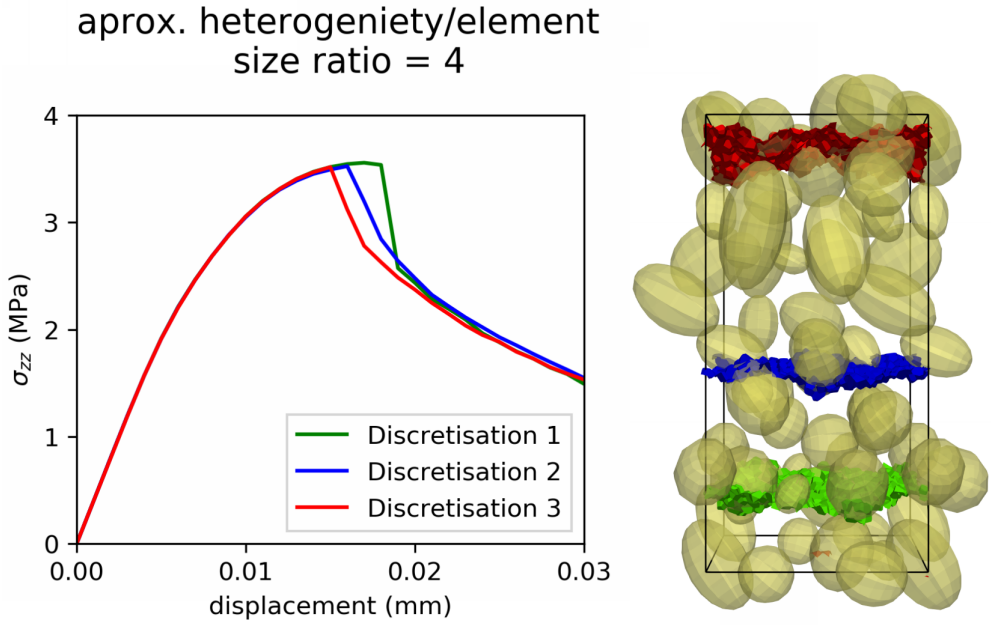

Figure 4.5: Comparison of stress-displacement curves and crack patterns from analyses with fixed mesostructure and element sizes (heterogeneity/element ratio = 4) but varying discretisation (tension $+ve$). Three crack patterns, corresponding to three discretisations, are shown via highlighting mid-cross-sections with active cracks in green, blue and red.

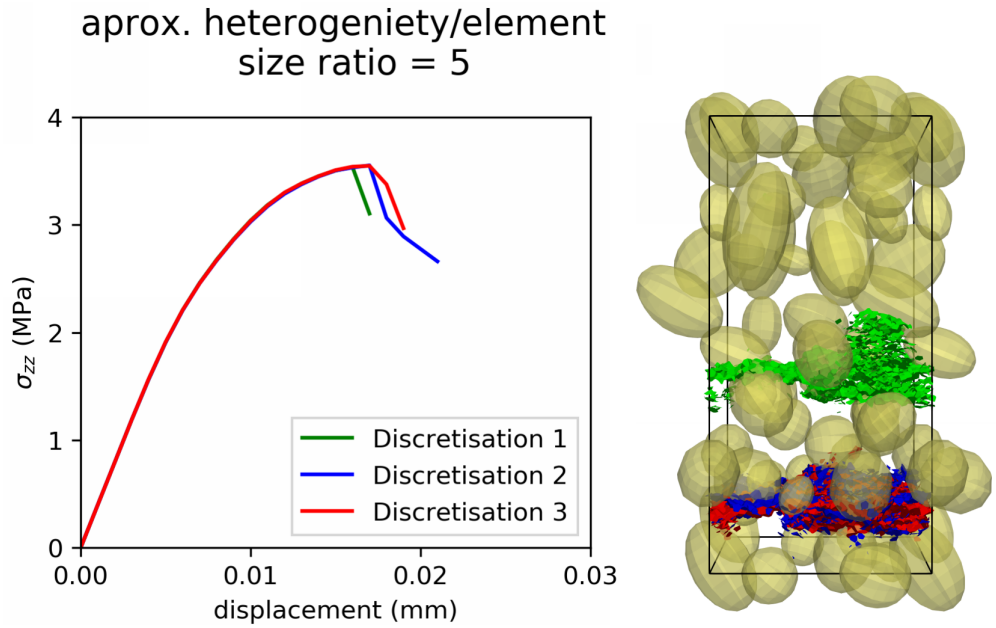

Figure 4.6: Comparison of stress-displacement curves and crack patterns from analyses with fixed mesostructure and element sizes (heterogeneity/element ratio = 5) but varying discretisation (tension $+ve$). Three crack patterns, corresponding to three discretisations, are shown via highlighting mid-cross-sections with active cracks in green, blue and red.

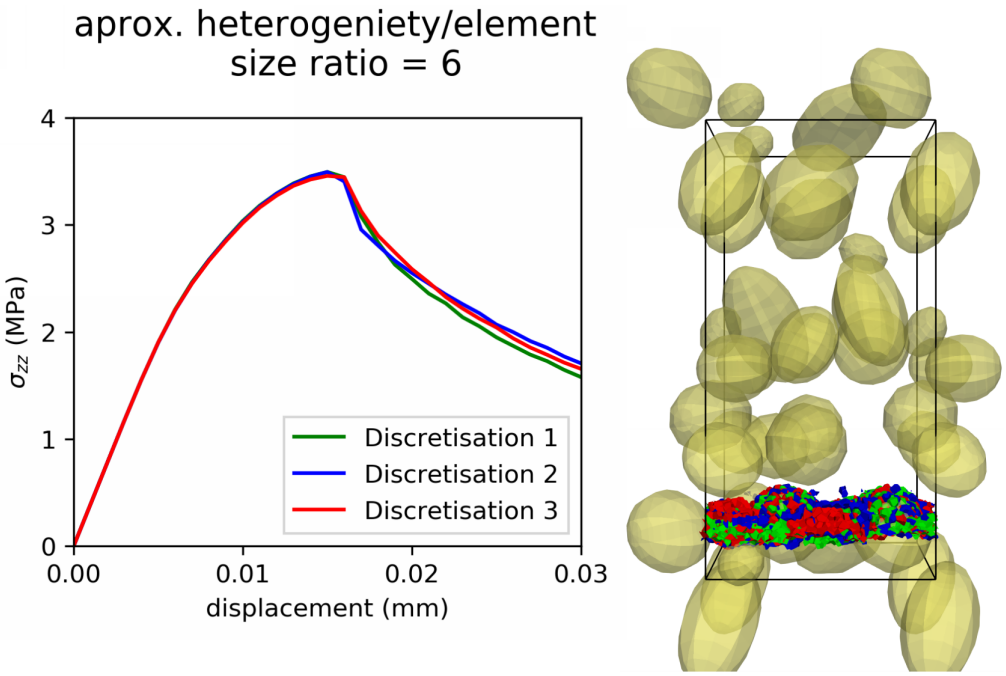

Figure 4.7: Comparison of stress-displacement curves and crack patterns from analyses with fixed mesostructure and element sizes (heterogeneity/element ratio = 6) but varying discretisation (tension $+ve$). Three crack patterns, corresponding to three discretisations, are shown via highlighting mid-cross-sections with active cracks in green, blue and red.

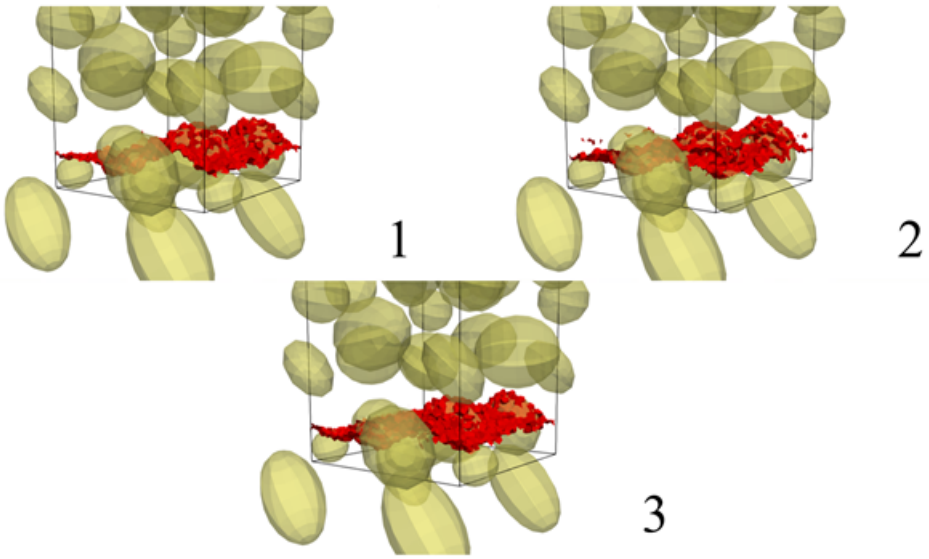

Figure 4.8: Crack patterns from the mesh converged analyses with fixed mesostructured and element sizes but varying discretisation. The mid-cross-sections with active cracks are highlighted in red.

4.2.5 Transition to localised cracking

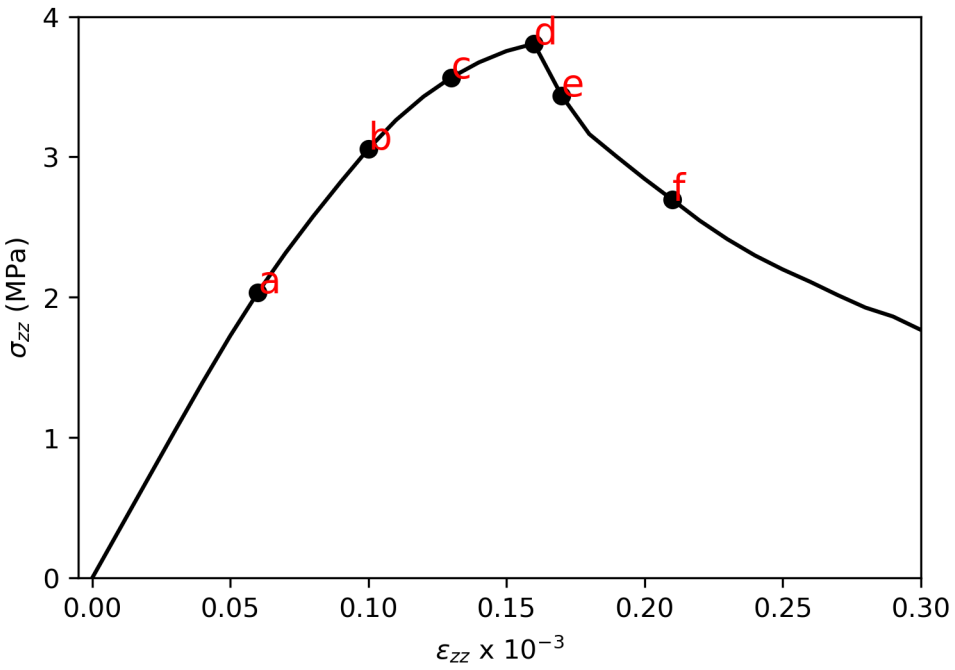

Figure 4.9: Stress-strain curve from lattice model simulation of uniaxial tension (tension $+ve$).

Lattice simulations were carried out using the size of the periodic cell, elements and aggregate particles described in section 4.2.4 and using the material parameters shown in Table 4.1. The results of a typical simulation, with a 40% total volume fraction of aggregates particles, are shown in Figure 4.9 and Figure 4.10. The crack patterns at different stages along the stress-strain curve are highlighted.

As seen from Figure 4.10, the lattice simulations capture very well the cracking mechanisms in cementitious composite materials. Microcracking is initiated at the interface between the mortar and aggregate particles (stage "a" in Figure 4.10). As the loading increases, the interfacial microcracks continue to form and grow. Microcracks begin to propagate and grow in the mortar phase leading to a state of diffuse microcracking associated with pre-peak nonlinearity (see stages "b" to "d" in Figure 4.10). The results of the lattice simulations are consistent with previous observations that the growth and propagation of the microcracks results in pre-peak non-linearity in the typical tensile response of concrete (Karihaloo 1995), a stage often difficult to capture in standard tensile experimental tests.

Furthermore, the lattice simulations show that between the pre-peak stage "c" and the peak stress at stage "d", microcracks begin to coalesce in the region

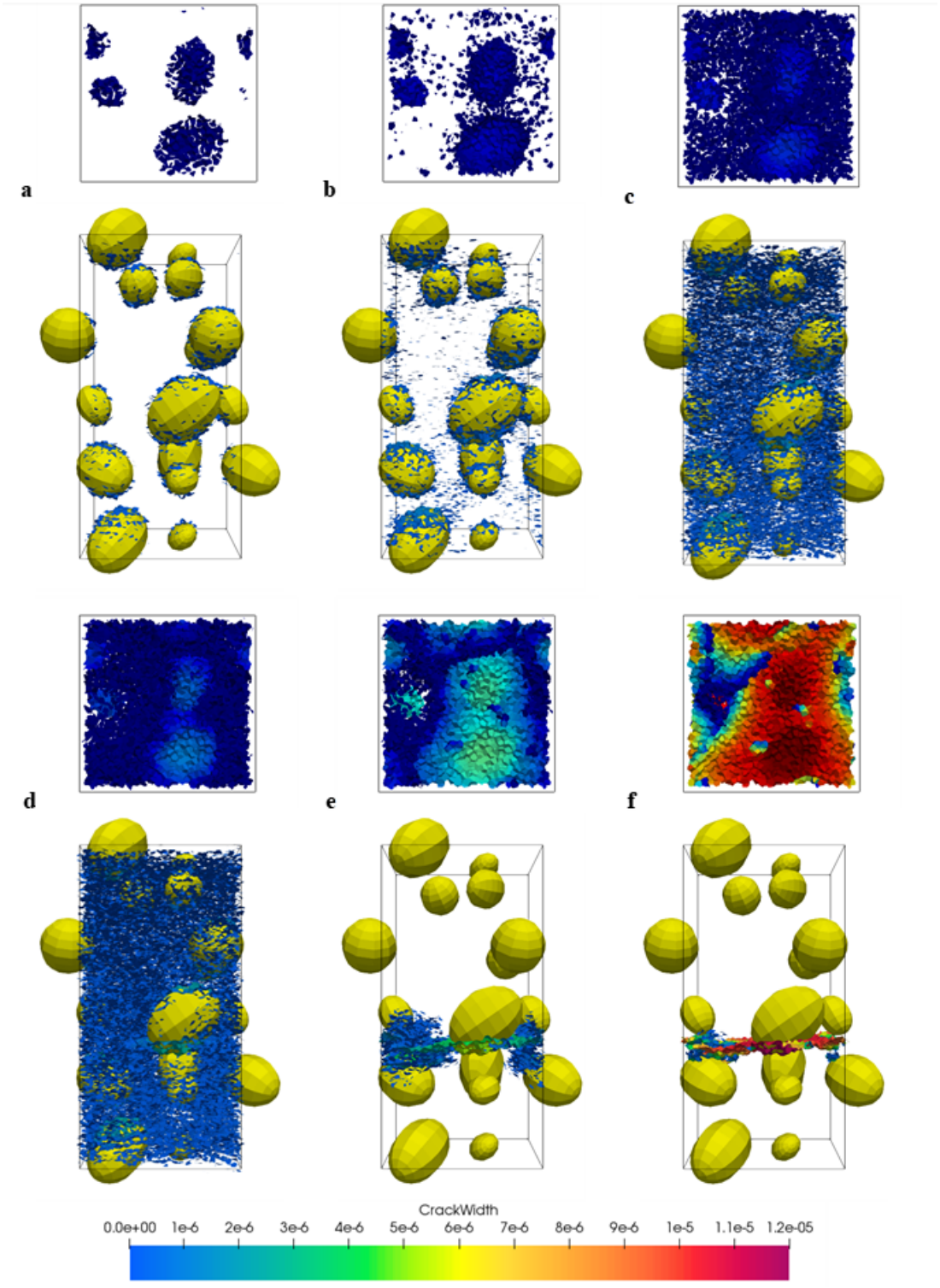

Figure 4.10: Illustration of the progression from diffuse microcracking to localised cracking. Slices through the zone in which localised cracking occurs are also included. Note: Only the mid-cross-sections with active cracks are shown. The different stages a - f correspond to those marked in Figure 4.9.

where localised macrocracking will eventually occur. The post-peak response is controlled by localised macrocracking as is shown in stages "e" to "f" in Figure 4.10. Note that in Figure 4.10, mid-cross sections for which cracks are not growing have been omitted for clarity. Therefore, in Figure 4.10e and Figure 4.10f the diffuse microcracks that were shown in the previous stages, which are no longer growing due to crack localisation occurring, are omitted.

The point of transition to localised cracking suggested by the lattice simulations agrees reasonably well with experiments. Acoustic emission (AE) monitoring of concrete samples subjected to uniaxial tension showed that most AE events recorded within a load interval of approximately 80%-100% of the peak load, both pre and post-peak, were concentrated in a localised region, with a clear increase in the rate of AE events (Li & Shah 1994, Li 1996). Furthermore, all AE events logged post peak, when the load fell below 80% of the peak load were recorded in the localised zone. Li & Shah (1994) attribute the jump in AE events to the transition to localised cracking.

According to Shah et al. (1995), crack localisation begins in the pre-peak region between around 80% of the pre-peak load and the post-peak load, with diffuse microcracks starting to coalesce and form a macrocrack. The growth of this macrocrack is stable (the crack only propagates with increasing load). In the post-peak regime, unstable localised macrocracking occurs with unloading of the material outside of the localised region.

During uniaxial tension tests on plain mortar and mortar with pre-arranged aggregates Maji & Shah (1988) also observed a sharp increase in AE events prior to the peak load. However, the highest rate of AE events occurred just after the peak load. This is consistent with the notion that unstable macrocrack growth occurs after the peak load.

For uniaxial compressive loading, experimental studies employing methods such as stereophotogrammetry and AE to analyse cracking patterns observed that crack localisation occurred at the peak compressive stress (Vonk 1992, Torrenti et al. 1991, 1993).

The lattice simulations have given an insight into the fracture process that occurs in cementitious composite materials. These insights are used to guide the development of the micromechanics constitutive model described in the next section.

4.3 Micromechanics based constitutive model

4.3.1 Model components

The model proposed here builds on the work of Mihai & Jefferson (2011, 2017) and aims to simulate directly the transition from diffuse microcrack to localised macrocracking. Diffuse directional microcracking is modelled based on a micromechanical formulation that builds on Mihai & Jefferson (2011) and Mihai & Jefferson (2017). For this, it is assumed that the cementitious composite is a two-phase material in which series of microcracks with the same orientation are equivalent to bands of material, or 'crack-planes', containing these cracks. The novel component of the model is a formulation which allows for cracking to become localised to macrocracks. Figure 4.11 shows the main concepts of the model and Figure 4.12 shows a schematic representation of a crack-plane. The components are detailed in the sections which follow. The crack localisation mechanism, which is the main contribution of the author, is detailed in section 4.3.5. Further new research such as the solution procedure for the proposed mechanism and the predictions resulting from implementing the mechanism follow on from section 4.3.5.

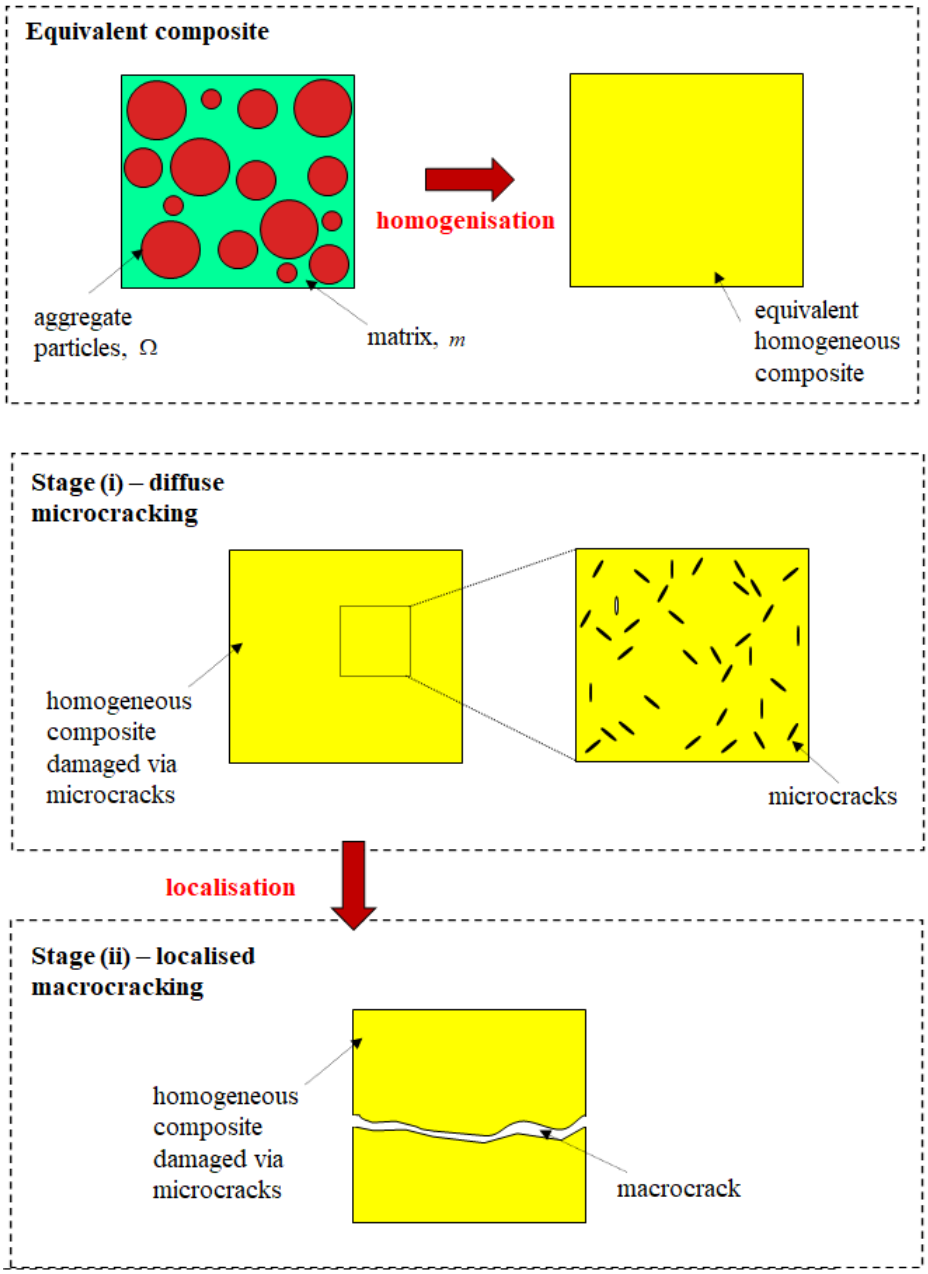

Figure 4.11: The main model concepts. Adapted from Mihai & Jefferson (2017).

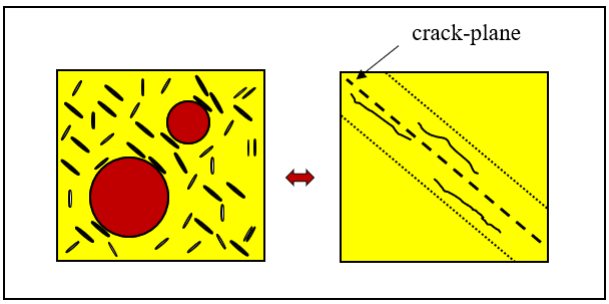

Figure 4.12: Schematic representation of a crack-plane containing microcracks. Adapted from Mihai & Jefferson (2017).

4.3.2 Two-phase composite

The Mori-Tanaka homogenisation scheme approximates the interactions between the inclusions by approximating the stress acting on an inclusion by an average matrix stress (Böhm 2021). The matrix stress and strain fields are disturbed, by ellipsoidal inclusions embedded in the matrix. i.e. the fields are not uniform. However, the volume average of the disturbances is zero if inclusions are assumed to be inside a coaxial domain (Mura 1987). The use of the averaging scheme which results is based on the assumption that concrete can be idealised as a two-phase composite comprising of ellipsoidal inclusions embedded in a matrix.

The model represents the heterogeneous structure of concrete by considering the material as a two-phase composite that consists of a matrix phase m and an inclusion phase Ω. The elasticity tensor of the composite $\boldsymbol{D}_{m\Omega}$ is based on the Eshelby solution for spherical inclusions embedded in a matrix (Eshelby 1957) and the Mori-Tanaka homogenisation scheme (Mura 1987):

$$\boldsymbol{D}_{m\Omega} = (f_m \boldsymbol{D}_m + f_\Omega \boldsymbol{D}_\Omega \cdot \boldsymbol{T}_\Omega) \cdot \left(f_m \boldsymbol{I}^{4s} + f_\Omega \boldsymbol{T}_\Omega\right)^{-1} \tag{4.4}$$

where f_m and f_Ω are the volume fractions of the matrix and inclusion phases respectively, $\boldsymbol{D}_m$ and $\boldsymbol{D}_\Omega$ are the elastic stiffness tensors of the matrix and inclusion phases respectively and I^{4s} is the fourth order identity tensor. Note that $f_m + f_\Omega = 1$. $\boldsymbol{T}_\Omega$ is defined below, where $\boldsymbol{S}_\Omega$ is the Eshelby tensor for spherical inclusions (Nemat-Nasser & Hori 1999):

$$\boldsymbol{T}_\Omega = \boldsymbol{I}^{4s} + \boldsymbol{S}_\Omega \cdot ((\boldsymbol{D}_\Omega - \boldsymbol{D}_m) \cdot \boldsymbol{S}_\Omega + \boldsymbol{D}_m)^{-1} \cdot (\boldsymbol{D}_m - \boldsymbol{D}_\Omega) \tag{4.5}$$

4.3.3 Directional microcracking

The added strain due to a dilute series of penny shaped cracks with the same orientation is given as (Nemat-Nasser & Hori 1999, Budiansky & O'Connell 1976):

$$\boldsymbol{\varepsilon}_\alpha = \boldsymbol{C}_\alpha(\psi, \theta) : \boldsymbol{\sigma}_L = f(\psi, \theta) \boldsymbol{C}_{\alpha c} : \boldsymbol{\sigma}_L \tag{4.6}$$

where $\boldsymbol{\varepsilon}_\alpha$ is the added strain tensor for the dilute series of cracks with the same orientation, ψ and θ are the angles which represent the orientation of the crack as shown in Figure 4.13, $f(\psi, \theta)$ is the crack density parameter of Budiansky & O'Connell (1976) which describes the progress of cracking and $\boldsymbol{C}_{\alpha c}$ is the additional compliance tensor due to the cracks.

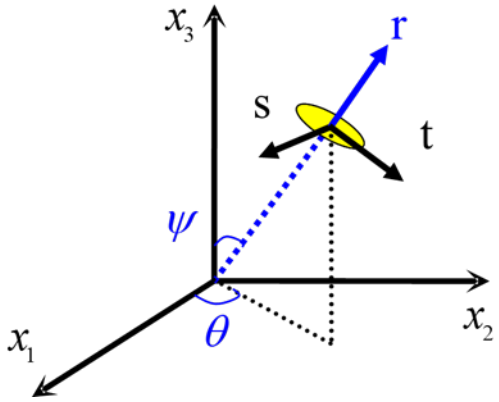

Figure 4.13: Local coordinate system of cracks. Reproduced from Mihai & Jefferson (2017).

$\boldsymbol{\sigma}_L$ is the 'local', i.e. crack-plane, stress tensor. $\boldsymbol{\sigma}_L$ and $\boldsymbol{\varepsilon}_\alpha$ are considered in reduced vector form ($\begin{bmatrix}\sigma_r & \sigma_s & \sigma_t\end{bmatrix}^{\mathrm{T}}$ and $\begin{bmatrix}\varepsilon_{\alpha r} & \varepsilon_{\alpha s} & \varepsilon_{\alpha t}\end{bmatrix}^{\mathrm{T}}$) containing only the non-zero components. The local crack plane vectors $\boldsymbol{v} = \begin{bmatrix}v_r & v_s & v_t\end{bmatrix}^{\mathrm{T}}$ consist of a normal component v_r and two shear components v_s and v_t. The matrix form of $\boldsymbol{C}_{\alpha c}$ which relates the local vectors is (Nemat-Nasser & Hori 1999):

$$\boldsymbol{C}_{\alpha c} = \frac{16(1-{\nu_m}^2)}{3E_m}\begin{bmatrix}1 & 0 & 0\\ 0 & \frac{4}{2-\nu_m} & 0\\ 0 & 0 & \frac{4}{2-\nu_m}\end{bmatrix} \tag{4.7}$$

The local stress is related to the average stress $\bar{\boldsymbol{\sigma}}$ as:

$$\boldsymbol{\sigma}_L = \boldsymbol{N}(\psi,\theta) : \bar{\boldsymbol{\sigma}} \tag{4.8}$$

and the local strain is related to the average strain $\bar{\boldsymbol{\varepsilon}}$ as:

$$\boldsymbol{\varepsilon}_L = \boldsymbol{N}_\varepsilon(\psi,\theta) : \bar{\boldsymbol{\varepsilon}} \tag{4.9}$$

where $\boldsymbol{N}(\psi,\theta)$ and $\boldsymbol{N}_\varepsilon(\psi,\theta)$ are the stress and strain transformation tensors respectively and are given in Jefferson (2003). Using the transformation tensors the stress and strain tensors in Cartesian coordinates (x,y,z) can be related to the local coordinates (r,s,t) of a crack plane with orientations (ψ,θ).

Jefferson & Bennett (2007) expressed the crack density parameter in terms of a directional damage parameter $\omega(\psi,\theta)$ which grows from 0 at no damage to 1 at complete damage. The directional damage parameter is defined such that:

$$f(\psi,\theta) = \frac{3}{16(1-{\nu_m}^2)}\frac{\omega(\psi,\theta)}{1-\omega(\psi,\theta)} \tag{4.10}$$

$$\boldsymbol{C}_\alpha(\psi,\theta) = f((\psi,\theta))\boldsymbol{C}_{\alpha c} = \frac{\omega(\psi,\theta)}{1-\omega((\psi,\theta))}\boldsymbol{C}_L \tag{4.11}$$

$\boldsymbol{C}_L$ is the local compliance tensor. The matrix form of the local compliance tensor which corresponds to local vectors is:

$$\boldsymbol{C}_L = \frac{1}{E_m}\begin{bmatrix} 1 & 0 & 0 \\ 0 & \frac{4}{2-\nu_m} & 0 \\ 0 & 0 & \frac{4}{2-\nu_m} \end{bmatrix} \tag{4.12}$$

The total added strain due to microcracks is obtained by summing the added strain of series of cracks from every orientation (Nemat-Nasser & Hori 1999, Budiansky & O'Connell 1976):

$$\boldsymbol{\varepsilon}_{\mathrm{a}} = \frac{1}{2\pi}\int_0^{2\pi}\int_0^{\pi/2} \boldsymbol{N}_\varepsilon(\psi,\theta) : \boldsymbol{\varepsilon}_\alpha \sin(\psi)\mathrm{d}\psi\mathrm{d}\theta \tag{4.13}$$

$\boldsymbol{\varepsilon}_{\mathrm{a}}$ is the total added strain tensor.

The total added strain is superimposed on the composite such that:

$$\bar{\boldsymbol{\sigma}} = \boldsymbol{D}_{m\Omega} : (\bar{\boldsymbol{\varepsilon}} - \boldsymbol{\varepsilon}_a) = \boldsymbol{D}_{mc} : \bar{\boldsymbol{\varepsilon}} \tag{4.14}$$

where $\bar{\boldsymbol{\varepsilon}}$ is the average strain tensor and $\boldsymbol{D}_{mc}$ is the microcrack damaged stiffness tensor.

Using equations 4.6, 4.8, 4.11, 4.13 in Equation 4.14, the microcrack damaged stiffness tensor is given by (Mihai & Jefferson 2017):

$$\boldsymbol{D}_{mc} = \left(\boldsymbol{I}^{4s} + \frac{\boldsymbol{D}_{m\Omega}}{2\pi}\cdot\int_0^{2\pi}\int_0^{\pi/2} \boldsymbol{N}_\varepsilon(\psi,\theta) : \boldsymbol{F}_\omega(\psi,\theta)\cdot\boldsymbol{C}_L : \boldsymbol{N}(\psi,\theta)\sin(\psi)d\psi d\theta\right)^{-1}\cdot\boldsymbol{D}_{m\Omega} \tag{4.15}$$

where $\boldsymbol{F}_\omega(\psi,\theta) = \frac{\omega(\psi,\theta)}{1-\omega(\psi,\theta)}\cdot\boldsymbol{I}^{4s}$.

4.3.4 Damage surface and damage evolution

An effective strain parameter ζ is obtained from the damage surface of Jefferson & Bennett (2007):

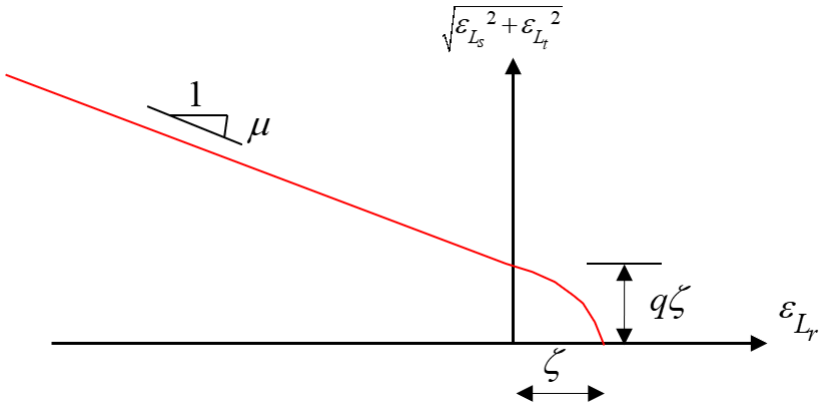

Figure 4.14: Damage surface. Reproduced from Jefferson & Bennett (2007).

$$\mathrm{f}_d(\boldsymbol{\varepsilon}_L,\zeta)=\frac{\boldsymbol{\varepsilon}_{L_r}}{2}\left(1+\left(\frac{\mu}{q}\right)^2\right)+\frac{1}{2q^2}\sqrt{(q^2-\mu^2)\,\boldsymbol{\varepsilon}_{L_r}{}^2+4q^2\left(\boldsymbol{\varepsilon}_{L_s}{}^2+\boldsymbol{\varepsilon}_{L_t}{}^2\right)}-\zeta \tag{4.16}$$

where the parameters q and μ are derived from their stress equivalents ($q=\frac{c}{f_t}\frac{E}{G}$ and $\mu=\mu_s\frac{E}{G}$), μ_s is the angle of friction, c is the shear strength at first damage and the conditions $\mathrm{f_d}\leq 0;\dot{\zeta}\geq 0;\mathrm{f_d}\dot{\zeta}=0$ apply. The damage surface is illustrate in Figure 4.14.

The local strain of the microcrack planes $\boldsymbol{\varepsilon}_L$ drives microcrack damage and is given by Equation 4.9.

ζ is used to calculate the evolution of ω via an exponential evolution function:

$$\omega(\zeta)=1-\frac{\varepsilon_t}{\zeta}e^{-c_1\left(\frac{\zeta-\varepsilon_t}{\varepsilon_0-\varepsilon_t}\right)} \tag{4.17}$$

where c_1 is a constant which controls the slope of the tension softening curve. ε_t is tensile strain given by $\varepsilon_t=\frac{f_t}{E_{itz}}$ where f_t is the tensile strength of the composite.

4.3.5 Macrocracking

Crack localisation is a key mechanism that governs the post-peak response in cementitious materials. Diffuse microcracks coalesce to form a macrocrack and crack growth becomes concentrated to the macrocrack. In the post-peak regime, macrocrack growth becomes unstable and material outside of the localised region unloads. Growth of localised cracks leads to structural changes that are in the order of the specimen size (Van Mier 1997) and to failure (Zhao et al. 2018). As shown in section 4.2.5, this mechanism is captured well by lattice simulations that represent the meso-structure and heterogeneous nature of concrete. A mechanism

is proposed below which is able to model the effects of macrocrack propagation in the post-peak regime.

The model assumes that macrocracks form when the overall stress reaches its peak value i.e.:

$$\frac{d\sigma_I}{d\varepsilon_I} = 0 \tag{4.18}$$

where σ_I and ε_I are the major principal stress and strain respectively. This is consistent with the findings from the lattice simulations that show that macrocrack growth is predominantly concentrated to the post-peak regime and that the overall crack localisation process occurs between roughly 80% of the pre-peak and the post-peak load (see section 4.2.5).

Under tensile loading, the normal to the macrocrack plane is based on the orientation of the major principal strain and a maximum of two macrocracks are allowed to form. When two macrocracks form, the growth of both macrocracks is initiated in the same increment. Under compressive loading, a macrocrack forms with the normal to the crack plane given by the direction which maximises the effective strain parameter at the peak stress. The shear directions are generated following the method used by Hasegawa & Bažant (1993) to generate consistent shear directions for micro-planes.

The formation of macrocracks is taken into account in the overall constitutive relationship by removing the inelastic strain of the macrocracks from the average strain:

$$\bar{\boldsymbol{\sigma}} = \boldsymbol{D}_{mc} : \left(\bar{\boldsymbol{\varepsilon}} - \sum_{i=1}^{n_{sd}} \boldsymbol{N}_{\varepsilon}(\alpha_i, \beta_i) : \hat{\boldsymbol{\varepsilon}}_i \right) \tag{4.19}$$

where n_{sd} is the total number of macrocrack planes and $\hat{\boldsymbol{\varepsilon}}$ is the macrocrack inelastic strain. α and β are the macrocrack plane orientation angles (defined similarly to ψ and θ in Figure 4.13).

The local stress $\tilde{\boldsymbol{\sigma}}(\alpha, \beta)$ of the macrocrack planes is given by the following constitutive relationship:

$$\tilde{\boldsymbol{\sigma}}(\alpha, \beta) = (1 - \tilde{\omega}(\alpha, \beta))\boldsymbol{I}\boldsymbol{C_L}^{-1} : \tilde{\boldsymbol{\varepsilon}}(\alpha, \beta) \tag{4.20}$$

where $\tilde{\boldsymbol{\varepsilon}}$ is the macrocrack local strain, $\tilde{\omega}$ is the macrocrack damage parameter and $\boldsymbol{C_L}$ is the local compliance tensor where the matrix form is given by Equation

4.12. The above equation can be used to write the inelastic strain of macrocracks $\hat{\boldsymbol{\varepsilon}}$ in terms of the macrocrack local strain. First consider that the inelastic macrocrack strain can be obtrained by removing the local strain component $\tilde{\boldsymbol{\varepsilon}}_{\boldsymbol{Le}}$ from the macrocrack local strain:

$$\hat{\boldsymbol{\varepsilon}} = \tilde{\boldsymbol{\varepsilon}} - \tilde{\boldsymbol{\varepsilon}}_{\boldsymbol{Le}} = \tilde{\boldsymbol{\varepsilon}} - \boldsymbol{C}_L : \tilde{\boldsymbol{\sigma}} \tag{4.21}$$

Note that dependencies have been dropped for clarity. Next, substitute $\tilde{\boldsymbol{\sigma}}$ from Equation 4.20 into the above:

$$\hat{\boldsymbol{\varepsilon}} = (\boldsymbol{I} - \tilde{\boldsymbol{M}}_s) : \tilde{\boldsymbol{\varepsilon}} \tag{4.22}$$

where

$$\tilde{\boldsymbol{M}}_s = (1 - \tilde{\omega})\boldsymbol{I}$$

The dependencies of $\tilde{\omega}$ above, including orientation, have been dropped for clarity.

The same damage surface 4.16 and evolution function 4.17 employed for microcracks applies for calculating the effective strain parameter of macrocracks $\tilde{\zeta}$ and the evolution of the macrocrack damage parameter $\tilde{\omega}$ respectively.

Once the transition to localised damage has been initiated, there is an inelastic strain due to macrocracking (the calculation of which is detailed in section 4.4). Microcracks are assumed to be situated in the band of material outside of the zone of localised cracking. Subsequently to model the effect of macrocrack growth on microcrack growth, the inelastic macrocrack strain is removed from the local macrocrack strains:

$$\boldsymbol{\varepsilon}_L(\psi_k, \theta_k) = \boldsymbol{N}_\varepsilon(\psi_k, \theta_k) : \left(\bar{\boldsymbol{\varepsilon}} - \sum_{isd=1}^{n_{sd}} \boldsymbol{N}_\varepsilon(\alpha_{isd}, \beta_{isd}) : \hat{\boldsymbol{\varepsilon}}(\alpha_{isd}, \beta_{isd}) \right) \tag{4.23}$$

4.4 Numerical implementation

The model is implemented in Mathcad. A constitutive driver algorithm and a Gauss solver with fixities are used. The algorithm allows for mixed stress and strain paths to be prescribed. Integration over the surface of a sphere is carried out using McLaren's 50 point rule for a sphere (Stroud 1971) adapted via symmetry to use 29 sample points over a hemisphere. Consistent shear directions for each sample point are generated using the method by Hasegawa & Bažant

(1993) which eliminates directional bias. The staggered solving method used to calculate $\hat{\boldsymbol{\varepsilon}}$ is shown in Algorithm 1 and detailed in section 4.4.1.

4.4.1 Staggered solution algorithm

Non-linear coupled equations are formulated, Equation 4.24 and Equation 4.25, such that the equations represent the requirement that the total stress transformed onto a macrocrack plane is equal to the local stress of the macrocrack. To determine the inelastic strains of macrocracks, the non-linear coupled equations must be solved.

$$\boldsymbol{\Psi}_{\alpha_i} = \boldsymbol{N}\left(\alpha_i, \beta_i\right) : \boldsymbol{D}_{mc} : \left(\bar{\boldsymbol{\varepsilon}} - \sum_{j=1}^{n_{sd}} \boldsymbol{N}_{\varepsilon}(\alpha_j, \beta_j) : (\boldsymbol{I}^{4s} - \tilde{\boldsymbol{M}}_{s_j}) : \tilde{\boldsymbol{\varepsilon}}_j \right) - \boldsymbol{D}_L \cdot \tilde{\boldsymbol{M}}_{s_i} : \tilde{\boldsymbol{\varepsilon}}_i = \boldsymbol{0} \tag{4.24}$$

$$\boldsymbol{\Psi}_{\beta_k} = \boldsymbol{\varepsilon}_{L_k} - \boldsymbol{N}_{\varepsilon}\left(\psi_k, \theta_k\right) : \left(\bar{\boldsymbol{\varepsilon}} - \sum_{j=1}^{n_{sd}} \boldsymbol{N}_{\varepsilon}(\alpha_j, \beta_j) : (\boldsymbol{I}^{4s} - \tilde{\boldsymbol{M}}_{s_j}) : \tilde{\boldsymbol{\varepsilon}}_j \right) = \boldsymbol{0} \tag{4.25}$$

$\boldsymbol{D}_L$ is the local crack-plane elastic stiffness tensor consistent with Equation 4.15, subscript i denotes the macrocrack plane number, subscript k denotes the microcrack plane number and some dependencies have been dropped for clarity.

Equating $\boldsymbol{\Psi}_{\alpha}$ to zero and performing a first-order Taylor's series expansion 4.26 followed by re-arrangement gives the iterative update to the stacked local strain vector $\tilde{\boldsymbol{E}}$ 4.27:

$$\boldsymbol{0} = \boldsymbol{\Psi}(\tilde{\boldsymbol{E}} + \delta\tilde{\boldsymbol{E}}) = \boldsymbol{\Psi}(\tilde{\boldsymbol{E}}) + \boldsymbol{B}_E \delta\tilde{\boldsymbol{E}} \tag{4.26}$$

$$\delta\tilde{\boldsymbol{E}} = -\boldsymbol{B}_E^{-1}\boldsymbol{\Psi}(\tilde{\boldsymbol{E}}) \tag{4.27}$$

where equivalent reduced vector and matrix notation has been adopted, $\tilde{\boldsymbol{E}} = \begin{bmatrix} \tilde{\boldsymbol{\varepsilon}}_1 \\ \tilde{\boldsymbol{\varepsilon}}_2 \\ \vdots \\ \tilde{\boldsymbol{\varepsilon}}_n \end{bmatrix}$, $\boldsymbol{\Psi} = \begin{bmatrix} \boldsymbol{\Psi}_{\alpha_1} \\ \boldsymbol{\Psi}_{\alpha_2} \\ \vdots \\ \boldsymbol{\Psi}_{\alpha_n} \end{bmatrix}$, and B_E is the matrix of derivatives which is equal to $\frac{d\boldsymbol{\Psi}_{\boldsymbol{\alpha}}}{d\tilde{\boldsymbol{\varepsilon}}}$.

The updated micro-strain vectors $\tilde{\boldsymbol{\varepsilon}}_i$ from solving Equation 4.24 are used to update the inelastic macro-strain $\hat{\boldsymbol{\varepsilon}}_i$. The error caused by the difference in $\boldsymbol{\varepsilon}_L$ used

to calculate $\boldsymbol{D}_{mc}$ in Equation 4.24 and $\boldsymbol{\varepsilon}_L$ calculated using the updated $\hat{\boldsymbol{\varepsilon}}$ is given by Equation 4.25.

4.4.2 Matrix of derivatives

For the case where there is a single macrocrack, the incremental change in $\boldsymbol{\Psi}$ is given by the following:

$$\begin{aligned} \boldsymbol{d\Psi} = -\boldsymbol{N}\boldsymbol{D}_{\boldsymbol{m\Omega}}\boldsymbol{N}^{\boldsymbol{T}}\left(\boldsymbol{I}-\tilde{\boldsymbol{M}}_{\boldsymbol{s}}\right)\boldsymbol{d\tilde{\varepsilon}} + \boldsymbol{N}\boldsymbol{D}_{\boldsymbol{m\Omega}}\boldsymbol{N}^{\boldsymbol{T}}\frac{\boldsymbol{d\tilde{M}_s}}{\boldsymbol{d\omega}}\frac{d\omega}{d\xi}\frac{\boldsymbol{d\xi}}{\boldsymbol{d\tilde{\varepsilon}}}\boldsymbol{d\tilde{\varepsilon}\tilde{\varepsilon}} \\ -\boldsymbol{D_L}\tilde{\boldsymbol{M}}_{\boldsymbol{s}}\boldsymbol{d\tilde{\varepsilon}} - \boldsymbol{D_L}\frac{\boldsymbol{d\tilde{M}_s}}{\boldsymbol{d\omega}}\frac{d\omega}{d\xi}\frac{\boldsymbol{d\xi}}{\boldsymbol{d\tilde{\varepsilon}}}\boldsymbol{d\tilde{\varepsilon}\tilde{\varepsilon}} \end{aligned} \tag{4.28}$$

Note that in the second and third terms on the RHS of Equation 4.28 $\frac{\boldsymbol{d\xi}}{\boldsymbol{d\tilde{\varepsilon}}}\boldsymbol{d\tilde{\varepsilon}}$ forms a scalar which can be moved to the end of those terms. Then by also taking note that $\frac{\boldsymbol{d\tilde{M}_s}}{\boldsymbol{d\omega}} = -\boldsymbol{I}$, Equation 4.28 is re-arranged such that $\boldsymbol{d\tilde{\varepsilon}}$ can eliminated from the RHS and the matrix of derivatives can be formed:

$$\begin{aligned} \boldsymbol{d\Psi} = -\boldsymbol{N}\boldsymbol{D}_{\boldsymbol{m\Omega}}\boldsymbol{N}^{\boldsymbol{T}}\left(\boldsymbol{I}-\tilde{\boldsymbol{M}}_{\boldsymbol{s}}\right)\boldsymbol{d\tilde{\varepsilon}} \; - \boldsymbol{N}\boldsymbol{D}_{\boldsymbol{m\Omega}}\boldsymbol{N}^{\boldsymbol{T}}\boldsymbol{I}\frac{d\omega}{d\xi}\tilde{\boldsymbol{\varepsilon}}\frac{\boldsymbol{d\xi}}{\boldsymbol{d\tilde{\varepsilon}}}\boldsymbol{d\tilde{\varepsilon}} \\ -\boldsymbol{D_L}\tilde{\boldsymbol{M}}_{\boldsymbol{s}}\boldsymbol{d\tilde{\varepsilon}} + \boldsymbol{D_L}\boldsymbol{I}\frac{d\omega}{d\xi}\tilde{\boldsymbol{\varepsilon}}\frac{\boldsymbol{d\xi}}{\boldsymbol{d\tilde{\varepsilon}}}\boldsymbol{d\tilde{\varepsilon}} \end{aligned} \tag{4.29}$$

The matrix of derivatives $\boldsymbol{B_E}$ for a single macrocrack is then given by:

$$\begin{aligned} \boldsymbol{B_E} = \frac{\boldsymbol{\Psi}}{\boldsymbol{d\tilde{\varepsilon}}} = -\boldsymbol{N}\boldsymbol{D}_{\boldsymbol{m\Omega}}\boldsymbol{N}^{\boldsymbol{T}}\left(\boldsymbol{I}-\tilde{\boldsymbol{M}}_{\boldsymbol{s}}\right) - \boldsymbol{N}\boldsymbol{D}_{\boldsymbol{m\Omega}}\boldsymbol{N}^{\boldsymbol{T}}\boldsymbol{I}\frac{d\omega}{d\xi}\tilde{\boldsymbol{\varepsilon}}\frac{\boldsymbol{d\xi}}{\boldsymbol{d\tilde{\varepsilon}}} \\ -\boldsymbol{D_L}\tilde{\boldsymbol{M}}_{\boldsymbol{s}} + \boldsymbol{D_L}\boldsymbol{I}\frac{d\omega}{d\xi}\tilde{\boldsymbol{\varepsilon}}\frac{\boldsymbol{d\xi}}{\boldsymbol{d\tilde{\varepsilon}}} \end{aligned} \tag{4.30}$$

In the case where more than one macrocrack forms, calculating the matrix $\boldsymbol{B_E}$ involves additional steps. For example, see the first order Taylor's series expansion of $\boldsymbol{\Psi}$ for a system with two macrocracks 4.31:

$$\begin{bmatrix} \boldsymbol{\Psi_1} \\ \boldsymbol{\Psi_2} \end{bmatrix}^{K+1} = \begin{bmatrix} \boldsymbol{\Psi_1} \\ \boldsymbol{\Psi_2} \end{bmatrix}^{K} + \boldsymbol{B}_{\boldsymbol{E}}^{K}\begin{bmatrix} \boldsymbol{d\tilde{\varepsilon}_1} \\ \boldsymbol{d\tilde{\varepsilon}_2} \end{bmatrix} \tag{4.31}$$

where

Algorithm 1: Algorithm to calculate the inelastic strain of macrocrack planes

▷Enter with the strain vector and set macrocrack plane parameters to initial values or those from the previously converged step

$\bar{\boldsymbol{\varepsilon}}$; $\tilde{\boldsymbol{\varepsilon}}_i = \tilde{\boldsymbol{\varepsilon}}_i^{prv}$

$\tilde{\zeta}_i = \tilde{\zeta}_i^{prv}$; $\tilde{\omega}_i = \tilde{\omega}_i^{prv}$; $\tilde{\boldsymbol{M}}_{s_i} = \tilde{\boldsymbol{M}}_{s_i}^{prv}$;

▷Enter iteration loop of the staggered solution method

for *iter = 1* **to** $iter_{max}$ **do**

- ▷Calculate the matrix of derivatives and the stacked local error from the first coupled equation using Algorithm 2
- ▷Calculate the local crack plane strains and macrocrack plane variables using Algorithm 3
- ▷Calculate the stacked local error from the second coupled equation using Algorithm 4
- ▷Check if the error is within the required tolerance and exit if converged
- **if** $(|\boldsymbol{\Psi}_\alpha| < tol_\alpha) \wedge (|\boldsymbol{\Psi}_\beta| < tol_\beta)$ **then**
  - exit
- **end**
- ▷Exit the procedure and reduce the global step size if the maximum number of iterations has been reached
- **if** $i == iter_{max}$ **then**
  - exit
- **end**

end

Algorithm 2: Algorithm to calculate the matrix of derivatives and the stacked local error from the first coupled equation

▷ Enter from Algorithm 1

▷ Loop over microcrack planes n_p

for $i = 1$ **to** n_p **do**

  ▷ Compute microcrack plane variables from equations 4.16,4.17 and 4.23

  compute ζ_i, ω_i, $\boldsymbol{\varepsilon}_{L_i}$

  ▷ Compute the microcrack based stiffness and the corresponding local stiffness matrix from Equation 4.15

  compute $\boldsymbol{D_{mc}}$, $\boldsymbol{D}_L$

end

▷ Loop over macrocrack planes n_{sd}

for $i = 1$ **to** n_{sd} **do**

  ▷ Calculate the stacked local error vector from Equation 4.24

  compute $\boldsymbol{\Psi}_{\alpha_i}$

end

▷ Loop over macrocrack planes n_{sd}

for $i = 1$ **to** n_{sd} **do**

  for $j = 1$ **to** n_{sd} **do**

    ▷ Calculate the matrix of derivatives from Equation 4.33

    compute $\boldsymbol{B}_{E_{i,j}}$

  end

end

Algorithm 3: Algorithm to update the local crack plane strains and macro-crack plane variables

▷ Enter from Algorithm 1

▷ Calculate the stacked local strain vector for macrocrack planes from Equation 4.27

compute $\boldsymbol{\delta \tilde{E}}$

▷ Loop over macrocrack planes n_{sd}

for $i = 1$ **to** n_{sd} **do**

▷ Update local crack plane strains and calculate the macrocrack plane variables from equations 4.16 and 4.17

compute $\tilde{\boldsymbol{\varepsilon}}_i = \tilde{\varepsilon}_{\mathbf{i}} + \delta\tilde{\varepsilon}_{\mathbf{i}}$

compute $\tilde{\zeta}_i$, $\tilde{\omega}_i$, $\tilde{\boldsymbol{M}}_{s_i}$, $\hat{\boldsymbol{\varepsilon}}_i$

end

Algorithm 4: Algorithm to calculate the stacked local error from the second coupled equation

▷ Enter from Algorithm 1

▷ Loop over macrocrack planes n_{sd}

for $i = 1$ **to** n_{sd} **do**

▷ Calculate the stacked local error vector from Equation 4.25

compute $\boldsymbol{\Psi}_{\beta_i}$

end

$$\boldsymbol{B}_{\boldsymbol{E}}^{K} = \begin{bmatrix} \boldsymbol{d\Psi_1/d\tilde{\varepsilon}_1} & \boldsymbol{d\Psi_1/d\tilde{\varepsilon}_2} \\ \boldsymbol{d\Psi_2/d\tilde{\varepsilon}_1} & \boldsymbol{d\Psi_2/d\tilde{\varepsilon}_2} \end{bmatrix}^{K} \tag{4.32}$$

and K represents the staggered solution iteration.

$\boldsymbol{B_E}$ can be calculated via iterating through the set of macrocracks and stacking the sets of $\boldsymbol{d\Psi_i/d\tilde{\varepsilon}_j}$. The derivative terms are given by:

$$\begin{aligned} \frac{\boldsymbol{d\Psi_i}}{\boldsymbol{d\tilde{\varepsilon}_j}} = -\boldsymbol{N_i D_{m\Omega} N_j^T} \left(\boldsymbol{I} - \tilde{\boldsymbol{M}}_{\boldsymbol{s_j}} \right) - \boldsymbol{N_i D_{m\Omega} N_j^T I} \frac{d\omega_j}{d\xi_j} \tilde{\boldsymbol{\varepsilon}}_{\boldsymbol{j}} \frac{\boldsymbol{d\xi_j}}{\boldsymbol{d\tilde{\varepsilon}_j}} \\ -\delta_{ij} \boldsymbol{D_L} \tilde{\boldsymbol{M}}_{\boldsymbol{s_i}} + \delta_{ij} \boldsymbol{D_L I} \frac{d\omega_i}{d\xi_i} \tilde{\boldsymbol{\varepsilon}}_{\boldsymbol{i}} \frac{\boldsymbol{d\xi_i}}{\boldsymbol{d\tilde{\varepsilon}_i}} \end{aligned} \tag{4.33}$$

Compare equations 4.30 and 4.33. The Kronecker delta δ_{ij} is introduced to the last two terms of Equation 4.33. Those terms are only part of the derivative when $i = j$.

4.5 Uniaxial tension simulations

In the following sections, results from comparative analyses carried out with two versions of the above model are given. The first version included both microcrack and macrocrack growth, i.e. the "micro-macro transition model", whereas the second version only included microcracking. The purpose of the comparative analyses was to demonstrate that the inclusion of the crack localisation mechanism better models the cracking mechanisms that occur in concrete and subsequently gives more realistic results.

4.5.1 Constitutive model simulation compared to lattice simulations

Predictions from the two versions of the model (only microcracking and both microcrack and macrocrack growth) were compared to uniaxial tension lattice simulations of 10 random arrangements of aggregate particles. The intention of the comparisons was to show how a micromechanics based constitutive model for concrete which includes a crack localisation mechanism agrees well with more computationally expensive lattice simulations that discretely model the influence of the heterogeneous material structure of concrete at the meso-scale.

Table 4.3 shows the parameters used for the numerical simulations. The parameter c_1 was adjusted to tune the predictions to the lattice simulation results. The

lattice simulations were carried out using a 40% total volume fraction of aggregate particles and by maintaining the periodic cell and element, dimensions and material parameters described in section 4.2.4.

The results are shown in Figure 4.15. From Figure 4.15a the microcracking only model is excessively ductile to the extent that the predictions fall outside of the envelope of results from the lattice model analyses. Inclusion of the transition to localised cracking in the constitutive model give more realistic results with the predictions agreeing much better with the lattice simulations. From Figure 4.15b and Figure 4.15c, damage can be seen to become localised to a macrocrack plane after the peak stress in the micro-macro transition model whereas in the microcracking only model the microcrack planes continue to become damaged.

Table 4.3: Material parameters used for the constitutive model to simulate the results of lattice model analyses.

E_m (MPa)	E_Ω (MPa)	ν_m	ν_Ω	f_m	f_Ω (MPa)	c_1	q	μ	f_t	ε_0
30,000	45,000	0.19	0.21	0.6	0.4	10	3.3	4.2	3	0.003

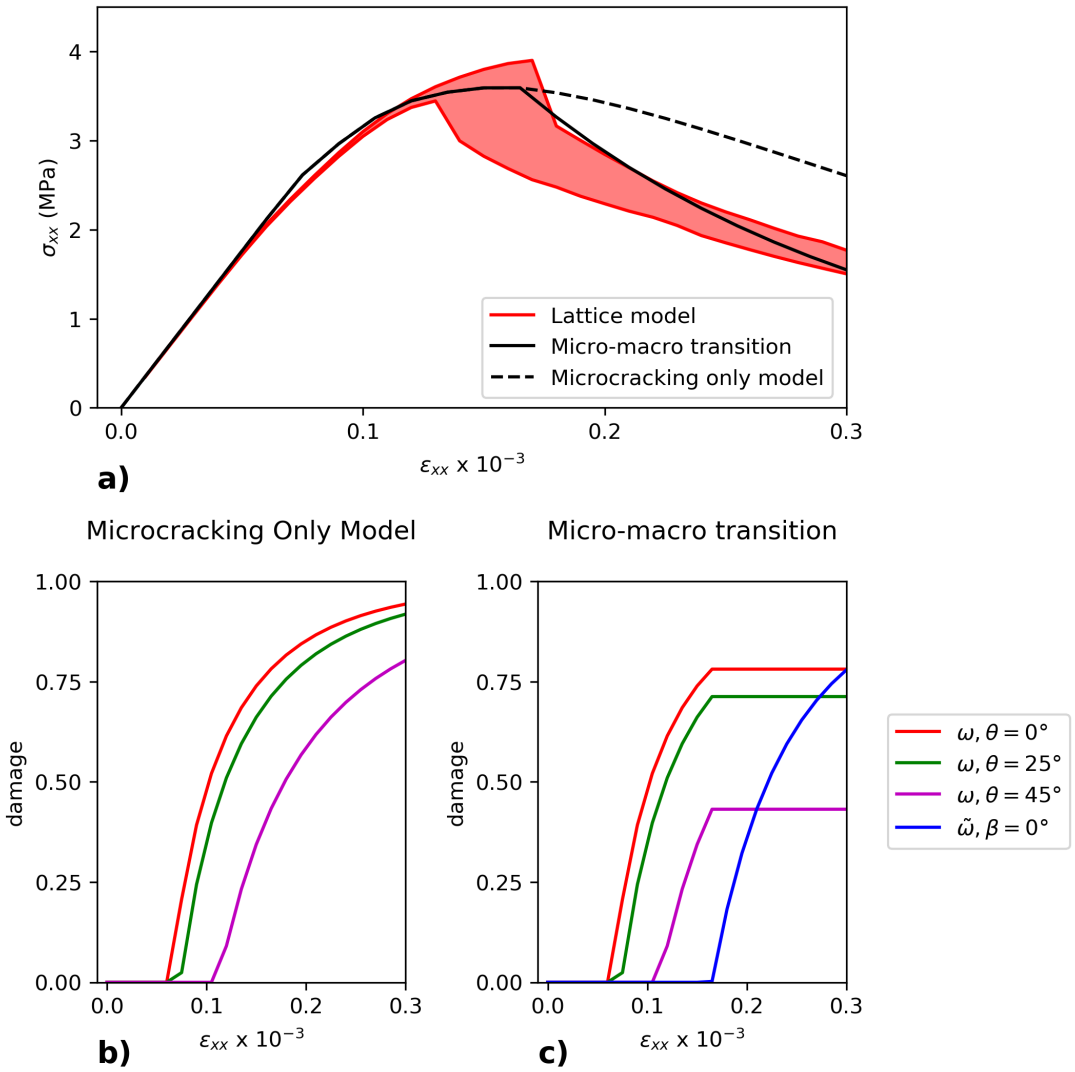

Figure 4.15: Comparison of predictions from the versions of the constitutive model with microcracking only and both microcracking and macrocracking with predictions from the lattice model (tension $+ve$). The envelope of results from the lattice model was obtained from 10 simulations with varying meso-structures.

4.5.2 Constitutive model simulation compared to experimental data

To show that inclusion of the transition of localised cracking gives more realistic predictions, the results from numerical simulations of uniaxial tension from the constitutive model, with and without the transition to localised cracking, were compared to experimental data from Reinhardt (1984). The material parameters used for the simulations are shown below in Table 4.4. The parameter c_1 was adjusted to tune the predictions to the experimental results. The maximum size of coarse aggregate particles is assumed to be 10mm and is taken to be the characteristic length from which strains can be related to displacements.

Table 4.4: Material parameters used for the constitutive model to compare with experimental data from Reinhardt (1984).

E_m (MPa)	E_Ω (MPa)	ν_m	ν_Ω	f_m	f_Ω (MPa)	c_1	q	μ	f_t	ε_0
30,000	60,000	0.19	0.21	0.5	0.5	4	3.3	4.2	1.37	0.015

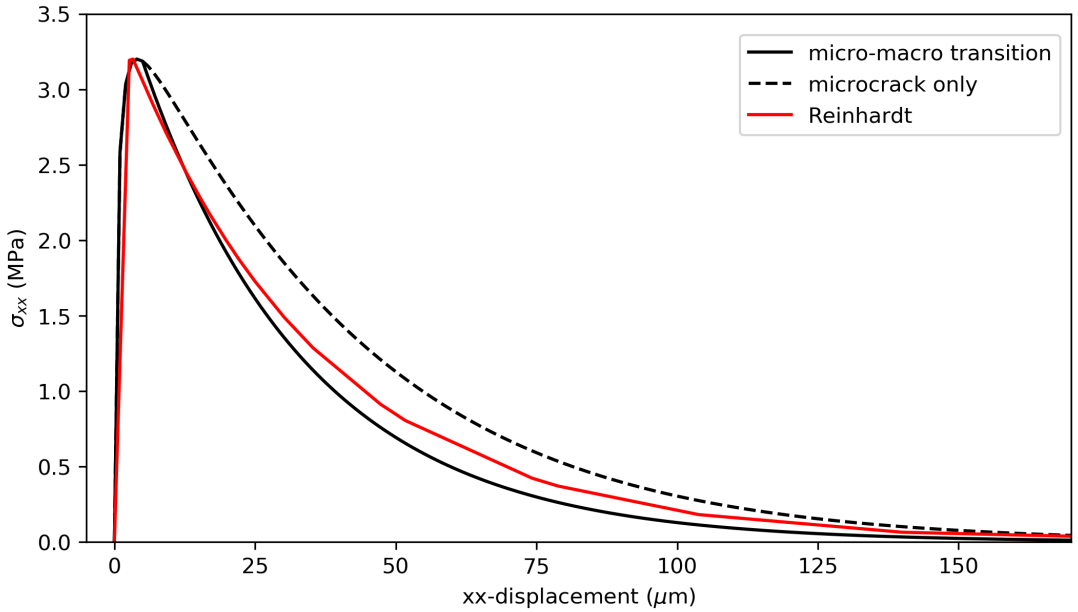

Figure 4.16: Comparison of predictions from the versions of the constitutive model with microcracking only and both microcracking and macrocracking with experimental data from Reinhardt (1984) (tension $+ve$).

The results are shown in Figure 4.16. Immediately after the peak stress, the predictions from the microcracking only model are excessively ductile. The micro-macro transition model betters agrees with the experimental data albeit being slightly too brittle later in the post-peak response.

4.5.3 Comparison of the micro-macro transition model to the microcracking only model

The third set of uniaxial tension simulations focuses on directly comparing the micro-macro transition model to the microcracking only model. Table 4.5 shows the material parameters used for the simulations.

Table 4.5: Material parameters used for the uniaxial tension numerical simulations

E_m (MPa)	E_Ω (MPa)	ν_m	ν_Ω	f_m	f_Ω (MPa)	c_1	q	μ	f_t	ε_0
30,000	60,000	0.19	0.21	0.5	0.5	10	3.3	4.2	1.9	0.01

Figure 4.17 shows the results of simulating the uniaxial tension loading path. The orientation angles α and β of the macrocracks are 90° and 0° (i.e. cracks are parallel to the direction of the applied strain) respectively.

Figure 4.17c and Figure 4.17d illustrate that the formation of macrocracks causes a transition where microcracks stop growing and damage is driven by macrocrack growth. The transition can also be observed through the differences in the damage surfaces, Figure 4.17e and Figure 4.17f, from analyses with the full model and analyses with microcracking only. Further, introduction of macrocracks reduces the predicted ductility of the response in the post peak regime and leads to the relaxation of the lateral strain, which is the expected characteristic response as the formation of a macrocrack causes unloading of lateral strain . Experimental data from uniaxial tests of reinforced concrete panels shows that there is a reversal in the lateral strains (the incremental lateral strains change from being negative to positive) immediately after cracking (Vecchio & DeRoo 1995). According to Vecchio & DeRoo (1995), the lateral strain reversal indicates the occurrence of a tensile-splitting mechanism. In the present case, the relaxation of lateral strains after the development of a macrocracking plane is also indicative of tensile-splitting.

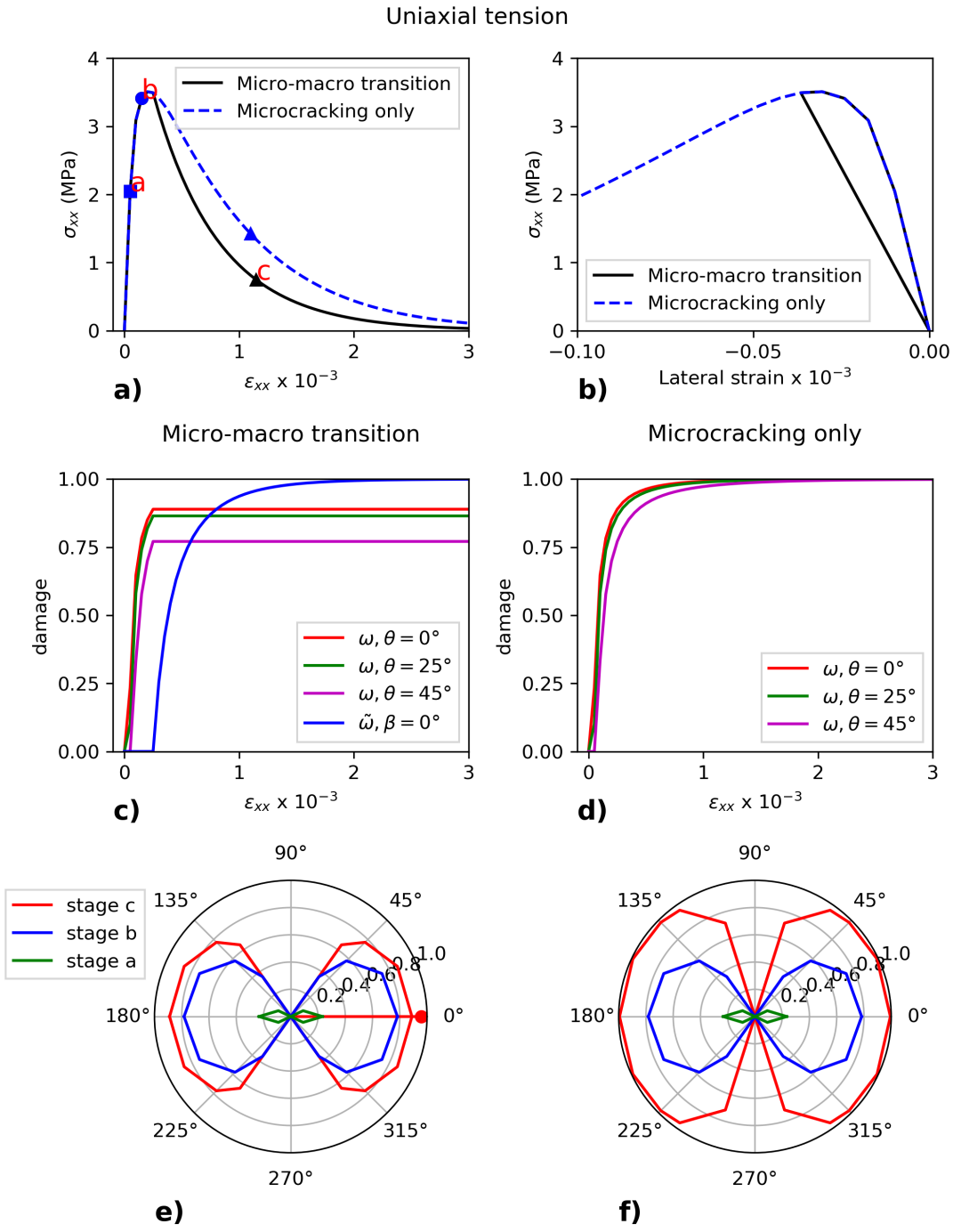

Figure 4.17: Results from numerical simulation of uniaxial tension (tension $+ve$). (a) σ_{xx}– ε_{xx} response. (b) σ_{xx}– ε_{yy} response. (c) $\tilde{\omega}$- ε_{xx} for the full model. (d) $\tilde{\omega}$- ε_{xx} for the microcracking only model. (e) $\tilde{\omega}$- crack plane normal orientation with respect to the loading axis (xx direction) for the full model. Macrocrack damage is indicated on the damage surface plots using markers with stems. (f) ω- crack plane normal orientation with respect to the loading axis for the microcracking only model. The stages in (e) and (f) correspond to those marked in (a).

4.6 Single-point path simulations

4.6.1 Parameters and paths

Simulations of other loading paths were carried out using a single set of parameters. The parameters, which relate to plain concrete, that were used are shown in Table 4.5.

The stress-strain paths considered with the model, included uniaxial tension, combined uniaxial tension and shear, biaxial tension, combined biaxial tension and shear, uniaxial compression and biaxial compression. For all biaxial paths, the ratios between the applied strains ε_{xx} and ε_{yy} are 1:1. When shearing is applied to a tensile path, the ratio between the applied strains ε_{xx} and ε_{xy} is 5:1. Note that the uniaxial tension path was previously explored in section 4.5.3.

Tensile paths

The results of the tensile path simulations are shown in Figure 4.18 - 4.20. The biaxial tension case is similar to the uniaxial tension case in that the orientation angle $\alpha$is 90° for all macrocracks and a macrocrack forms parallel to the direction of the applied strain. In the biaxial tension simulation , an additional macrocrack also forms perpendicular to the applied strain direction (β =90°).

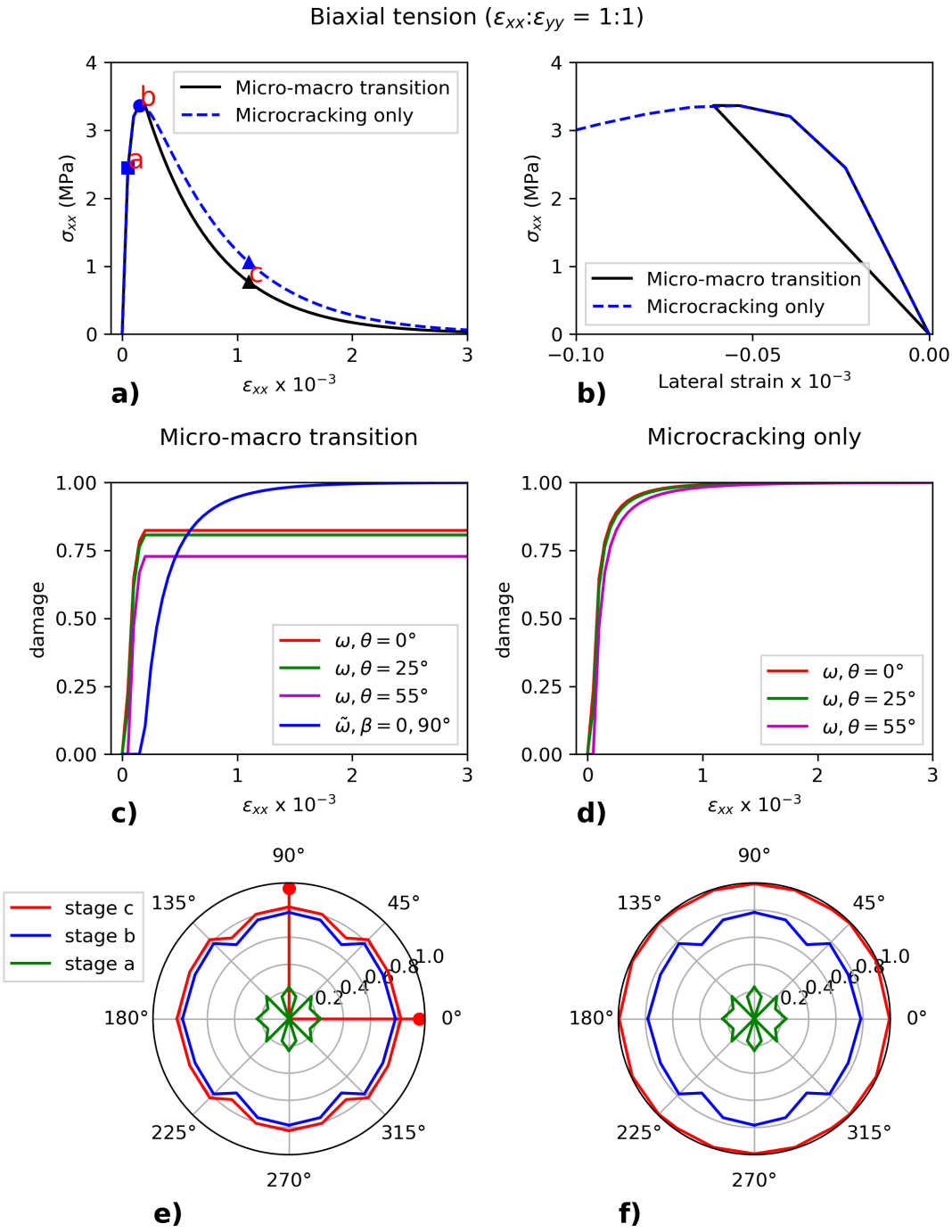

Figure 4.18: Results from numerical simulation of biaxial tension (tension $+ve$). (a) σ_{xx}– ε_{xx} response. (b) σ_{xx}– ε_{yy} response. (c) $\tilde{\omega}$- ε_{xx} for the full model. (d) $\tilde{\omega}$- ε_{xx} for the microcracking only model. (e) $\tilde{\omega}$- crack plane normal orientation for the full model. (f) ω- crack plane normal for the microcracking only model.

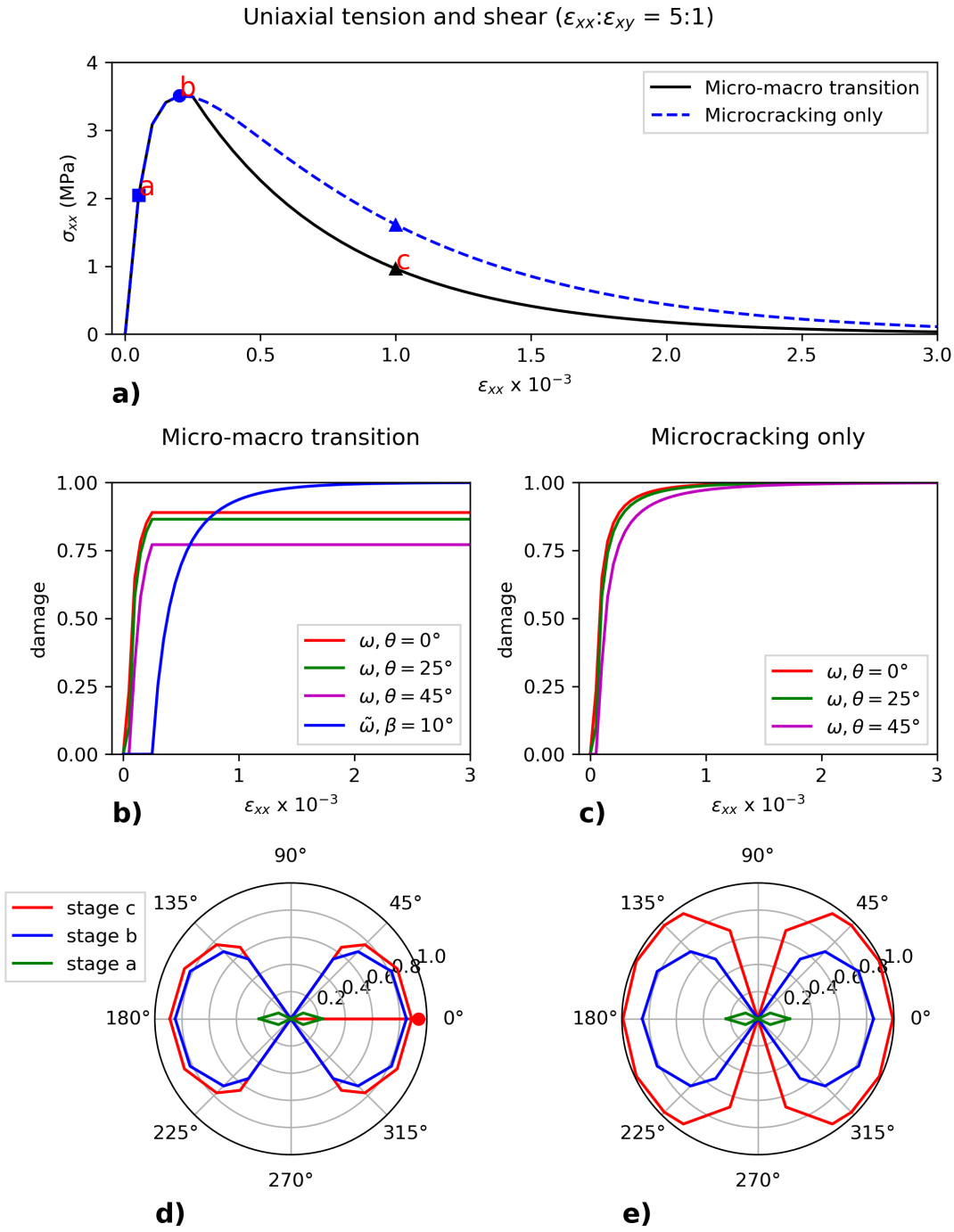

Figure 4.19: Results from numerical simulation of uniaxial tension and shear (tension $+ve$). (a) σ_{xx}– ε_{xx} response. (b) $\tilde{\omega}$- ε_{xx} for the full model. (c) $\tilde{\omega}$- ε_{xx} for the microcracking only model. (d) $\tilde{\omega}$- crack plane normal orientation for the full model. (e) ω- crack plane normal for the microcracking only model.

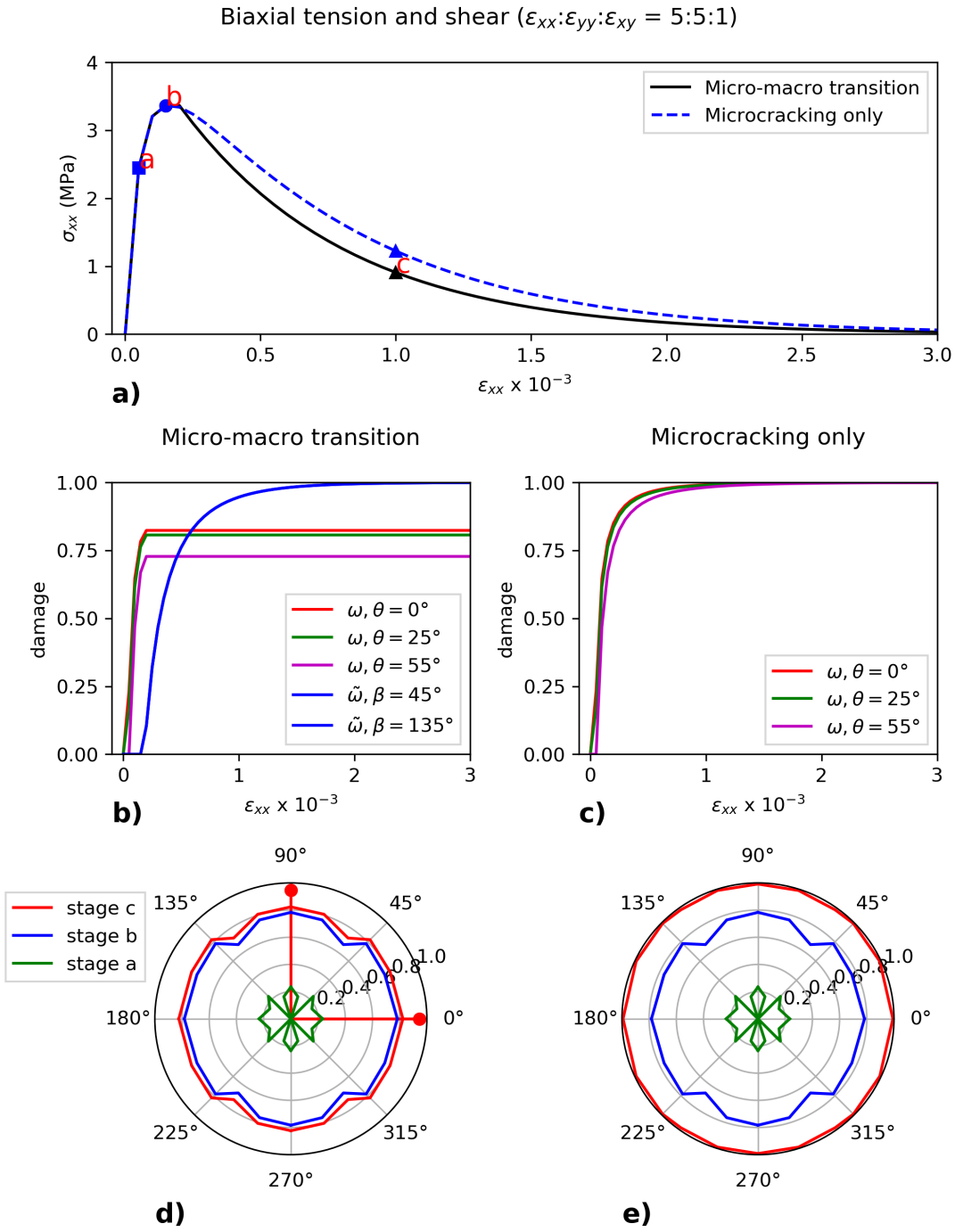

Figure 4.20: Results from numerical simulation of biaxial tension and shear (tension $+ve$). (a) σ_{xx}– ε_{xx} response. (b) $\tilde{\omega}$- ε_{xx} for the full model. (c) $\tilde{\omega}$- ε_{xx} for the microcracking only model. (d) $\tilde{\omega}$- crack plane normal orientation for the full model. (e) ω- crack plane normal for the microcracking only model.

From the stress-strain curves (figures 4.18a, 4.19a, and 4.20a), the inclusion of the transition to localised cracking can be seen to reduce the post-peak ductility. In section 4.5, it was shown that this reduction in post-peak ductility gives more realistic predictions of material behaviour. Figure 4.18b shows that the tensile-

splitting mechanism, indicated by relaxation of lateral strain after localisation to macrocracking, can be captured by the model in multi-axial stress states. The effects of inclusion of the micro-macro transition can be seen in the damage evolution profiles (figures 4.18c-f,4.19b-e and 4.20b-e). In all of the simulations, once macrocracking is initiated in the micro-macro transition model, damage growth of the microcrack planes in all directions slows down and eventually stops whilst macrocrack damage continues to increase throughout the post-peak regime.

Compressive paths

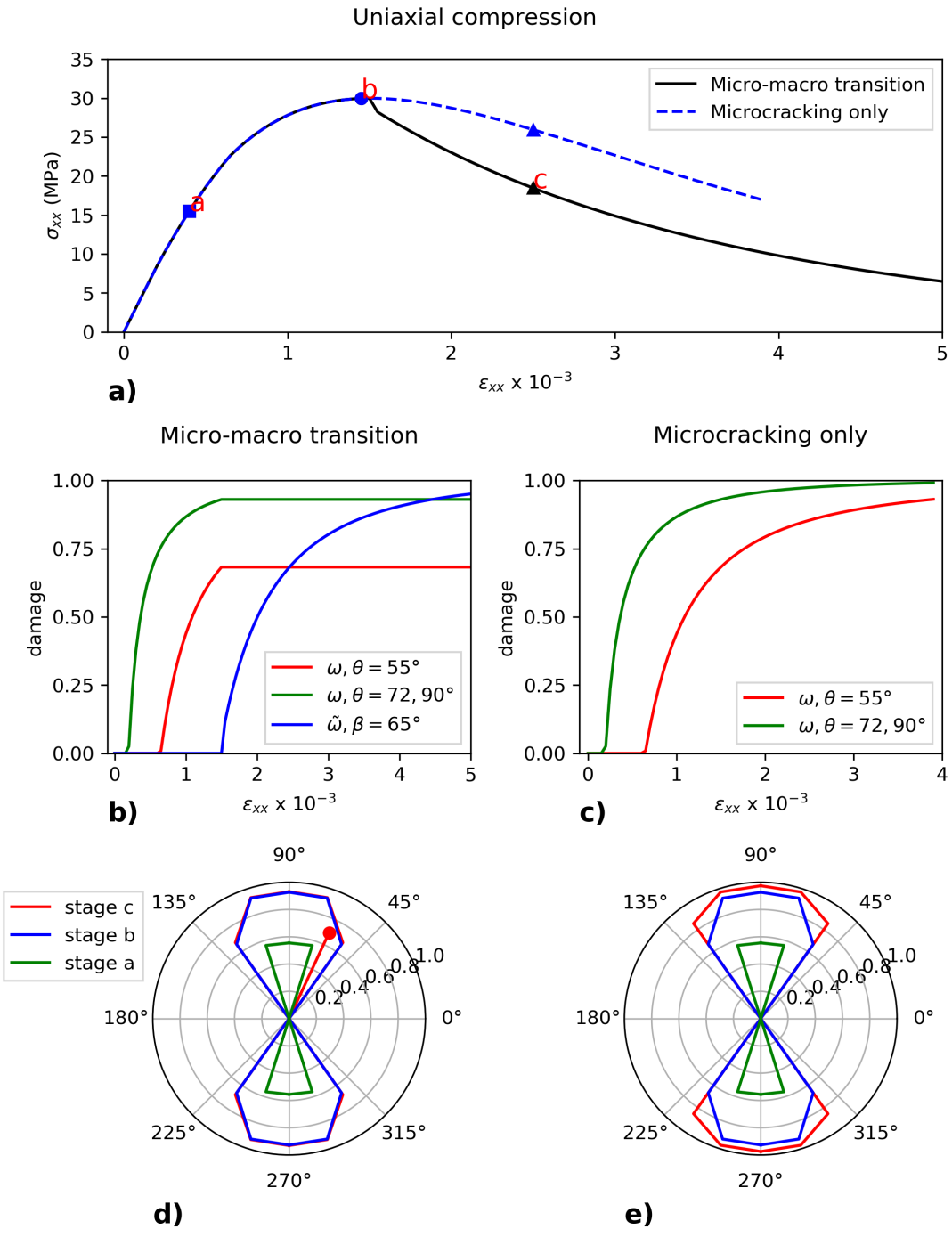

Figure 4.21: Results from numerical simulation of uniaxial compression (compression+ve). (a) σ_{xx}– ε_{xx} response. (b) $\tilde{\omega}$- ε_{xx} for the full model. (c) $\tilde{\omega}$- ε_{xx} for the microcracking only model. (d) $\tilde{\omega}$- crack plane normal orientation for the full model. (e) ω- crack plane normal for the microcracking only model.

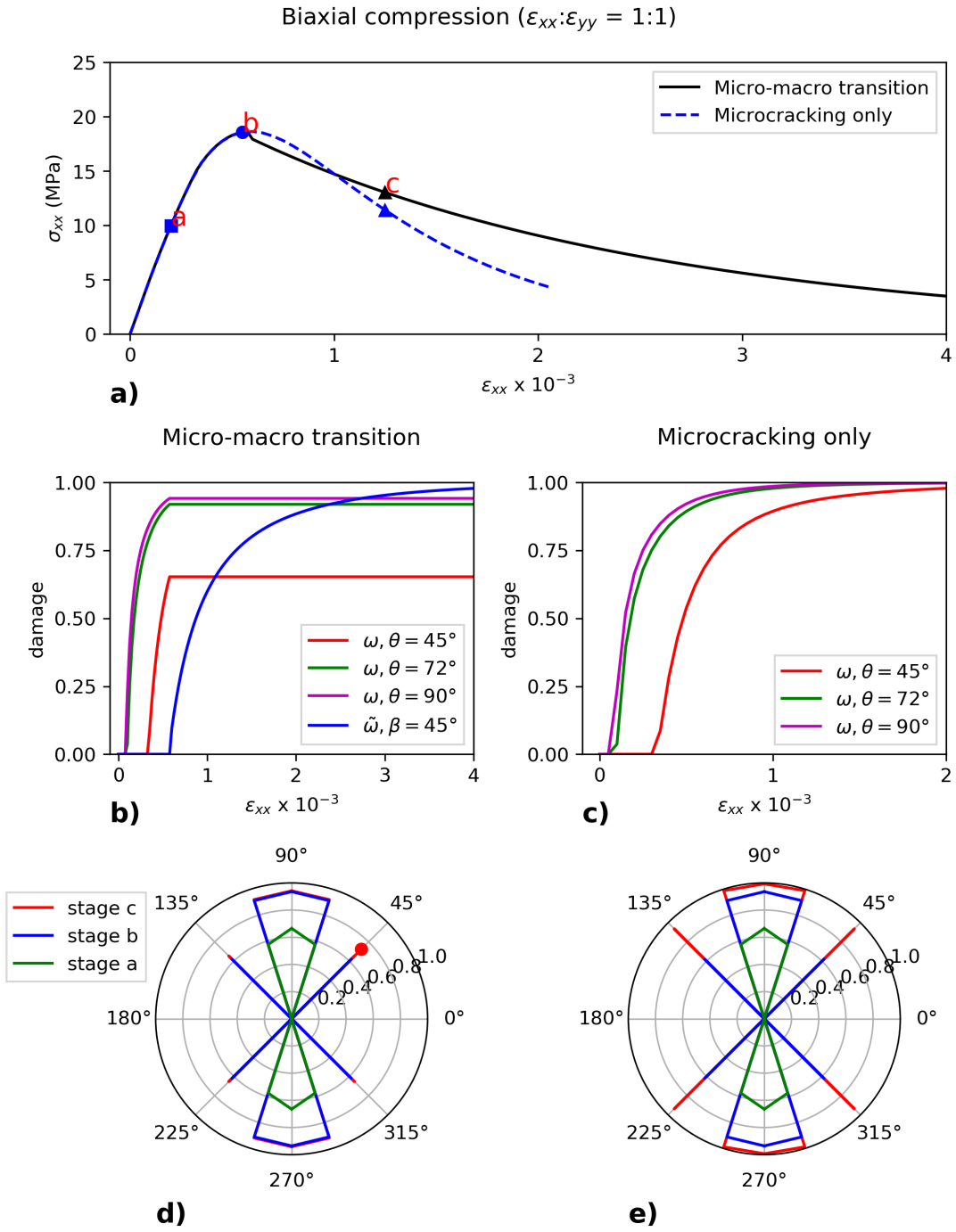

Figure 4.22: Results from numerical simulation of biaxial compression (compression+ve). (a) σ_{xx}– ε_{xx} response. (b) $\tilde{\omega}$- ε_{xx} for the full model. (c) $\tilde{\omega}$- ε_{xx} for the microcracking only model. (d) $\tilde{\omega}$- crack plane normal orientation for the full model. (e) ω- crack plane normal for the microcracking only model.

Figure 4.21 and Figure 4.22 show numerical simulations of uniaxial and biaxial compression loading paths. Under uniaxial compression, the orientation angles α and β of the macrocrack are 45° and 65° respectively. Under biaxial compression, the orientation angles α and β of the macrocrack are 25° and 45° respectively.

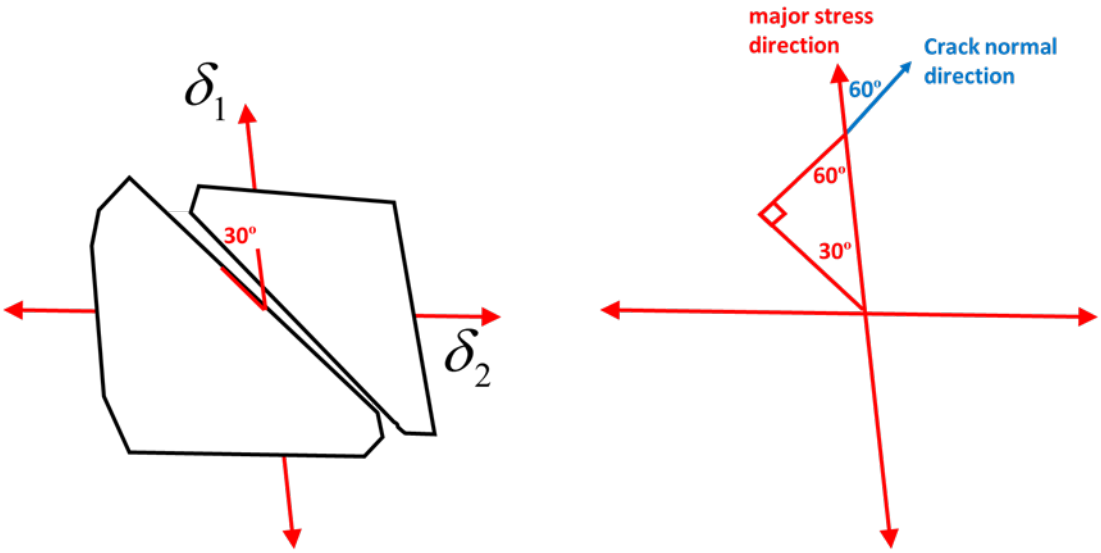

Figure 4.23: Average angle of the inclined shear bands from the major stress from uniaxial compression tests by Kupfer et al. (1969) and approximation of the inclination of the normal to the shear band from the direction of the major stress.

Similar to the tensile simulations, in the damage evolution profiles of compressive paths (figures 4.21b-e and 4.22b-e) a transition to localised cracking upon formation of macrocracks is also observed. Uniaxial compression tests of concrete specimens were carried out by Kupfer (1973). Kupfer (1973) measured that the average angle of the inclined shear bands from the major stress was approximately 30° for uniaxial loading. Based on the aforementioned tests, the orientation angles β of the macrocracks or the orientation of the normal of the shear bands with respect to the major stress should be approximately 60° (shown in Figure 4.23). It can be observed from figures 4.21b and 4.21d that the orientation of β given by the model is reasonable for uniaxial compression and the full model captures well the characteristic response.

It may be observed that the proposed constitutive model predicts a biaxial/uniaxial strength ratio significantly less than those observed in experimental tests e.g. Kupfer et al. (1969). However, it should be noted that rough contact on micro and macrocrack surfaces, shown to be a key mechanism for an accurate representation of the characteristic response in compression (and shear) (Jefferson & Bennett 2007, Mihai & Jefferson 2017), was not included in this work for expediency; the aim of this model is to accurately capture the crack localisation process and the transition from diffuse/ distributed microcracking to localised macrocracking. Nevertheless, it is acknowledged that rough contact should be included in order to capture the characteristic behaviour of cementitious composites in a

comprehensive manner and this will be the focus of future work.

4.7 Conclusions

A constitutive model for quasi-brittle materials that can capture the transition from diffuse microcracking to localised cracking was proposed. Micromechanics based solutions were used to model the elastic properties of a two-phase composite, directional microcracking and the formation of localised cracks. Based on lattice model simulations, macrocracks are initiated at the peak stress and their effect on microcrack growth was modelled. The main findings of this work can be summarised as following:

- Inclusion of the transition to localised cracking from diffuse microcracking reduces the post-peak ductility of predictions of under tensile loading paths when compared to when the transition is not included. The reduced post-peak ductility is more realistic and agrees well with experimental data for plain concrete.
- Modelling the transition from diffuse microcracking to localised macrocracking also significantly improves agreement of predictions from the constitutive model to predictions from a more computationally expensive lattice analyses.
- By allowing macrocracking planes to develop, the tension-splitting mechanism is captured via relaxation of lateral strains. This mechanism is not predicted when only microcracking is allowed for.
- The model predicts realistic orientations of the localised cracking plane(s) under different loading conditions.

The addition of rough contact on microcrack and macrocrack surfaces to the formulation, which will be the subject of future work, is expected to further improve the capability of the model to capture the characteristic behaviour of cementitious materials.

Chapter 5

Extension of micromechanical constitutive model to fibre-reinforced cementitious composites

5.1 Introduction

The model presented in this chapter is an extension of the constitutive model presented in chapter 4. The current model aims to capture the crack-bridging effects of fibre-reinforcement in cementitious composites using a micromechanics based formulation.

The structure of this chapter is as following: section 5.2 describes the constitutive model which is then followed by details of the numerical implementation in section 5.3. In section 5.4, the results of simulations of steel fibre-reinforced concrete are given. The results are discussed in section 5.5 followed by conclusions drawn in section 5.6.

5.2 Micromechanics based constitutive model

5.2.1 Model components

The micromechanical model presented in 4.3 is extended to include the influence of randomly distributed short fibre-reinforcement as shown in Figure 5.1. It is again assumed that the composite is a two-phase material and it is also assumed that series of microcracks with the same orientation are equivalent to bands of material, or 'crack-planes', containing these cracks. The crack-planes are bridged

by the fibres as illustrated in Figure 5.2.

For details of the two-phase composite and directional microcracking components of the model see sections 4.3.2, 4.3.3 and 4.3.4. The following sections detail the fibre crack-bridging component of the model which is based on the work of Mihai & Jefferson (2017). Note that some parts of the crack-bridging component have been briefly described in section 3.4.2 but those details are repeated for completeness.

The crack localisation mechanism, which is the main contribution of the author, is detailed in section 5.2.4 for the proposed fibre-reinforced cementitious composite model. Further new research such as the solution procedure for the proposed mechanism and the predictions resulting from implementing the mechanism follow on from section 5.2.4.

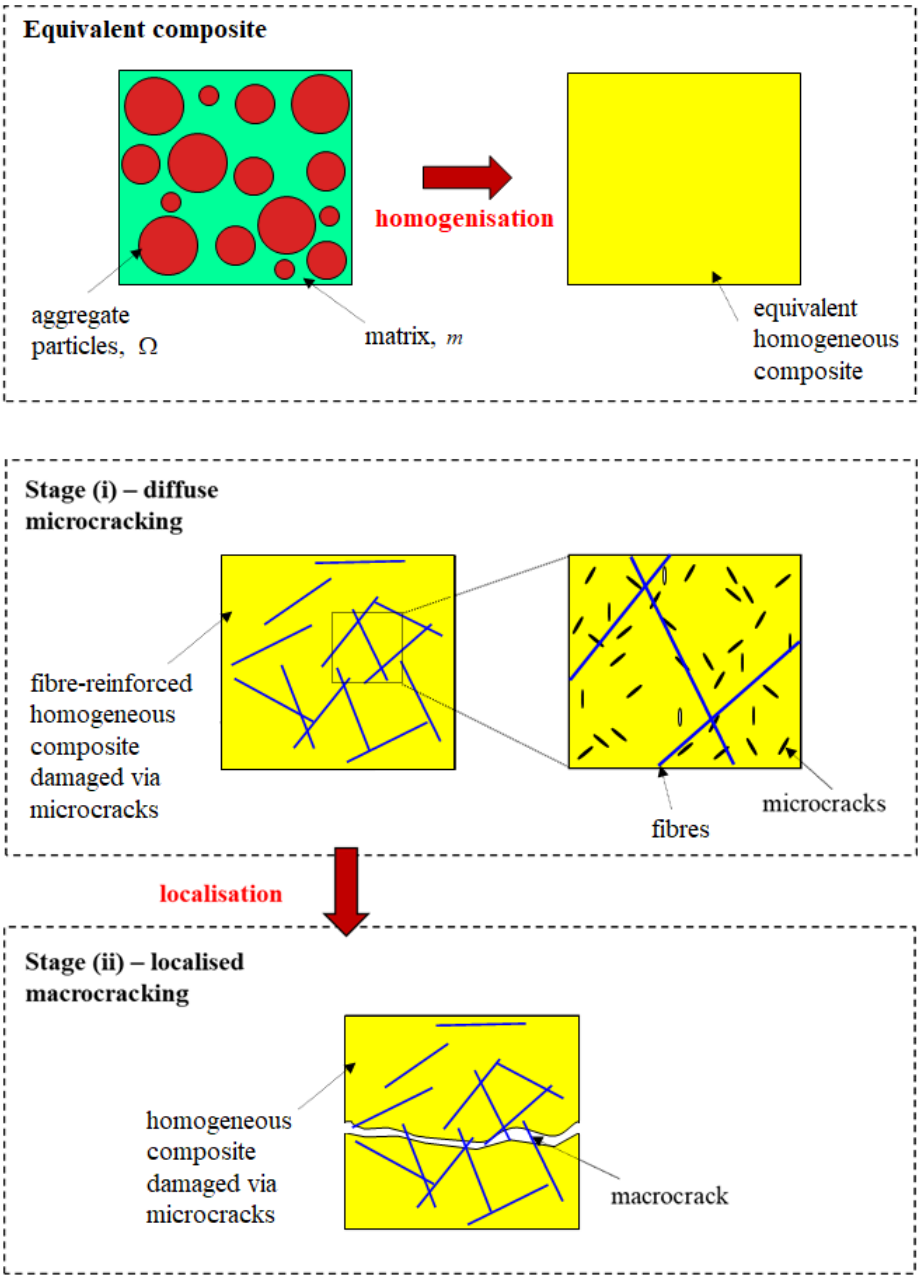

Figure 5.1: The main model concepts. Adapted from Mihai & Jefferson (2017).

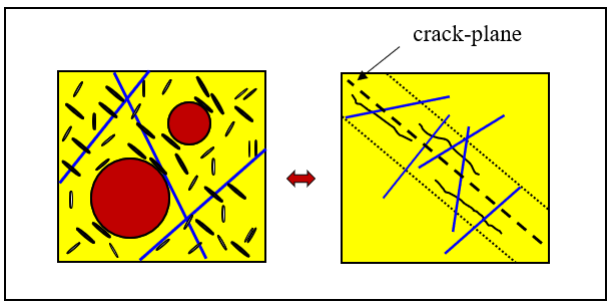

Figure 5.2: Schematic representation of a crack-plane containing microcracks. Adapted from Mihai & Jefferson (2017).

5.2.2 Fibre crack-bridging stress

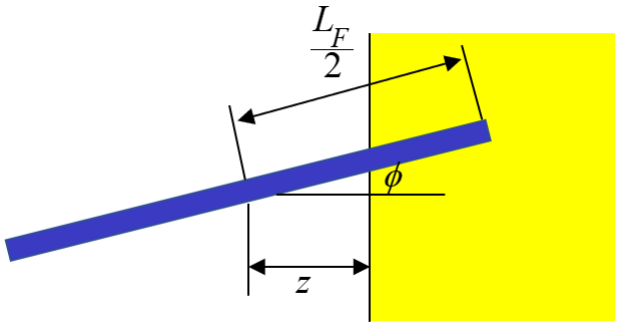

Figure 5.3: Illustration of the fibre centroidal distance and the orientation angle. Adapted from Li et al. (1991).

The stress that is transferred by the pull-out of fibres between two opposing faces of a crack under normal opening displacements is the crack-bridging stress σ_{cb}.

When fibres are randomly distributed and oriented, the crack-bridging stresses of individual fibres that bridge cracks can be summed to give the overall crack-bridging stress based on the work of Li et al. (1991). The mathematical expression is shown below in Equation 5.1.

In terms of the normal opening displacement w, σ_{cb} is given by:

$$\sigma_{cb}(w) = \frac{V_f}{A_f} \int_{\phi} \left(\int_{z} P(\phi, z, \boldsymbol{\Theta}, \boldsymbol{b}, w) p(\phi) d\phi \right) p(z) dz \tag{5.1}$$

where V_f is the volume fraction of fibres, A_f is the cross-sectional area of fibres, ϕ is the orientation angle of fibres relative to the crack-plane and z is the fibre centroidal distance from the crack-plane. See Figure 5.3.

$P(\phi, z, \boldsymbol{\Theta}, \boldsymbol{b}, w)$ is the pull-out force of individual fibres. $\boldsymbol{\Theta}$ and $\boldsymbol{b}$ are the sets of properties that relate to the fibre material and geometric properties and the fibre-matrix bond properties. $p(\phi)$ and $p(z)$ are the probability density functions of the fibre orientation and fibre centroidal distance from the crack-plane respectively.

For a uniform random distribution of fibres, $p(\phi) = sin(\phi)$ and $p(z) = 2/L_F$ (Li et al. 1991). The use of the probability density functions results in only those fibres that cross a crack-plane being included in the integration. The limits of integration account for the orientation and location of fibres such that fibres that are debonding or slipping can be considered separately.

A choice of different fibre pull-out models (describing $P(\phi, z, \boldsymbol{\Theta}, \boldsymbol{b}, w)$) can be incorporated into Equation 5.1. Following Mihai & Jefferson (2017), the proposed

formulation of Lin & Li (1997) which incorporates the phenomenological slip-hardening model of Bao & Song (1993) was used. The slip-hardening model uses two parameters: τ_0, which is frictional sliding shear stress at the tip of the debonding zone before any slip has occured, and β, a non-dimensional hardening parameter. The linear slip-hardening constitutive relation between the interfacial shear stress τ and the interfacial slip S is:

$$\tau = \tau_0 \left(1 + \beta \frac{S}{d_f}\right) \tag{5.2}$$

where d_f is the fibre diameter.

In terms of the normal opening displacement $\tilde{w}$, σ_{cb} is given by:

$$\sigma_{cb}(\tilde{w}) = \sigma_0 f(\tilde{w}) \tag{5.3}$$

where $f(\tilde{w})$ is defined by:

$$f(\tilde{w}) = \begin{cases} \frac{2}{k}\left\{\left[1 - \frac{1}{k} cosh^{-1}\left(1 + \lambda \frac{\tilde{w}}{\tilde{w}_{df}}\right)\right]\sqrt{\left(1 + \lambda \frac{\tilde{w}}{\tilde{w}_{df}}\right)^2 - 1} + \frac{\lambda}{k}\frac{\tilde{w}}{\tilde{w}_{df}}\right\} & 0 \leq \tilde{w} \leq \tilde{w}_{df} \\ \left(1 + \frac{\beta L_f}{2 d_f}\tilde{w}\right)(1 - \tilde{w})^2 & \tilde{w}_{df} < \tilde{w} \leq 1 \\ 0 & \tilde{w} > 1 \end{cases} \tag{5.4}$$

and where:

$$\tilde{w} = \frac{w}{L_f/2} \qquad \sigma_0 = 0.5 g_s \tau_0 V_f (1 + \eta_f)\frac{L_f}{d_f} \qquad k = \overline{\omega}\frac{L_f}{2 d_f}$$

$$\lambda = cosh(k) - 1 \qquad \eta_f = \frac{V_f E_f}{(1 - V_f)\overline{E}} \qquad \overline{\omega} = \sqrt{4(1 + \eta_f)\beta \tau_0 / E_f}$$

$$\tilde{w}_{df} = \frac{w_{df}}{L_f/2} \qquad w_{df} = \frac{2 d_f}{\beta}(cosh(k) - 1) \qquad g_s = \frac{2}{4 + {f_s}^2}\left(1 + e^{\pi f_s/2}\right)$$

The first two cases of Equation 5.4 correspond to the debonding and pull-out stages respectively. The third case corresponds to complete pullout of fibres from the matrix. $\overline{E}$ is the elastic modulus consistent with the two-phase homogenisation scheme, E_f is the Young's modulus of fibres and L_F is the fibre length. Note that f_s is a snubbing coefficient which takes into account the fact that as the inclination of a fibre from the loading axis increases, the fibre pull-out force

also increases. ω_{df} is the opening at the end of the debonding stage.

For the current model, it assumed that the debonding phase is linear elastic and the pull-out stage is based on the non-linear solution by Lin & Li (1997). Hence, in term of crack opening parameter ζ_f, the fibre crack-bridging stress, now denoted as σ_B, is calculated by:

$$\sigma_B(\zeta_f) = \begin{cases} E_{df}\zeta_f & 0 \leq \zeta_f \leq \varepsilon_{df} \\ \sigma_0 \left(1 + \frac{\beta L_f}{2d_f}\frac{\zeta_f}{\varepsilon_{pf}}\right)\left(1 - \frac{\zeta_f}{\varepsilon_{pf}}\right)^2 & \varepsilon_{df} \leq \zeta_f \leq \varepsilon_{pf} \\ 0 & \varepsilon_{pf} < \zeta_f \end{cases} \tag{5.5}$$

ε_{df} and ε_{pf} represent the strain measure at the end of the debonding and pull-out stage respectively and are defined as:

$$\varepsilon_{df} = \frac{\omega_{df}}{h} \qquad \varepsilon_{pf} = \frac{L_f/2}{h}$$

and E_{df} is the effective elastic modulus of fibres that is given by:

$$E_{df} = \frac{\sigma_0}{\varepsilon_{df}}\left(1 + \frac{\beta L_f}{2d_f}\varepsilon_{df}\right)(1 - \varepsilon_{df})^2 \tag{5.6}$$

h is the width of the fracture process zone which is taken to be the maximum size of the aggregate particles d_{max}.

5.2.3 Influence of fibres on microcrack planes

To capture the influence of crack-bridging by fibres, the local constitutive relationship is set as (dependencies have been dropped for clarity):

$$\boldsymbol{\sigma_L} = (1 - \omega)\boldsymbol{C_L^{-1}}\boldsymbol{\varepsilon_L} + \omega(1 - \omega_f)\boldsymbol{D_{Lf}}\boldsymbol{\varepsilon_L} \tag{5.7}$$

where $\boldsymbol{D_{Lf}}$ is the local elastic stiffness given by the interface bond of fibres prior to pull-out, assuming that fibres have negligible bending stiffness and that debonding is a linear behaviour. ω_f in the second term is an effective fibre damage parameter. The effective fibre damage parameter describes the state of crack-bridging by varying from 0 when no fibre pull-out has occurred to 1 when pull-out of all fibres has been completed. The evolution of ω_f is linked to the

crack bridging stress via the following:

$$(1-\omega_f)E_{df}\zeta_f = \sigma_{cb} \tag{5.8}$$

The evolution of the crack opening parameter is controlled by the following function (Mihai & Jefferson 2017):

$$\mathrm{F}_{\zeta f}(\boldsymbol{\varepsilon_L}, \zeta_f) = \frac{1}{2}\left({\varepsilon_{Lrr}}^2 + \sqrt{{\varepsilon_{Lrr}}^2 + 4({\varepsilon_{Lrs}}^2 + {\varepsilon_{Lrt}}^2)}\right) - \zeta_f \tag{5.9}$$

where the conditions $\mathrm{F}_{\zeta f} \leq 0; \dot{\zeta}_f \geq 0; \mathrm{F}_{\zeta f}\dot{\zeta}_f = 0$ apply.

The inelastic strain of the microcrack planes $\boldsymbol{\varepsilon_\alpha}$ is derived by removing the local elastic strain component $\boldsymbol{\varepsilon_{Le}}$ from the local strain:

$$\boldsymbol{\varepsilon_\alpha} = \boldsymbol{\varepsilon_L} - \boldsymbol{\varepsilon_{Le}} = \boldsymbol{\varepsilon_L} - \boldsymbol{C}_L\boldsymbol{\sigma_L} \tag{5.10}$$

Next, re-arranging Equation 5.7 for $\boldsymbol{\varepsilon_L}$ and substituting in the above gives:

$$\boldsymbol{\varepsilon_\alpha} = ([(1-\omega)\boldsymbol{C_L}^{-1} + \omega(1-\omega_f)\boldsymbol{D_{Lf}}]^{-1} - \boldsymbol{C}_L)\boldsymbol{\sigma_L} \tag{5.11}$$

To obtain the stiffness tensor $\boldsymbol{D}_{mcf}$ that takes into account microcrack damage and crack-bridging by fibres on the microcrack planes, the same procedure that was used to derive the microcrack damaged stiffness tensor (Equation 4.15 in the previous chapter) is used. Note that $\boldsymbol{\varepsilon_\alpha}$ from Equation 5.11 is substituted into Equation 4.13.

Finally, $\boldsymbol{D}_{mcf}$ is derived as:

$$\boldsymbol{D}_{mcf} = \left(\boldsymbol{I}^{4s} + \frac{\boldsymbol{D}_{m\Omega}}{2\pi}\cdot\int_0^{2\pi}\int_0^{\pi/2}\boldsymbol{N}_\varepsilon(\theta_1,\theta_2) : \boldsymbol{C}_{add}(\theta_1,\theta_2) : \boldsymbol{N}(\theta_1,\theta_2)\sin(\theta_1)d\theta_1 d\theta_2\right)^{-1}\cdot\boldsymbol{D}_{m\Omega} \tag{5.12}$$

where

$$\boldsymbol{C}_{add} = [(1-\omega)\boldsymbol{C_L}^{-1} + \omega(1-\omega_f)\boldsymbol{D_{Lf}}]^{-1} - \boldsymbol{C}_L \tag{5.13}$$

5.2.4 Macrocracking

The following constitutive relationship gives the local stress $\tilde{\boldsymbol{\sigma}}(\alpha,\beta)$ of the macrocrack planes:

$$\tilde{\boldsymbol{\sigma}}(\alpha,\beta) = (1-\tilde{\omega}(\alpha,\beta))\boldsymbol{C_L}^{-1}\tilde{\boldsymbol{\varepsilon}}(\alpha,\beta) + \tilde{\omega}(\alpha,\beta)(1-\tilde{\omega}_f(\alpha,\beta))\boldsymbol{D_{Lf}}\tilde{\varepsilon}(\alpha,\beta) \quad (5.14)$$

The above equation can be used to write the inelastic strain of macrocracks $\hat{\boldsymbol{\varepsilon}}$ in terms of the macrocrack local strain. Removing the local elastic strain component $\tilde{\boldsymbol{\varepsilon}}_{\boldsymbol{Le}}$ from the macrocrack local strain gives the inelastic macrocrack strain:

$$\hat{\boldsymbol{\varepsilon}} = \tilde{\boldsymbol{\varepsilon}} - \tilde{\boldsymbol{\varepsilon}}_{\boldsymbol{Le}} = \tilde{\boldsymbol{\varepsilon}} - \boldsymbol{C_L}\tilde{\boldsymbol{\sigma}} \quad (5.15)$$

Note that dependencies have been dropped for clarity. Substitute $\tilde{\boldsymbol{\sigma}}$ from Equation 5.14 into 5.15:

$$\hat{\boldsymbol{\varepsilon}} = (\boldsymbol{I} - \tilde{\boldsymbol{M}}_s - \boldsymbol{C_L}\boldsymbol{D_{Lf}}\tilde{\boldsymbol{M}}_f) : \tilde{\boldsymbol{\varepsilon}} \quad (5.16)$$

where

$$\tilde{\boldsymbol{M}}_s = (1-\tilde{\omega})\boldsymbol{I} \qquad\qquad \tilde{\boldsymbol{M}}_f = \tilde{\omega}(1-\tilde{\omega}_f)\boldsymbol{I}$$

As with the previous model, macrocrack growth is initiated at the peak stress and the orientations of macrocracks under tensile loading conditions are based on the major principal strain direction. Under compressive loading conditions, the macrocrack orientations are based on the orientations which maximise the effective strain parameter of macrocrack planes.

Evolution of the effective strain parameter $\tilde{\zeta}$ and the damage parameter $\tilde{\omega}$ for macrocrack planes is based on equations 4.16 and 4.17 respectively. The variables related to fibres are denoted using similar notation and are calculated based on the equations provided in the preceding sections.

The crack-bridging stress $\tilde{\sigma}_B$ of macrocracks is given by the following:

$$\tilde{\sigma}_B(\tilde{\zeta}_{f_i}) = \begin{cases} E_{df}\tilde{\zeta}_{f_i} & 0 \le \tilde{\zeta}_{f_i} \le \varepsilon_{pf} \\ \sigma_0\left(1+\frac{\beta L_f}{2d_f}\frac{\tilde{\zeta}_{f_i}}{\varepsilon_{pf}}\right)\left(1-\frac{\tilde{\zeta}_{f_i}}{\varepsilon_{pf}}\right)^2 & \varepsilon_{df} \le \tilde{\zeta}_{f_i} \le \varepsilon_{pf} \\ 0 & \varepsilon_{pf} < \tilde{\zeta}_{f_i} \end{cases} \quad (5.17)$$

The effective strain parameter of macrocrack planes is denoted as $\tilde{\zeta}_{f_i}$ and is cal-

culated according to Equation 5.18.

$$\mathrm{F}_{\tilde{\zeta}_{f_i}}(\tilde{\boldsymbol{\varepsilon}}_{\boldsymbol{i}}, \tilde{\zeta}_{f_i}) = \frac{1}{2} = \left(\tilde{\varepsilon}^2_{irr} + \sqrt{\tilde{\varepsilon}^2_{irr} + 4(\tilde{\varepsilon}^2_{irs} + \tilde{\varepsilon}^2_{irt})}\right) - \tilde{\zeta}_{f_i} \tag{5.18}$$

The evolution of the macrocrack effective fibre parameter $\tilde{\omega}_f$ is given by:

$$(1 - \tilde{\omega}_{f_i}) E_{df} \tilde{\zeta}_{f_i} = \tilde{\sigma}_{cb} \tag{5.19}$$

In the above three equations, the subscript i refers to the macrocrack plane.

Though the same governing functions have been used to account for crack-bridging for microcracking and macrocracking, the expected characteristic behaviour is captured. This is demonstrated and discussed in sections 5.4.2 and 5.5.

5.2.5 Overall constitutive relationship

Similarly to the model in the previous chapter, the overall constitutive relationship is obtained by removing the inelastic strain of macrocracks from the average strain:

$$\bar{\boldsymbol{\sigma}} = \boldsymbol{D}_{mcf} : \left(\bar{\boldsymbol{\varepsilon}} - \sum_{i=1}^{n_{sd}} \boldsymbol{N}_{\varepsilon}(\alpha_i, \beta_i) : \hat{\boldsymbol{\varepsilon}}_i\right) \tag{5.20}$$

the difference being that $\hat{\boldsymbol{\varepsilon}}$ is not given by Equation 4.22 but instead by Equation 5.16 which takes into account the effects of crack-bridging by fibres on the planes of macrocracks.

5.3 Numerical implementation

The model is implemented in Mathcad following the same methodology that was used for the plain concrete micromechanical model (described in section 4.4). Again, McLaren's 50 point rule for a sphere (Stroud 1971) is adapted for integrating over the surface of a sphere and the method of Hasegawa & Bažant (1993) is used to generate consistent shear directions without directional bias. To calculate $\hat{\boldsymbol{\varepsilon}}$, the staggered solution method shown in Algorithm 5 is used.

5.3.1 Staggered solution algorithm

The non-linear coupled equations that must be solved to calculate the inelastic strain $\hat{\boldsymbol{\varepsilon}}$ now involve terms accounting for the effects of fibres:

Algorithm 5: Algorithm to calculate the inelastic strain of macrocrack planes (with fibres)

▷Enter with the strain vector and set macrocrack plane parameters to initial values or those from the previously converged step

$\bar{\boldsymbol{\varepsilon}}$; $\tilde{\boldsymbol{\varepsilon}}_i = \tilde{\boldsymbol{\varepsilon}}_i^{prv}$

$\tilde{\zeta}_i = \tilde{\zeta}_i^{prv}$; $\tilde{\omega}_i = \tilde{\omega}_i^{prv}$; $\tilde{\boldsymbol{M}}_{s_i} = \tilde{\boldsymbol{M}}_{s_i}^{prv}$

$\tilde{\zeta}_{f_i} = \tilde{\zeta}_{f_i}^{prv}$; $\tilde{\sigma}_{B_i} = \tilde{\sigma}_{B_i}^{prv}$; $\tilde{\omega}_{f_i} = \tilde{\omega}_{f_i}^{prv}$; $\tilde{\boldsymbol{M}}_{f_i} = \tilde{\boldsymbol{M}}_{f_i}^{prv}$;

▷Enter iteration loop of the staggered solution method

for *iter = 1* **to** $iter_{max}$ **do**

▷Calculate the matrix of derivatives and the stacked local error from the first coupled equation using Algorithm 6

▷Calculate the local crack plane strains and macrocrack plane variables using Algorithm 7

▷Calculate the stacked local error from the second coupled equation using Algorithm 8

▷Check if the error is within the required tolerance and exit if converged

if $(|\boldsymbol{\Psi}_\alpha| < tol_\alpha) \wedge (|\boldsymbol{\Psi}_\beta| < tol_\beta)$ **then**

exit

end

▷Exit the procedure and reduce the global step size if the maximum number of iterations has been reached

if $i == iter_{max}$ **then**

exit

end

end

Algorithm 6: Algorithm to calculate the matrix of derivatives and the stacked local error from the first coupled equation (with fibres)

▷ Enter from Algorithm 5

▷ Loop over microcrack planes n_p

for $i = 1$ **to** n_p **do**

  ▷ Compute microcrack plane variables from equations 4.16, 4.17, 5.9, 5.5, 5.8 and 4.23

  get ζ_i, ω_i, ζ_{f_i}, σ_{B_i}, ω_{f_i}, $\boldsymbol{\varepsilon}_{L_i}$

  ▷ Compute the microcrack based stiffness and the corresponding local stiffness matrix from Equation 5.12

  get $\boldsymbol{D_{mcf}}$, $\boldsymbol{D}_L$

end

▷ Loop over macrocrack planes n_{sd}

for $i = 1$ **to** n_{sd} **do**

  ▷ Calculate the stacked local error vector from Equation 5.21

  get $\boldsymbol{\Psi}_{\alpha_i}$

end

▷ Loop over macrocrack planes n_{sd}

for $i = 1$ **to** n_{sd} **do**

  for $j = 1$ **to** n_{sd} **do**

    ▷ Calculate the matrix of derivatives from Equation A.4

    get $\boldsymbol{B}_{E_{i,j}}$

  end

end

Algorithm 7: Algorithm to update the local crack plane strains and macro-crack plane variables (with fibres)

▷ Enter from Algorithm 5

▷ Calculate the stacked local strain vector for macrocrack planes from Equation 4.27

get $\boldsymbol{\delta\tilde{E}}$

▷ Loop over macrocrack planes n_{sd}

for $i = 1$ **to** n_{sd} **do**

  ▷ Update local crack plane strains and calculate the macrocrack plane variables from equations 4.16, 4.17, 5.18, 5.17 and 5.19

  get $\tilde{\boldsymbol{\varepsilon}}_i = \tilde{\varepsilon}_{\mathbf{i}} + \delta\tilde{\varepsilon}_{\mathbf{i}}$

  get $\tilde{\zeta}_i$, $\tilde{\omega}_i$, $\tilde{\boldsymbol{M}}_{s_i}$, $\tilde{\zeta}_{f_i}$, $\tilde{\sigma}_{B_i}$, $\tilde{\omega}_{f_i}$, $\tilde{\boldsymbol{M}}_{f_i}$ $\hat{\boldsymbol{\varepsilon}}_i$

end

Algorithm 8: Algorithm to calculate the stacked local error from the second coupled equation (with fibres)

▷ Enter from Algorithm 5

▷ Loop over macrocrack planes n_{sd}

for $i = 1$ **to** n_{sd} **do**

  ▷ Calculate the stacked local error vector from Equation 5.22

  get $\boldsymbol{\Psi}_{\beta_i}$

end

$$\boldsymbol{\Psi}_{\alpha_i} = \boldsymbol{N}\left(\alpha_i, \beta_i\right) : \boldsymbol{D}_{mcf} : \left(\bar{\boldsymbol{\varepsilon}} - \sum_{j=1}^{n_{sd}} \boldsymbol{N}_{\varepsilon}(\alpha_j, \beta_j) : (\boldsymbol{I}^{4s} - \tilde{\boldsymbol{M}}_{s_j} - \boldsymbol{C}_L \boldsymbol{D}_{\boldsymbol{Lf}} \tilde{\boldsymbol{M}}_{f_j}) : \tilde{\boldsymbol{\varepsilon}}_j \right) - \boldsymbol{D}_L \cdot \tilde{\boldsymbol{M}}_{s_i} : \tilde{\boldsymbol{\varepsilon}}_i - \boldsymbol{D}_{Lf} \cdot \tilde{\boldsymbol{M}}_{f_i} : \tilde{\boldsymbol{\varepsilon}}_i = \boldsymbol{0} \tag{5.21}$$

$$\boldsymbol{\Psi}_{\beta_k} = \boldsymbol{\varepsilon}_{L_k} - \boldsymbol{N}_{\varepsilon}\left(\psi_k, \theta_k\right) : \left(\bar{\boldsymbol{\varepsilon}} - \sum_{j=1}^{n_{sd}} \boldsymbol{N}_{\varepsilon}(\alpha_j, \beta_j) : (\boldsymbol{I}^{4s} - \tilde{\boldsymbol{M}}_{s_j} - \boldsymbol{C}_L \boldsymbol{D}_{\boldsymbol{Lf}} \tilde{\boldsymbol{M}}_{f_j}) : \tilde{\boldsymbol{\varepsilon}}_j \right) = \boldsymbol{0} \tag{5.22}$$

Subscript i denotes the macrocrack plane number, subscript k denotes the microcrack plane number. See Equation 4.24 and Equation 4.25 for comparison with the coupled equations for plain concrete. The inelastic strain which satisfied the coupled equations satisfies the requirement for the total stress transformed onto a macrocrack plane to be equal to the local stress of the macrocrack plane.

As with the previous formulation, the iterative update to the stacked local strain vector 5.24 is found by equating the first coupled equation to zero and carrying out a first-order Taylor's series expansion 5.23:

$$\boldsymbol{0} = \begin{bmatrix} \boldsymbol{\Psi_1} \\ \boldsymbol{\Psi_2} \end{bmatrix} + \boldsymbol{B_E} \begin{bmatrix} \boldsymbol{d\tilde{\varepsilon}_1} \\ \boldsymbol{d\tilde{\varepsilon}_2} \end{bmatrix} \tag{5.23}$$

$$\begin{bmatrix} \boldsymbol{d\tilde{\varepsilon}_1} \\ \boldsymbol{d\tilde{\varepsilon}_2} \end{bmatrix} = -\boldsymbol{B}_E^{-1} \begin{bmatrix} \boldsymbol{\Psi_1} \\ \boldsymbol{\Psi_2} \end{bmatrix} \tag{5.24}$$

where $\boldsymbol{\Psi} = \begin{bmatrix} \boldsymbol{\Psi}_{\alpha_1} \\ \boldsymbol{\Psi}_{\alpha_2} \\ \vdots \\ \boldsymbol{\Psi}_{\alpha_n} \end{bmatrix}$

and the matrix of derivative $\boldsymbol{B_E}$ is given by:

$$\boldsymbol{B}_{\boldsymbol{E}}^{K} = \begin{bmatrix} \boldsymbol{d\Psi_1}/\boldsymbol{d\tilde{\varepsilon}_1} & \boldsymbol{d\Psi_1}/\boldsymbol{d\tilde{\varepsilon}_2} \\ \boldsymbol{d\Psi_2}/\boldsymbol{d\tilde{\varepsilon}_1} & \boldsymbol{d\Psi_2}/\boldsymbol{d\tilde{\varepsilon}_2} \end{bmatrix}^{K} \tag{5.25}$$

Note that for the purpose of clarity, the Taylor's series expansion and the subsequent derivations shown above are based on a system with two macrocracks. See Appendix A for a detailed derivation of the matrix of derivatives.

5.4 Simulations

5.4.1 Parameters

Table 5.1: Material parameters used for plain concrete in the simulations.

E_m (GPa)	E_Ω (GPa)	ν_m	ν_Ω	c_1	q	μ	ε_0	d_{max} (mm)
30	60	0.19	0.21	5	3.3	4.2	0.005	20

Table 5.2: Material parameters used for fibres in the simulations.

Fibre type	L_f (mm)	d_f (mm)*	E_f (GPa)	τ_0 (MPa)	β_f	f_s
F1	30	0.542	200	2.5	0.1	0.75
F3	32	0.580		2.0		

**equivalent diameter.*

Single point path simulations were carried out and compared to experimental data from uniaxial tension tests of fibre-reinforced concrete by Meng et al. (2006). Two types of steel fibres, denoted as type F1 and F3, from Meng et al. (2006) were selected for comparison with predictions. F1 fibres are wire cut with a circular cross-section and F3 fibres are snipped with a rectangular cross-section. Both fibre types have hooked ends.

The behaviour of fibres in three different concrete mixes, namely C30, C60 and C80, were investigated. The differences in the strength of the different mixes was accounted for by setting the tensile strength f_t to 1 MPa, 2 MPa and 2.6 MPa for mixes C30, C60 and C80 respectively.

See Table 5.1 for the material parameters used for plain concrete in the simulations. Parameter c_1 was adjusted to tune the predictions from the model to the experimental results. For the material parameters used for the fibres in the simulations, see Table 5.2. The cases of F1 fibres in C60 concrete and F3 fibres in C30 concrete were used for calibration of τ_0 and β_f. τ_0 and β_f were tuned using the procedure described in Lin & Li (1997).

For each of the concrete mixes, the cases studied include plain concrete, reinforcement with F1 fibres at a volume fraction V_f= 1% and reinforcement with F3 fibres at volume fraction V_f = 0.5%, 1% and 1.5%.

5.4.2 Results

The results of the simulations are shown in figures 5.4 - 5.9. Figures 5.4, 5.6, 5.8 and 5.10 show the results of simulations of the plain concrete mixes and also of

the mixes reinforced with F1 fibres. Figures 5.5, 5.7 and 5.9 show the results of simulations for the concrete mixes reinforced with F3 fibres.

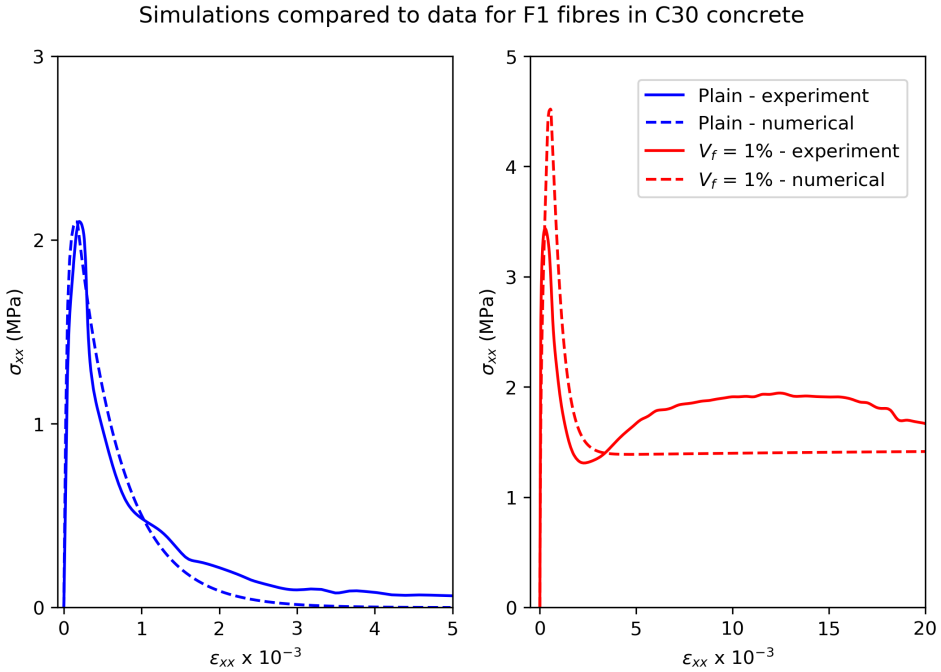

Figure 5.4: $\sigma_{xx} - \varepsilon_{xx}$ response from numerical simulations compared to experimental data from Meng et al. (2006). (a) Plain C30 concrete. (b) $V_f = 1\%$ F1 fibre-reinforced C30 concrete.

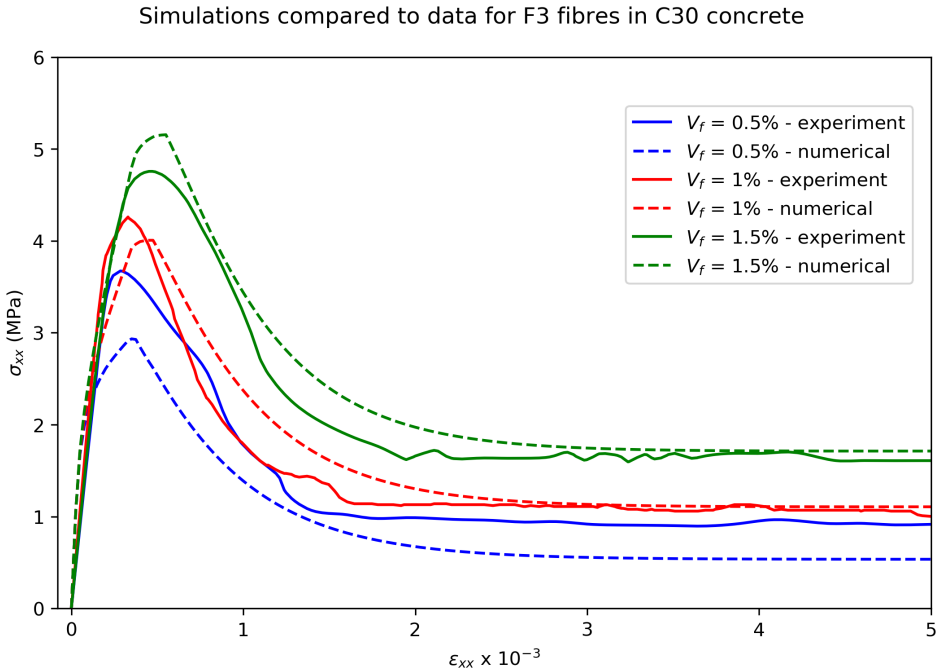

Figure 5.5: Comparison of $\sigma_{xx} - \varepsilon_{xx}$ response of C30 concrete reinforced with different volume fractions of F3 fibres from numerical simulations and experimental data from Meng et al. (2006).

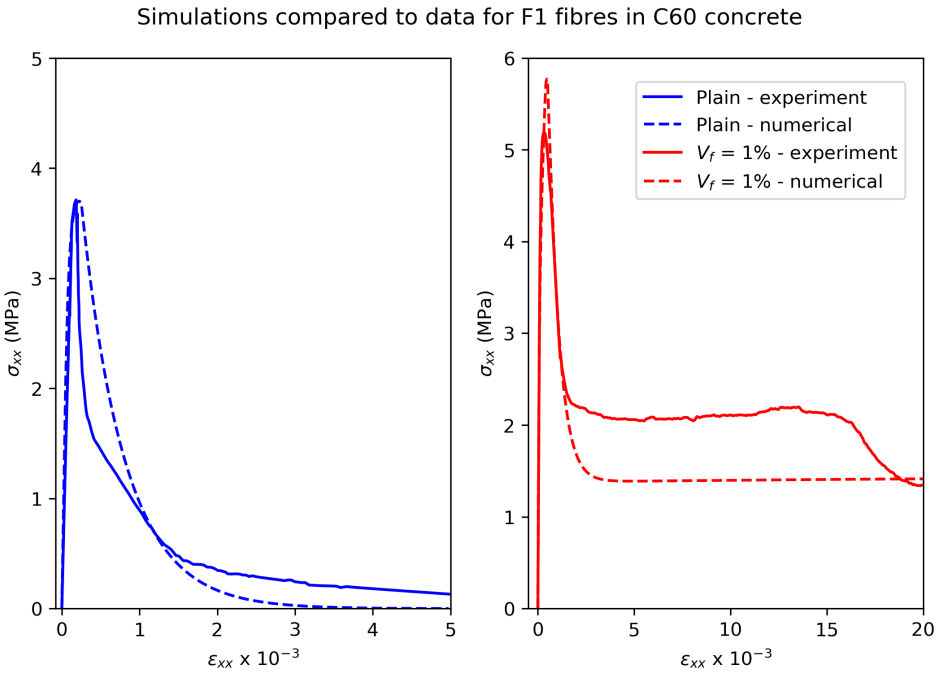

Figure 5.6: $\sigma_{xx} - \varepsilon_{xx}$ response from numerical simulations compared to experimental data from Meng et al. (2006). (a) Plain C60 concrete. (b) $V_f = 1\%$ F1 fibre-reinforced C60 concrete.

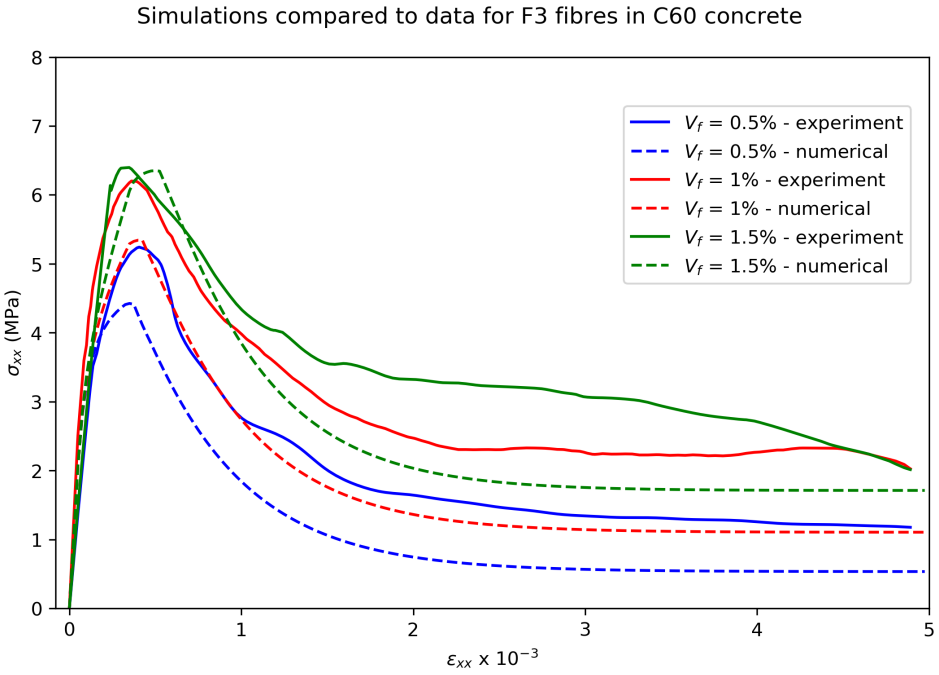

Figure 5.7: Comparison of $\sigma_{xx} - \varepsilon_{xx}$ response of C60 concrete reinforced with different volume fractions of F3 fibres from numerical simulations and experimental data from Meng et al. (2006).

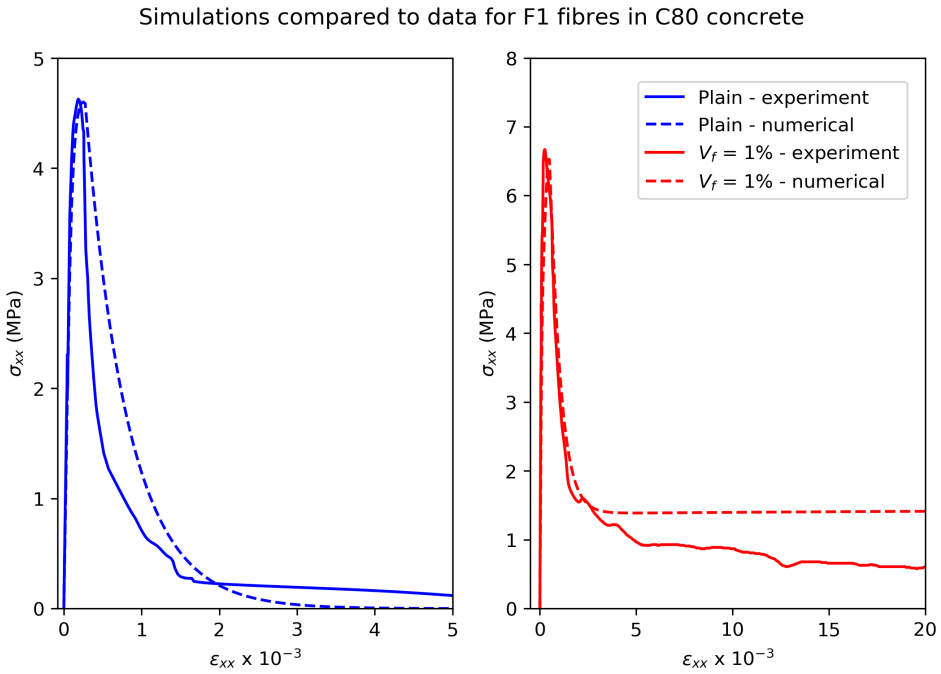

Figure 5.8: $\sigma_{xx} - \varepsilon_{xx}$ response from numerical simulations compared to experimental data from Meng et al. (2006). (a) Plain C80 concrete. (b) $V_f = 1\%$ F1 fibre-reinforced C80 concrete.

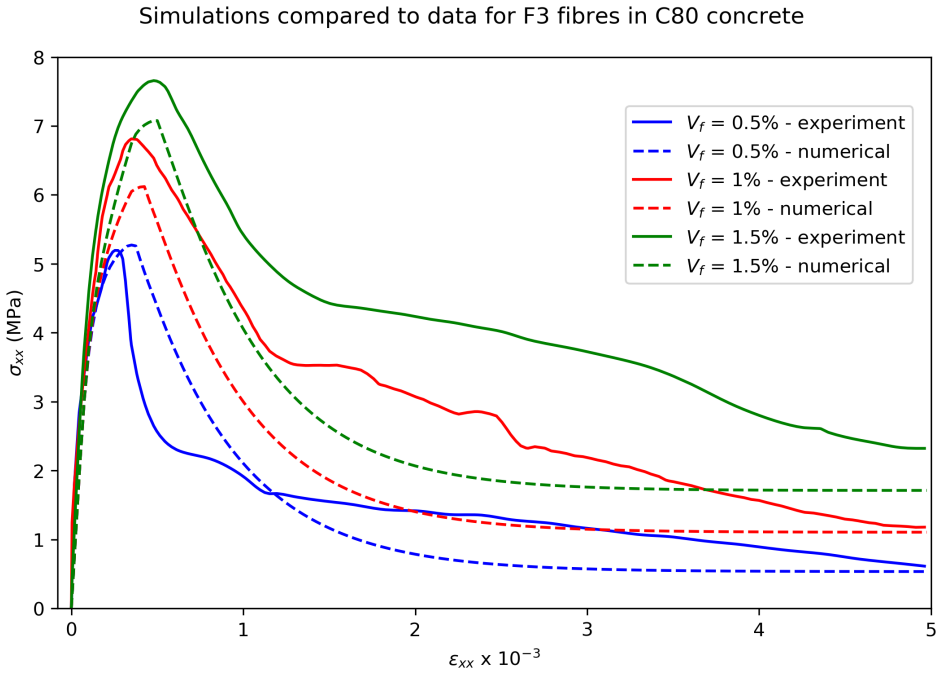

Figure 5.9: Comparison of $\sigma_{xx} - \varepsilon_{xx}$ response of C80 concrete reinforced with different volume fractions of F3 fibres from numerical simulations and experimental data from Meng et al. (2006).

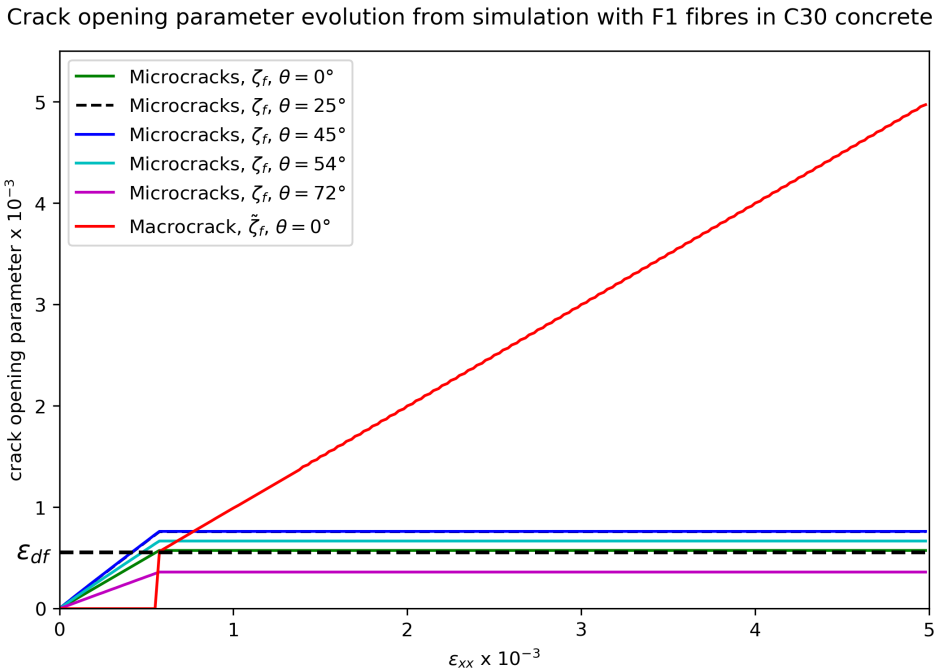

Figure 5.10: Evolution of the crack opening parameter from the simulation with F1 fibres in C30 concrete. The strain at the end of the debonding phase, or the start of the pull-out stage, is marked.

5.5 Discussion

The predictions, based on a single set of parameters, from the constitutive model agree well with the experimental data presented - see Figures 5.4 to 5.9. The characteristic shape of the experimental curves is captured as well as the the increase in strength and toughness with the increase in V_F. For the majority of cases the magnitude of the peaks stress also agrees with the data. The deviation from the experimental results, e.g. for $V_f = 1\%$ F1 fibres in C30 concrete, can be addressed by calibrating τ_0 and β to account for the improvement in fibre-matrix properties with increasing concrete strength. However, for the current study an emphasis is placed on demonstrating that realistic behaviour can be predicted using a single set of parameters.

Figure 5.10 shows that prior to crack localisation, the microcracking stage is dominated by fibre debonding rather than fibre pull-out. Once crack localisation has occurred and a macrocrack has developed, the debonding stage is completed and fibre pull-out occurs. According to Choi et al. (2016), once a macrocrack forms in a fibre-reinforced cementitious composite, the tensile behaviour is determined by the pull-out of fibres. Hence, the predicted behaviour agrees well with the expected behaviour.

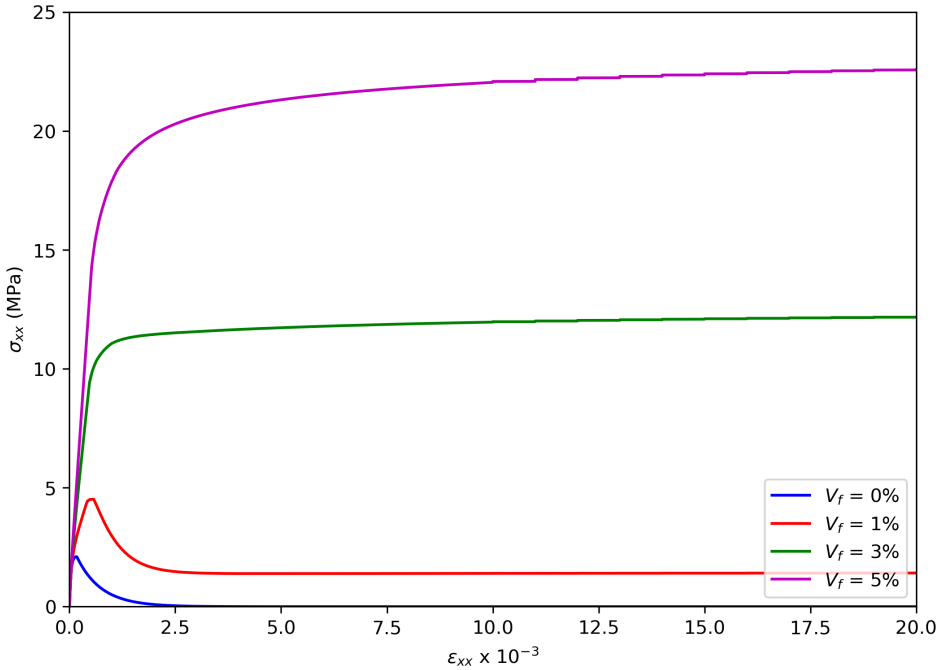

Figure 5.11: Effect of varying V_f on the predicted stress-strain response of C30 concrete reinforced with F1 fibres.

In addition to being able to predict realistic behaviour, unlike phenomenological models, the formulation uses parameters with physical meaning to simulate the effects of fibres. τ_0 and β can be determined from an experimental single fibre pull-out P-δ (pull-out force - pull-out distance) curve using the procedure detailed in Lin & Li (1997).

Whilst the current chapter is focused on extension of the plain concrete model with the new mechanism for crack localisation to fibre-reinforced composites, it should be noted that future work could explore simulation of the strain-hardening phenomena. The governing functions for crack-bridging by fibres used in the present work are capable of modelling strain-hardening as demonstrated by Mihai & Jefferson (2017). A brief parametric study where the volume fraction of F1 fibres in C30 concrete is varied is shown below in Figure 5.11. Strain hardening behaviour is observed at higher volume fractions of fibres.

Another possible avenue for future work is the implementation of the mechanism of straightening of the hooked-ends of the fibres. According to Abbas & Khan (2016), typical fibre pull-out load-end slip curves for hooked end steel fibres show that after the ultimate pull-out load has been achieved, the pull-out behaviour can be broken down into three stages. The three stages are: pull-out softening immediately after the ultimate pull-out load, pull-out hardening due to the pull-out of the hooked-ends which partially straighten and frictional pull-out. Although

the current model does include a mechanism linked to slip-hardening, the model does not allow for the partial straightening of hooked-end fibres. Note that the constitutive relationship for the crack-bridging stress is based on the work of Lin & Li (1997) which is focused on the behaviour of synthetic fibre/cement matrix systems.

5.6 Conclusions

A micromechanical constitutive model for fibre-reinforced cementitious composites was developed by extending the model for plain concrete (or more generally quasi-brittle materials) described in chapter 4. The underlying crack-bridging mechanism of short fibres was implemented in the model. The work can be summarised as following:

- Single point path simulations carried out using the proposed model show that realistic behaviour can be predicted using a single set of material parameters. The simulated behaviour agreed well with experimental data.
- The model is able to capture the main characteristic behaviour resulting from the addition of fibre-reinforcement - the characteristic shape of the stress-strain response, the increase in tensile strength and toughness with increasing volume fractions of fibres and the pull-out of fibres after the development of macrocracks.
- Unlike phenomenological models, the current model uses parameters with physical meanings to model crack bridging by fibres. Two input micromechanical parameters which can be determined from experiments are used to simulate the effects of fibre-reinforcement.
- The behaviour of strain-hardening composites can be modelled.

Chapter 6

Micromechanical plastic-damage constitutive model

6.1 Introduction

As mentioned in section 3.2, using a micromechanical damage approach, such as the models presented and successfully applied in the previous two chapters, is not suitable for describing inelastic deformation. On the other hand, models based on plasticity are able to capture inelastic deformations but they lack the capability to predict the degradation of stiffness. Models based on combining the approaches in a single formulation address this issue by relating damage to deformation. As the failure of concrete is characterised by both permanent deformations and stiffness degradation (Grassl & Jirásek 2006), models formulated using a plastic-damage approach are better able to capture the characteristic behaviour of concrete than models formulated using a damage only or plasticity only approach. This chapter presents a micromechanical plastic-damage model for concrete which simulates the development of crack-planes.

The structure of this chapter is as follows: section 6.2 describes the components of the constitutive model and section 6.3 describes the implementation of the model using the closest point projection (cpp) approach. Section 6.4 focuses on the sensitivity of the constitutive model to key parameters. In section 6.5 the results of numerical simulations are given, followed by a discussion of the results in section 6.6 and conclusions in section 6.7.

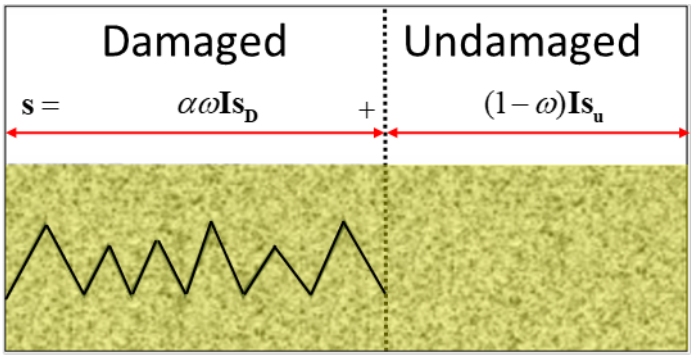

Figure 6.1: Split of the crack-plane stress into a damaged and undamaged component.

6.2 Model components

The micromechanical plastic-damage model is based on modelling crack-planes, each represented by a local plastic yield surface. Stresses on the crack-planes $\boldsymbol{s}$ are divided into undamaged (elastic) $\boldsymbol{s_u}$ and damaged components $\boldsymbol{s_D}$ with the plastic yield surface being applicable to the damaged stress components. Note that $\boldsymbol{s_u}$ and $\boldsymbol{s_D}$ are defined later in equations 6.10 and 6.11 respectively. The micromechanics based effective strain ζ and damage parameter ω, discussed in chapter 4, are used to control the proportion of undamaged to damaged stress as shown in Figure 6.1. α is a contact reduction parameter, detailed in section 6.2.7, which is introduced to take into account the reducing potential for the transfer of stress between crack faces with increasing crack opening.

In the formulation of the model, the overall strain $\boldsymbol{\varepsilon}$ is split into recoverable and plastic contributions from the crack-planes as shown in Figure 6.2.

The following sections detail the components of the micromechanical plastic-damage model which are based on the work of Jefferson (2002), Mihai & Jefferson (2015), Jefferson et al. (2016). Details of the micromechanical damage component have previously been provided in section 4.3.4. The novel component of the work is the use of a static constraint which sets the requirement that the total stress transformed onto a crack-plane is equal to the stress on the crack-plane. The use of this constraint allows for interactions between the crack-planes. The use of the static constraint in the stress recovery computations is detailed in Appendix C.

6.2.1 Hoek-Brown failure envelope

A local yield function formulated by Jefferson (2002) is adopted. The yield function is an approximation of the local form of the Hoek-Brown function:

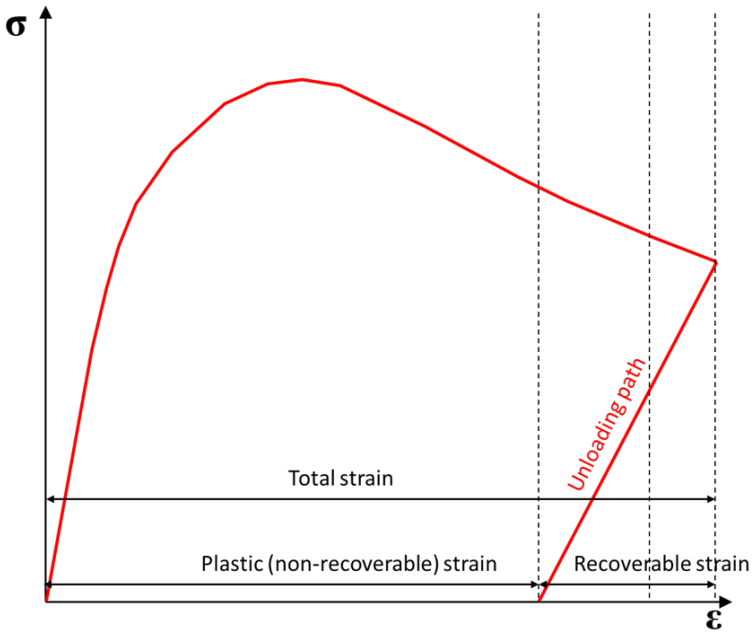

Figure 6.2: Split of the total strain into elastic and inelastic components.

$$\left(\frac{\tau}{r_u}\right)^{3/2} + \sigma_n - f_t = 0 \tag{6.1}$$

where σ_n and τ are the normal and shear stresses of the local-planes respectively. The tensile strength is denoted as usual by f_t. The yield surface corresponding to Equation 6.1, and shown in Figure 6.3, can be set to match the Hoek-Brown function at peak uniaxial compression f_c by calculating the cohesion-friction factor r_u as following Jefferson (2002):

$$r_u = \frac{\tau_c}{(f_t - \sigma_{n_c})^{2/3}} \tag{6.2}$$

where:

$$\tau_c = \frac{f_c}{2}\sqrt{1 - \cos^2(2\alpha_c)} \tag{6.3}$$

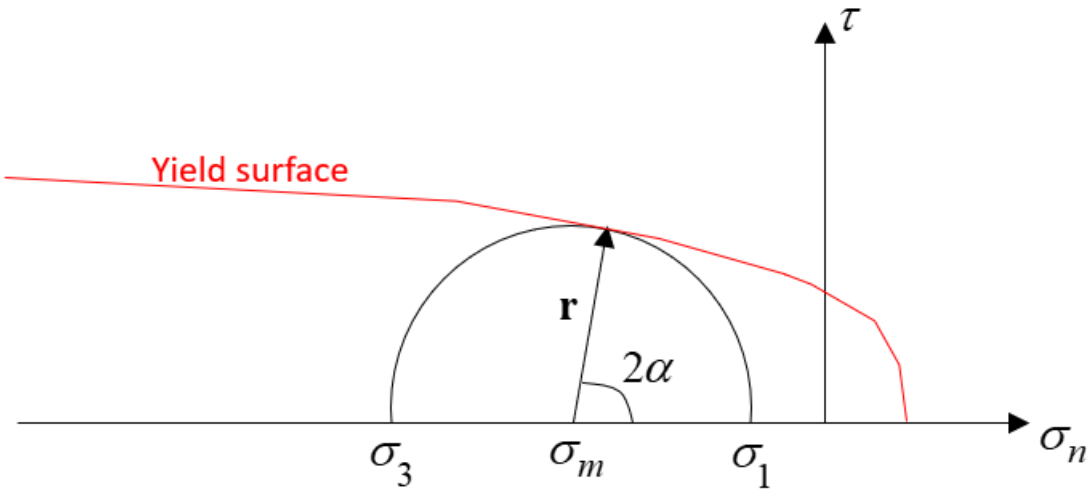

Figure 6.3: Local Hoek-Brown yield surface.

$$\sigma_{n_c} = \frac{f_c}{2}\left(1 + \cos(2\alpha_c)\right) \tag{6.4}$$

$$\cos(2\alpha_c) = \frac{1}{1 + 4\frac{f_t}{f_c}} \tag{6.5}$$

The normal to a crack-plane is defined by:

$$\boldsymbol{r} = \boldsymbol{T_p}\begin{bmatrix} \cos(\alpha) & 0 & \sin(\alpha) \end{bmatrix}^T \tag{6.6}$$

in the principal plane I-III. $\boldsymbol{T_p}$ is a 3x3 transformation matrix for principal to Cartesian axes. The rows of the matrix correspond to the eigenvectors of the principal axes. 2α is the angle of the normal from the direction of the major principal stress and is given by:

$$\sin(2\alpha) = \frac{-2{r_f}^3}{9R} + \sqrt{\left(\frac{2{r_f}^3}{9R}\right) + 1} \tag{6.7}$$

where $R = \frac{1}{2}(\sigma_1 - \sigma_3)$. See Appendix B for a summary of the Mohr's circle based proof of this equation.

6.2.2 Constitutive relationship

The overall constitutive relationship is given by removing the sum of the inelastic crack-plane strains $\hat{\boldsymbol{\varepsilon}}$ from the total strain $\boldsymbol{\varepsilon}$:

$$\boldsymbol{\sigma} = \boldsymbol{D}\left(\varepsilon - \sum_{i=1}^{n_{total}} \boldsymbol{N_{\varepsilon_i}}^T \hat{\boldsymbol{\varepsilon}}_i\right) \tag{6.8}$$

where n_{total} is the total number of crack-planes.

As shown in Figure 6.1, the crack-plane stress s is divided into an undamaged, or elastic, component $\boldsymbol{s_u}$ and a damaged component $\boldsymbol{s_D}$ giving a crack-plane stress of the following form:

$$\boldsymbol{s} = (1-\omega)\boldsymbol{I}\boldsymbol{s_u} + \alpha\omega\boldsymbol{I}\boldsymbol{s_D} \tag{6.9}$$

where:

$$\boldsymbol{s_u} = \boldsymbol{D_L}\tilde{\boldsymbol{\varepsilon}} \tag{6.10}$$

$$\boldsymbol{s_D} = \boldsymbol{D_L}(\tilde{\boldsymbol{\varepsilon}} - \boldsymbol{e_p}) \tag{6.11}$$

$\boldsymbol{e_p}$ is the plastic strain resulting from application of the plastic yield surface to $\boldsymbol{s_D}$ and $\tilde{\boldsymbol{\varepsilon}}$ is used to denote the local strain of the crack-plane.

As the crack-plane strain $\tilde{\boldsymbol{\varepsilon}}$ can be divided into an elastic component $\boldsymbol{\varepsilon_e}$ and in-elastic component $\hat{\boldsymbol{\varepsilon}}$:

$$\tilde{\boldsymbol{\varepsilon}} = \boldsymbol{\varepsilon_e} + \hat{\boldsymbol{\varepsilon}} \tag{6.12}$$

the inelastic crack-plane strain component can be obtained by removing the elastic component from the total strain as follows:

$$\hat{\boldsymbol{\varepsilon}} = \tilde{\boldsymbol{\varepsilon}} - \boldsymbol{\varepsilon_e} = \tilde{\boldsymbol{\varepsilon}} - \boldsymbol{C_L}\boldsymbol{s} \tag{6.13}$$

Substituting for $\boldsymbol{s}$ from Equation 6.9 into Equation 6.13 and re-arranging for $\hat{\boldsymbol{\varepsilon}}$ gives:

$$\hat{\boldsymbol{\varepsilon}} = \left[\boldsymbol{I} - (1-\omega)\boldsymbol{I} - \alpha\omega\boldsymbol{I}\right]\tilde{\boldsymbol{\varepsilon}} + \alpha\omega\boldsymbol{I}\boldsymbol{e_p} \tag{6.14}$$

Now, by substituting Equation 6.14 into Equation 6.8, the constitutive relationship can be written as shown below.

$$\boldsymbol{\sigma} = \boldsymbol{D}\left(\boldsymbol{\varepsilon} - \sum_{i=1}^{n_{total}} \boldsymbol{N_{\varepsilon_i}}^T \left[\boldsymbol{I} - (1-\omega_i)\boldsymbol{I} - \alpha_i\omega_i\boldsymbol{I}\right]\tilde{\boldsymbol{\varepsilon}} + \boldsymbol{N_{\varepsilon_i}}^T \left[\alpha_i\omega_i\boldsymbol{I}\right]\boldsymbol{e_p}\right) \tag{6.15}$$

6.2.3 Local yield and plastic potential functions

The local yield function and plastic potential apply only to the damaged component of the local stress $\boldsymbol{s_D}$. The yield function is given by (Jefferson 2002):

$$F(\boldsymbol{s_D}, r_f, f_s) = s_{D_r} + \left(\frac{\sqrt{{s_{D_s}}^2 + {s_{D_t}}^2}}{r_f}\right)^{3/2} - f_s = 0 \tag{6.16}$$

where the conditions $r_u \geq r_f \geq r_i$ apply. The variable r_f and the parameter r_i are detailed in section 6.2.5. f_s is the current tensile strength. See Figure 6.4.

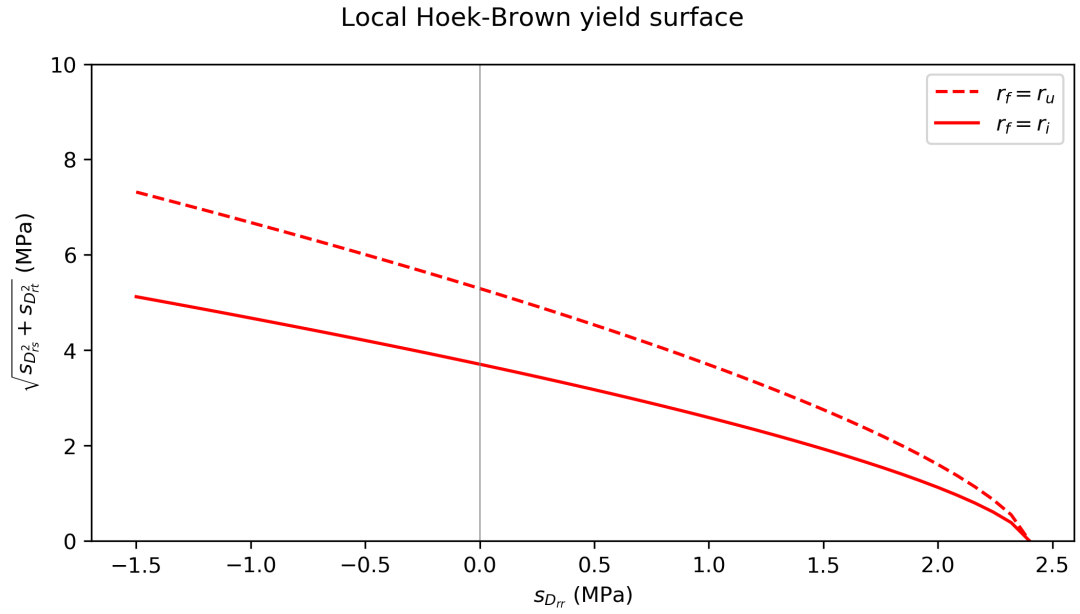

Figure 6.4: Local Hoek-Brown yield surface.

Similarly, the plastic potential is given by (Jefferson 2002):

$$G(\boldsymbol{s_D}, r_\psi, f_s) = s_{D_r} + \left(\frac{\sqrt{{s_{D_s}}^2 + {s_{D_t}}^2}}{r_\psi}\right)^{3/2} - f_s = 0 \tag{6.17}$$

where r_ψ is a dilatancy variable. Note that r_f and r_ψ have units of the cube root of stress.

6.2.4 Tensile strength

Separate directional κ_D and isotropic κ_I plastic hardening variables are used in order to model hardening and softening effects due to tensile and compressive stress states respectively. Consequently, tensile strength reduction can be implemented using functions that best fit the characteristic behaviour under the corresponding stress states - see Figure 6.5 generated using the parameters in Table 6.1. Some of these parameters are defined later in the sections that follow.

To model tensile strength reduction, f_s in equations 6.16 and 6.17 is replaced by f_D (Jefferson 2002):

$$f_D = f_I e^{-\rho_D \left(\frac{\kappa_D}{\kappa_{D_m}}\right)} \tag{6.18}$$

where

$$f_I = f_t \left(\frac{\rho_f \left(1 - \eta_I\right)}{\left(\rho_f - 1\right)\left(1 - \eta_I\right) + 1} \right) \tag{6.19}$$

and ρ_f is the roughness hardening factor, ρ_D is the directional softening factor and $\eta_I = \frac{\kappa_I - \kappa_{I_p}}{\kappa_{I_m} - \kappa_{I_p}}$. κ_{D_m} is the value of the directional plastic parameter at the end of directional hardening. The value of the isotropic plastic parameter at peak hardening κ_{I_p} is calculated as $\kappa_{I_p} = \varepsilon_c - \frac{f_c}{E}$ where ε_c is the strain at the peak uniaxial compressive strength. κ_{I_m} is the value of the isotropic plastic parameter at the end of isotropic hardening and is set as $5\varepsilon_{cm}$.

Figure 6.5a, shows that the incorporation of tensile strength reduction is a major component of the model for simulating tensile behaviour. Under compressive loading, the hardening softening variable r_f plays a more significant role.

Table 6.1: Material parameters used to generate the curves shown in Figure 6.5.

E_m (MPa)	ν	f_t (MPa)	f_c (MPa)	ε_c	ε_{cm}	ε_{tm}	c_1	ρ_f	ρ_D
37,000	0.18	2.4	30	0.0022	0.01	0.005	12	5	1

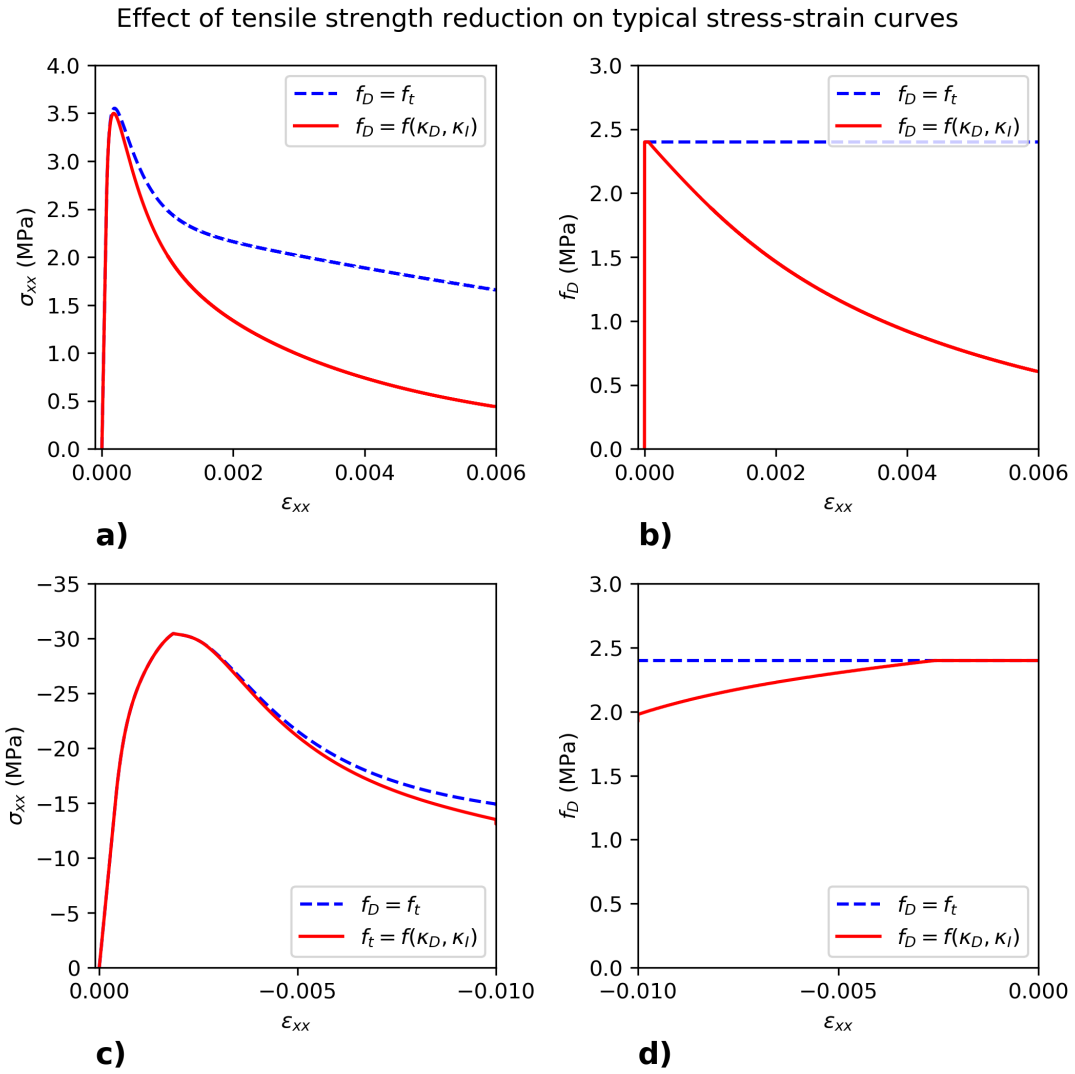

Figure 6.5: (a) Typical uniaxial tension stress-strain curve given by model with and without tensile strength reduction implemented. (b) The tensile strengths corresponding to (a). (c) Typical uniaxial compression stress-strain curve given by model with and without tensile strength reduction implemented. (d) The tensile strengths corresponding to (c).

6.2.5 Pre-peak hardening and post-peak softening

To model pre-peak hardening and post-peak softening under compressive loading, r_f in the local yield function 6.16 is given by:

$$r_f = r_i + (r_u - r_i)h_f \tag{6.20}$$

where $r_i = 0.7r_u$ and h_f is the hardening softening parameter give by:

$$h_f = m_a \left(\frac{m_r}{m_a} + e^{-c_{11}\left(\frac{\kappa_I}{\kappa_{I_p}}\right)} \right) \left(1 - e^{-c_{22}\left(\frac{\kappa_I}{\kappa_{I_p}}\right)} \right) \tag{6.21}$$

The hardening softening function curve is illustrated in the figure below. The ability of the function, shown in Figure 6.6, to match the characteristic shape of pre-peak hardening and post-peak softening of concrete under uniaxial compression loading is demonstrated later in Figure 6.10 in section 6.5. The constants m_p and m_r define the peak and residual values of the hardening function respectively. The constants are fixed as $m_p = 1$ and $m_r = 0.1$.

c_{11} is a constant that is fixed as 1. The constants c_{22} and m_a are calculated iteratively as shown in Algorithm 9.

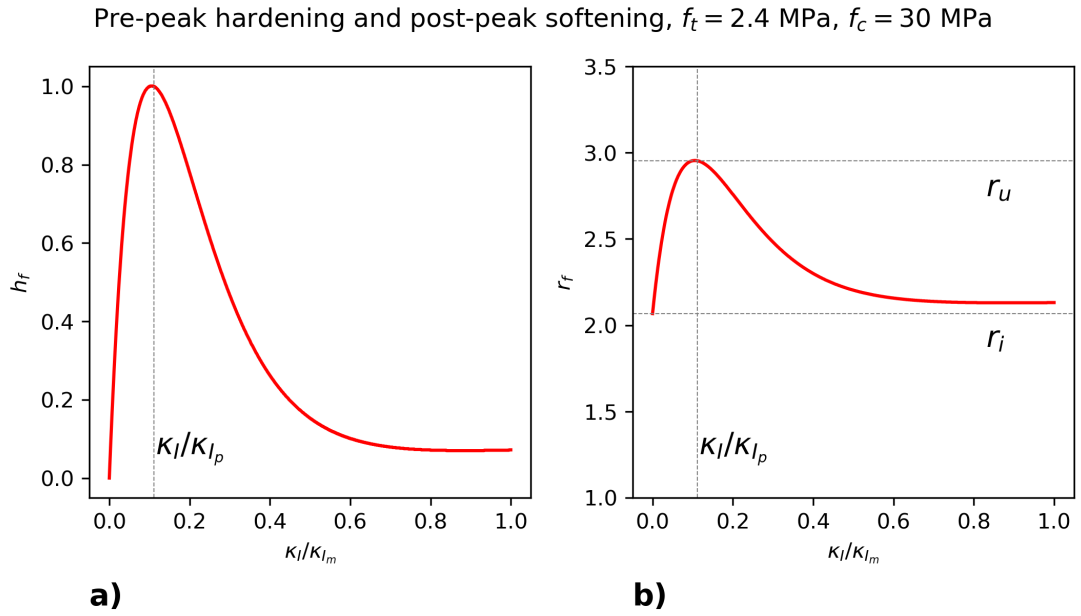

Figure 6.6: Plots showing the evolution of (a) the hardening softening parameter h_f and (b) the hardening softening variable r_f.

Algorithm 9: Iterative process for calculating the constants c_{22} and m_a

▷ Guess c_{22} and m_a

e.g. $c_{22} = 0.5$; $m_a = 1$

▷ Enter iteration loop

while $iter = 1$ **to** $iter_{max}$ **do**

▷ Calculate γ_1

$\gamma_1 = \frac{c_{11} m_a}{c_{22} m_r + (c_{11}+c_{22}) m_a e^{-c_{11}}}$

▷ Update c_{22}

$c_{22} = c_{11} - \ln(\gamma_1)$

▷ Update m_a

$m_a = \frac{m_p - m_r\left(1-\gamma_1 e^{-c_{11}}\right)}{e^{-c_{11}}\left(1-\gamma_1 e^{-c_{11}}\right)}$

▷ Exit loop when the change in c_{22} and m_a is less than the tolerance

if $\delta c_{22} \leq$ tol; $\delta m_a \leq$ tol **then**

exit

end

end

6.2.6 Plastic parameters

Two plastic hardening parameters are used to describe the evolution of the local yield surfaces. As shown in the previous sections, using two hardening parameters allows for characteristic hardening and softening effects under tensile and compressive stress states to be captured using separate functions that best represent the behaviour under that particular stress state.

Compressive stress states contribute to hardening of all local yield surfaces via the isotropic plastic parameter κ_I defined by (Jefferson 2002):

$$\kappa_I = \int_t \dot{\kappa}_I \tag{6.22}$$

and

$$\dot{\kappa}_I = \sum_{i=1}^{n_{total}} \left(\frac{1 - \beta(\boldsymbol{s_{D_i}})}{\chi(\boldsymbol{s_{D_i}})} \right) \sqrt{\dot{\boldsymbol{e}}_{\boldsymbol{p_i}}^{\,T} \dot{\boldsymbol{e}}_{\boldsymbol{p_i}}} \tag{6.23}$$

where the subscript i represents the yield surface corresponding to crack-plane i, β is the directional-isotropic transition function and χ is the ductility function. β

and χ are described below. For each yield surface i, hardening due to tensile stress states is captured via the directional plastic parameter κ_D defined by (Jefferson 2002):

$$\kappa_{D_i} = \int_t \dot{\kappa}_{D_i} \tag{6.24}$$

and

$$\dot{\kappa}_{D_i} = \beta(\boldsymbol{s_{D_i}})\sqrt{\dot{\boldsymbol{e}}_{\boldsymbol{p}_i}^{\,T}\dot{\boldsymbol{e}}_{\boldsymbol{p}_i}} \tag{6.25}$$

The directional-isotropic transition function β is used to divide the contributions to yield surface hardening between the isotropic plastic parameter and the directional plastic parameter. The function is given by:

$$\beta = 1 - \left(\frac{s_{D_r}/\sqrt{{s_{D_r}}^2 + {s_{D_s}}^2 + {s_{D_t}}^2}}{(0.9\sigma_{n_c})/\sqrt{{\sigma_{n_c}}^2 + {\tau_c}^2}} \right) \tag{6.26}$$

When in a state of pure tension, β takes the value of 1. In states of pure compression, β takes the value of 0. Between the two extremities of tension and compression, β transitions between 1 and 0.

To account for the fact that ductility increases with increasing confining pressure, the ductility function χ, shown in Equation 6.27, is used in Equation 6.23.

$$\chi = -1.75\frac{s_{D_r}}{\sqrt{{s_{D_s}}^2 + {s_{D_t}}^2}} \tag{6.27}$$

With overdots denoting derivatives with respect to time, the flow rule is given by:

$$\dot{\boldsymbol{e}}_{\boldsymbol{p}_i} = \frac{\partial G}{\partial s_{D_i}}\dot{\lambda}_i \tag{6.28}$$

6.2.7 Contact reduction

The contact reduction parameter (Mihai & Jefferson 2015), calculated via Equation 6.29 below, represents the reducing potential for stress transfer between crack faces with increasing crack opening. Stress transfer across a total n_c of 2 material phases is modelled. Figure 6.7 shows the effect of the contact reduction function on the ductility of the post-peak response.

p_1 and p_2 represent the proportion of stress transfer across two different aggregate phases (i.e. two asperity heights are considered) and must sum to 1. c_1 and c_2 are the associated material parameters.

$$\alpha = \sum_{i=1}^{n_c} p_i e^{-\left(\frac{\tilde{\varepsilon}_r - \varepsilon_k}{c_i \varepsilon_m}\right)} \tag{6.29}$$

From Equation 6.29, the stress transfer across two different aggregate phases decreases according to an exponential softening function. $\varepsilon_k = a_k \varepsilon_t$ is the strain below which there is no loss of contact between crack faces. a_k is a constant, taken to be 1.35 based on typical values from Jefferson et al. (2016). ε_m is the effective end of the contact reduction curve and is set to be equal to the effective end of tension softening.

As explained in Mihai & Jefferson (2015), the parameters p_i and c_i should ideally be determined from shear tests on cracked concrete specimens. However, for the present model, the material parameters are set as $p_1 = p_2 = 0.5$, $c_1 = 1$ and $c_2 = 2$.

Note that in Mihai & Jefferson (2015), stress recovery due to rough crack faces coming into contact when cracks close and under combinations of shear and opening displacements was modelled. The contact reduction function 6.7 was used in Mihai & Jefferson (2015) to represent the reducing potential for shear transfer across a crack-plane as the crack-plane opening increased.

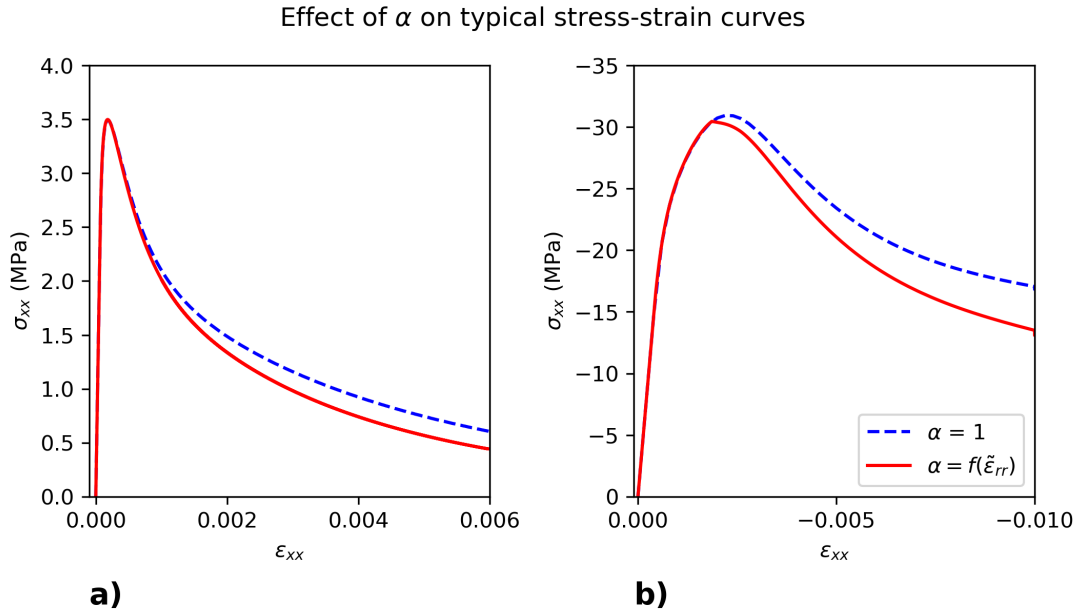

Figure 6.7: The effect of contact reduction on the (a) typical uniaxial tension stress-strain curve and (b) typical uniaxial compression stress-strain curve.

6.2.8 Dilatancy

In a compressive stress state, volumetric dilation is observed. To model this behaviour, r_f in the yield function 6.16 is replaced by the dilatancy parameter r_ψ giving the plastic potential 6.17. Subsequently, the evolution of plastic strains is decoupled from the gradient of the yield function and coupled to the gradient of the plastic potential, i.e. a non-associated flow rule is used. A form of r_ψ is chosen such that the evolution of plastic strains simulates volumetric dilation.

The dilatancy parameter is given by (Jefferson 2002):

$$r_\psi = \left(\psi_0 + (\psi_m - \psi_0)\,\frac{\kappa_I}{2\kappa_{I_m}}\right) r_u \tag{6.30}$$

where the constant $\psi_0 = 0.25$ and $\psi_m = 0.001$.

When in a tensile stress state, the dilatancy parameter is equal to the friction-cohesion constant i.e. $r_\psi = r_u$. .

6.3 Solution algorithm

This section describes the solution algorithm of the model which is based on the closest-point projection method. In the following sections, δ will be used to denote differential quantities and Δ will be used to denote the total change of variables since the last converged state. "Active" crack-planes, the total number of which is given by n_{active}, refers to the crack-planes for which the stress has exceeded the elastic limit ($\Delta\lambda > 0$). Likewise, crack-planes for which the stress has not exceeded the elastic limit are denoted as being "non-active".

6.3.1 Stress recovery computations

Derivations for the stress recovery procedure are provided in Appendix C. Based on the derivations, the coupled equations can be solved iteratively via Algorithm 10.

Algorithm 14 is used to carry out the stress recovery procedure. The algorithm consists of two main parts.

In the first part of the algorithm, all cracks are initially assumed to be plastically active. A single iterative update of the crack-plane variables is made using Algorithm 10. If the incremental plasticity multiplier is negative this indicates that a crack-plane initially assumed to be plastically active is not plastically active. The crack-plane with the smallest value of the incremental plasticity multiplier is "de-activated" if appropriate. This process is repeated until there is no change

in the total number of active crack-planes or if there are no active crack-planes.

The second part of the algorithm is dependent on whether there are any active crack-planes. If there are no active crack-planes, a simple iterative method is used to solve the static constraint condition. When there are active cracks, Algorithm 10 is used to solve the coupled equations. In addition, there are checks to determine whether crack-planes were correctly guessed to be active in the first part of the algorithm.

Algorithm 10: Iterative solution of coupled equations

▷Enter from stress recovery algorithm with strain and crack-plane variables

$\boldsymbol{\varepsilon}$, $\tilde{\boldsymbol{\varepsilon}}$, $\boldsymbol{\varepsilon_p}$, κ_D, κ_I, ζ, $\boldsymbol{r_d}$, $\boldsymbol{s_d}$, $\boldsymbol{t_d}$, n_{active}

▷Initialise total change of variables since the last converged state

$\Delta\boldsymbol{\lambda} = 0$, $\Delta\kappa_I = 0$, $\Delta\boldsymbol{\kappa_D} = 0$, $\Delta\boldsymbol{e_p} = \mathbf{0}$

▷Enter iterations loop

for $i_{iter} = 1$ **to** lim_{iters} **do**

▷Calculate the crack-plane variables, stress and conditions from Algorithm 11

▷Calculate the derivatives matrix and residuals matrix from Algorithm 12

▷Solve for local strains and update variables using Algorithm 13

▷Calculate the crack-plane variables, stress and conditions from Algorithm 11

▷Exit loop if the conditions are within tolerances

if $(F < tol) \wedge (\boldsymbol{\psi} < tol) \wedge (\boldsymbol{R_\varepsilon} < tol) \wedge (R_D < tol) \wedge (R_i < tol)$ **then**

▷ Exit

end

end

Algorithm 11: Calculation of crack-plane variables, stress and conditions

▷ Enter from Algorithm 10

▷ Calculate the crack-plane variables, stress and conditions from equations 4.16, 4.17, 6.29, 6.26, 6.27, 6.11, C.1, C.2, C.3, C.5, 6.15, C.4

For all crack-planes calculate: ζ, ω, α, β, χ, $\boldsymbol{s_D}$ F, $\boldsymbol{\psi}$, $\boldsymbol{R_\varepsilon}$, R_D

Calculate $\boldsymbol{\sigma}$, R_i

Algorithm 12: Calculate derivatives matrix and residuals matrix

▷ Enter from Algorithm 10

▷ Calculate derivatives matrix and residuals matrix from equations C.47, C.37, C.52

Calculate $\boldsymbol{M_E}$, $\boldsymbol{b_E}$, $\boldsymbol{M_\lambda}$, $\boldsymbol{b_{\lambda 2}}$

Calculate $\boldsymbol{\Xi}$, $\boldsymbol{\Gamma}$

Algorithm 13: Solve for local strains and update variables

▷ Enter from Algorithm 10

▷ Solve Equation C.52 for local strains

Solve $\boldsymbol{\Gamma} = \boldsymbol{\Xi}\delta\boldsymbol{\Lambda}$ for $\delta\boldsymbol{\Lambda}$

Calculate $\delta\boldsymbol{\lambda}$; $\delta\tilde{\boldsymbol{\varepsilon}}$

▷ Update differential quantities from equations C.39, C.31, C.11, C.10, C.6

Calculate $\delta\boldsymbol{\sigma}$, $\delta\boldsymbol{s_D}$, $\delta\boldsymbol{e_p}$, $\delta\boldsymbol{\kappa_D}$, $\delta\kappa_I$

▷ Update total change of variables

$\Delta\boldsymbol{e_p} = \Delta\boldsymbol{e_p} + \delta\boldsymbol{e_p}$, $\Delta\boldsymbol{\kappa_D} = \Delta\boldsymbol{\kappa_D} + \delta\boldsymbol{\kappa_D}$, $\Delta\kappa_I = \Delta\kappa_I + \delta\kappa_I$

$\Delta\boldsymbol{\lambda} = \Delta\boldsymbol{\lambda} + \delta\boldsymbol{\lambda}$

▷ Update crack-plane variables

$\tilde{\boldsymbol{\varepsilon}} = \tilde{\boldsymbol{\varepsilon}} + \delta\tilde{\boldsymbol{\varepsilon}}$, $\boldsymbol{e_p} = \boldsymbol{e_p} + \delta\boldsymbol{e_p}$, $\boldsymbol{\kappa_D} = \boldsymbol{\kappa_D} + \delta\boldsymbol{\kappa_D}$, $\kappa_I = \kappa_I + \delta\kappa_I$

Algorithm 14: Stress recovery algorithm

▷ Enter algorithm from constitutive driver

▷ Initially assume all crack-planes to be plastically active (i.e. local yield function = 0)

▷ Enter crack formation loop

for $i_{loop} = 1$ **to** lim_{logic} **do**

- ▷ Perform 1 iteration of solving the coupled equations
- ▷ Check if the smallest value of the plastic incremental multiplier is negative and if so make the associated crack-plane not active and reset variables
- ▷ Exit if there is no change in the number of active crack-planes or if there are no active cracks

end

▷ Enter main loop if there is at least one active crack-plane

if *number of active cracks* > 0 **then**

- Enter negative incremental placitiy multiplier loop
- **for** $i_{negativecheck} = 1$ **to** n_{active} **do**
  - ▷ Iteratively solve the coupled equations
  - ▷ Check if the smallest value of the plastic incremental multiplier is negative and if so make the associated crack-plane not active and reset variables
  - ▷ Exit if there is no change in the number of active crack-planes or if there are no active cracks
- **end**

end

▷ If there are no active cracks, enter if logic

if *number of active cracks* $= 0$ **then**

- ▷ Iteratively solve only the static constraint condition

end

▷ Exit and return to constitutive driver

6.3.2 Consistent tangent

The derivation of the consistent tangent is detailed in Appenix D. From the derivation, the consistent tangent can be calculated using Algorithm 15.

Algorithm 15: Calculation of the consistent tangent

▷ Enter with strain and crack-plane variables and the total change of variables since the last converged state

$\boldsymbol{\varepsilon}$, $\tilde{\boldsymbol{\varepsilon}}$, $\boldsymbol{\varepsilon_p}$, κ_D, κ_I, ζ, $\boldsymbol{r_d}$, $\boldsymbol{s_d}$, $\boldsymbol{t_d}$, n_{active}

$\Delta\lambda$, $\Delta\kappa_I$, $\Delta\kappa_D$, $\Delta\boldsymbol{e_p}$

▷ Calculate the crack-plane variables and stress from equations 4.16, 4.17, 6.29, 6.26, 6.27, 6.11, 6.15

For all crack-planes get: ζ, ω, α, β, χ, $\boldsymbol{s_D}$

Calculate $\boldsymbol{\sigma}$

▷ Calculate matrices needed for the consistent tangent using equations D.15, D.12, D.23, D.24

Calculate $\boldsymbol{Ac}$, $\boldsymbol{B_{2m}}$, $\boldsymbol{X_m}$, $\boldsymbol{Y_m}$

▷ Calculate the consistent tangent from Equation D.26

Calculate

$$\boldsymbol{D_{tan}} = \boldsymbol{A_C} + \boldsymbol{A_C} \left[\begin{array}{ccc} \boldsymbol{N_1}^T & \cdots & \boldsymbol{N_{n_{total}}}^T \end{array} \right] [\boldsymbol{B_{2m}}] [\boldsymbol{X_m}]^{-1} [\boldsymbol{Y_m}]$$

6.4 Sensitivity to key parameters

Figure 6.8 shows the sensitivity of the model to key model parameters. The material parameters in Table 6.1 were used to generate the results. Predictions from the model are as expected with variations in the key parameters.

In the previous section the sensitivity of the predictions to the various components of the formulation was demonstrate - see figures 6.5 and 6.7. Note that the effects the chosen function for pre-peak hardening and post-peak softening (section 6.2.5) are concentrated in the region of peak load.

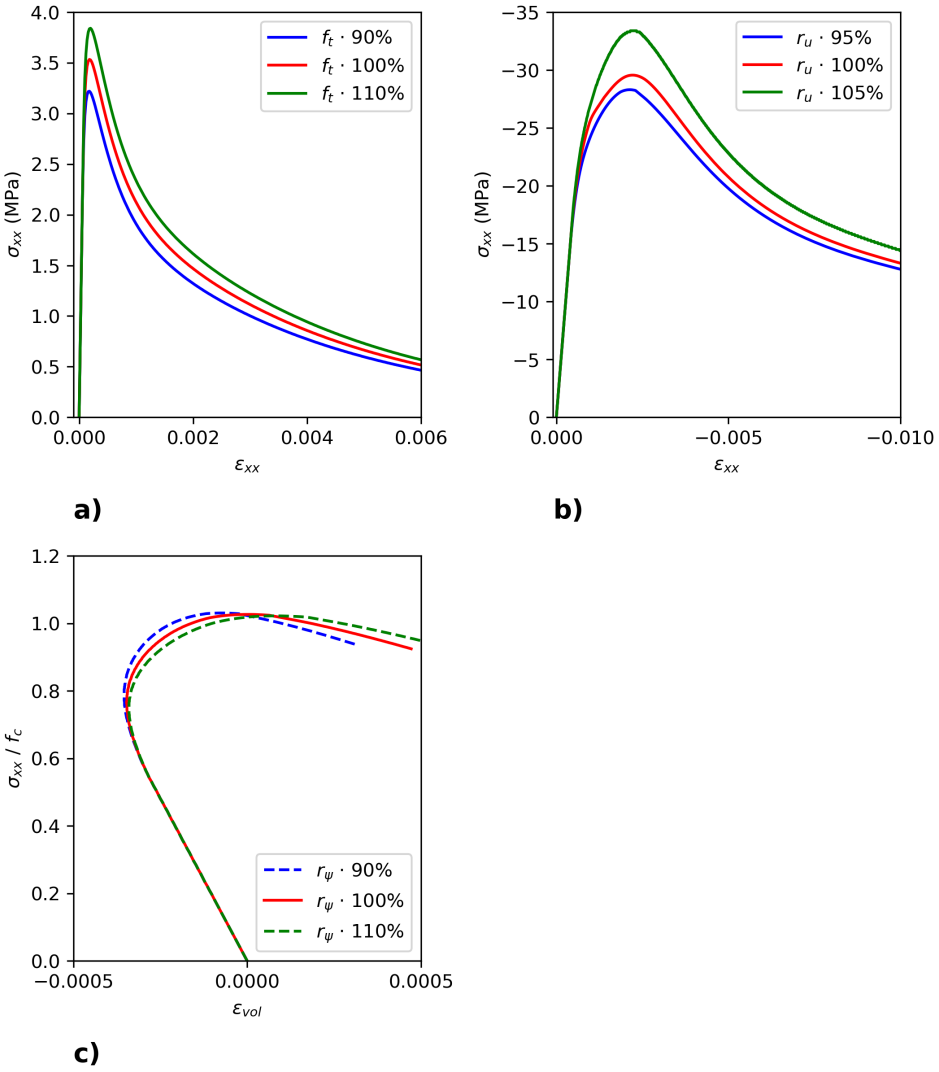

Figure 6.8: (a) Uniaxial tension predictions considering variations in the tensile strength (tension + ve). (b) Uniaxial compression predictions considering variations in the cohesion-friction factor. (c) Normalised σ_{xx}-volumetric response under uniaxial compression considering variations in the dilatancy parameter.

6.5 Single-point path simulations

6.5.1 Numerical implementation

The current model was implemented in a Mathcad sheet using a constitutive driver algorithm which allowed for mixed stress/strain paths to be applied. The driver was based on the Newton-Raphson method.

The maximum allowable iterations for the solution of the coupled equations (lim_{iters} in Algorithm 10) and the Newton-Raphson method was set to be 100. The maximum number of iterations encountered was significantly less than the maximum permitted for most cases. The tolerance for the conditions, *tol* in Algorithm 10, was set as 10^{-8}. 10^{-6} was set for the maximum value of relative error of out of balance stress (i.e. the norm of the total applied stress divided by the norm of the norm of the out of balance stress).

6.5.2 Parameters

To demonstrate the capability of the micromechanical plastic-damage model to predict the characteristic behaviour of concrete, numerical simulations were carried out. All of the simulations use a single set of input parameters that are shown below in Table 6.2. The maximum size of coarse aggregate particles d_{max} is taken to be 10 mm and is assumed to be the characteristic length. Deformations are related to the predicted strains via this characteristic length.

Table 6.2: Material parameters used for the micromechanical plastic-damage model simulations.

E_m (MPa)	ν	f_t (MPa)	f_c (MPa)	ε_c	ε_{cm}	ε_{tm}	c_1	ρ_f	ρ_D
37,000	0.18	2.4	30	0.0022	0.01	0.008	12	5	1

6.5.3 Results

The results of the numerical simulations are shown in figures 6.9 to 6.11. $f_{t_{ult}}$ is the ultimate (peak) uniaxial tensile strength and is equal to 3.7 MPa. f_{tri} is consistent with the maximum compressive stress state in a triaxial test i.e. the minor principal stress in a tension $+ve$ convention.

In Figure 6.9a and 6.9c, uniaxial tension simulation results are compared to experimental data by Reinhardt (1984) and Hordijk (1991). The corresponding lateral strain response is shown in Figure 6.9b.

Figure 6.10a compares the results of uniaxial and biaxial compression to experimental data by Kupfer et al. (1969). The corresponding volumetric strain response is shown in Figure 6.10b.

The third figure, Figure 6.11, shows a comparison of triaxial behaviour under varying cell pressures. In Figure 6.11a, the axial stress at varying levels of cell pressure is plotted against the applied strain. In Figure 6.11b, the triaxial strength is plotted for various cell pressures and the results are compared to those from an empirical function by Newman (1979).

To illustrate that the consistent tangent formulated gives quadratic convergence, an example convergence history is given in Figure 6.12.

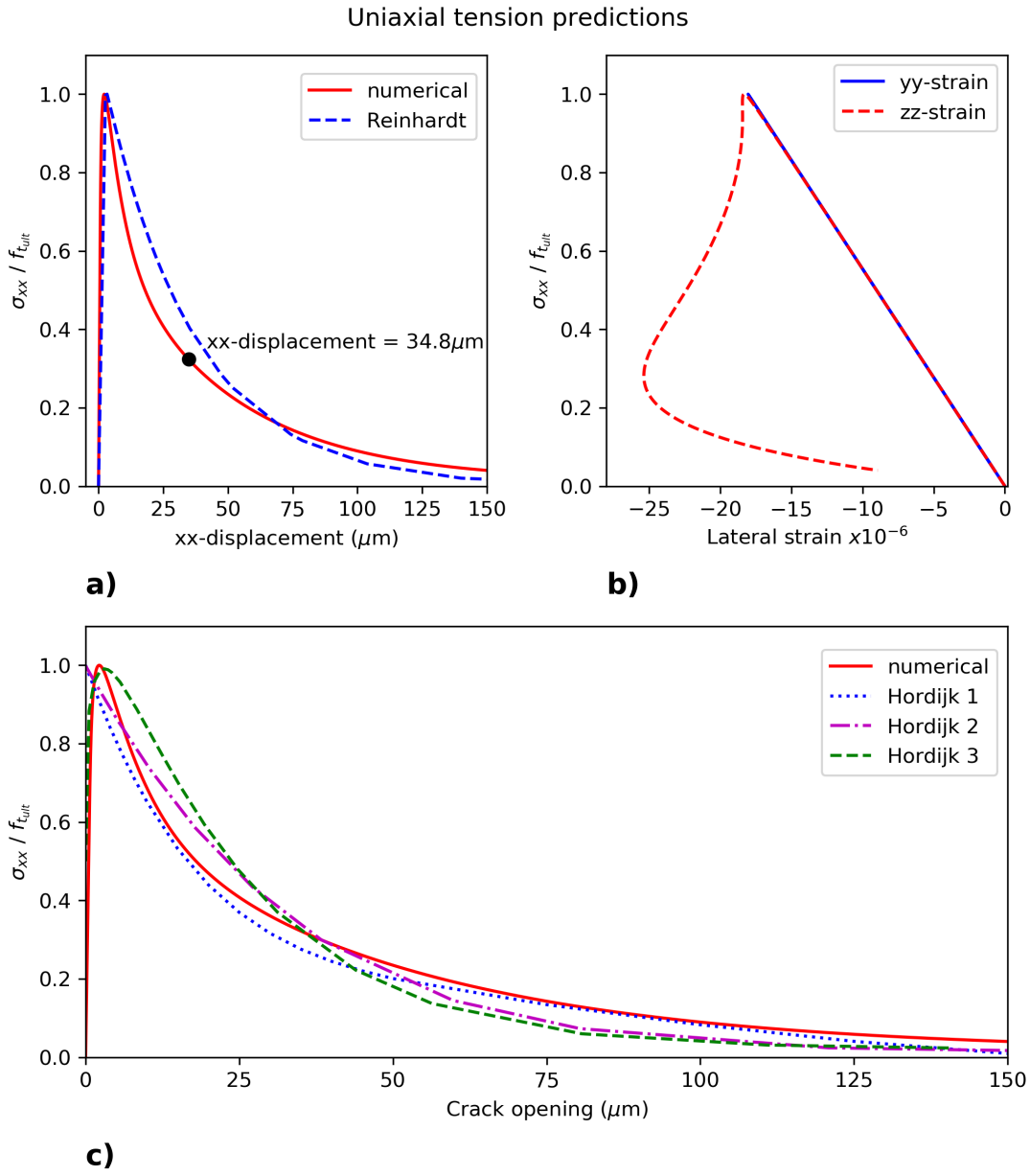

Figure 6.9: Results from numerical simulation of uniaxial tension (tension + *ve*) compared to experimental results from (a) Reinhardt (1984) and (c) Hordijk (1991). The numerical predictions of the stress-lateral strains are shown in (b). The convergence history corresponding to the point marked in (a) is shown on Figure 6.12.

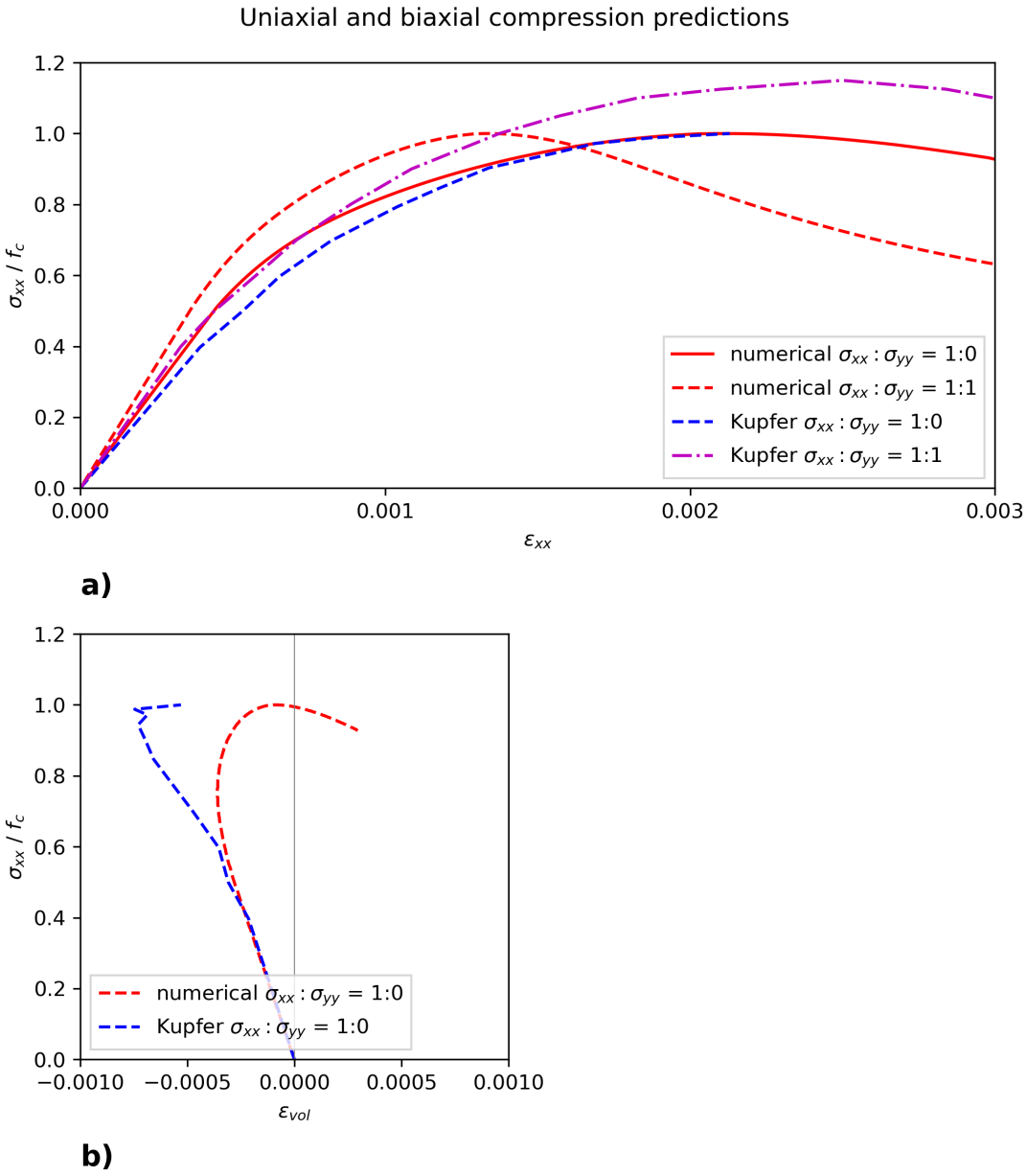

Figure 6.10: Results from numerical simulation of uniaxial and biaxial compressive paths compared to experimental results from Kupfer et al. (1969). (a) Normalised $\sigma_{xx} - \varepsilon_{xx}$ response (compression $+ve$). (b) Normalised $\sigma_{xx}-$ volumetric strain response (tension $+ve$).

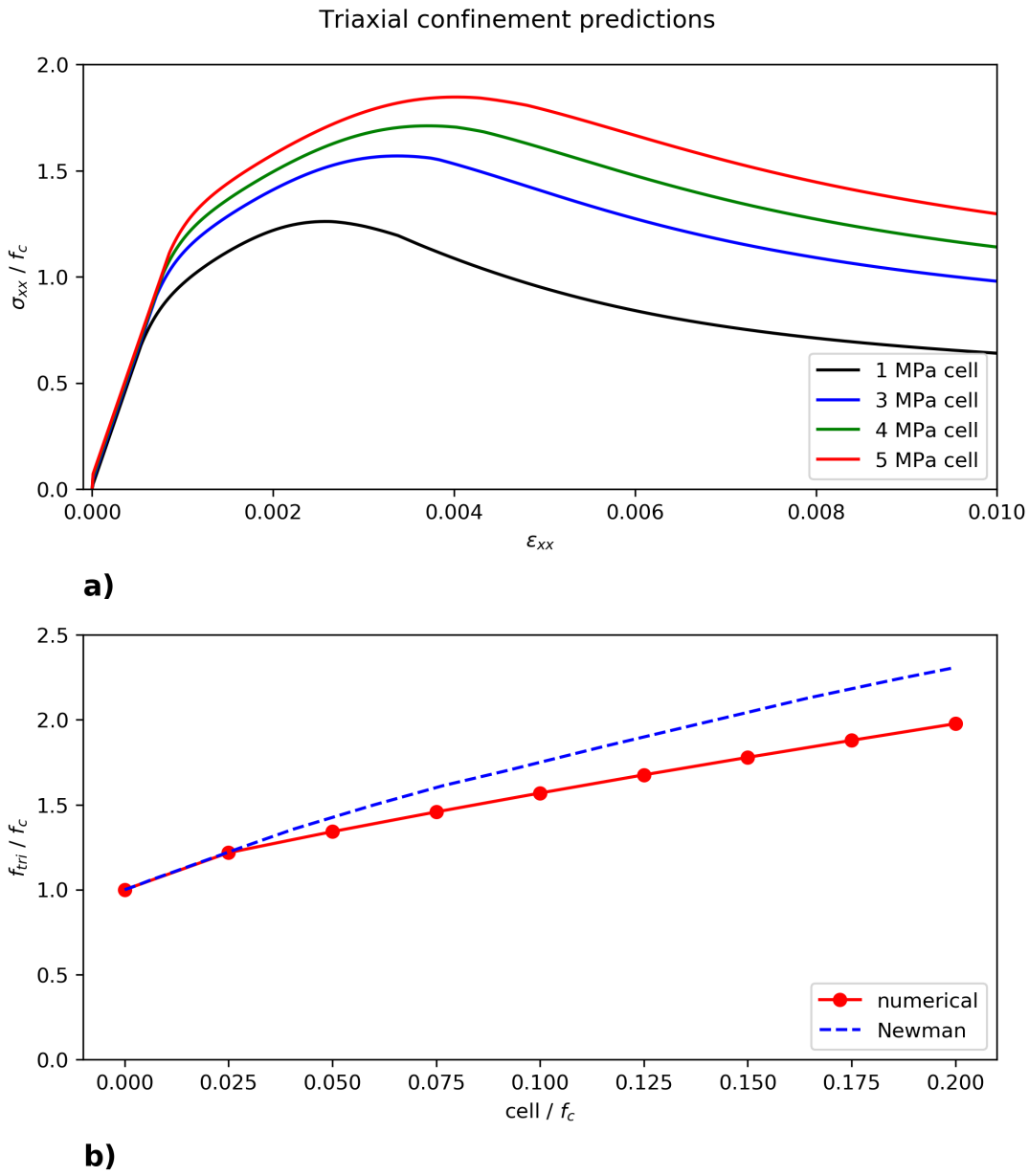

Figure 6.11: Results from numerical simulations of triaxial confinement paths with varying cell pressure. (a) Normalised axial stress $-\varepsilon_{xx}$ response (compression $+ve$). (b) Normalised triaxial confinement strength predictions compared to Newman (1979) at varying levels of cell pressures.

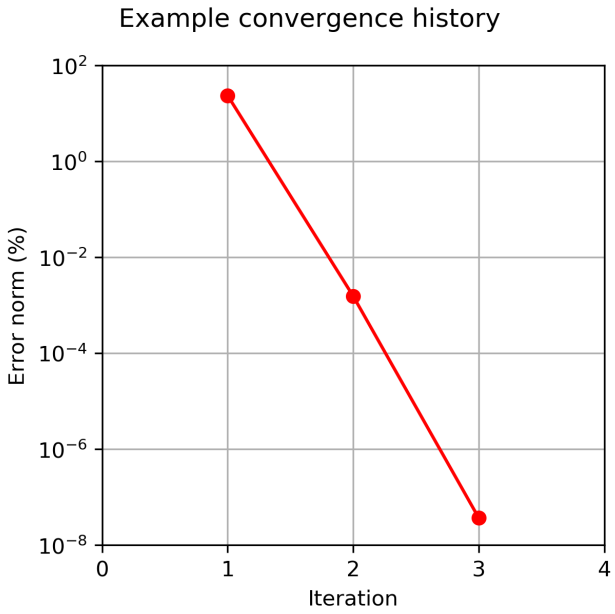

Figure 6.12: Example convergence history corresponding to a xx-displacement of 34.8 μm in Figure 6.9a. The corresponding displacement is marked on Figure 6.9a with a black circle.

6.6 Discussion

Generally, the predictions show that the micromechanical plastic-damage model is able to capture the characteristic behaviour of concrete. Results from simulating uniaxial paths especially agree well with experimental data including the dilatant behaviour observed under uniaxial compression. Like the previous micromechanical damage models presented in the earlier two chapters, the current model also predicts relaxation of lateral strains following the peak uniaxial stress. Reversal of lateral strains immediately after cracking has been shown by experimental data for uniaxial tests of reinforced concrete panels and is indicative of a tensile-splitting mechanism (Vecchio & DeRoo 1995).

The biaxial model underestimates the biaxial strength of concrete under compression. As discussed previously in Chapter 4, rough contact between crack faces should be included in the model as it is a key mechanism for representing the characteristic response under compression. The implementation of rough crack contact will be the focus of future work. However, whilst the biaxial strength is underestimated, the model improves upon the previous micromechanical damage model for plain concrete where the ratio of biaxial to uniaxial strength was less than 1.

Predictions for triaxial confinement paths considerably improve upon those from

the micromechanical damage only model albeit slightly underestimating the strength. As discussed previously in the context of the micromechanics based damage models, the inclusion of rough contract on crack surfaces is necessary to correctly predict compressive behaviour (Jefferson & Bennett 2007, Mihai & Jefferson 2017). It is also possible to improve the triaxial strength predictions by adjusting the slope of the Hoek-Brown yield surface.

6.7 Conclusions

A constitutive model formulated using a micromechanical plastic-damage framework was proposed and was found to successfully predict the characteristic behaviour of concrete. The formation of crack-planes subject to local yield surfaces was modelled using two separate hardening variables for isotropic and directional behaviour. The conclusions of the work can be summarised as follows:

- Predictions from the model agree well with experimental data - this is especially true for uniaxial loading paths. The triaxial performance of the model is considerably better than the microcracking damage only model.
- The model simulates the permanent strains that develop when concrete cracks and crushes. These strains are not simulated in the previous models.
- Like the models in the previous chapters which were formulated using a damage only approach, the current model is also able to capture the tensile-splitting mechanism. This mechanism was not captured using the directional microcracking only models that this series of work builds on.

Compressive strength is underestimated under biaxial loading and triaxial confinement however the predictions are an improvement over previous models and there are solutions available which can be implemented in future work.

Chapter 7

Finite element implementation of the micromechanical plastic-damage model

7.1 Introduction

The micromechanical plastic-damage model described in chapter 6 was implemented in the commercial finite element package LUSAS. The package contains a material model interface through which the constitutive model was implemented using the Fortran programming language. Example finite element simulations were carried out and the results compared to experimental data.

The structure of this chapter is as follows: section 7.2 gives a summary of the key theory used to implement the constitutive model. This is followed by example finite element simulations in sections 7.3 and 7.4. Finally, conclusions are made in section 7.5.

7.2 Implementation of the constitutive model

7.2.1 General theory

Many textbooks are available which cover the finite element method in detail e.g. De Borst et al. (2012), Owen & Hinton (1980) and Zienkiewicz et al. (2014). However, for the sake of completeness, a summary of the key equations of the finite element method is shown on the pages that follow. An illustration of how the constitutive model is implemented in a generic formulation of finite element code is given in Figure 7.1 making references to the key equations and to the algorithms given in the previous chapter.

The governing system of equations can be derived using a virtual work approach. Inside a domain $\Omega \in \mathbb{R}^2$ with boundary Γ the total virtual work $\delta\Pi$ is given as (Owen & Hinton 1980, Bower 2009):

$$\begin{aligned} &\delta\Pi = \int_\Omega \delta\boldsymbol{\varepsilon} : \boldsymbol{\sigma} d\Omega - \int_\Omega \delta\boldsymbol{u} : \boldsymbol{F_B} d\Omega - \int_{\delta\Omega} \delta\boldsymbol{u} : \boldsymbol{F_{\delta\Omega}} d\delta\Omega = 0 && \text{in } \Omega \\ &\boldsymbol{u} = \boldsymbol{u_D} && \text{on } \Gamma_D \\ &\vec{\boldsymbol{n}} \cdot \boldsymbol{\sigma} = \boldsymbol{t_D} && \text{on } \Gamma_N \end{aligned} \tag{7.1}$$

Γ_D and Γ_N denote the boundaries with prescribed displacements $\boldsymbol{u_D}$ and tractions $\boldsymbol{t_D}$ respectively. $\boldsymbol{F_B}$ and $\boldsymbol{F_{\delta\Omega}}$ denote the external body and surface force vectors. δ is used to denote virtual quantities.

Equation 7.2 below is the standard non-linear matrix equation which results from discretising the governing equations (Logan 2016):

$$\boldsymbol{F_g} = \boldsymbol{K_g}(\boldsymbol{u_g})\boldsymbol{u_g} \tag{7.2}$$

where $\boldsymbol{F_g}$ is the global general force vector and $\boldsymbol{u_g}$ is the global nodal displacement vector. $\boldsymbol{K_g}$ is the global stiffness matrix that is assembled from the stiffness matrices $\boldsymbol{K_e}$ of individual elements. The standard form of $\boldsymbol{K_e}$ is given by (De Borst et al. 2012):

$$\boldsymbol{K_e} = \int_\Omega \boldsymbol{B^T D_s B} d\Omega \tag{7.3}$$

$\boldsymbol{B}$ is the strain-displacement matrix relating elemental nodal displacements to elemental strains, D_s is the secant matrix relating stresses to strains.

The incremental elemental nodal displacements $\Delta\boldsymbol{u^e}$ corresponding to a load increment are calculated by solving (De Borst et al. 2012):

$$\Delta\boldsymbol{f^e} = \boldsymbol{K_t}\Delta\boldsymbol{u^e} \tag{7.4}$$

where $\Delta\boldsymbol{f^e}$ is the incremental element force vector and $\boldsymbol{K_t}$ is the elemental tangential stiffness matrix.

When equilibrium has been achieved the global out-of-balance force vector $\boldsymbol{\Psi}$ is null (Owen & Hinton 1980):

$$\boldsymbol{\Psi} = \sum^{g} \int_{\Omega} \boldsymbol{B^T} \boldsymbol{\sigma^e} d\Omega - \boldsymbol{f_\lambda} = 0 \tag{7.5}$$

In Equation 7.5 above, $\sum^{g}$ represents the element assembly process, $\boldsymbol{f_\lambda}$ is the global applied force vector and $\boldsymbol{\sigma^e}$ is the elemental nodal stress vector.

Convergence is achieved when the norm of the global out-of-balance force vector has been reduced to a chosen tolerance *tol*:

$$\frac{|\boldsymbol{\Psi}|}{|\boldsymbol{f_g}|} \leq tol \tag{7.6}$$

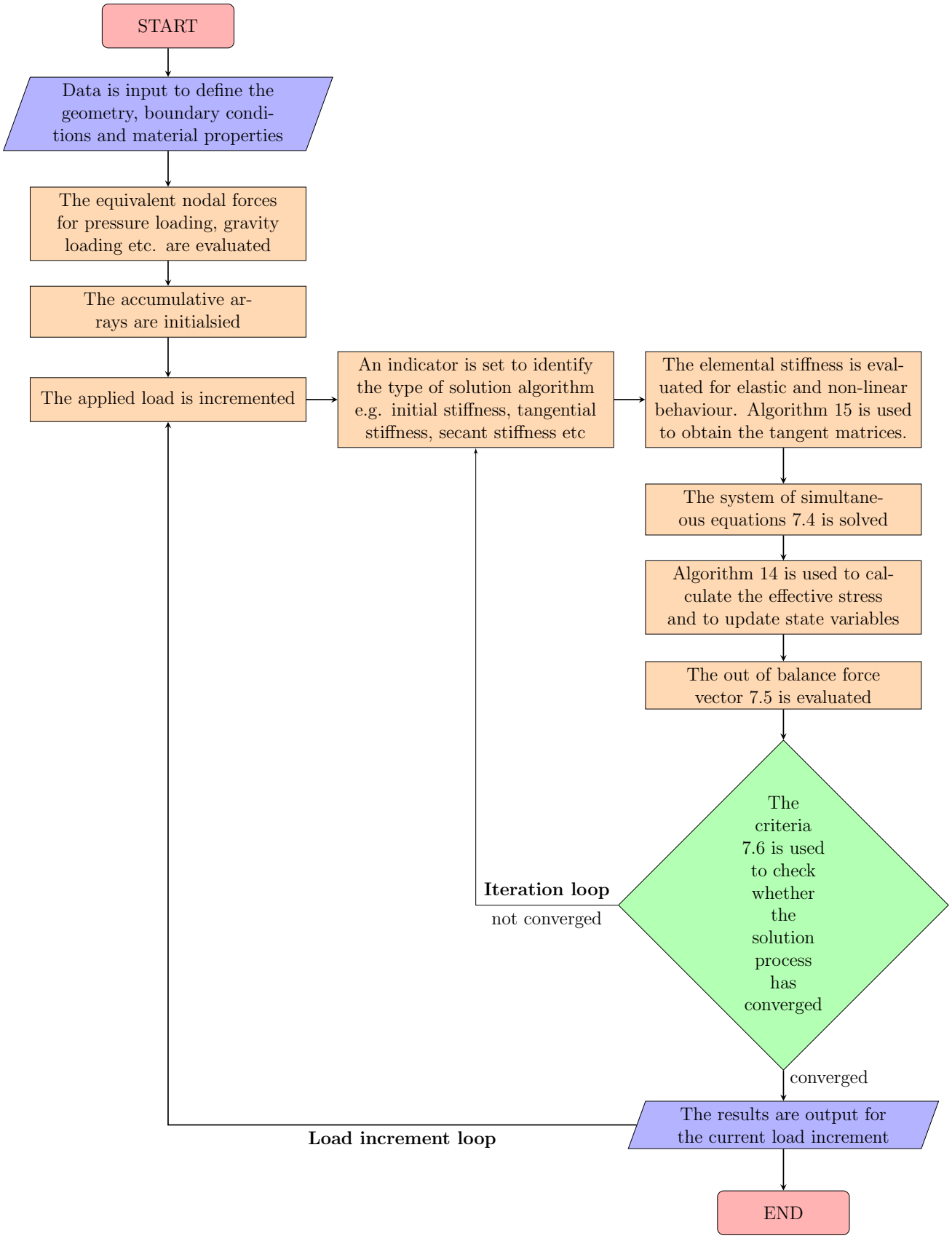

Figure 7.1: Illustration of how the plastic-damage constitutive model is implemented in a generic formulation of non-linear finite element code. Adapted from Mihai (2012).

7.2.2 Regularisation using the crack band method

Strain softening models cause mesh sensitivity problems (see section 3.6). Unless a regularisation scheme is implemented, damage becomes localised to an increasingly narrow region as the finite element mesh is refined (Pijaudier-Cabot & Bažant 1987). To tackle this issue, the crack band theory of Bažant & Oh (1983) is used to regularise the present model. The approach involves adjusting the end of the softening curve ε_{tm} so that the fracture energy G_f is constant for different element characteristic lengths l_{ch}.

From Bažant & Oh (1983), the standard expression for fracture energy is given by:

$$G_f = \int_0^\infty \sigma du = l_{ch} \int_0^\infty \sigma d\varepsilon \tag{7.7}$$

Evaluating the above integral leads to:

$$G_f = \frac{f_t l_{ch} \varepsilon_{tm}}{f_a} \tag{7.8}$$

and so the end of the softening curve can be obtained via:

$$\varepsilon_{tm} = \frac{f_a G_f}{f_t l_{ch}} \tag{7.9}$$

f_a is a constant which arises from evaluating the integral 7.7. Typically, models use a single evolution function that is derived from the tensile softening curve and the constant f_a would be present in the function. However, the current model is more complex with tensile strength reduction being modelled with two different hardening parameters and functions. For expediency, f_a can be evaluated by fitting a simpler 1D stress-strain relationship to the tensile softening curve. Then, the integral is evaluated for the simpler relationship. See Appendix E.

7.3 Direct fracture simulation

7.3.1 Test arrangement and parameters

To illustrate the effectiveness of the plastic-damage constitutive model, a direct fracture simulation was carried out and compared to the results of Petersson (1981). Displacement control was used to apply direct tension to the un-reinforced concrete specimen as shown in Figure 7.2. Figure 7.3 shows the restraints applied to the specimen for the analysis.

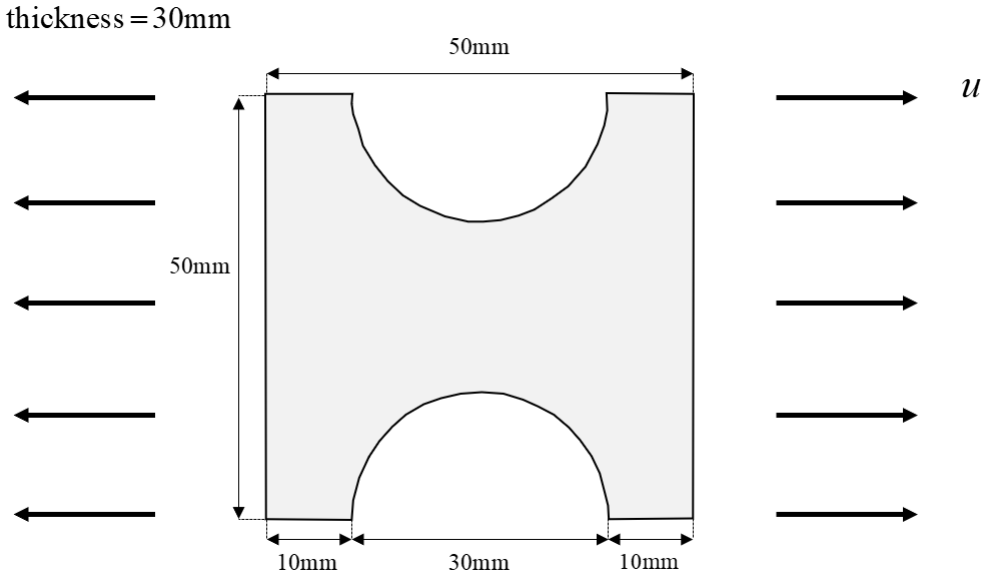

Figure 7.2: Test arrangement and specimen dimensions.

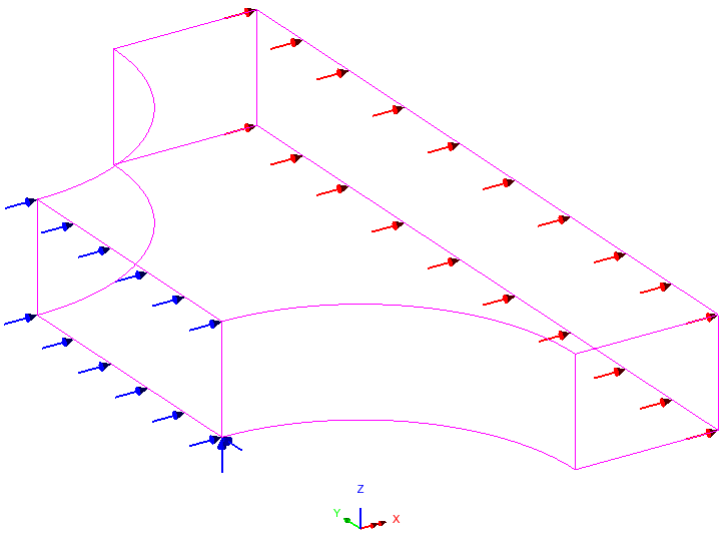

Figure 7.3: Restraints (blue) and displacements (red) applied to the specimen.

Simulations were carried out using two different meshes, illustrated in Figure 7.4,

with the second mesh being finer than the first. The purpose of using two meshes was to check whether mesh convergence had been achieved. Also, due to the symmetry of the problem, only half the specimen with a quarter of the thickness was analysed.

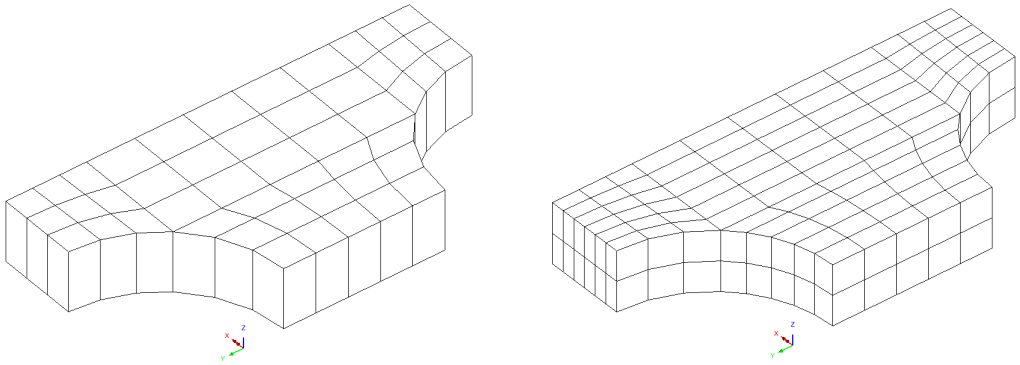

(a) Mesh 1 - 48 elements (b) Mesh 2 - 182 elements

Figure 7.4: Meshes used for the direct fracture simulation.

The parameters used for the simulations are shown in Table 7.1 below.

Table 7.1: Material parameters used for the direct fracture simulation.

E_m (MPa)	ν	f_t (MPa)	f_c (MPa)	ε_c	$f_a G_f$ (N/mm)	c_1	ρ_f	ρ_D
37,000	0.18	1.85	30	0.0022	0.2	12	5	1

7.3.2 Results

Figure 7.5 shows the stress-displacement curves resulting from the simulations and data from Petersson (1981). The responses from the meshes are virtually indistinguishable and so the results are satisfactorily mesh-independent. The numerical results can also be seen to agree well with the experimental data.

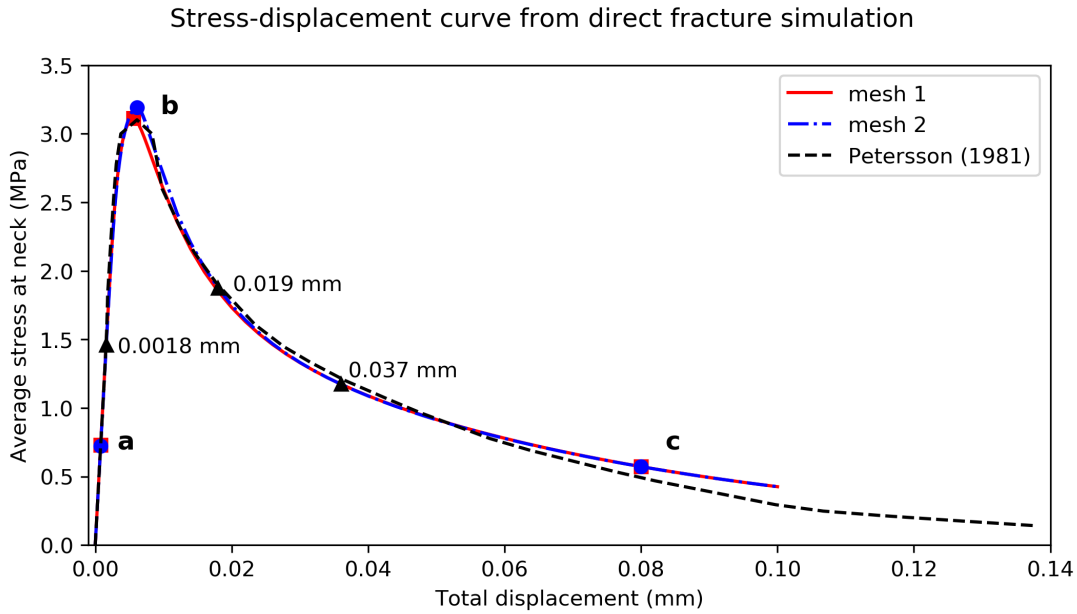

Figure 7.5: Comparison of the predicted stress-displacement response to experimental data from Petersson (1981). Note that the displacement shown in the plot is double the displacement resulting from the simulations because only half of the specimen was analysed.

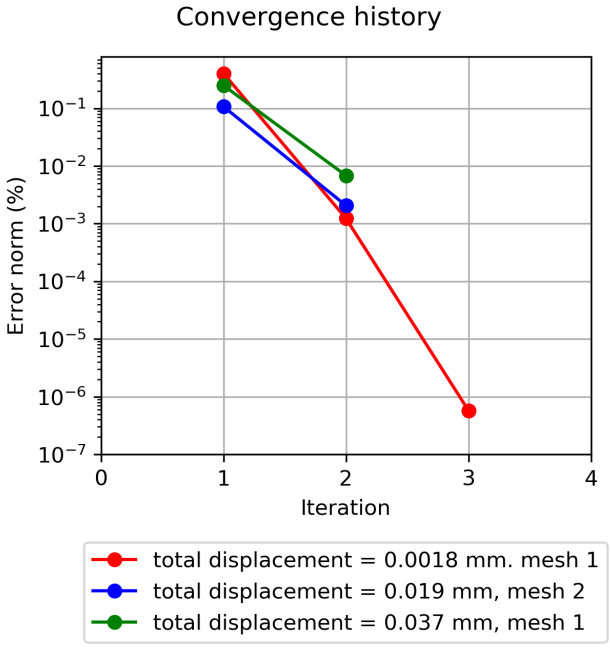

Figure 7.6: Example convergence histories at different total displacements. See points marked on Figure 7.5.

For the simulation, the tolerance *tol* was set to 1.0 (i.e. 1.0%). A total of 75 and 355 steps were used to carry out the analysis of meshes 1 and 2 respectively. The max number of iterations allowed was 10 and the first iteration was always carried

out using the elastic stiffness. The next four iterations used the secant stiffness and the remainder of the iterations followed by using the tangential stiffness matrix. In order to demonstrate convergence properties of the mode, simulations were carried out using a tighter tolerance (0.1%) and with the tangential stiffness used for all iterations besides the first. The results from the study could not be distinguished from the results presented in this chapter. Example convergence histories from the study, which show quadratic convergence, are shown in Figure 7.6. Figure 7.6 shows that using the tangential stiffness on the second iteration reduces error norm by approximately two orders of magnitude. The example with three steps (mesh 1 with total displacement = 0.00018 mm) shows that a further iteration again reduces the error norm. In this case by about 3 orders of magnitude.

The deformation of mesh 2 at the end of the simulation, i.e. at a total displacement of 0.1mm, is shown in Figure 7.7. Contour plots of the major principal stresses and strains, at the stages marked in Figure 7.5, are shown in Figures 7.8 to 7.11 for mesh 2. Initially at stage a, the stress appears to be concentrated in the region near the boundaries of the narrowing section of the dog-bone specimen (Figure 7.8). This represents the occurrence of microcracking in this zone prior to the propagation of a macroscopic crack across the specimen. At the peak load, the strain field shows that a crack is starting to grow across the neck of the specimen (Figure 7.10). In the post-peak regime, the strains localised in a band of elements across the neck of the specimen (Figure 7.11). A macrocrack has formed across the neck of the specimen which is the expected response based on the tests of Petersson (1981).

Results for mesh 1 are available in Appendix F.

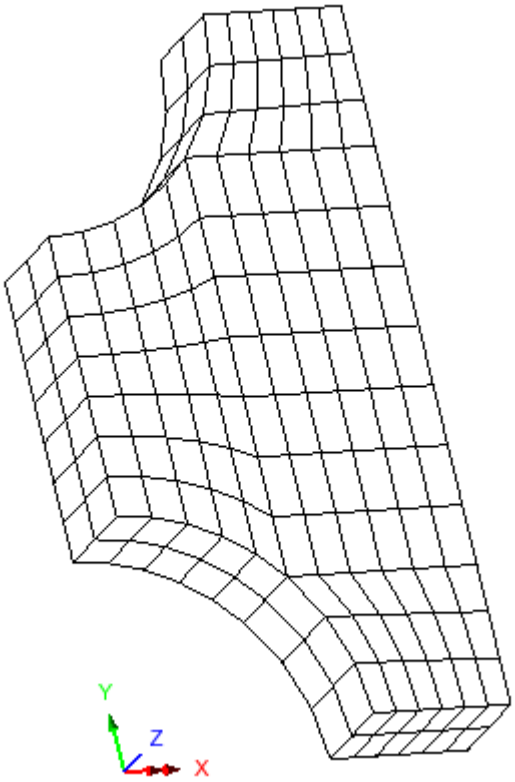

(a) Undeformed mesh

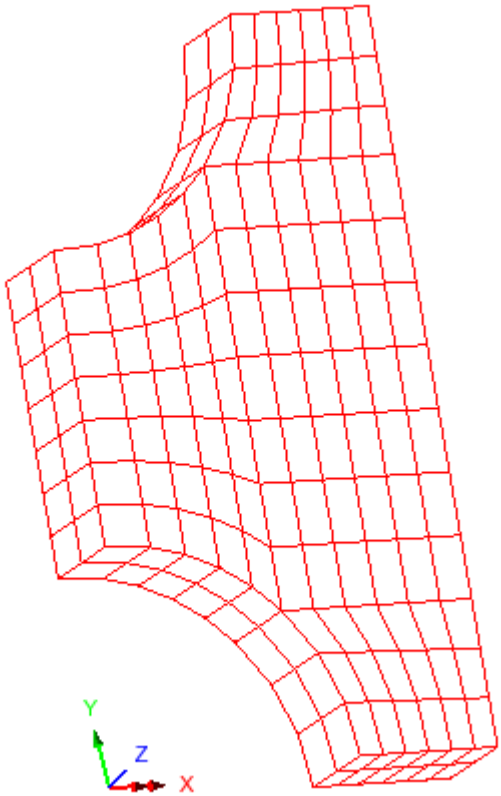

(b) Deformed mesh (30x exaggeration)

Figure 7.7: Mesh 2 deformation.

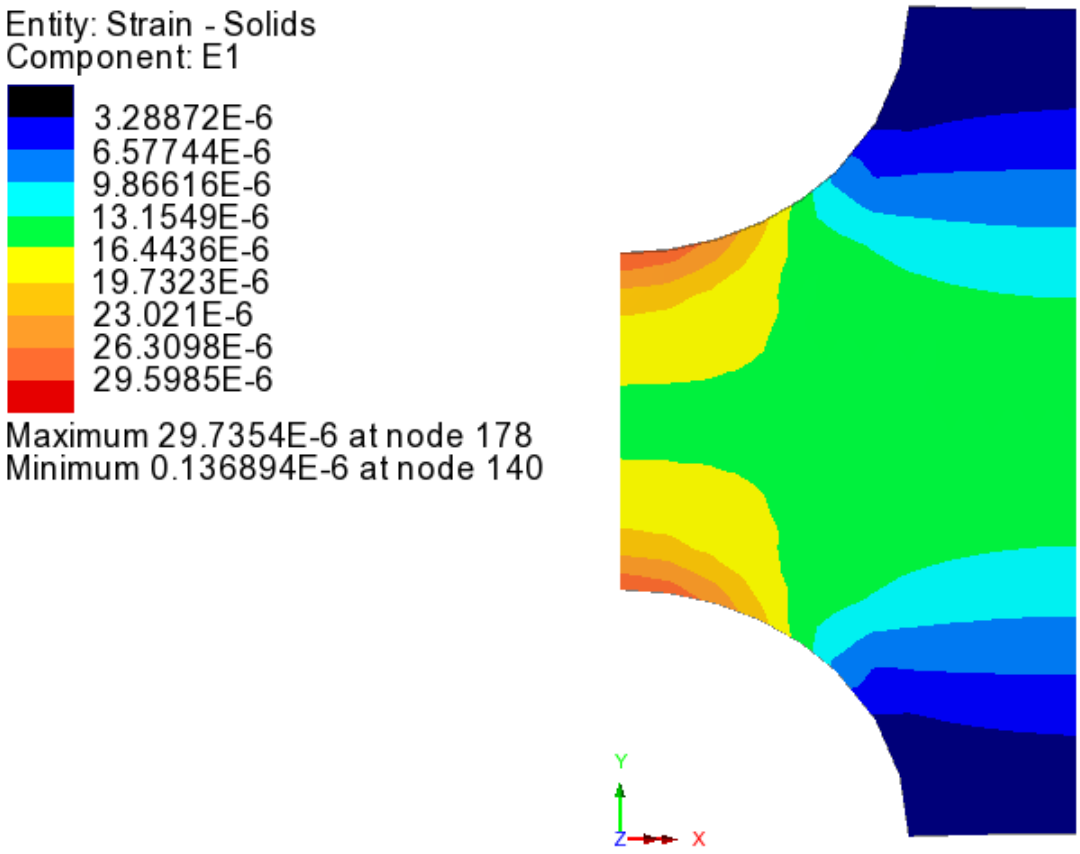

(a) Major principal strains

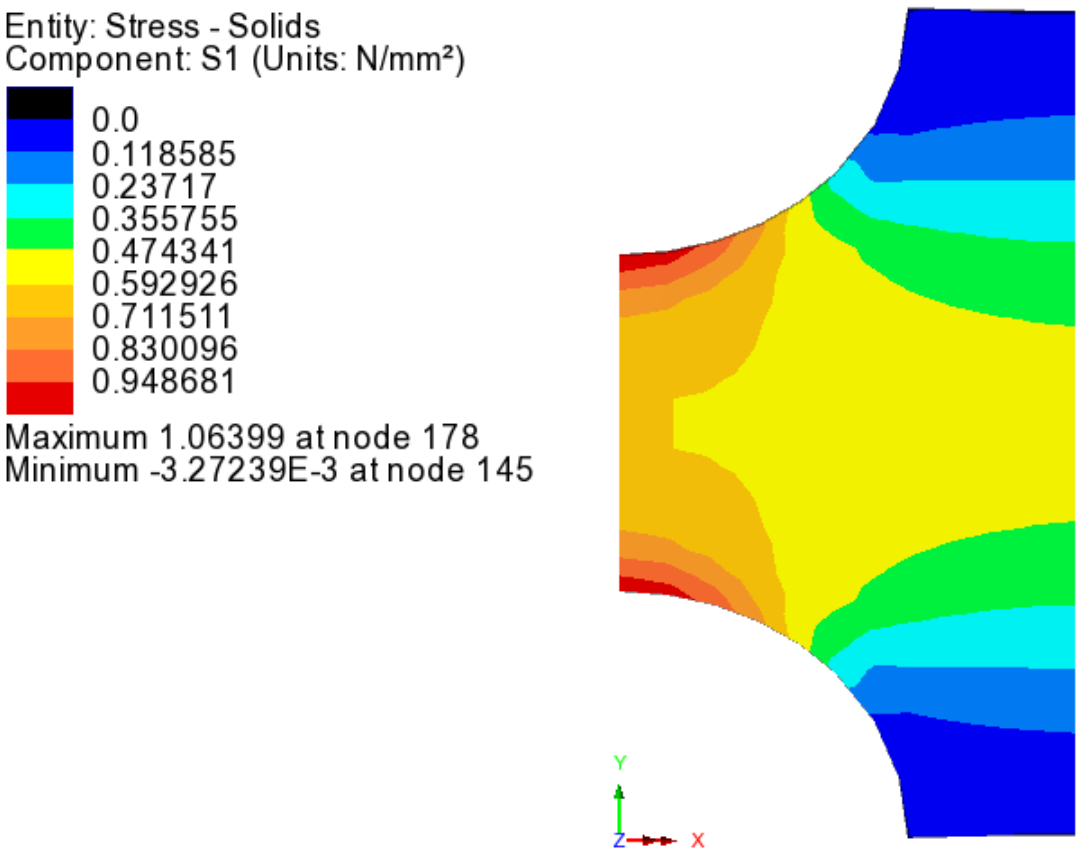

(b) Major principal stresses

Figure 7.8: Major principal stresses and strains of mesh 2 at stage a in Figure 7.5.

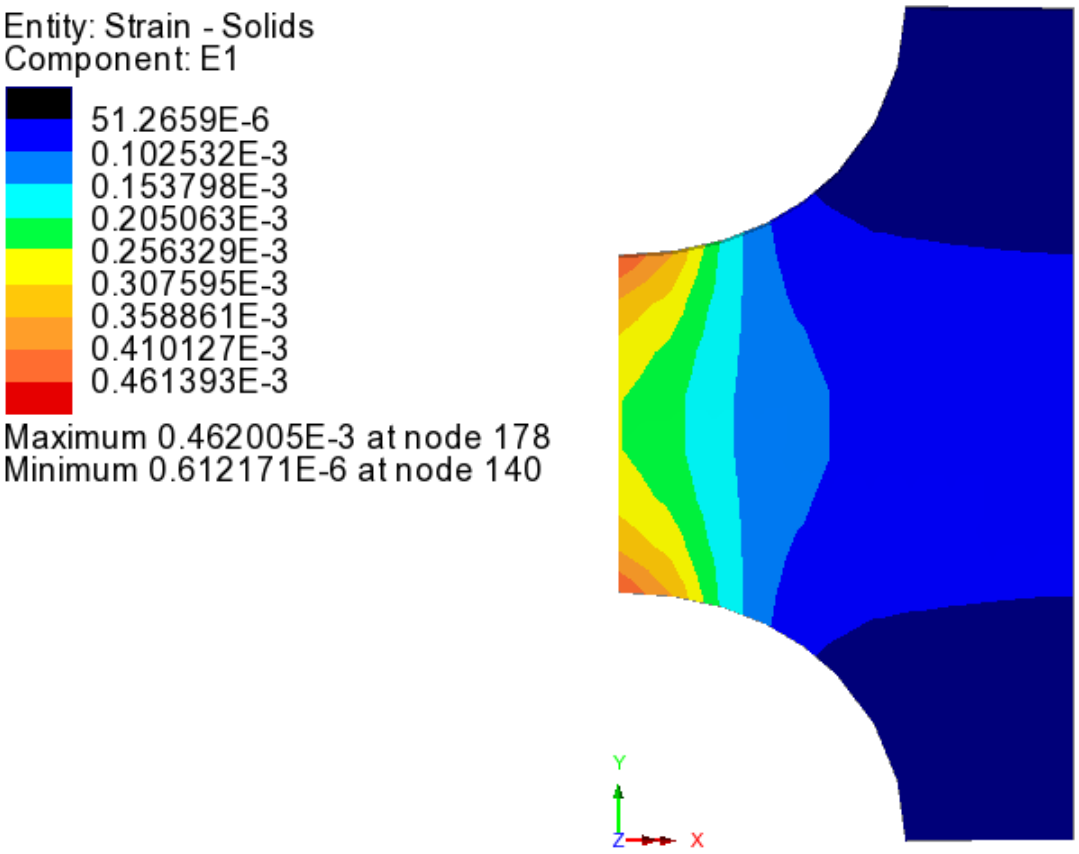

(a) Major principal strains

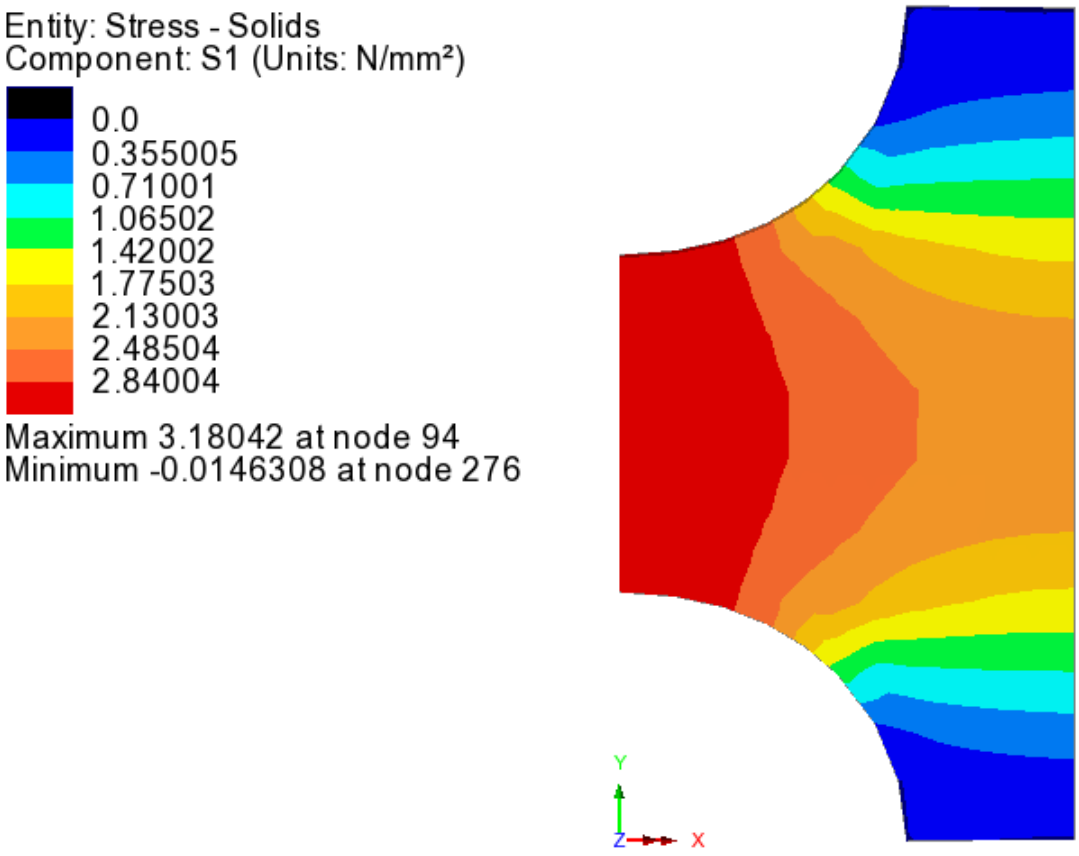

(b) Major principal stresses

Figure 7.9: Major principal stresses and strains of mesh 2 at stage b in Figure 7.5.

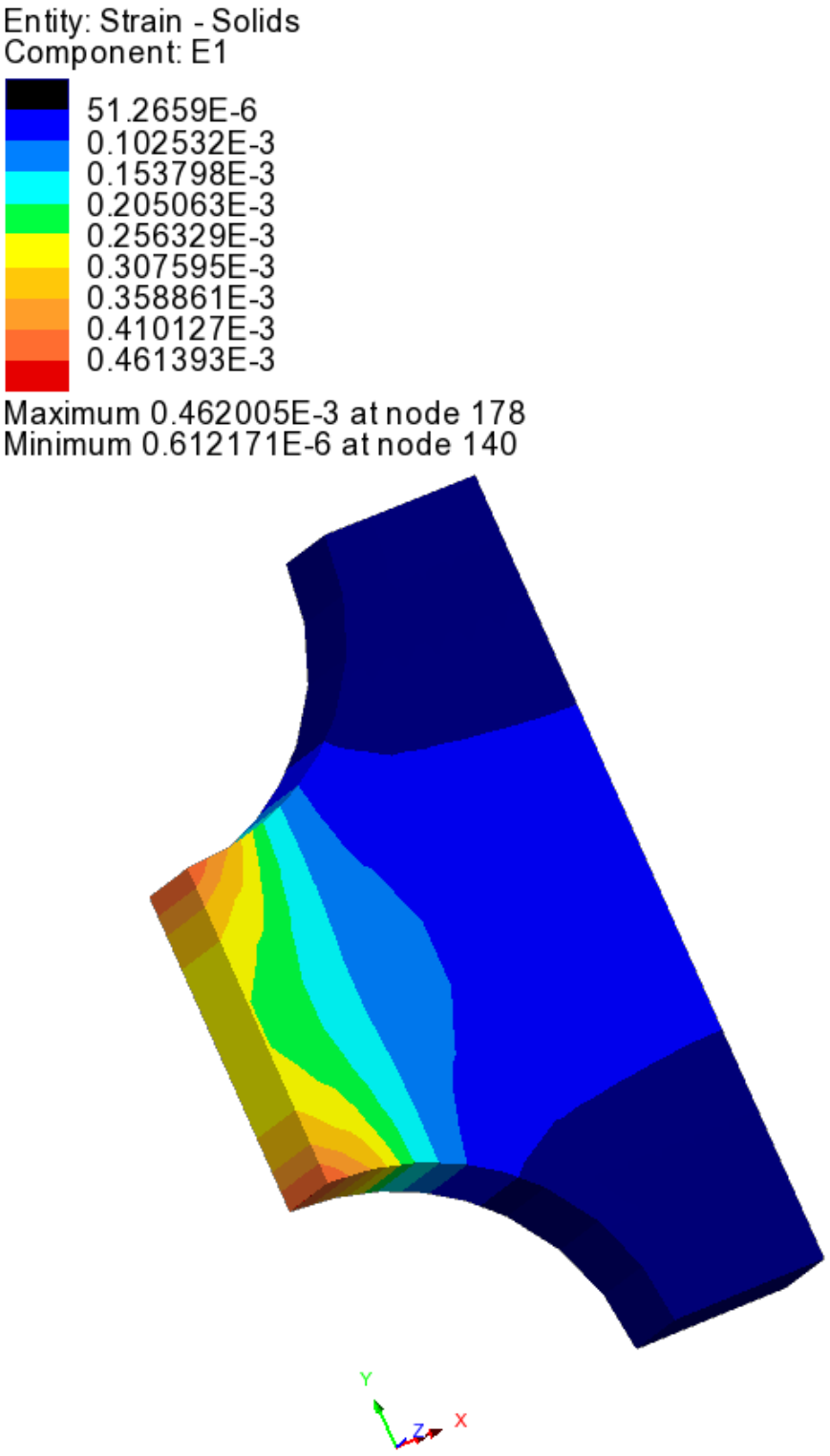

Figure 7.10: 3D plot of major principal strains of mesh 2 at stage b in Figure 7.5 showing the through thickness response.

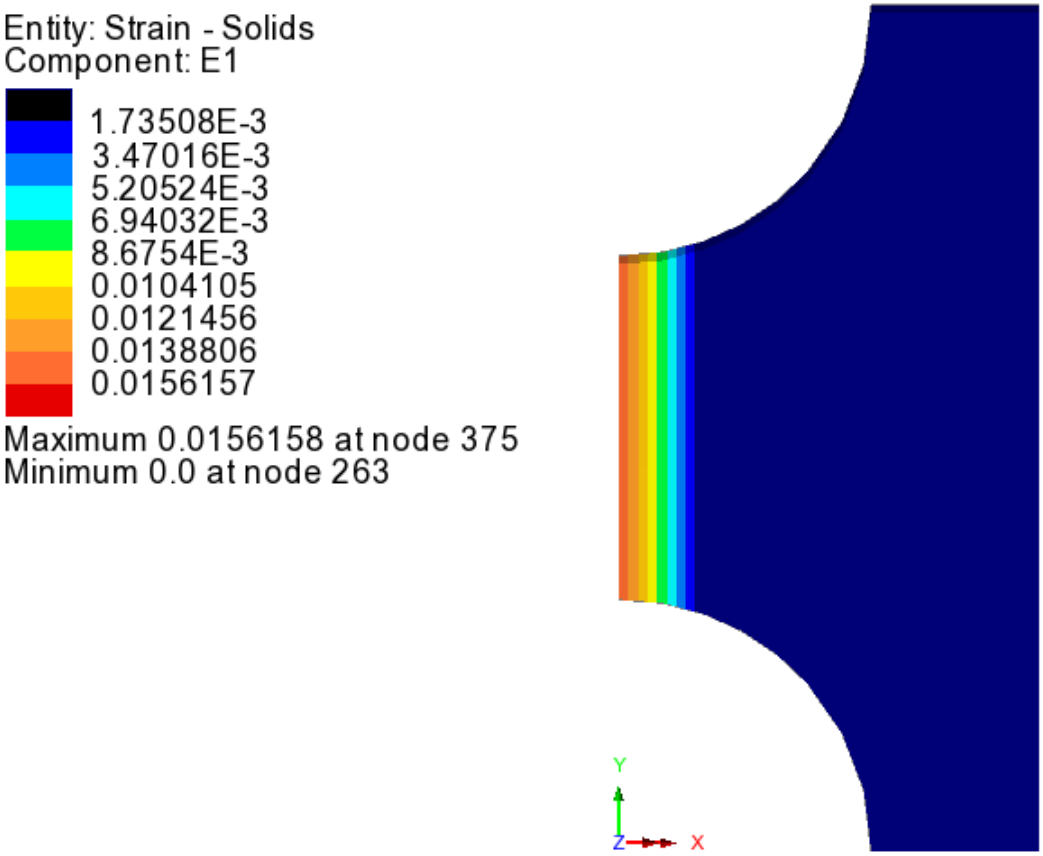

(a) Major principal strains

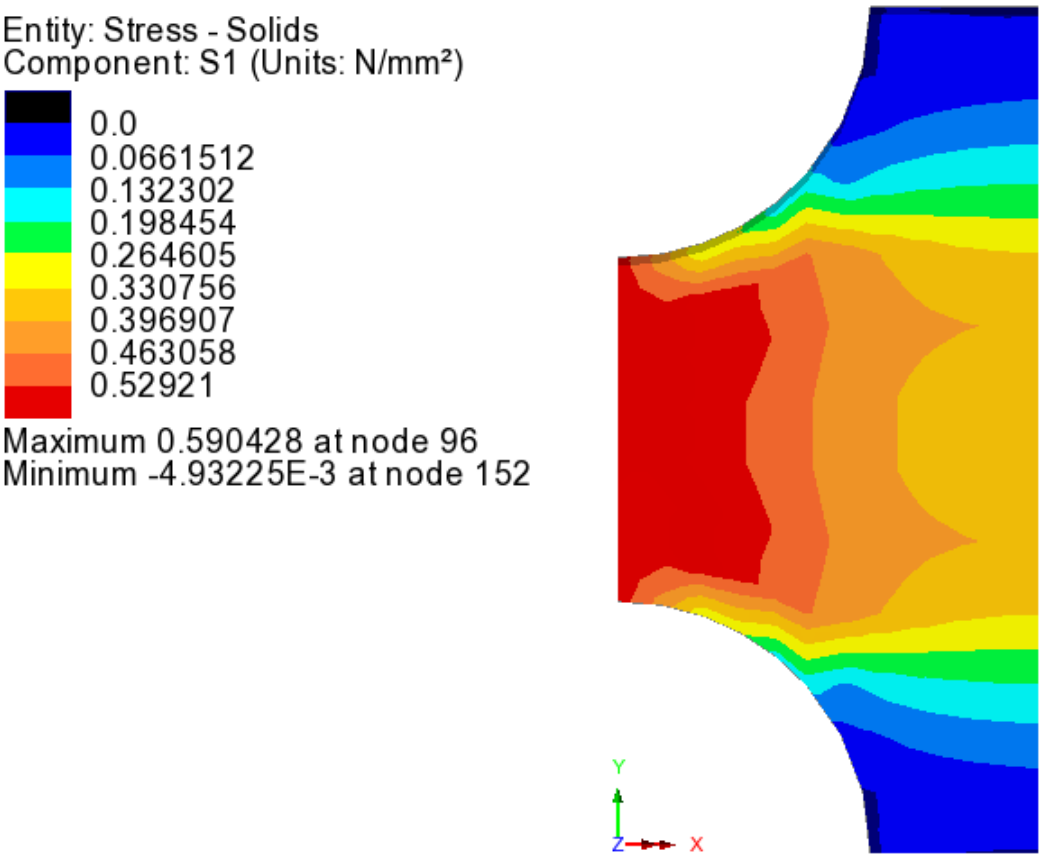

(b) Major principal stresses

Figure 7.11: Major principal stresses and strains of mesh 2 at stage c in Figure 7.5.

7.4 Four-point bending simulation

7.4.1 Test arrangement and parameters

A second example of a finite element simulation using the plastic-damage model was carried out. An analysis was undertaken of a concrete beam with conventional and shear reinforcement subject to four-point bending as shown in Figure 7.12. Restraints were applied to the beam as shown in 7.13. Experimental data from tests carried out at Cardiff University was compared to the simulation results. The conventional reinforcement consisted of a single mild steel ⌀10mm longitudinal rebar and the shear reinforcement consisted of mild steel ⌀6mm shear links at 50mm c/c.

Tables 7.2 and 7.3 show the parameters used for the simulation. The finite element mesh is illustrated in Figure 7.14. Because of the symmetry of the beam, only half the length of the beam and half of the thickness of the beam was analysed.

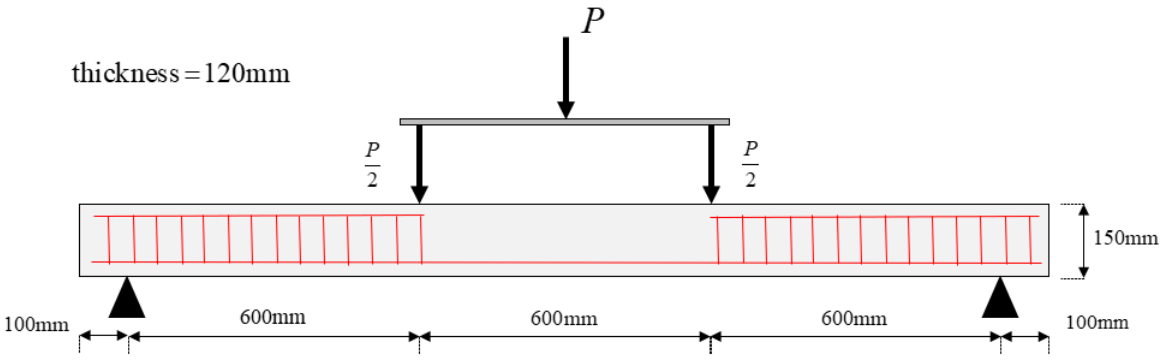

Figure 7.12: Test arrangement and specimen dimensions.

Table 7.2: Concrete material parameters used for the simulation of four-point bending.

E_m (MPa)	ν	f_t (MPa)	f_c (MPa)	ε_c	$f_a G_f$ (N/mm)	c_1	ρ_f	ρ_D
25,000	0.2	1.2	40	0.0022	0.12	12	5	1

Table 7.3: Steel reinforcement material parameters used for the simulation of four-point bending. f_y is the yield stress, H is the hardening modulus and ε_m is the hardening strain limit.

Reinforcement	E (MPa)	ν	f_y (MPa)	H (MPa)	ε_m
Longitudinal	205,000	0.3	590	800	0.02
Shear	205,000	0.3	560	800	0.02

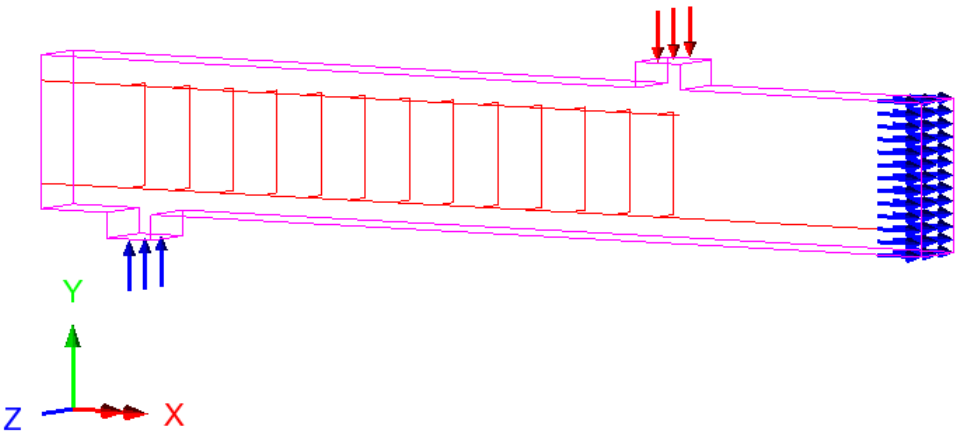

(a)

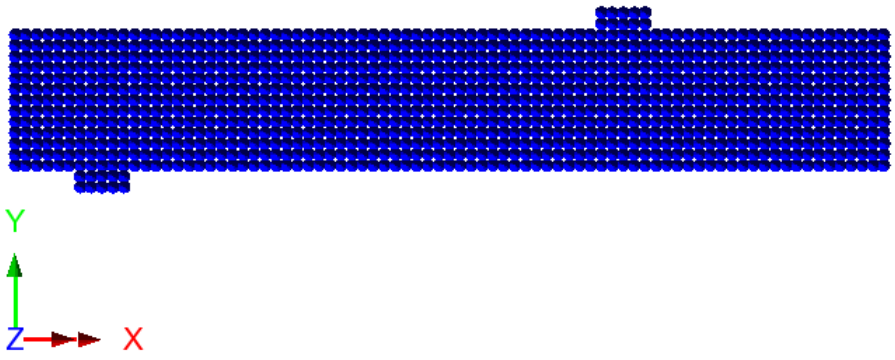

(b)

Figure 7.13: Restraints (blue) and displacements (red) applied to the beam are shown in (a) with the exception of restrains in the z direction which are shown separately in (b) for clarity. Note that the restraints in the z direction are applied to the inner face of the beam.

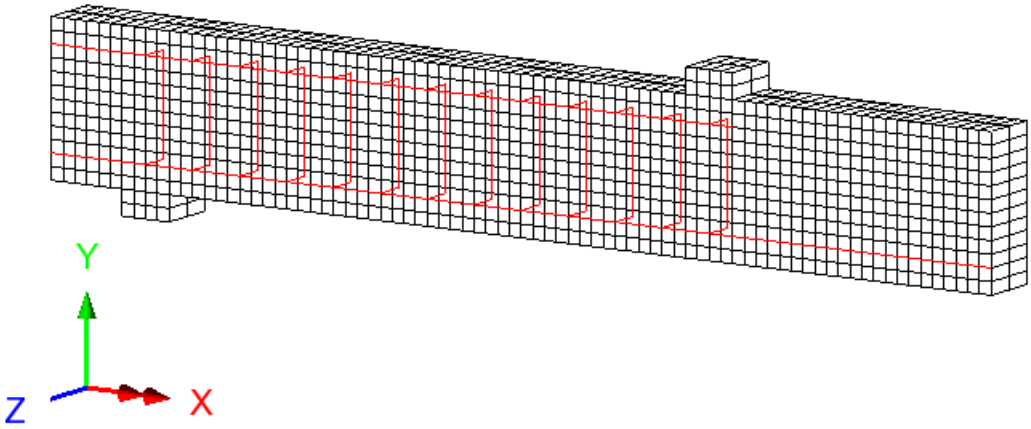

Figure 7.14: Finite element mesh of the beam. There are 2082 elements.

7.4.2 Results

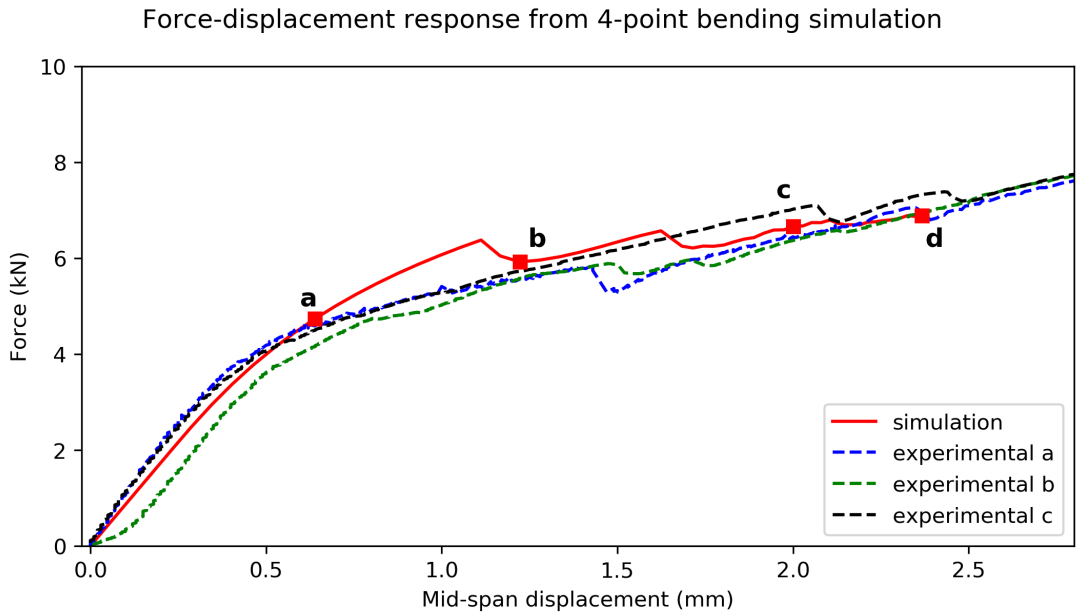

Figure 7.15: Force displacement response from the simulation of four-point bending compared to data from experiments carried out at Cardiff University. Data from tests on three identical beams is shown.

A comparison of the force-displacement results from the simulation and the experimental data is made in Figure 7.15. The results were achieved using 279 steps and $tol = 1.0$ i.e. 1%. The predicted behaviour agrees reasonably well with the experimental data.

Figure 7.16 shows the deformation of the mesh and profiles of the major principal strains, at the stages marked in Figure 7.15, are shown in figures 7.17 to 7.21.

The plots show that initially the major principal strains were concentrated in the tension zone of the beam (figures 7.17 and 7.18). As the applied force increased up to stage b, the strain field became more non-uniform with the major principal strains concentrated to a crack that developed in tension zone (Figure 7.19). The strains of the material outside of the crack appears to have relaxed due to the model capturing strain localisation. A second crack forms as the applied force increases further to stage c and the original macrocrack also continues to grow (Figure 7.20). At stage d, a third crack forms (Figure 7.21).

Appendix G contains the xx-strain profiles resulting from the simulation.

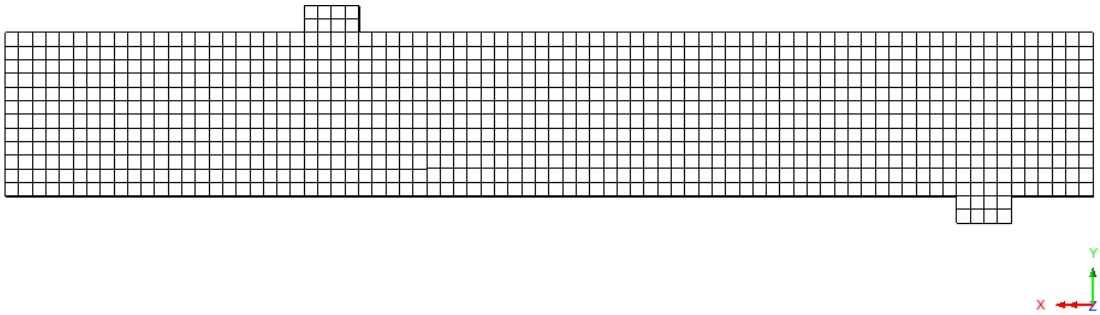

(a) Undeformed mesh

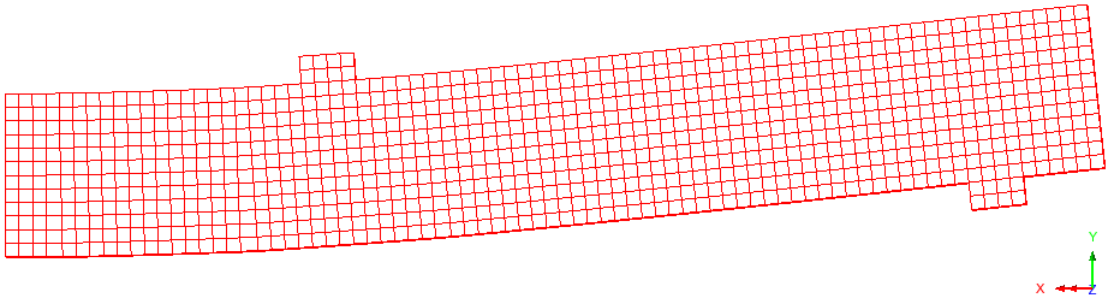

(b) Deformed mesh (30x exaggeration)

Figure 7.16: Beam deformation

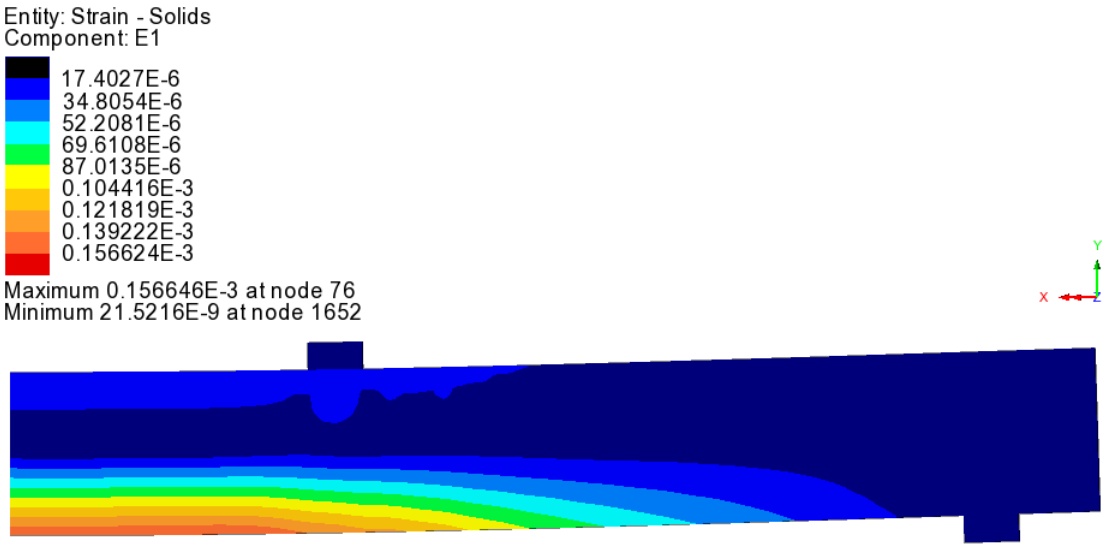

Figure 7.17: Major principal strain profile at stage a in Figure 7.15.

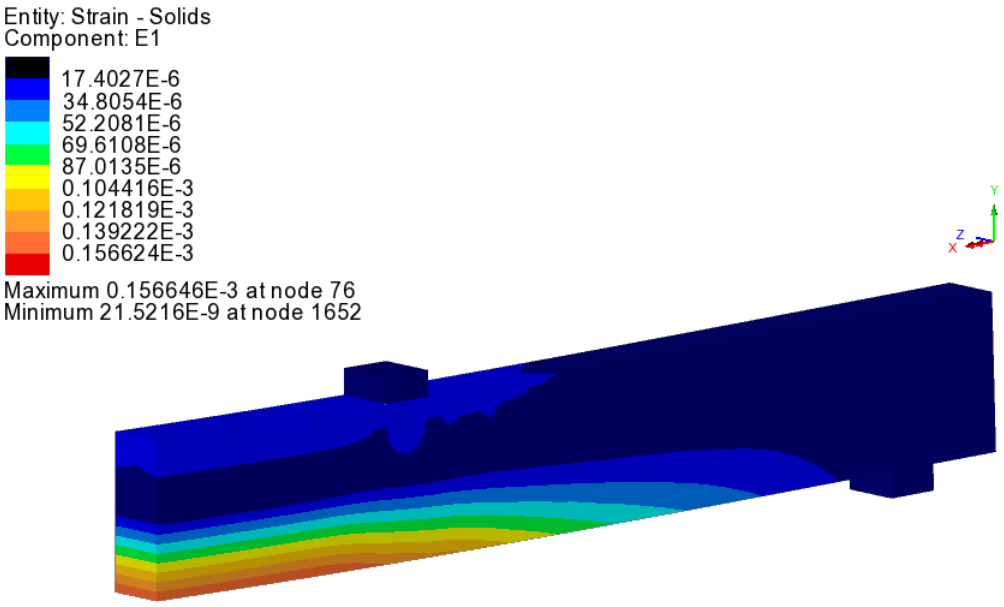

Figure 7.18: 3D plot of the major principal strains at stage a in Figure 7.15 showing the through thickness response.

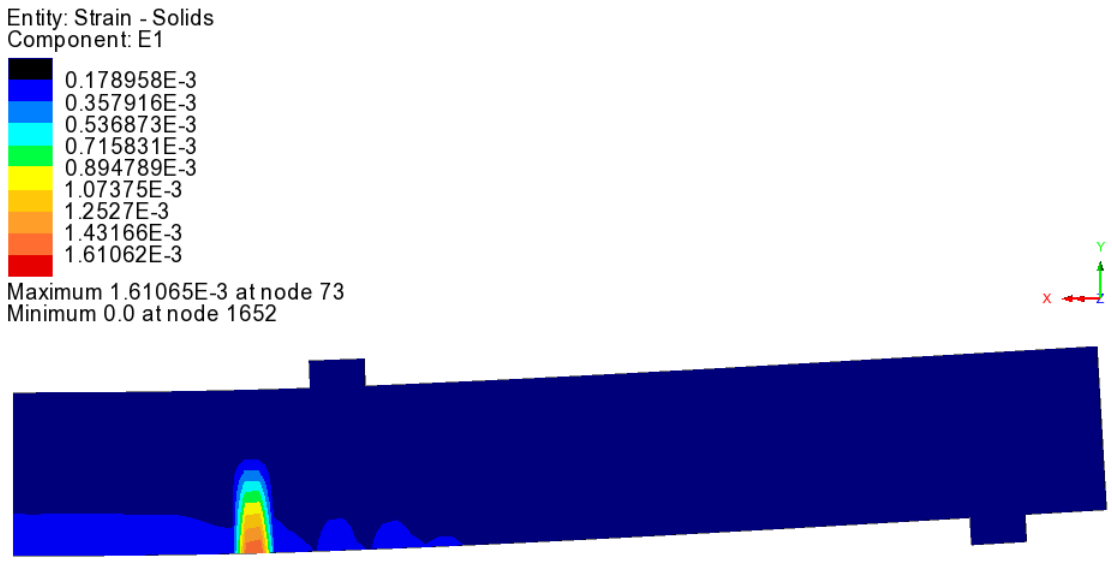

Figure 7.19: Major principal strain profile at stage b in Figure 7.15.

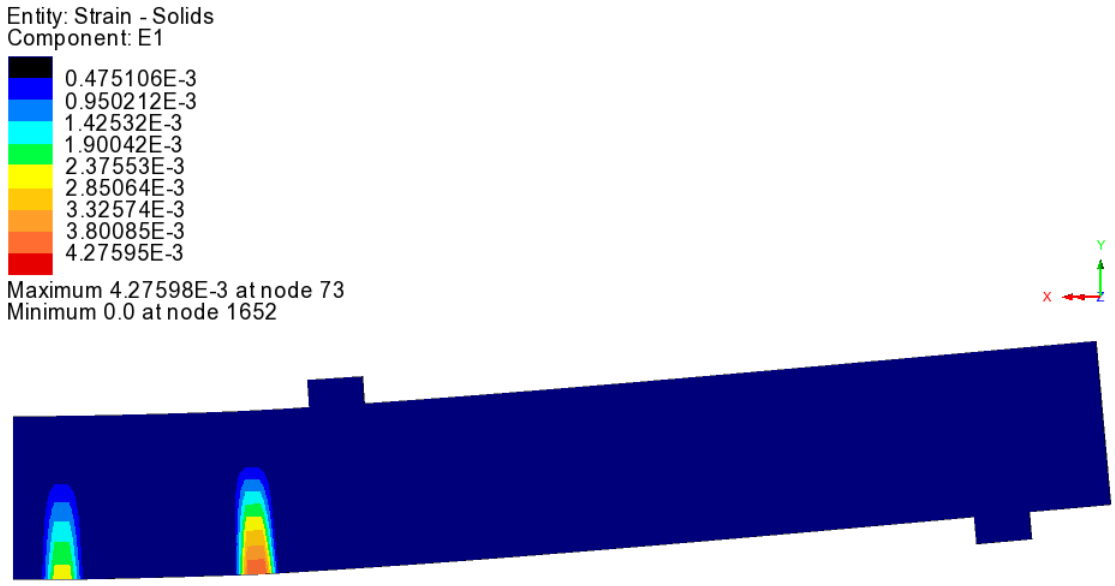

Figure 7.20: Major principal strain profile at stage c in Figure 7.15.

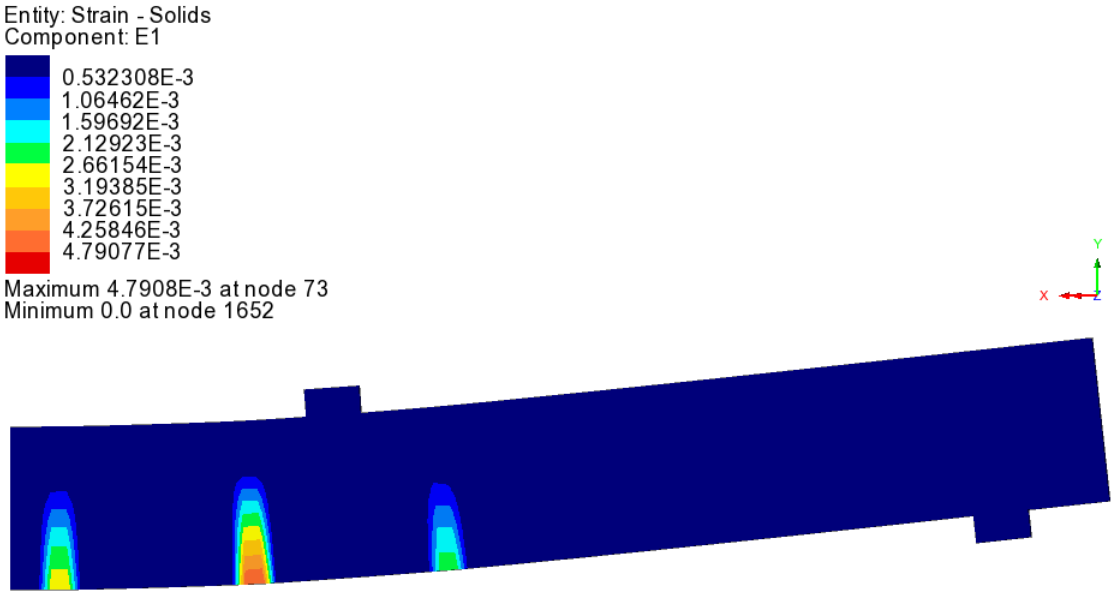

Figure 7.21: Major principal strain profile at stage d in Figure 7.15.

7.5 Conclusions

The plastic damage constitutive model was successfully implemented in a commercial finite element package. The simulation of a direct fracture test and a four-point bending test suggests that the model is capable of giving realistic results that agree well with experimental data. The model is capable of simulating localised cracking behaviour. A potential aim for future work would be to improve upon the numerical performance of the model, for example via more efficient programming, so that fewer steps and less computational time is required to carry out simulations.

Chapter 8

Conclusions and recommendations for future work

The objectives of the research presented in this thesis were given in the introductory chapter, chapter 1. This chapter summarises how these objectives were achieved via the formulation and implementation of novel constitutive models and carrying out meso-scale (lattice) simulations. Some recommendations are also provided on different avenues of research that can be pursued to improve the models.

8.1 Conclusions

A micromechanics based constitutive model for plain concrete was formulated that improved upon its predecessors by better describing the evolution of cracking in concrete. The predecessor models simulated microcracking alone whereas the new model simulated both microcracking and macrocracking behaviour. Directional microracking and homogenised elastic properties were simulated using micromechanics based solutions. A novel mechanism to transition to localised macrocracking was developed by studying the results of lattice simulations that were carried out along with observations from non-destructive experiments reported in the literature. It was concluded that diffuse microcracks grow and begin to coalesce to form a stable macrocrack between an interval of approximately 80%-100% of the pre-peak and post-peak load and that unstable, localised macrocrack growth is concentrated to the post-peak regime. Then, the peak stress was selected to be the point of transition to localised cracking as it was consistent with both experimental observations and the lattice model simulations.

Implementing the transition to localised cracking was found to give more realistic

predictions of material behaviour compared to a model in which the transition was not considered. Validation of the model using experimental data showed that the reduced post-peak ductility from allowing a macrocrack to develop gave better agreement with both the experimental data and lattice simulation results for uniaxial tension loading paths. Single-point path simulations using the consitutive model also showed that the model can predict realistic orientations of the localised cracking plane(s) under different loading conditions.

The plain concrete micromechanical model was extended to formulate a model capable of simulating fibre-reinforced concrete behaviour. The fibre-crack bridging mechanism, which is the main underlying mechanism for the difference in behaviour caused by the addition of fibres, was implemented using micromechanics based solutions.

The new model for fibre-reinforced cementitious composites improved upon its predecessors by better simulating the cracking process. This was achieved by inclusion of the crack localisation mechanism. Validation of the model using experimental data showed that the predicted stress-strain curves were realistic.

The characteristic behaviour of cementitious composites includes the development of permanent deformations. However, the damage based approach used for the above-mentioned constitutive models can not simulate permanent deformations. Hence, a new model for plain cementitious composites was developed using a micromechanical plastic-damage approach. In the model, crack planes were represented by local plastic yield surfaces. Tensile stress states lead to the development of directional macrocracks in cementitious composites. The cracking behaviour differs when compressive stress states are applied. Under compression, diffuse micro-cracks develop which have an isotopic effect. Hence, two separate plastic hardening variables were used for directional (tensile) and isotropic (compressive) effects. The use of two separate hardening variables allowed for separate functions to be used that best represent the characteristic behaviour under a particular stress state. To aid robustness of the model, the consistent tangent was derived.

Validation of the plastic-damage model using experimental data showed good agreement with experimental data for different loading paths with the exception of biaxial compression and to a lesser extent triaxial compression. This was also an issue for the above micromechanics based plain concrete model. The next section discusses a known remedy that can be implemented in future work.

All of the new constitutive models presented in the thesis were able to capture the

tensile-splitting that occurs immediately after cracking under tensile loads. The predecessor micro-mechanical models lacked this capability as they did not model the formation of macrocracks and the subsequent relaxation of lateral strains. Whilst other predecessor models could capture the formation of macrocracks, they could not predict microcracking behaviour. The new models address both of these issues.

Initially, there was an intention for the research to cover the extension of the plastic-damage model to account for the effects of fibre-reinforcement and the implementation of the extended model in a commercial finite element software package. Instead, research efforts were devoted to finite element implementation of the plastic-damage model for plain concrete as an initial assessment of the performance of the model. Nonetheless, the research carried out is a useful first step and fibre reinforcement can be added in the future.

A direct fracture simulation and a four-point bending simulation were carried out using the implemented model. The model was implemented in LUSAS and regularised using the crack band theory. The results were promising with the model being able to predict the characteristic localised cracking behaviour and agreeing well with experimental data.

8.2 Recommendations for future work

An issue common to the proposed constitutive models was the under prediction of the ratio of biaxial to uniaxial compression strength. This was expected as rough crack contact on crack surfaces, a key mechanisms for simulating the characteristic response in compression, was not incorporated in the models. The mechanism was not included for expediency reasons and because the focus of the research was the new mechanism for the transition to localised cracking. Literature is available (Jefferson & Bennett 2007, Mihai & Jefferson 2017) which shows that including the mechanism corrects the low biaxial strength predictions. A recommendation is made for the rough crack contact mechanism to be added to the plastic-damage model. It is anticipated that the improved model will then be able to capture the entire characteristic response of concrete.

Once the plastic-damage model for plain concrete has been improved, attention can be diverted to extending the model to fibre-reinforced cementitious composites. Additionally, simulation of the strain-hardening phenomena could be explored.

Finally, once the constitutive model for fibre-reinforced concrete has been devel-

oped and validated, finite element implementation of the model should be carried out. Whilst using the crack-band method was shown to give satisfactory results in the current work, the use of a more rigorous regularisation scheme could be explored. Also, assessment of the performance of the model should be significantly more extensive than the initial assessment made in the current work. Future work will explore industrial applications of the implemented model.

Appendix A

Derivation of the matrix of derivatives for the micromechanical fibre-reinforced cementitious composites constitutive model

The incremental change in $\boldsymbol{\Psi}$ is given below:

$$\begin{aligned} \boldsymbol{d\Psi}_i = -\boldsymbol{N}_i \boldsymbol{D}_{mcf} \boldsymbol{N}_j^T \left(\boldsymbol{I}^{4s} - \tilde{\boldsymbol{M}}_{s_j} - \boldsymbol{C}_L \boldsymbol{D}_{\boldsymbol{Lf}} \tilde{\boldsymbol{M}}_{f_j} \right) \boldsymbol{I} d\tilde{\boldsymbol{\varepsilon}}_{\boldsymbol{j}} \\ + \boldsymbol{N}_i \boldsymbol{D}_{mcf} \boldsymbol{N}_j^T \frac{\tilde{\boldsymbol{M}}_{s_j}}{d\tilde{\boldsymbol{\varepsilon}}_{\boldsymbol{j}}} d\tilde{\boldsymbol{\varepsilon}}_{\boldsymbol{j}} \tilde{\boldsymbol{\varepsilon}}_{\boldsymbol{j}} + \boldsymbol{N}_i \boldsymbol{D}_{mcf} \boldsymbol{N}_j^T \boldsymbol{C}_L \boldsymbol{D}_{\boldsymbol{Lf}} \frac{\tilde{\boldsymbol{M}}_{f_j}}{d\tilde{\boldsymbol{\varepsilon}}_{\boldsymbol{j}}} d\tilde{\boldsymbol{\varepsilon}}_{\boldsymbol{j}} \tilde{\boldsymbol{\varepsilon}}_{\boldsymbol{j}} \\ - \delta_{ij} \boldsymbol{D}_L \tilde{\boldsymbol{M}}_{s_j} \tilde{\boldsymbol{\varepsilon}}_{\boldsymbol{j}} - \delta_{ij} \boldsymbol{D}_L \frac{\tilde{\boldsymbol{M}}_{s_j}}{d\tilde{\boldsymbol{\varepsilon}}_{\boldsymbol{j}}} d\tilde{\boldsymbol{\varepsilon}}_{\boldsymbol{j}} \tilde{\boldsymbol{\varepsilon}}_{\boldsymbol{j}} \\ - \delta_{ij} \boldsymbol{D}_L \tilde{\boldsymbol{M}}_{f_j} \tilde{\boldsymbol{\varepsilon}}_{\boldsymbol{j}} - \delta_{ij} \boldsymbol{D}_L \frac{\tilde{\boldsymbol{M}}_{f_j}}{d\tilde{\boldsymbol{\varepsilon}}_{\boldsymbol{j}}} d\tilde{\boldsymbol{\varepsilon}}_{\boldsymbol{j}} \tilde{\boldsymbol{\varepsilon}}_{\boldsymbol{j}} \end{aligned} \tag{A.1}$$

$\tilde{\boldsymbol{M}}_{\boldsymbol{s}}$ and $\tilde{\boldsymbol{M}}_{\boldsymbol{f}}$ from Equation 5.16 are substituted into Equation A.1 and the associated incremental derivative terms calculated:

$$
\begin{aligned}
\boldsymbol{d\Psi}_i = &-\boldsymbol{N}_i\boldsymbol{D}_{mcf}\boldsymbol{N}_j^T\left(\boldsymbol{I}-(1-\tilde{\omega}_j)\boldsymbol{I}-\boldsymbol{C}_L\boldsymbol{D}_{Lf}\tilde{\omega}_j(1-\tilde{\omega}_{f_j})\boldsymbol{I}\right)\tilde{\boldsymbol{\varepsilon}}_{\boldsymbol{j}}\\
&+\boldsymbol{N}_i\boldsymbol{D}_{mcf}\boldsymbol{N}_j^T\frac{d(1-\tilde{\omega}_j)}{d\tilde{\omega}_j}\frac{d\tilde{\omega}_j}{d\tilde{\xi}_j}\frac{\boldsymbol{d\tilde{\xi}_j}}{\boldsymbol{d\tilde{\varepsilon}_j}}\boldsymbol{I}\boldsymbol{d\tilde{\varepsilon}_j}\tilde{\varepsilon}_j+\boldsymbol{N}_i\boldsymbol{D}_{mcf}\boldsymbol{N}_j^T\boldsymbol{C}_L\boldsymbol{D}_{Lf}\frac{d\tilde{\omega}_j}{d\tilde{\xi}_j}\frac{\boldsymbol{d\tilde{\xi}_j}}{\boldsymbol{d\tilde{\varepsilon}_j}}\boldsymbol{d\tilde{\varepsilon}_j}(1-\tilde{\omega}_{f_j})\boldsymbol{I}\tilde{\boldsymbol{\varepsilon}}_{\boldsymbol{j}}\\
&+\boldsymbol{N}_i\boldsymbol{D}_{mcf}\boldsymbol{N}_j^T\boldsymbol{C}_L\boldsymbol{D}_{Lf}\tilde{\omega}_j\frac{d(1-\tilde{\omega}_{f_j})}{d\tilde{\omega}_{f_j}}\frac{d\tilde{\omega}_{f_j}}{d\tilde{\xi}_{f_j}}\frac{\boldsymbol{d\tilde{\xi}_{f_j}}}{\boldsymbol{d\tilde{\varepsilon}_j}}\boldsymbol{d\tilde{\varepsilon}_j}\boldsymbol{I}\tilde{\boldsymbol{\varepsilon}}_{\boldsymbol{j}}-\delta_{ij}\boldsymbol{D}_L(1-\tilde{\omega}_i)\boldsymbol{I}\boldsymbol{d\tilde{\varepsilon}_j}\\
&-\delta_{ij}\boldsymbol{D}_L\frac{d(1-\tilde{\omega}_i)}{d\tilde{\omega}_i}\frac{d\tilde{\omega}_i}{d\tilde{\xi}_i}\frac{\boldsymbol{d\tilde{\xi}_i}}{\boldsymbol{d\tilde{\varepsilon}_i}}\boldsymbol{I}\boldsymbol{d\tilde{\varepsilon}_j}\tilde{\boldsymbol{\varepsilon}}_{\boldsymbol{i}}-\delta_{ij}\boldsymbol{D}_{Lf}\tilde{\omega}_i(1-\tilde{\omega}_{f_i})\boldsymbol{I}\boldsymbol{d\tilde{\varepsilon}_j}\\
&-\delta_{ij}\boldsymbol{D}_{Lf}\frac{d\tilde{\omega}_i}{d\tilde{\xi}_i}\frac{\boldsymbol{d\tilde{\xi}_i}}{\boldsymbol{d\tilde{\varepsilon}_i}}\boldsymbol{d\tilde{\varepsilon}_j}(1-\tilde{\omega}_{f_i})\boldsymbol{I}\tilde{\boldsymbol{\varepsilon}}_i-\delta_{ij}\boldsymbol{D}_{Lf}\tilde{\omega}_i\frac{d(1-\tilde{\omega}_{f_i})}{d\tilde{\omega}_{f_i}}\frac{d\tilde{\omega}_{f_i}}{d\tilde{\xi}_{f_i}}\frac{\boldsymbol{d\tilde{\xi}_i}}{\boldsymbol{d\tilde{\varepsilon}_i}}\boldsymbol{d\tilde{\varepsilon}_j}\boldsymbol{I}\tilde{\boldsymbol{\varepsilon}}_{\boldsymbol{i}}
\end{aligned}
\tag{A.2}
$$

The scalar terms $\frac{\boldsymbol{d\xi}}{\boldsymbol{d\tilde{\varepsilon}}}\boldsymbol{d\tilde{\varepsilon}}$ in Equation A.2 can be re-arranged to give an equation where $\boldsymbol{d\tilde{\varepsilon}}$ can be removed from the RHS:

$$
\begin{aligned}
\boldsymbol{d\Psi}_i = &-\boldsymbol{N}_i\boldsymbol{D}_{mcf}\boldsymbol{N}_j^T\left(\boldsymbol{I}-(1-\tilde{\omega}_j)\boldsymbol{I}-\boldsymbol{C}_L\boldsymbol{D}_{Lf}\tilde{\omega}_j(1-\tilde{\omega}_{f_j})\boldsymbol{I}\right)\boldsymbol{d\tilde{\varepsilon}_j}\\
&+\boldsymbol{N}_i\boldsymbol{D}_{mcf}\boldsymbol{N}_j^T\frac{d(1-\tilde{\omega}_j)}{d\tilde{\omega}_j}\frac{d\tilde{\omega}_j}{d\tilde{\xi}_j}\boldsymbol{I}\tilde{\boldsymbol{\varepsilon}}_{\boldsymbol{j}}\frac{\boldsymbol{d\tilde{\xi}_j}}{\boldsymbol{d\tilde{\varepsilon}_j}}\boldsymbol{d\tilde{\varepsilon}_j}+\boldsymbol{N}_i\boldsymbol{D}_{mcf}\boldsymbol{N}_j^T\boldsymbol{C}_L\boldsymbol{D}_{Lf}\frac{d\tilde{\omega}_j}{d\tilde{\xi}_j}(1-\tilde{\omega}_{f_j})\boldsymbol{I}\tilde{\boldsymbol{\varepsilon}}_j\frac{\boldsymbol{d\tilde{\xi}_j}}{\boldsymbol{d\tilde{\varepsilon}_j}}\boldsymbol{d\tilde{\varepsilon}_j}\\
&+\boldsymbol{N}_i\boldsymbol{D}_{mcf}\boldsymbol{N}_j^T\boldsymbol{C}_L\boldsymbol{D}_{Lf}\tilde{\omega}_j\frac{d(1-\tilde{\omega}_{f_j})}{d\tilde{\omega}_{f_j}}\frac{d\tilde{\omega}_{f_j}}{d\tilde{\xi}_{f_j}}\boldsymbol{I}\tilde{\boldsymbol{\varepsilon}}_{\boldsymbol{j}}\frac{\boldsymbol{d\tilde{\xi}_j}}{\boldsymbol{d\tilde{\varepsilon}_j}}\boldsymbol{d\tilde{\varepsilon}_j}\\
&-\delta_{ij}\boldsymbol{D}_L(1-\tilde{\omega}_i)\boldsymbol{I}\boldsymbol{d\tilde{\varepsilon}_j}-\delta_{ij}\boldsymbol{D}_L\frac{d(1-\tilde{\omega}_i)}{d\tilde{\omega}_i}\frac{d\tilde{\omega}_i}{d\tilde{\xi}_i}\boldsymbol{I}\tilde{\boldsymbol{\varepsilon}}_{\boldsymbol{i}}\frac{\boldsymbol{d\tilde{\xi}_i}}{\boldsymbol{d\tilde{\varepsilon}_i}}\boldsymbol{d\tilde{\varepsilon}_j}-\delta_{ij}\boldsymbol{D}_{Lf}\tilde{\omega}_i(1-\tilde{\omega}_{f_i})\boldsymbol{I}\boldsymbol{d\tilde{\varepsilon}_j}\\
&-\delta_{ij}\boldsymbol{D}_{Lf}\frac{d\tilde{\omega}_i}{d\tilde{\xi}_i}(1-\tilde{\omega}_{f_i})\boldsymbol{I}\tilde{\boldsymbol{\varepsilon}}_i\frac{\boldsymbol{d\tilde{\xi}_i}}{\boldsymbol{d\tilde{\varepsilon}_i}}\boldsymbol{d\tilde{\varepsilon}_j}-\delta_{ij}\boldsymbol{D}_{Lf}\tilde{\omega}_i\frac{d(1-\tilde{\omega}_{f_i})}{d\tilde{\omega}_{f_i}}\frac{d\tilde{\omega}_{f_i}}{d\tilde{\xi}_{f_i}}\boldsymbol{I}\tilde{\boldsymbol{\varepsilon}}_i\frac{\boldsymbol{d\tilde{\xi}_i}}{\boldsymbol{d\tilde{\varepsilon}_i}}\boldsymbol{d\tilde{\varepsilon}_j}
\end{aligned}
\tag{A.3}
$$

Finally, the terms of the matrix of derivates $\boldsymbol{B_E}$ 5.25 can be calculated via following:

$$\frac{\boldsymbol{d\Psi_i}}{\boldsymbol{d\tilde{\varepsilon}_j}} = -\boldsymbol{N}_i\boldsymbol{D}_{mcf}\boldsymbol{N}_j^T\left(\boldsymbol{I} - (1-\tilde{\omega}_j)\boldsymbol{I} - \boldsymbol{C}_L\boldsymbol{D}_{Lf}\tilde{\omega}_j(1-\tilde{\omega}_{f_j})\boldsymbol{I}\right)$$
$$+\boldsymbol{N}_i\boldsymbol{D}_{mcf}\boldsymbol{N}_j^T\frac{d(1-\tilde{\omega}_j)}{d\tilde{\omega}_j}\frac{d\tilde{\omega}_j}{d\tilde{\xi}_j}\boldsymbol{I}\tilde{\boldsymbol{\varepsilon}}_{\boldsymbol{j}}\frac{\boldsymbol{d\tilde{\xi}_j}}{\boldsymbol{d\tilde{\varepsilon}_j}} + \boldsymbol{N}_i\boldsymbol{D}_{mcf}\boldsymbol{N}_j^T\boldsymbol{C}_L\boldsymbol{D}_{Lf}\frac{d\tilde{\omega}_j}{d\tilde{\xi}_j}(1-\tilde{\omega}_{f_j})\boldsymbol{I}\tilde{\boldsymbol{\varepsilon}}_j\frac{\boldsymbol{d\tilde{\xi}_j}}{\boldsymbol{d\tilde{\varepsilon}_j}}$$
$$+\boldsymbol{N}_i\boldsymbol{D}_{mcf}\boldsymbol{N}_j^T\boldsymbol{C}_L\boldsymbol{D}_{Lf}\tilde{\omega}_j\frac{d(1-\tilde{\omega}_{f_j})}{d\tilde{\omega}_{f_j}}\frac{d\tilde{\omega}_{f_j}}{d\tilde{\xi}_{f_j}}\boldsymbol{I}\tilde{\boldsymbol{\varepsilon}}_{\boldsymbol{j}}\frac{\boldsymbol{d\tilde{\xi}_j}}{\boldsymbol{d\tilde{\varepsilon}_j}}$$
$$-\delta_{ij}\boldsymbol{D}_L(1-\tilde{\omega}_i)\boldsymbol{I} - \delta_{ij}\boldsymbol{D}_L\frac{d(1-\tilde{\omega}_i)}{d\tilde{\omega}_i}\frac{d\tilde{\omega}_i}{d\tilde{\xi}_i}\boldsymbol{I}\tilde{\boldsymbol{\varepsilon}}_{\boldsymbol{i}}\frac{\boldsymbol{d\tilde{\xi}_i}}{\boldsymbol{d\tilde{\varepsilon}_i}} - \delta_{ij}\boldsymbol{D}_{Lf}\tilde{\omega}_i(1-\tilde{\omega}_{f_i})\boldsymbol{I}$$
$$-\delta_{ij}\boldsymbol{D}_{Lf}\frac{d\tilde{\omega}_i}{d\tilde{\xi}_i}(1-\tilde{\omega}_{f_i})\boldsymbol{I}\tilde{\boldsymbol{\varepsilon}}_i\frac{\boldsymbol{d\tilde{\xi}_i}}{\boldsymbol{d\tilde{\varepsilon}_i}} - \delta_{ij}\boldsymbol{D}_{Lf}\tilde{\omega}_i\frac{d(1-\tilde{\omega}_{f_i})}{d\tilde{\omega}_{f_i}}\frac{d\tilde{\omega}_{f_i}}{d\tilde{\xi}_{f_i}}\boldsymbol{I}\tilde{\boldsymbol{\varepsilon}}_i\frac{\boldsymbol{d\tilde{\xi}_i}}{\boldsymbol{d\tilde{\varepsilon}_i}} \tag{A.4}$$

Appendix B

Summarised proof of the normal from the direction of the major principal stress

The local Hoek-Brown yield surface is given by B.1 and the normal to the yield surface is given by B.2.

$$F = \left(\frac{\tau}{r_u}\right)^{3/2} + \sigma_n - f_t = 0 \tag{B.1}$$

$$F_{normal} = \frac{dF}{d\sigma_n} + \frac{dF}{d\tau} \tag{B.2}$$

The terms in B.2 are given by:

$$\frac{dF}{d\sigma_n} = 1 \tag{B.3}$$

$$\frac{dF}{d\tau} = \frac{3}{2r_u^{3/2}}(Rsin(2\alpha))^{1/2} \tag{B.4}$$

Next, the derivative components are normalised and algebraic manipulation is carried out on B.2 giving:

$$\frac{3}{2r_u^{3/2}}(Rsin(2\alpha))^{1/2} - \frac{sin(2\alpha)}{cos(2\alpha)} = 0 \tag{B.5}$$

Further algebraic manipulation are performed giving:

$$\frac{9}{4{r_u}^3}R(1 - sin(2\alpha)^2) - sin(2\alpha) = 0 \tag{B.6}$$

The above can be re-arranged as a quadratic formula and then solved for the normal from the direction of the major principal stress:

$$\sin(2\alpha) = \frac{-2{r_f}^3}{9R} + \sqrt{\left(\frac{2{r_f}^3}{9R}\right) + 1} \tag{B.7}$$

Appendix C

Stress recovery computations for the micromechanical plastic-damage constitutive model

Conditions

For every crack-plane i , stresses must satisfy the local yield criterion C.1, the static constraint C.2, the plastic strain error condition C.3 and the directional plastic parameter error condition C.5. Also, stresses must satisfy the isotropic plastic parameter error condition C.4. The conditions are shown below:

$$F_i = F(\boldsymbol{s_{D_i}}, \kappa_I, \kappa_{D_i}) = 0 \tag{C.1}$$

$$\boldsymbol{\psi}_i = \boldsymbol{N}_i\boldsymbol{\sigma} - [\boldsymbol{D_L}(1-\omega_i)\boldsymbol{I}\tilde{\boldsymbol{\varepsilon}}_{\boldsymbol{i}} + \boldsymbol{D_L}\alpha_i\omega_i\boldsymbol{I}(\tilde{\boldsymbol{\varepsilon}}_{\boldsymbol{i}} - \boldsymbol{e_{p_i}})] = \boldsymbol{0} \tag{C.2}$$

$$\boldsymbol{R}_{\boldsymbol{\varepsilon}_i} = -\boldsymbol{\Delta e_{p_i}} + \frac{\partial G}{\partial \boldsymbol{s_{D_i}}}\Delta\lambda_i = \boldsymbol{0} \tag{C.3}$$

$$R_I = -\Delta\kappa_I + \sum_{j=1}^{n_{tot}} \left(\frac{1-\beta_j}{\chi_j}\right) \sqrt{\frac{\partial G}{\partial \boldsymbol{s_{D_j}}}^T \frac{\partial G}{\partial \boldsymbol{s_{D_j}}}}\Delta\lambda_j = 0 \tag{C.4}$$

$$R_{D_i} = -\Delta\kappa_{D_i} + \beta_i \sqrt{\frac{\partial G}{\partial \boldsymbol{s_{D_i}}}^T \frac{\partial G}{\partial \boldsymbol{s_{D_i}}}}\Delta\lambda_i = 0 \tag{C.5}$$

Coupled equations

First expand Equation C.4 such that $R_I + \delta R_I = 0$:

$$\delta\kappa_I = a_k \left(R_I + \sum_{w=1}^{n_{active}} \boldsymbol{K_{s_w}} \delta \boldsymbol{s_{D_w}} + \sum_{w=1}^{n_{active}} c_{k_w} \delta\lambda_w \right) \tag{C.6}$$

where

$$a_k = \left[1 - \sum_{w=1}^{n_{active}} \left(\frac{1-\beta_w}{\chi_w} \right) \frac{\partial}{\partial \kappa_I} \left(\sqrt{\frac{\partial G}{\partial \boldsymbol{s_{D_w}}}^T \frac{\partial G}{\partial \boldsymbol{s_{D_w}}}} \right) \Delta\lambda_w \right]^{-1} \tag{C.7}$$

$$\boldsymbol{K_{s_w}} = \sqrt{\frac{\partial G}{\partial \boldsymbol{s_{D_w}}}^T \frac{\partial G}{\partial \boldsymbol{s_{D_w}}}} \Delta\lambda_w \frac{\partial}{\partial \boldsymbol{s_{D_w}}} \left(\frac{1-\beta_w}{\chi_w} \right) + \left(\frac{1-\beta_w}{\chi_w} \right) \Delta\lambda_w \frac{\partial}{\partial \boldsymbol{s_{D_w}}} \left(\sqrt{\frac{\partial G}{\partial \boldsymbol{s_{D_w}}}^T \frac{\partial G}{\partial \boldsymbol{s_{D_w}}}} \right) \tag{C.8}$$

$$c_{k_w} = \left(\frac{1-\beta_w}{\chi_w} \right) \sqrt{\frac{\partial G}{\partial \boldsymbol{s_{D_w}}}^T \frac{\partial G}{\partial \boldsymbol{s_{D_w}}}} \tag{C.9}$$

Similarly, expand Equation C.5 such that $R_D + \delta R_D = 0$ and expand Equation C.3 such that $R_\varepsilon + \delta R_\varepsilon = 0$:

$$\delta\kappa_{D_j} = R_{DI_j} + \sum_{w=1}^{n_{active}} \boldsymbol{e_{k_{j,w}}} \delta\lambda_w + \sum_{w=1}^{n_{active}} \boldsymbol{K_{3s_{j,w}}} \delta \boldsymbol{s_{D_w}} \tag{C.10}$$

$$\delta \boldsymbol{e_{p_j}} = \boldsymbol{R_{\varepsilon I_j}} + \sum_{w=1}^{n_{active}} \boldsymbol{P_{1_{j,w}}} \delta\lambda_w + \sum_{w=1}^{n_{active}} \boldsymbol{P_{2_{j,w}}} \delta \boldsymbol{s_{D_w}} \tag{C.11}$$

where

$$R_{DI_j} = R_{D_j} + d_{k_j} a_k R_I \tag{C.12}$$

$$\boldsymbol{R_{\varepsilon I_j}} = \boldsymbol{R_{\varepsilon_j}} + \frac{\partial}{\partial \kappa_I} \left(\frac{\partial G}{\partial \boldsymbol{s_{D_j}}} \right) \Delta\lambda_j a_k R_I \tag{C.13}$$

$$e_{k_{j,w}} = \delta_{j,w} b_{k_j} + d_{k_j} a_k c_{k_w} \tag{C.14}$$

$$K_{3\sigma_{j,w}} = \delta_{j,w} K_{2\sigma_j} + d_{k_j} a_k K_{\sigma_w} \tag{C.15}$$

$$\boldsymbol{P_{1_{J,W}}} = \delta_{j,w}\frac{\partial G}{\partial \boldsymbol{s_{D_j}}} + \frac{\partial}{\partial \kappa_I}\left(\frac{\partial G}{\partial \boldsymbol{s_{D_j}}}\right)\Delta\lambda_j a_k c_{k_w} \tag{C.16}$$

$$\boldsymbol{P_{2_{j,w}}} = \delta_{j,w}\frac{\partial}{\partial \boldsymbol{s_{D_j}}}\left(\frac{\partial G}{\partial \boldsymbol{s_{D_j}}}\right)\Delta\lambda_j + \frac{\partial}{\partial \kappa_I}\left(\frac{\partial G}{\partial \boldsymbol{s_{D_j}}}\right)\Delta\lambda_j a_k \boldsymbol{K_{\sigma_w}} \tag{C.17}$$

and

$$b_{k_j} = \beta_j\sqrt{\frac{\partial G}{\partial \boldsymbol{s_{D_j}}}^T\frac{\partial G}{\partial \boldsymbol{s_{D_j}}}} \tag{C.18}$$

$$d_{k_j} = \beta_j\Delta\lambda_j\frac{\partial}{\partial \kappa_I}\left(\sqrt{\frac{\partial G}{\partial \boldsymbol{s_{D_w}}}^T\frac{\partial G}{\partial \boldsymbol{s_{D_w}}}}\right) \tag{C.19}$$

$$K_{2\sigma_j} = \sqrt{\frac{\partial G}{\partial \boldsymbol{s_{D_j}}}^T\frac{\partial G}{\partial \boldsymbol{\sigma_{D_j}}}}\Delta\lambda_j\frac{\partial \beta_j}{\partial \boldsymbol{s_{D_j}}} + \beta_j\Delta\lambda_j\frac{\partial}{\partial \boldsymbol{s_{D_j}}}\left(\sqrt{\frac{\partial G}{\partial \boldsymbol{s_{D_j}}}^T\frac{\partial G}{\partial \boldsymbol{s_{D_j}}}}\right) \tag{C.20}$$

The yield function consistency condition may be written as:

$$F_j + \frac{\partial F_j}{\partial \boldsymbol{s_{D_j}}}^T\delta\boldsymbol{s_{D_j}} + \frac{\partial F_j}{\partial \kappa_I}\delta\kappa_I + \frac{\partial F_j}{\partial \kappa_{D_j}}\delta\kappa_{D_j} = 0 \tag{C.21}$$

Substituting for $\delta\kappa_I$ from Equation C.6 and $\delta\kappa_D$ from Equation C.10 in the yield function consistency condition gives:

$$F_j + R_{ID2_j} + \sum_{w=1}^{n_{active}} \boldsymbol{f_{k_{j,w}}}\delta\boldsymbol{s_{D_w}} + \sum_{w=1}^{n_{active}} h_{k_{j,w}}\delta\lambda_w = 0 \tag{C.22}$$

where

$$R_{ID2_j} = \frac{\partial F_j}{\partial \kappa_I}a_k R_I + \frac{\partial F_j}{\partial \kappa_{D_J}}R_{DI_j} \tag{C.23}$$

$$f_{k_{j,w}} = \delta_{j,w}\frac{\partial F_j}{\partial \boldsymbol{s_{D_j}}}^T + \frac{\partial F_j}{\partial \kappa_I}a_k K_{\sigma_w} + \frac{\partial F_j}{\partial \kappa_{D_j}}K_{3\sigma_{j,w}} \tag{C.24}$$

$$h_{k_{j,w}} = \frac{\partial F_j}{\partial \kappa_I}a_k c_{k_w} + \frac{\partial F_j}{\partial \kappa_{D_j}}e_{k_{j,w}} \tag{C.25}$$

Expanding the static constraint C.2 such that $\boldsymbol{\psi} + \boldsymbol{\delta\psi} = 0$ for cracks that are

plastically active gives:

$$\boldsymbol{\psi_j} + \boldsymbol{N_j}\delta\boldsymbol{\sigma} + \boldsymbol{Z_{1_j}}\delta\boldsymbol{e_{p_j}} - \boldsymbol{Z_{2_j}}\delta\tilde{\boldsymbol{\varepsilon}}_{\boldsymbol{j}} = \mathbf{0} \tag{C.26}$$

and, noting that $\delta\boldsymbol{e_p}$ is $\mathbf{0}$ when a crack-plane is not plastically active, the same expansion of the static constraint for cracks that are not plastically active gives:

$$\psi_j + \boldsymbol{N_j}\delta\boldsymbol{\sigma} - \boldsymbol{Z_{2_j}}\delta\tilde{\boldsymbol{\varepsilon}}_{\boldsymbol{j}} = \mathbf{0} \tag{C.27}$$

where:

$$\boldsymbol{Z_{1_j}} = \boldsymbol{D_L}\boldsymbol{I}\alpha_j\omega_j \tag{C.28}$$

$$\boldsymbol{Z_{2_j}} = \boldsymbol{D_L}\boldsymbol{I}\tilde{\boldsymbol{\varepsilon}}_{\boldsymbol{j}}\frac{\partial}{\partial\tilde{\boldsymbol{\varepsilon}}_{\boldsymbol{j}}}(1-\omega_j) + \boldsymbol{D_L}\boldsymbol{I}(1-\omega_j) + \boldsymbol{D_L}\boldsymbol{I}\left(\tilde{\boldsymbol{\varepsilon}}_{\boldsymbol{j}} - \boldsymbol{e_{p_j}}\right)\frac{\partial}{\partial\tilde{\boldsymbol{\varepsilon}}_{\boldsymbol{j}}}(\alpha_j\omega_j) + \boldsymbol{D_L}\boldsymbol{I}\alpha_j\omega_j \tag{C.29}$$

The iterative change in the damaged stress component for cracks have active plasticity is:

$$\delta\boldsymbol{s_{D_j}} = \boldsymbol{D_L}\left(\delta\tilde{\boldsymbol{\varepsilon}}_{\boldsymbol{j}} - \delta\boldsymbol{e_{p_j}}\right) \tag{C.30}$$

Substituting for $\delta\boldsymbol{e_p}$ from Equation C.11 in Equation C.30 gives:

$$\begin{bmatrix} \delta\boldsymbol{s_{D_1}} \\ \vdots \\ \delta\boldsymbol{s_{D_{n_{active}}}} \end{bmatrix} = \boldsymbol{M_m^{-1}}\left(\begin{bmatrix} \boldsymbol{D_L} & \mathbf{0} & \mathbf{0} \\ \mathbf{0} & \ddots & \mathbf{0} \\ \mathbf{0} & \mathbf{0} & \boldsymbol{D_L} \end{bmatrix}\begin{bmatrix} \delta\tilde{\boldsymbol{\varepsilon}}_{\mathbf{1}} \\ \vdots \\ \delta\tilde{\boldsymbol{\varepsilon}}_{\boldsymbol{n_{active}}} \end{bmatrix} - \begin{bmatrix} \boldsymbol{D_L} & \mathbf{0} & \mathbf{0} \\ \mathbf{0} & \ddots & \mathbf{0} \\ \mathbf{0} & \mathbf{0} & \boldsymbol{D_L} \end{bmatrix}\begin{bmatrix} \boldsymbol{R_{\varepsilon\mathbf{I}_1}} \\ \vdots \\ \boldsymbol{R_{\varepsilon\mathbf{I}_{n_{active}}}} \end{bmatrix} - \begin{bmatrix} \boldsymbol{D_L}\boldsymbol{P_{1_{1,1}}} & \cdots & \boldsymbol{D_L}\boldsymbol{P_{1_{1,n_{active}}}} \\ \vdots & \ddots & \vdots \\ \boldsymbol{D_L}\boldsymbol{P_{1_{n_{active},1}}} & \cdots & \boldsymbol{D_L}\boldsymbol{P_{1_{n_{active},n_{active}}}} \end{bmatrix}\begin{bmatrix} \delta\lambda_1 \\ \vdots \\ \delta\lambda_{n_{active}} \end{bmatrix}\right) \tag{C.31}$$

where

$$\boldsymbol{M_m} = \boldsymbol{I} + \begin{bmatrix} \boldsymbol{D_L P_{2_{1,1}}} & \cdots & \boldsymbol{D_L P_{2_{1,n_{active}}}} \\ \vdots & \ddots & \vdots \\ \boldsymbol{D_L P_{2_{n_{active},1}}} & \cdots & \boldsymbol{D_L P_{2_{n_{active},n_{active}}}} \end{bmatrix} \tag{C.32}$$

Substituting for $\delta \boldsymbol{s_D}$ from Equation C.31 in Equation C.32 gives the first coupled equation:

$$\boldsymbol{F_\lambda} + \boldsymbol{M_\lambda} \delta \boldsymbol{\lambda} + \boldsymbol{b_\lambda} \begin{bmatrix} \delta \tilde{\boldsymbol{\varepsilon}}_{\mathbf{1}} \\ \vdots \\ \delta \tilde{\boldsymbol{\varepsilon}}_{\boldsymbol{n_{active}}} \end{bmatrix} = \mathbf{0} \tag{C.33}$$

where

$$\boldsymbol{F_\lambda} = \begin{bmatrix} F_1 \\ \vdots \\ F_{n_{active}} \end{bmatrix} + \begin{bmatrix} 1 & 0 & 0 \\ 0 & \ddots & 0 \\ 0 & 0 & 1 \end{bmatrix} \begin{bmatrix} R_{ID2_1} \\ \vdots \\ R_{ID2_{n_{active}}} \end{bmatrix}$$

$$- \begin{bmatrix} f_{k_{1,1}} & \cdots & f_{k_{1,n_{active}}} \\ \vdots & \ddots & \vdots \\ f_{k_{n_{active},1}} & \cdots & f_{k_{n_{active},n_{active}}} \end{bmatrix} \boldsymbol{M_m}^{-1} \begin{bmatrix} \boldsymbol{D_L} & 0 & 0 \\ 0 & \ddots & 0 \\ 0 & 0 & \boldsymbol{D_L} \end{bmatrix} \begin{bmatrix} \boldsymbol{R_{\varepsilon I_1}} \\ \vdots \\ \boldsymbol{R_{\varepsilon I_{n_{active}}}} \end{bmatrix} \tag{C.34}$$

$$\boldsymbol{M_\lambda} = \begin{bmatrix} h_{k_{1,1}} & \cdots & h_{k_{1,n_{active}}} \\ \vdots & \ddots & \vdots \\ h_{k_{n_{active},1}} & \cdots & h_{k_{n_{active},n_{active}}} \end{bmatrix}$$

$$- \begin{bmatrix} f_{k_{1,1}} & \cdots & f_{k_{1,n_{active}}} \\ \vdots & \ddots & \vdots \\ f_{k_{n_{active},1}} & \cdots & f_{k_{n_{active},n_{active}}} \end{bmatrix} \boldsymbol{M_m}^{-1} \begin{bmatrix} \boldsymbol{D_L P_{1_{1,1}}} & \cdots & \boldsymbol{D_L P_{1_{1,n_{active}}}} \\ \vdots & \ddots & \vdots \\ \boldsymbol{D_L P_{1_{n_{active},1}}} & \cdots & \boldsymbol{D_L P_{1_{n_{active},n_{active}}}} \end{bmatrix} \tag{C.35}$$

$$\boldsymbol{b_\lambda} = \begin{bmatrix} f_{k_{1,1}} & \cdots & f_{k_{1,n_{active}}} \\ \vdots & \ddots & \vdots \\ f_{k_{n_{active},1}} & \cdots & f_{k_{n_{active},n_{active}}} \end{bmatrix} \boldsymbol{M_m}^{-1} \begin{bmatrix} \boldsymbol{D_L} & 0 & 0 \\ 0 & \ddots & 0 \\ 0 & 0 & \boldsymbol{D_L} \end{bmatrix} \tag{C.36}$$

and $\delta\boldsymbol{\lambda} = \begin{bmatrix} \delta\lambda_1 \\ \vdots \\ \delta\lambda_{n_{active}} \end{bmatrix}$

To write the first of the two coupled equations in terms of the stacked crack-plane strains vector $\delta\tilde{\boldsymbol{\varepsilon}} = \begin{bmatrix} \delta\tilde{\boldsymbol{\varepsilon}}_{\mathbf{1}} \\ \vdots \\ \delta\tilde{\boldsymbol{\varepsilon}}_{\boldsymbol{n_{total}}} \end{bmatrix}$, zero values are added to $\boldsymbol{b_\lambda}$ to form the matrix $\boldsymbol{b_{\lambda 2}}$. The zero values are added such that $\begin{bmatrix} \boldsymbol{b_\lambda} & \mathbf{0} \end{bmatrix} \delta\tilde{\boldsymbol{\varepsilon}} = \boldsymbol{b_{\lambda 2}}\delta\tilde{\boldsymbol{\varepsilon}}$. Hence, the first coupled equation can be written as:

$$\boldsymbol{F_\lambda} + \boldsymbol{M_\lambda}\delta\boldsymbol{\lambda} + \boldsymbol{b_{\lambda 2}}\delta\tilde{\boldsymbol{\varepsilon}} = \mathbf{0} \tag{C.37}$$

The iterative change in the overall stress 6.15 is given by:

$$\boldsymbol{\delta\sigma} = \boldsymbol{D}\left(\boldsymbol{\varepsilon} - \sum_{i=1}^{n_{total}} \boldsymbol{N_{\varepsilon_i}}^T \left[\boldsymbol{I} - (1-\omega_i)\boldsymbol{I} - \alpha_i\omega_i\boldsymbol{I}\right]\tilde{\boldsymbol{\varepsilon}} + \boldsymbol{N_{\varepsilon_i}}^T \left[\alpha_i\omega_i\boldsymbol{I}\right]\boldsymbol{e_p}\right) \tag{C.38}$$

Substituting for $\boldsymbol{\delta e}$ C.11 and $\boldsymbol{\delta\sigma_D}$ from C.31 into Equation C.38 gives:

$$\delta\boldsymbol{\sigma} = \boldsymbol{M_{x1}} + \boldsymbol{M_{x2}}\delta\boldsymbol{\lambda} + \boldsymbol{M_{x3}}\delta\tilde{\boldsymbol{\varepsilon}} \tag{C.39}$$

where

$$\boldsymbol{M_{x1}} = \begin{bmatrix} \boldsymbol{Q_{2_1}} & \cdots & \boldsymbol{Q_{2_{n_{active}}}} \end{bmatrix} \begin{bmatrix} \boldsymbol{R_{\varepsilon \mathbf{I}_1}} \\ \vdots \\ \boldsymbol{R_{\varepsilon \mathbf{I}_{n_{active}}}} \end{bmatrix}$$

$$- \begin{bmatrix} \boldsymbol{Q_{2_1}} & \cdots & \boldsymbol{Q_{2_{n_{active}}}} \end{bmatrix} \begin{bmatrix} \boldsymbol{P_{2_{1,1}}} & \cdots & \boldsymbol{P_{2_{1,n_{active}}}} \\ \vdots & \ddots & \vdots \\ \boldsymbol{P_{2_{n_{active},1}}} & \cdots & \boldsymbol{P_{2_{n_{active},n_{active}}}} \end{bmatrix} \boldsymbol{M_m}^{-1} \cdot$$

$$\begin{bmatrix} \boldsymbol{D_L} & 0 & 0 \\ 0 & \ddots & 0 \\ 0 & 0 & \boldsymbol{D_L} \end{bmatrix} \begin{bmatrix} \boldsymbol{R_{\varepsilon \mathbf{I}_1}} \\ \vdots \\ \boldsymbol{R_{\varepsilon \mathbf{I}_{n_{active}}}} \end{bmatrix} \tag{C.40}$$

$$\boldsymbol{M_{x2}} = \left[\begin{array}{ccc} \boldsymbol{Q_{2_1}} & \cdots & \boldsymbol{Q_{2_{n_{active}}}} \end{array}\right] \left[\begin{array}{ccc} \boldsymbol{P_{1_{1,1}}} & \cdots & \boldsymbol{P_{1_{1,n_{active}}}} \\ \vdots & \ddots & \vdots \\ \boldsymbol{P_{1_{n_{active},1}}} & \cdots & \boldsymbol{P_{1_{n_{active},n_{active}}}} \end{array}\right]$$

$$- \left[\begin{array}{ccc} \boldsymbol{Q_{2_1}} & \cdots & \boldsymbol{Q_{2_{n_{active}}}} \end{array}\right] \left[\begin{array}{ccc} \boldsymbol{P_{2_{1,1}}} & \cdots & \boldsymbol{P_{2_{1,n_{active}}}} \\ \vdots & \ddots & \vdots \\ \boldsymbol{P_{2_{n_{active},1}}} & \cdots & \boldsymbol{P_{2_{n_{active},n_{active}}}} \end{array}\right] \boldsymbol{M_m}^{-1} \cdot$$

$$\left[\begin{array}{ccc} \boldsymbol{D_L P_{1_{1,1}}} & \cdots & \boldsymbol{D_L P_{1_{1,n_{active}}}} \\ \vdots & \ddots & \vdots \\ \boldsymbol{D_L P_{1_{n_{active},1}}} & \cdots & \boldsymbol{D_L P_{1_{n_{active},n_{active}}}} \end{array}\right] \tag{C.41}$$

$$\boldsymbol{M_{x3}} = \left[\begin{array}{ccc} \boldsymbol{Q_{1_1}} & \cdots & \boldsymbol{Q_{1_{n_{total}}}} \end{array}\right] + \left[\begin{array}{ccc} \boldsymbol{Q_{3_1}} & \cdots & \boldsymbol{Q_{3_{n_{total}}}} \end{array}\right]$$

$$+ \left[\begin{array}{ccc} \boldsymbol{Q_{2_1}} & \cdots & \boldsymbol{Q_{2_{n_{active}}}} \end{array}\right] \left[\begin{array}{ccc} \boldsymbol{P_{2_{1,1}}} & \cdots & \boldsymbol{P_{2_{1,n_{active}}}} \\ \vdots & \ddots & \vdots \\ \boldsymbol{P_{2_{n_{active},1}}} & \cdots & \boldsymbol{P_{2_{n_{active},n_{active}}}} \end{array}\right] \boldsymbol{M_m^{-1}} \cdot$$

$$\left[\begin{array}{cccc} \boldsymbol{D_L} & 0 & 0 & \boldsymbol{0} \\ 0 & \ddots & 0 & \boldsymbol{0} \\ 0 & 0 & \boldsymbol{D_L} & \boldsymbol{0} \end{array}\right] \tag{C.42}$$

where

$$\boldsymbol{Q_{1_r}} = -\boldsymbol{D}\left(\boldsymbol{N_{\varepsilon_r}}^T\left(\boldsymbol{I} - \boldsymbol{I}\left(1-\omega_r\right) - \boldsymbol{I}\alpha_r\omega_r\right) + \boldsymbol{N_{\varepsilon_r}}^T\left(-\boldsymbol{I}\tilde{\boldsymbol{\varepsilon}}_{\boldsymbol{r}}\frac{\partial}{\partial\tilde{\boldsymbol{\varepsilon}}_{\boldsymbol{r}}}\left(1-\omega_r\right) - \boldsymbol{I}\tilde{\boldsymbol{\varepsilon}}_{\boldsymbol{r}}\frac{\partial}{\partial\tilde{\boldsymbol{\varepsilon}}_{\boldsymbol{r}}}\left(\alpha_r\omega_r\right)\right)\right) \tag{C.43}$$

$$\boldsymbol{Q_{2_w}} = -\boldsymbol{D}\boldsymbol{N_{\varepsilon_w}}^{\boldsymbol{T}}\boldsymbol{I}\alpha_w\omega_w \tag{C.44}$$

$$\boldsymbol{Q_{3_w}} = -\boldsymbol{D}\boldsymbol{N_{\varepsilon_w}}^T\boldsymbol{I}\boldsymbol{e_{p_w}}\frac{\partial}{\partial\tilde{\boldsymbol{\varepsilon}}_{\boldsymbol{w}}}\left(\alpha_w\omega_w\right) \tag{C.45}$$

$$\boldsymbol{Q_{4_s}} = -\boldsymbol{D}\boldsymbol{N_{\varepsilon_s}}^T\boldsymbol{I}\boldsymbol{e_{p_s}}\frac{\partial}{\partial\tilde{\boldsymbol{\varepsilon}}_{\boldsymbol{s}}}\left(\alpha_s\omega_s\right) \tag{C.46}$$

Note that the $\mathbf{0}$ terms in Equation C.42 are inserted so that $\delta\boldsymbol{\sigma}$ can be written in terms of the stacked crack-plane strains vector (see $\boldsymbol{b_\lambda}$ and $\boldsymbol{b_{\lambda 2}}$).

For the second coupled equation, substituting for $\delta\boldsymbol{\sigma}$ from Equation C.39, $\delta\boldsymbol{e}$ from Equation C.11 and $\delta\boldsymbol{\sigma_D}$ from Equation C.31 into equations C.26 and C.27 gives:

$$\boldsymbol{\psi_E} + \boldsymbol{M_E}\delta\boldsymbol{\lambda} + \boldsymbol{b_E}\delta\tilde{\boldsymbol{\varepsilon}} = \mathbf{0} \tag{C.47}$$

where

$$\boldsymbol{\psi_E} = \begin{bmatrix} \boldsymbol{\psi_1} \\ \vdots \\ \boldsymbol{\psi}_{n_{total}} \end{bmatrix} + \begin{bmatrix} \boldsymbol{N_1} \\ \vdots \\ \boldsymbol{N}_{n_{total}} \end{bmatrix} \boldsymbol{M_{x1}} + \begin{bmatrix} \boldsymbol{Z}_{1_1} & \mathbf{0} & \mathbf{0} & \mathbf{0} \\ \mathbf{0} & \ddots & \mathbf{0} & \mathbf{0} \\ \mathbf{0} & \mathbf{0} & \boldsymbol{Z}_{1_{n_{active}}} & \mathbf{0} \\ \mathbf{0} & \mathbf{0} & \mathbf{0} & \mathbf{0} \end{bmatrix} \begin{bmatrix} \boldsymbol{R}_{\varepsilon I_1} \\ \vdots \\ \boldsymbol{R}_{\varepsilon I_{n_{active}}} \\ \mathbf{0} \end{bmatrix}$$

$$- \begin{bmatrix} \boldsymbol{Z}_{1_1} & \mathbf{0} & \mathbf{0} & \mathbf{0} \\ \mathbf{0} & \ddots & \mathbf{0} & \mathbf{0} \\ \mathbf{0} & \mathbf{0} & \boldsymbol{Z}_{1_{n_{active}}} & \mathbf{0} \\ \mathbf{0} & \mathbf{0} & \mathbf{0} & \mathbf{0} \end{bmatrix} \begin{bmatrix} \boldsymbol{P}_{2_{1,1}} & \cdots & \boldsymbol{P}_{2_{1,n_{active}}} \\ \vdots & \ddots & \vdots \\ \boldsymbol{P}_{2_{n_{active},1}} & \cdots & \boldsymbol{P}_{2_{n_{active},n_{active}}} \\ \mathbf{0} & \mathbf{0} & \mathbf{0} \end{bmatrix} \boldsymbol{M_m}^{-1} \cdot$$

$$\begin{bmatrix} \boldsymbol{D_L} & 0 & 0 \\ 0 & \ddots & 0 \\ 0 & 0 & \boldsymbol{D_L} \end{bmatrix} \begin{bmatrix} \boldsymbol{R}_{\varepsilon \mathbf{I}_1} \\ \vdots \\ \boldsymbol{R}_{\varepsilon \mathbf{I}_{n_{active}}} \end{bmatrix} \tag{C.48}$$

$$\boldsymbol{M_E} = \begin{bmatrix} \boldsymbol{N_1} \\ \vdots \\ \boldsymbol{N}_{n_{total}} \end{bmatrix} \boldsymbol{M_{x2}} + \begin{bmatrix} \boldsymbol{Z}_{1_1} & \mathbf{0} & \mathbf{0} & \mathbf{0} \\ \mathbf{0} & \ddots & \mathbf{0} & \mathbf{0} \\ \mathbf{0} & \mathbf{0} & \boldsymbol{Z}_{1_{n_{active}}} & \mathbf{0} \\ \mathbf{0} & \mathbf{0} & \mathbf{0} & \mathbf{0} \end{bmatrix} \begin{bmatrix} \boldsymbol{P}_{1_{1,1}} & \cdots & \boldsymbol{P}_{1_{1,n_{active}}} \\ \vdots & \ddots & \vdots \\ \boldsymbol{P}_{1_{n_{active},1}} & \cdots & \boldsymbol{P}_{1_{n_{active},n_{active}}} \\ \mathbf{0} & \mathbf{0} & \mathbf{0} \end{bmatrix}$$

$$- \begin{bmatrix} \boldsymbol{Z}_{1_1} & \mathbf{0} & \mathbf{0} & \mathbf{0} \\ \mathbf{0} & \ddots & \mathbf{0} & \mathbf{0} \\ \mathbf{0} & \mathbf{0} & \boldsymbol{Z}_{1_{n_{active}}} & \mathbf{0} \\ \mathbf{0} & \mathbf{0} & \mathbf{0} & \mathbf{0} \end{bmatrix} \begin{bmatrix} \boldsymbol{P}_{2_{1,1}} & \cdots & \boldsymbol{P}_{2_{1,n_{active}}} \\ \vdots & \ddots & \vdots \\ \boldsymbol{P}_{2_{n_{active},1}} & \cdots & \boldsymbol{P}_{2_{n_{active},n_{active}}} \\ \mathbf{0} & \mathbf{0} & \mathbf{0} \end{bmatrix} \boldsymbol{M_m}^{-1} \cdot$$

$$\begin{bmatrix} \boldsymbol{D_L}\boldsymbol{P}_{1_{1,1}} & \cdots & \boldsymbol{D_L}\boldsymbol{P}_{1_{1,n_{active}}} \\ \vdots & \ddots & \vdots \\ \boldsymbol{D_L}\boldsymbol{P}_{1_{n_{active},1}} & \cdots & \boldsymbol{D_L}\boldsymbol{P}_{1_{n_{active},n_{active}}} \end{bmatrix} \tag{C.49}$$

$$\boldsymbol{b_E} = \begin{bmatrix} \boldsymbol{N_1} \\ \vdots \\ \boldsymbol{N_{n_{total}}} \end{bmatrix} \boldsymbol{M_{x3}} - \begin{bmatrix} \boldsymbol{Z_{1_1}} & \boldsymbol{0} & \boldsymbol{0} & \boldsymbol{0} \\ \boldsymbol{0} & \ddots & \boldsymbol{0} & \boldsymbol{0} \\ \boldsymbol{0} & \boldsymbol{0} & \boldsymbol{Z_{1_{n_{active}}}} & \boldsymbol{0} \\ \boldsymbol{0} & \boldsymbol{0} & \boldsymbol{0} & \boldsymbol{0} \end{bmatrix}$$

$$+ \begin{bmatrix} \boldsymbol{Z_{1_1}} & \boldsymbol{0} & \boldsymbol{0} & \boldsymbol{0} \\ \boldsymbol{0} & \ddots & \boldsymbol{0} & \boldsymbol{0} \\ \boldsymbol{0} & \boldsymbol{0} & \boldsymbol{Z_{1_{n_{active}}}} & \boldsymbol{0} \\ \boldsymbol{0} & \boldsymbol{0} & \boldsymbol{0} & \boldsymbol{0} \end{bmatrix} \begin{bmatrix} \boldsymbol{P_{2_{1,1}}} & \cdots & \boldsymbol{P_{2_{1,n_{active}}}} \\ \vdots & \ddots & \vdots \\ \boldsymbol{P_{2_{n_{active},1}}} & \cdots & \boldsymbol{P_{2_{n_{active},n_{active}}}} \\ \boldsymbol{0} & \boldsymbol{0} & \boldsymbol{0} \end{bmatrix} \boldsymbol{M_m^{-1}} \cdot$$

$$\begin{bmatrix} \boldsymbol{D_L} & \boldsymbol{0} & \boldsymbol{0} & \boldsymbol{0} \\ \boldsymbol{0} & \ddots & \boldsymbol{0} & \boldsymbol{0} \\ \boldsymbol{0} & \boldsymbol{0} & \boldsymbol{D_L} & \boldsymbol{0} \end{bmatrix} \tag{C.50}$$

Finally, the coupled equations C.37 and C.47 can be arranged as:

$$\begin{bmatrix} \boldsymbol{\psi_E} \\ \boldsymbol{F_\lambda} \end{bmatrix} = \begin{bmatrix} \boldsymbol{M_E} & \boldsymbol{b_E} \\ \boldsymbol{M_\lambda} & \boldsymbol{b_{\lambda 2}} \end{bmatrix} \begin{bmatrix} \delta\boldsymbol{\lambda} \\ \delta\tilde{\boldsymbol{\varepsilon}} \end{bmatrix} \tag{C.51}$$

or in compact matrix form:

$$\boldsymbol{\Gamma} = \boldsymbol{\Xi}\delta\boldsymbol{\Lambda} \tag{C.52}$$

where $\boldsymbol{\Gamma} = \begin{bmatrix} \boldsymbol{\psi_E} \\ \boldsymbol{F_\lambda} \end{bmatrix}$, $\boldsymbol{\Xi} = \begin{bmatrix} \boldsymbol{M_E} & \boldsymbol{b_E} \\ \boldsymbol{M_\lambda} & \boldsymbol{b_{\lambda 2}} \end{bmatrix}$ and $\delta\boldsymbol{\Lambda} = \begin{bmatrix} \delta\boldsymbol{\lambda} \\ \delta\tilde{\boldsymbol{\varepsilon}} \end{bmatrix}$

Appendix D

Consistent tangent derivation for the micromechanical plastic-damage constitutive model

The differential crack-plane stress can be written as:

$$\delta \boldsymbol{s_j} = -\boldsymbol{Z_{1_j}} \delta \boldsymbol{e_{p_j}} + \boldsymbol{Z_{2_j}} \delta \tilde{\boldsymbol{\varepsilon}}_{\boldsymbol{j}} \tag{D.1}$$

where $\delta \boldsymbol{s} = \begin{bmatrix} \delta \boldsymbol{s_1} \\ \vdots \\ \delta \boldsymbol{s_{n_{total}}} \end{bmatrix}$. Note that $\mathbf{0}$ terms have been added to $\boldsymbol{Z_1}$ such that the multiplication of $\boldsymbol{Z_1} \delta \boldsymbol{e_p}$ is possible (i.e. ensuring that $\delta \boldsymbol{e_p} = \mathbf{0}$ for non plastically active cracks).

Similarly, by adding $\mathbf{0}$ terms, the differential plastic strain can be written using Equation C.11 as:

$$\begin{bmatrix} \delta \boldsymbol{e_1} \\ \vdots \\ \delta \boldsymbol{e_{n_{active}}} \\ \delta \boldsymbol{e_{n_{active}+1}} \\ \vdots \\ \boldsymbol{\delta e_{n_{total}}} \end{bmatrix} = \begin{bmatrix} \boldsymbol{P_{1_{1,1}}} & \cdots & \boldsymbol{P_{1_{1,n_{active}}}} \\ \vdots & \ddots & \vdots \\ \boldsymbol{P_{1_{n_{active},1}}} & \cdots & \boldsymbol{P_{1_{n_{active},n_{active}}}} \\ \mathbf{0} & \mathbf{0} & \mathbf{0} \\ \vdots & \vdots & \vdots \\ \mathbf{0} & \mathbf{0} & \mathbf{0} \end{bmatrix} \begin{bmatrix} \delta \lambda_1 \\ \vdots \\ \delta \lambda_{1_{n_{active}}} \end{bmatrix}$$

$$+\begin{bmatrix} \boldsymbol{P}_{\mathbf{2}_{1,1}} & \cdots & \boldsymbol{P}_{\mathbf{2}_{1,n_{active}}} \\ \vdots & \ddots & \vdots \\ \boldsymbol{P}_{\mathbf{2}_{n_{active},1}} & \cdots & \boldsymbol{P}_{\mathbf{2}_{n_{active},n_{active}}} \\ \mathbf{0} & \mathbf{0} & \mathbf{0} \\ \vdots & \vdots & \vdots \\ \mathbf{0} & \mathbf{0} & \mathbf{0} \end{bmatrix} \begin{bmatrix} \delta \boldsymbol{s}_{\boldsymbol{D}_1} \\ \vdots \\ \delta \boldsymbol{s}_{\boldsymbol{D}_{n_{active}}} \end{bmatrix} \tag{D.2}$$

Substituting for $\delta \boldsymbol{s}_{\boldsymbol{D}}$ from Equation C.31 in Equation D.2 gives:

$$\delta \boldsymbol{e} = [\boldsymbol{A}_{\boldsymbol{m}}]\, \delta \boldsymbol{\lambda} + [\boldsymbol{B}_{\boldsymbol{m}}]\, \delta \tilde{\boldsymbol{\varepsilon}} \tag{D.3}$$

where

$$\boldsymbol{A}_{\boldsymbol{m}} = \begin{bmatrix} \boldsymbol{P}_{\mathbf{1}_{1,1}} & \cdots & \boldsymbol{P}_{\mathbf{1}_{1,n_{active}}} \\ \vdots & \ddots & \vdots \\ \boldsymbol{P}_{\mathbf{1}_{n_{active},1}} & \cdots & \boldsymbol{P}_{\mathbf{1}_{n_{active},n_{active}}} \\ \mathbf{0} & \mathbf{0} & \mathbf{0} \\ \vdots & \vdots & \vdots \\ \mathbf{0} & \mathbf{0} & \mathbf{0} \end{bmatrix}$$

$$-\begin{bmatrix} \boldsymbol{P}_{\mathbf{2}_{1,1}} & \cdots & \boldsymbol{P}_{\mathbf{2}_{1,n_{active}}} \\ \vdots & \ddots & \vdots \\ \boldsymbol{P}_{\mathbf{2}_{n_{active},1}} & \cdots & \boldsymbol{P}_{\mathbf{2}_{n_{active},n_{active}}} \\ \mathbf{0} & \mathbf{0} & \mathbf{0} \\ \vdots & \vdots & \vdots \\ \mathbf{0} & \mathbf{0} & \mathbf{0} \end{bmatrix} \boldsymbol{M}_{\boldsymbol{m}}^{-1} \begin{bmatrix} \boldsymbol{D}_{\boldsymbol{L}} \boldsymbol{P}_{\mathbf{1}_{1,1}} & \cdots & \boldsymbol{D}_{\boldsymbol{L}} \boldsymbol{P}_{\mathbf{1}_{1,n_{active}}} \\ \vdots & \ddots & \vdots \\ \boldsymbol{D}_{\boldsymbol{L}} \boldsymbol{P}_{\mathbf{1}_{n_{active},1}} & \cdots & \boldsymbol{D}_{\boldsymbol{L}} \boldsymbol{P}_{\mathbf{1}_{n_{active},n_{active}}} \end{bmatrix} \tag{D.4}$$

$$\boldsymbol{B}_{\boldsymbol{m}} = \begin{bmatrix} \boldsymbol{P}_{\mathbf{2}_{1,1}} & \cdots & \boldsymbol{P}_{\mathbf{2}_{1,n_{active}}} \\ \vdots & \ddots & \vdots \\ \boldsymbol{P}_{\mathbf{2}_{n_{active},1}} & \cdots & \boldsymbol{P}_{\mathbf{2}_{n_{active},n_{active}}} \\ \mathbf{0} & \mathbf{0} & \mathbf{0} \\ \vdots & \vdots & \vdots \\ \mathbf{0} & \mathbf{0} & \mathbf{0} \end{bmatrix} \boldsymbol{M}_{\boldsymbol{m}}^{-1} \begin{bmatrix} \boldsymbol{D}_{\boldsymbol{L}} & \mathbf{0} & \mathbf{0} & \mathbf{0} \\ \mathbf{0} & \ddots & \mathbf{0} & \mathbf{0} \\ \mathbf{0} & \mathbf{0} & \boldsymbol{D}_{\boldsymbol{L}} & \mathbf{0} \end{bmatrix} \tag{D.5}$$

and $\delta \boldsymbol{e} = \begin{bmatrix} \delta \boldsymbol{e_1} \\ \vdots \\ \delta \boldsymbol{e}_{n_{total}} \end{bmatrix}$

From Equation D.3, $\delta \boldsymbol{e}$ can be substituted into Equation D.1 giving:

$$\delta \boldsymbol{s} = [\boldsymbol{R_m}]\, \delta \boldsymbol{\lambda} + [\boldsymbol{S_m}]\, \delta \tilde{\boldsymbol{\varepsilon}} \tag{D.6}$$

where

$$\boldsymbol{R_m} = - \begin{bmatrix} \boldsymbol{Z}_{1_1} & \boldsymbol{0} & \boldsymbol{0} & \boldsymbol{0} \\ \boldsymbol{0} & \ddots & \boldsymbol{0} & \boldsymbol{0} \\ \boldsymbol{0} & \boldsymbol{0} & \boldsymbol{Z}_{1_{n_{active}}} & \boldsymbol{0} \\ \boldsymbol{0} & \boldsymbol{0} & \boldsymbol{0} & \boldsymbol{0} \end{bmatrix} [\boldsymbol{A_m}] \tag{D.7}$$

$$\boldsymbol{S_m} = \begin{bmatrix} \boldsymbol{Z}_{2_1} & \boldsymbol{0} & \boldsymbol{0} \\ \boldsymbol{0} & \ddots & \boldsymbol{0} \\ \boldsymbol{0} & \boldsymbol{0} & \boldsymbol{Z}_{2_{n_{total}}} \end{bmatrix} - \begin{bmatrix} \boldsymbol{Z}_{1_1} & \boldsymbol{0} & \boldsymbol{0} & \boldsymbol{0} \\ \boldsymbol{0} & \ddots & \boldsymbol{0} & \boldsymbol{0} \\ \boldsymbol{0} & \boldsymbol{0} & \boldsymbol{Z}_{1_{n_{active}}} & \boldsymbol{0} \\ \boldsymbol{0} & \boldsymbol{0} & \boldsymbol{0} & \boldsymbol{0} \end{bmatrix} [\boldsymbol{B_m}] \tag{D.8}$$

Subsequently, $\delta \tilde{\boldsymbol{\varepsilon}}$ can be found by:

$$\delta \tilde{\boldsymbol{\varepsilon}} = [\boldsymbol{S_m}]^{-1} \delta \boldsymbol{\sigma} - [\boldsymbol{S_m}]^{-1} [\boldsymbol{R_m}]\, \delta \boldsymbol{\lambda} \tag{D.9}$$

An expression for the inelastic crack-plane strain component can be derived by substituting $\delta \tilde{\boldsymbol{\varepsilon}}$ from above into Equation 6.13:

$$\delta \tilde{\boldsymbol{\varepsilon}} = [\boldsymbol{A_{2m}}]\, \delta \boldsymbol{s} + [\boldsymbol{B_{2m}}]\, \delta \boldsymbol{\lambda} \tag{D.10}$$

where

$$\boldsymbol{A_{2m}} = [\boldsymbol{S_m}]^{-1} - \boldsymbol{I C_L} \tag{D.11}$$

$$\boldsymbol{B_{2m}} = -[\boldsymbol{S_m}]^{-1} [\boldsymbol{R_m}] \tag{D.12}$$

Next substitute $\delta \boldsymbol{s_j} = \boldsymbol{N_j} \delta \boldsymbol{\sigma}$ into Equation D.10:

$$\delta\tilde{\boldsymbol{\varepsilon}} = [\boldsymbol{A_{2m}}] \begin{bmatrix} \boldsymbol{N_1} \\ \vdots \\ \boldsymbol{N}_{n_{total}} \end{bmatrix} \delta\boldsymbol{\sigma} + [\boldsymbol{B_{2m}}]\,\delta\boldsymbol{\lambda} \tag{D.13}$$

From Equation D.13, substitute $\delta\tilde{\boldsymbol{\varepsilon}}$ into the constitutive relationship 6.8 to obtain the following:

$$\delta\boldsymbol{\sigma} = \boldsymbol{A_c}\left(\delta\boldsymbol{\varepsilon} - \begin{bmatrix} \boldsymbol{N_1}^{\boldsymbol{T}} & \cdots & \boldsymbol{N}_{n_{total}}{}^{\boldsymbol{T}} \end{bmatrix} [\boldsymbol{B_{2m}}]\,\delta\boldsymbol{\lambda}\right) \tag{D.14}$$

with $\boldsymbol{A_c}$ given by

$$\boldsymbol{A_c} = \left(\boldsymbol{I} + \boldsymbol{D}\begin{bmatrix} \boldsymbol{N}_1^T & \cdots & \boldsymbol{N}_{n_{total}}^T \end{bmatrix} [\boldsymbol{A_{2m}}] \begin{bmatrix} \boldsymbol{N_1} \\ \vdots \\ \boldsymbol{N}_{n_{total}} \end{bmatrix}^{-1}\right)\boldsymbol{D} \tag{D.15}$$

Substituting $\delta\tilde{\boldsymbol{\varepsilon}}$ from Equation D.10 and $\delta\boldsymbol{s_j} = \boldsymbol{N_j}\delta\boldsymbol{\sigma}$ into Equation C.31 gives the damaged stress component as:

$$\delta\boldsymbol{\sigma_D} = [\boldsymbol{A_{3m}}]\,\delta\boldsymbol{\sigma} + [\boldsymbol{B_{3m}}]\,\delta\boldsymbol{\lambda} \tag{D.16}$$

where

$$\boldsymbol{A_{3m}} = \boldsymbol{M_m^{-1}} \begin{bmatrix} \boldsymbol{D_L} & \boldsymbol{0} & \boldsymbol{0} & \boldsymbol{0} \\ \boldsymbol{0} & \ddots & \boldsymbol{0} & \boldsymbol{0} \\ \boldsymbol{0} & \boldsymbol{0} & \boldsymbol{D_L} & \boldsymbol{0} \end{bmatrix} \left[\boldsymbol{S_m^{-1}}\right] \begin{bmatrix} \boldsymbol{N_1} \\ \vdots \\ \boldsymbol{N}_{n_{total}} \end{bmatrix} \tag{D.17}$$

$$\boldsymbol{B_{3m}} = -\boldsymbol{M_m^{-1}} \begin{bmatrix} \boldsymbol{D_L} & \boldsymbol{0} & \boldsymbol{0} & \boldsymbol{0} \\ \boldsymbol{0} & \ddots & \boldsymbol{0} & \boldsymbol{0} \\ \boldsymbol{0} & \boldsymbol{0} & \boldsymbol{D_L} & \boldsymbol{0} \end{bmatrix} \left[\boldsymbol{S_m^{-1}}\right] [\boldsymbol{R_m}] \cdot$$

$$- \begin{bmatrix} \boldsymbol{D_L P_{1_{1,1}}} & \cdots & \boldsymbol{D_L P_{1_{1,n_{active}}}} \\ \vdots & \ddots & \vdots \\ \boldsymbol{D_L P_{1_{n_{active},1}}} & \cdots & \boldsymbol{D_L P_{1_{n_{active},n_{active}}}} \end{bmatrix} \tag{D.18}$$

Substituting for $\delta\boldsymbol{s_D}$ from D.16, $\delta\kappa_I$ from Equation C.6 and $\delta\kappa_D$ from Equation C.10 into the yield function consistency condition C.21 and noting that $\delta F_j = 0$ gives:

$$[\boldsymbol{A_{4m}}] = \delta\boldsymbol{\sigma} + [\boldsymbol{B_{4m}}]\,\delta\boldsymbol{\lambda} = \mathbf{0} \tag{D.19}$$

where

$$\begin{aligned}
\boldsymbol{A_{4m}} = &\begin{bmatrix} \frac{\partial F_1}{\partial \boldsymbol{s_{D_1}}}^T & \mathbf{0} & \mathbf{0} \\ \mathbf{0} & \ddots & \mathbf{0} \\ \mathbf{0} & \mathbf{0} & \frac{\partial F_{n_{active}}}{\partial \boldsymbol{s_{D_{n_{active}}}}}^T \end{bmatrix} [\boldsymbol{A_{3m}}] \\
&+ \begin{bmatrix} \frac{\partial F_1}{\partial \kappa_I} \\ \vdots \\ \frac{\partial F_{n_{active}}}{\partial \kappa_{n_{active}}} \end{bmatrix} a_k \begin{bmatrix} \boldsymbol{K_{\sigma_1}} & \cdots & \boldsymbol{K_{\sigma_{n_{active}}}} \end{bmatrix} [\boldsymbol{A_{3m}}] \\
&\begin{bmatrix} \frac{\partial F_1}{\partial \kappa_{D_1}} & 0 & 0 \\ 0 & \ddots & 0 \\ 0 & 0 & \frac{\partial F_1}{\partial \kappa_{D_{n_{active}}}} \end{bmatrix} \begin{bmatrix} \boldsymbol{K_{3\sigma_{1,1}}} & \cdots & \boldsymbol{K_{3\sigma_{1,n_{active}}}} \\ \vdots & \ddots & \vdots \\ \boldsymbol{K_{3\sigma_{n_{active},1}}} & \cdots & \boldsymbol{K_{3\sigma_{n_{active},n_{active}}}} \end{bmatrix} [\boldsymbol{A_{3m}}]
\end{aligned} \tag{D.20}$$

$$\begin{aligned}
\boldsymbol{B_{4m}} = &\begin{bmatrix} \frac{\partial F_1}{\partial \boldsymbol{s_{D_1}}}^T & \mathbf{0} & \mathbf{0} \\ \mathbf{0} & \ddots & \mathbf{0} \\ \mathbf{0} & \mathbf{0} & \frac{\partial F_{n_{active}}}{\partial \boldsymbol{s_{D_{n_{active}}}}}^T \end{bmatrix} [\boldsymbol{B_{3m}}] \\
&+ \begin{bmatrix} \frac{\partial F_1}{\partial \kappa_I} \\ \vdots \\ \frac{\partial F_{n_{active}}}{\partial \kappa_{n_{active}}} \end{bmatrix} \left(a_k \begin{bmatrix} \boldsymbol{K_{\sigma_1}} & \cdots & \boldsymbol{K_{\sigma_{n_{active}}}} \end{bmatrix} [\boldsymbol{B_{3m}}] + \begin{bmatrix} c_{k_1} & \cdots & c_{k_{n_{active}}} \end{bmatrix} \right) \\
&+ \begin{bmatrix} \frac{\partial F_1}{\partial \kappa_{D_1}} & 0 & 0 \\ 0 & \ddots & 0 \\ 0 & 0 & \frac{\partial F_1}{\partial \kappa_{D_{n_{active}}}} \end{bmatrix} \left(\begin{bmatrix} e_{k_{1,1}} & \cdots & e_{k_{1,n_{active}}} \\ \vdots & \ddots & \vdots \\ e_{k_{n_{active},1}} & \cdots & e_{k_{n_{active},n_{active}}} \end{bmatrix} \right. \\
&\left. + \begin{bmatrix} \boldsymbol{K_{3\sigma_{1,1}}} & \cdots & \boldsymbol{K_{3\sigma_{1,n_{active}}}} \\ \vdots & \ddots & \vdots \\ \boldsymbol{K_{3\sigma_{n_{active},1}}} & \cdots & \boldsymbol{K_{3\sigma_{n_{active},n_{active}}}} \end{bmatrix} [\boldsymbol{B_{3m}}] \right)
\end{aligned} \tag{D.21}$$

Substitute $\delta\boldsymbol{\sigma}$ from Equation D.14 into the above to obtain an expression for $\delta\boldsymbol{\lambda}$:

$$\delta\boldsymbol{\lambda} = -[\boldsymbol{X_m}]^{-1}\,[\boldsymbol{Y_m}]\,\delta\boldsymbol{\varepsilon} \tag{D.22}$$

where

$$\boldsymbol{X_m} = [\boldsymbol{B_{4m}}] - [\boldsymbol{A_{4m}}]\,\boldsymbol{A_c}\left[\begin{array}{ccc} \boldsymbol{N_1}^{\boldsymbol{T}} & \cdots & \boldsymbol{N_{n_{total}}}^{\boldsymbol{T}} \end{array}\right][\boldsymbol{B_{2m}}] \tag{D.23}$$

$$\boldsymbol{Y_m} = [\boldsymbol{A_{4m}}]\,\boldsymbol{A_c} \tag{D.24}$$

Finally, the consistent tangent is derived by substituting $\delta\boldsymbol{\lambda}$ from Equation D.22 into Equation D.14:

$$\delta\boldsymbol{\sigma} = \boldsymbol{D_{tan}}\delta\boldsymbol{\varepsilon} \tag{D.25}$$

$$\boldsymbol{D_{tan}} = \boldsymbol{A_C} + \boldsymbol{A_C}\left[\begin{array}{ccc} \boldsymbol{N_1}^{T} & \cdots & \boldsymbol{N_{n_{total}}}^{T} \end{array}\right][\boldsymbol{B_{2m}}]\,[\boldsymbol{X_m}]^{-1}\,[\boldsymbol{Y_m}] \tag{D.26}$$

Appendix E

Fracture energy

The following simple relationship can be fit to the uniaxial tension response of the plastic-damage model:

$$\sigma_{xx} = f_{t_{ult}} e^{-c_2\left(\frac{\varepsilon_{xx}-\varepsilon_t}{\varepsilon_{cm}-\varepsilon_t}\right)} \tag{E.1}$$

Using a constant $c_2 = 6.5$ gave the best fit to the results from a simulation carried out with the properties shown in Table E.1. The results are shown in Figure E.1. Note that κ_{D_m} was set as $7\varepsilon_{cm}$ rather than $5\varepsilon_{cm}$ to give better agreement with the end of the softening curves from the fitted relationship and the plastic-damage model.

Table E.1: Material parameters used.

E_m (MPa)	ν	f_t (MPa)	f_c (MPa)	ε_c	ε_{cm}	ε_{tm}	c_1	ρ_f	ρ_D
37,000	0.18	2.4	30	0.0022	0.01	0.008	12	5	1

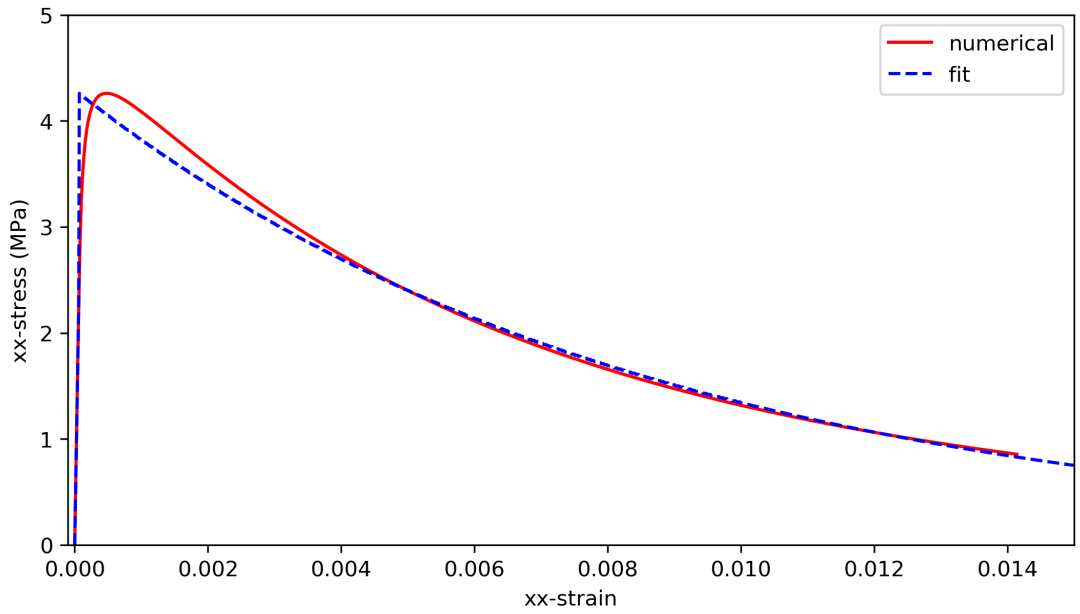

Figure E.1: A 1-D relationship fit to uniaxial tension numerical results.

Evaluating the integral 7.7, with $f_{t_{ult}} = 1.78 f_t$, gives:

$$\varepsilon_0 = \frac{\frac{c_2}{1.78} G_f}{l_{ch} f_t} = \frac{f_a G_f}{l_{ch} f_t} \tag{E.2}$$

and so in this case f_a is equal to 3.7.

Appendix F

Direction fracture simulation mesh 1 results

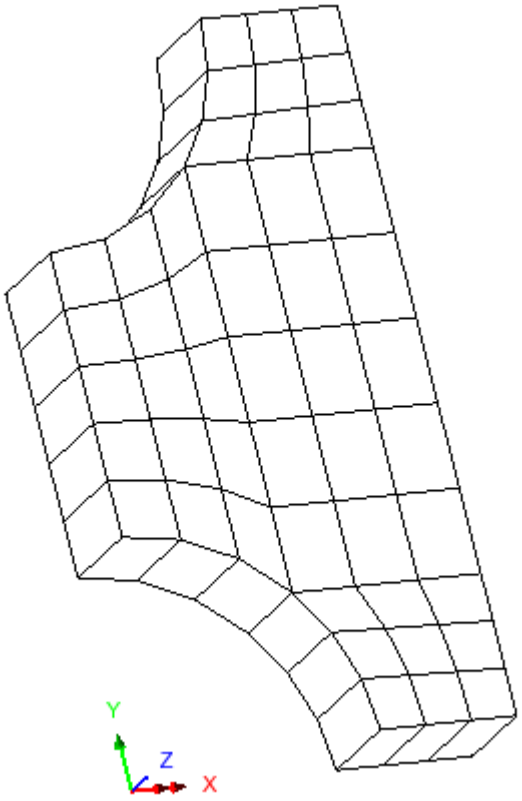

(a) Undeformed mesh

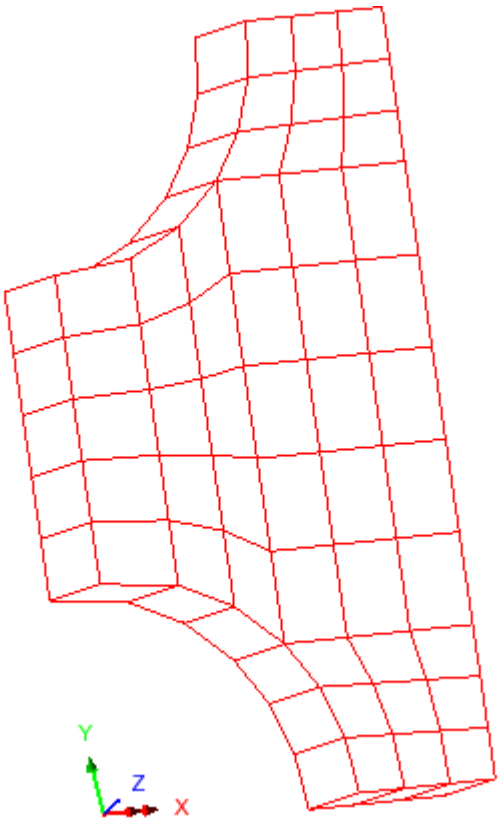

(b) Deformed mesh (30x exaggeration)

Figure F.1: Mesh 1 deformation.

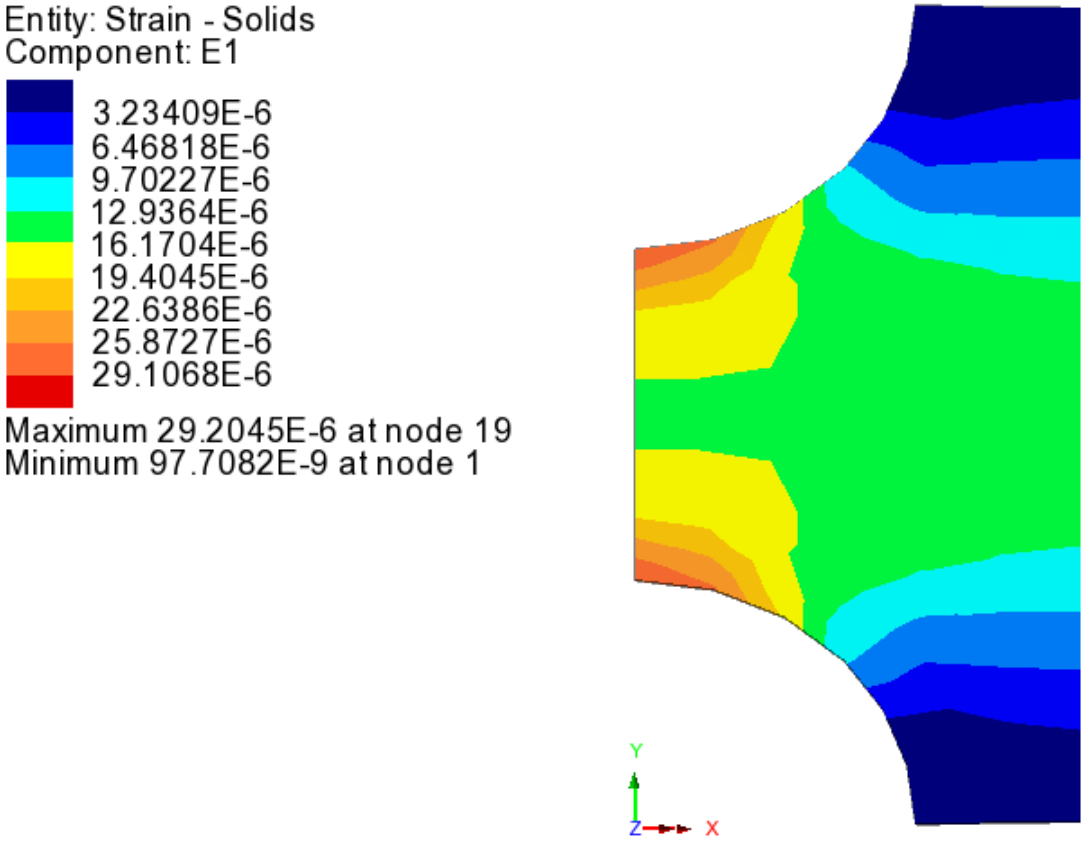

(a) Major principal strains

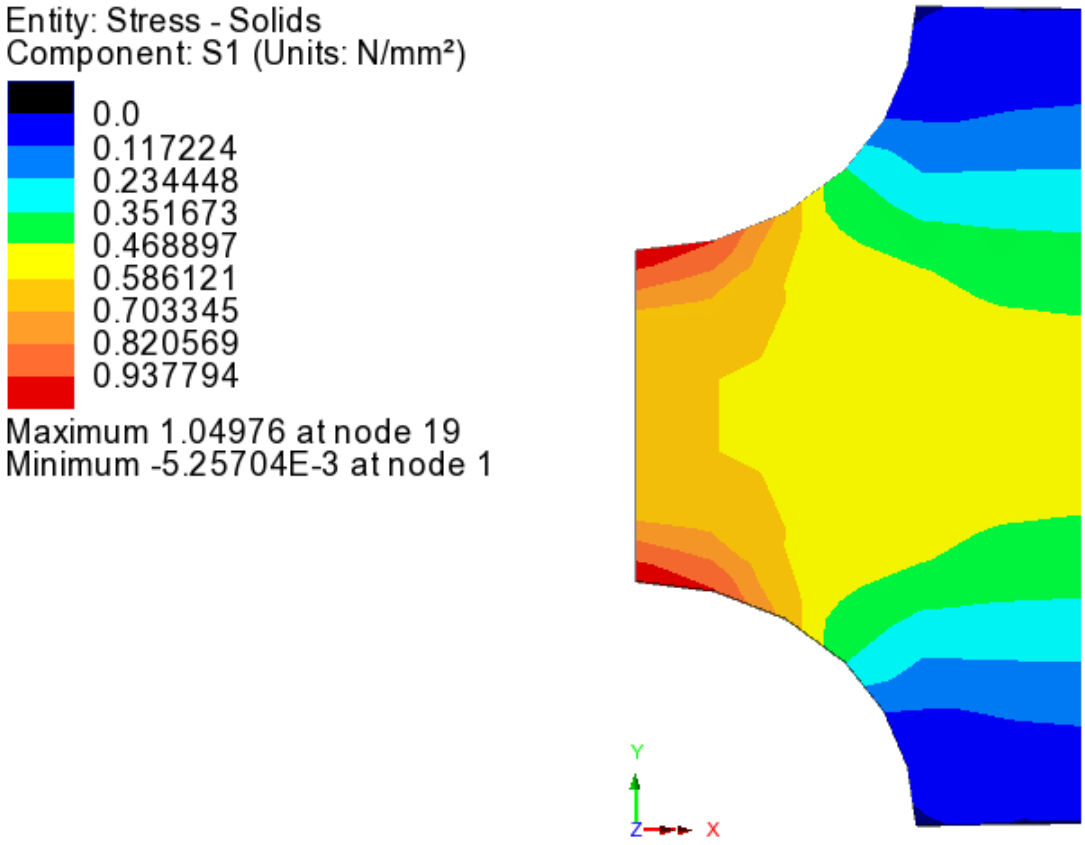

(b) Major principal stresses

Figure F.2: Major principal stresses and strains of mesh 1 at stage a in Figure 7.5.

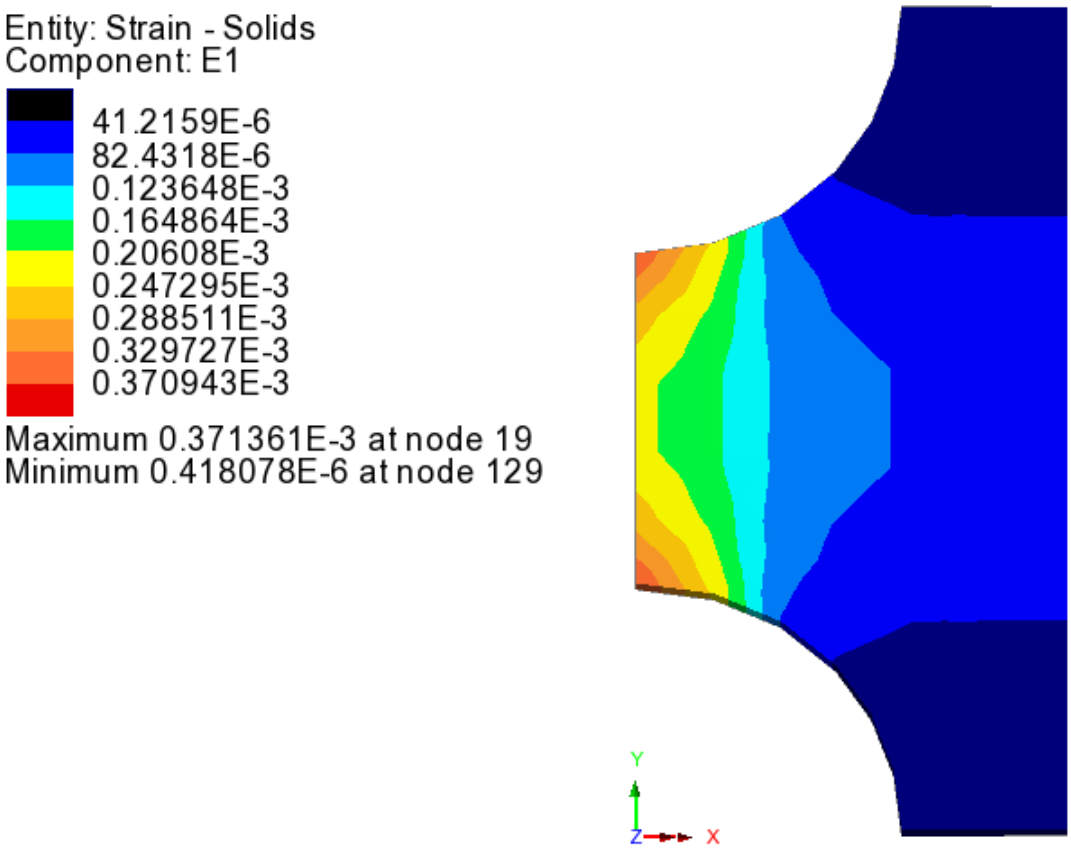

(a) Major principal strains

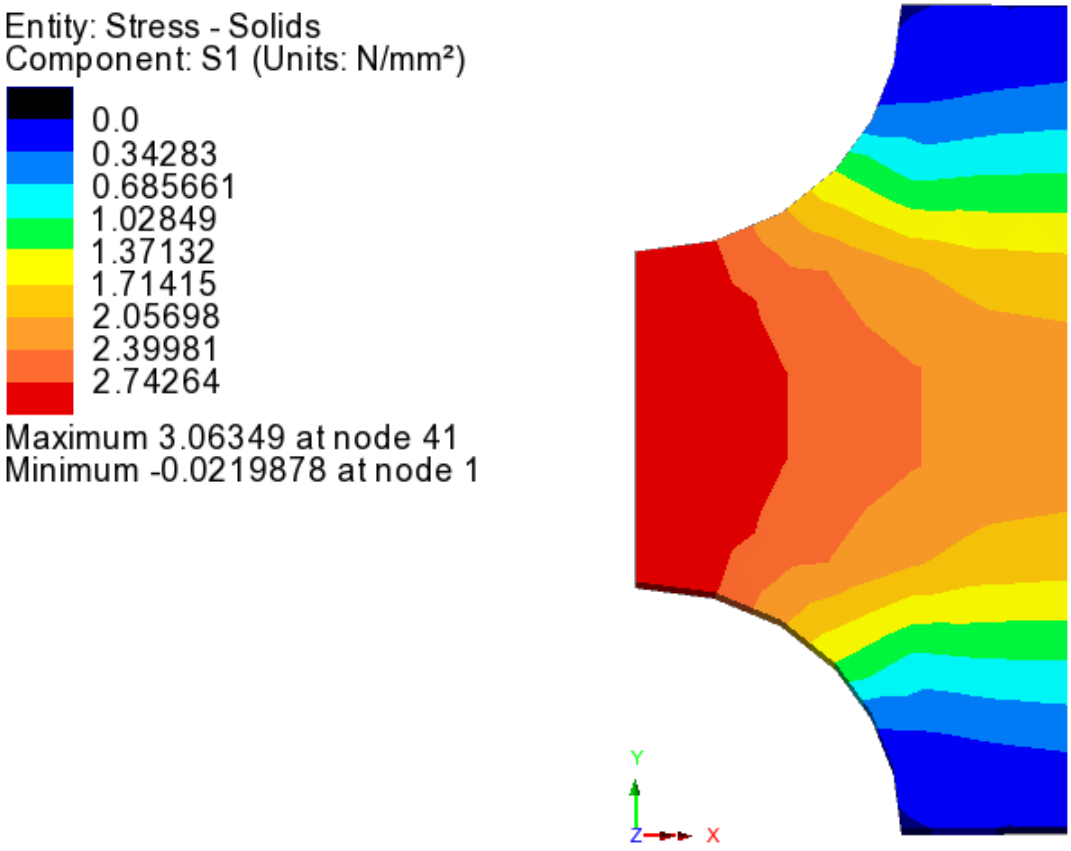

(b) Major principal stresses

Figure F.3: Major principal stresses and strains of mesh 1 at stage b in Figure 7.5.

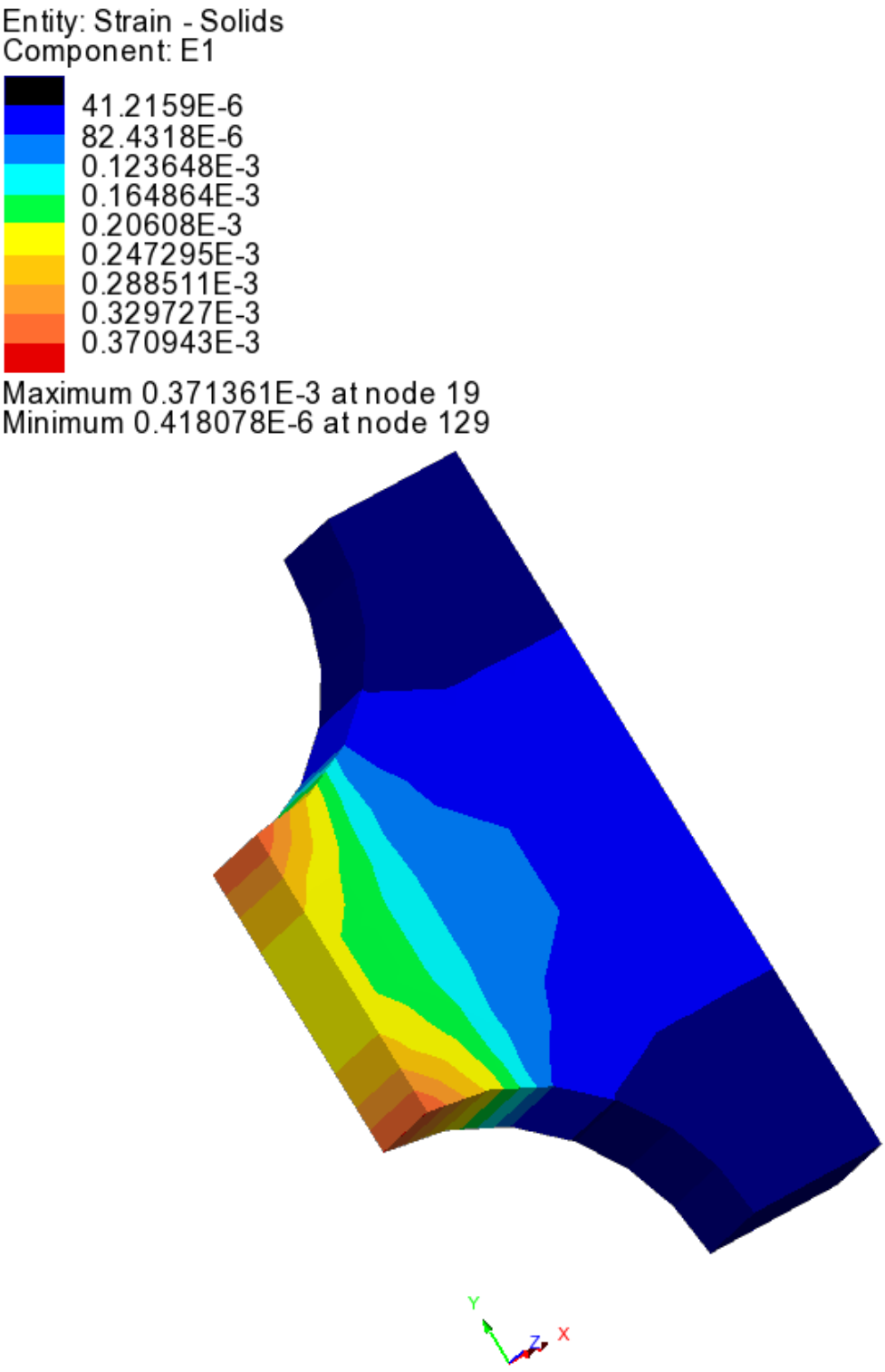

Figure F.4: 3d plot of major principal strains of mesh 1 at stage b in Figure 7.5 showing the through thickness response.

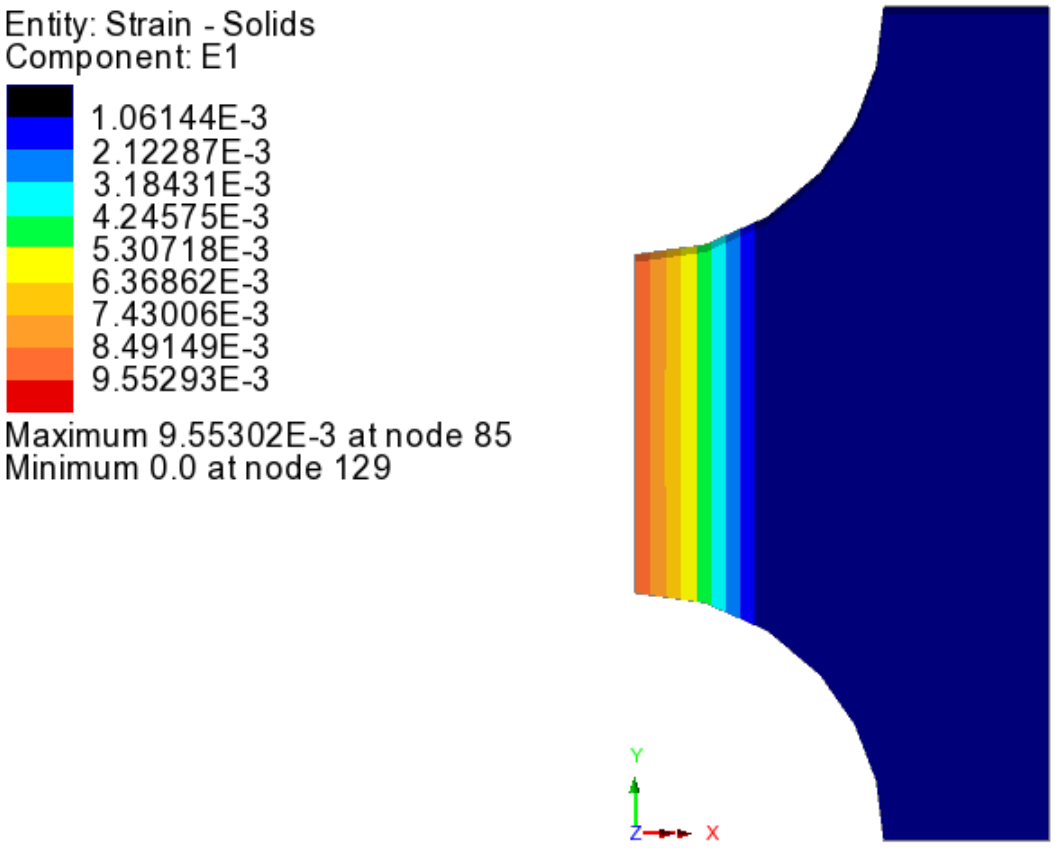

(a) Major principal strains

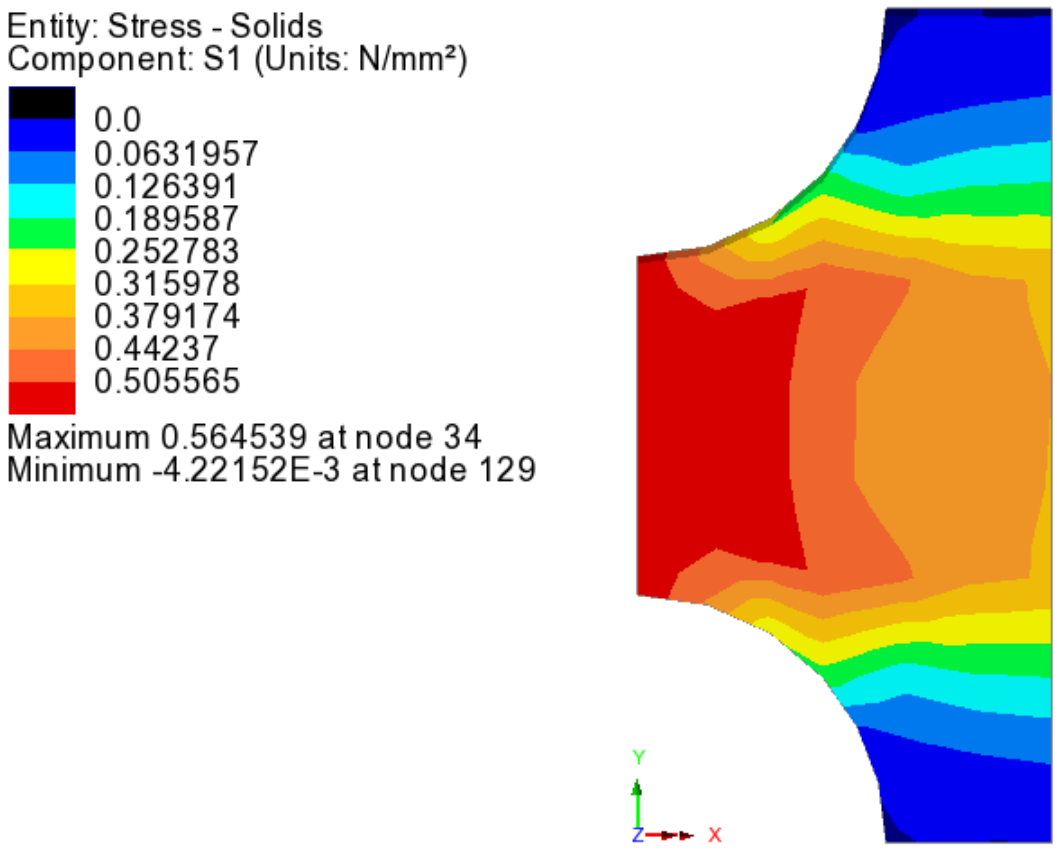

(b) Major principal stresses

Figure F.5: Major principal stresses and strains of mesh 1 at stage c in Figure 7.5.

Appendix G

Four-point bending simulation strain profiles

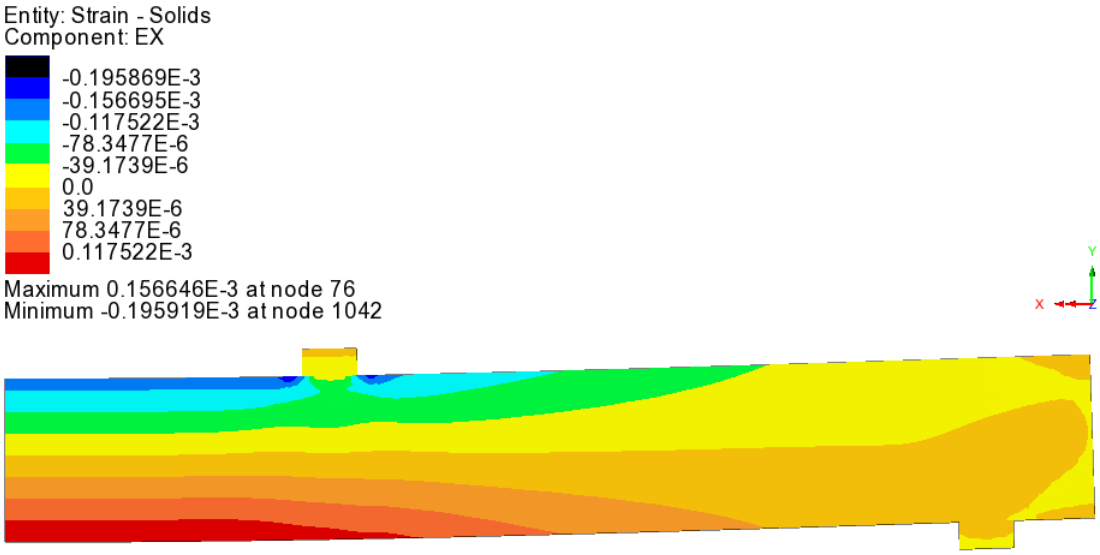

Figure G.1: Strain profile at stage a in Figure 7.15.

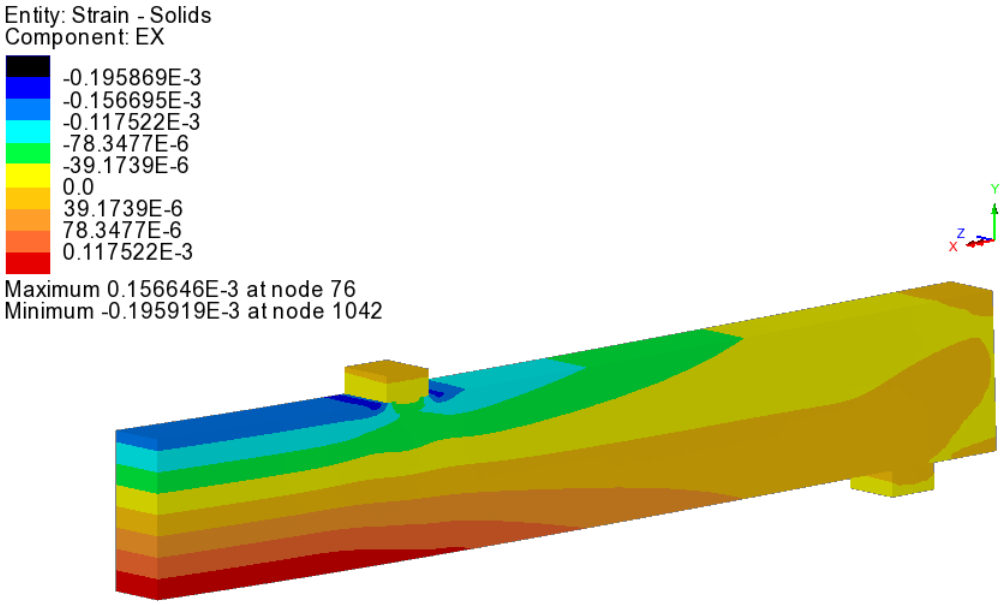

Figure G.2: 3d plot of the strain at stage a in Figure 7.15 showing the through thickness response.

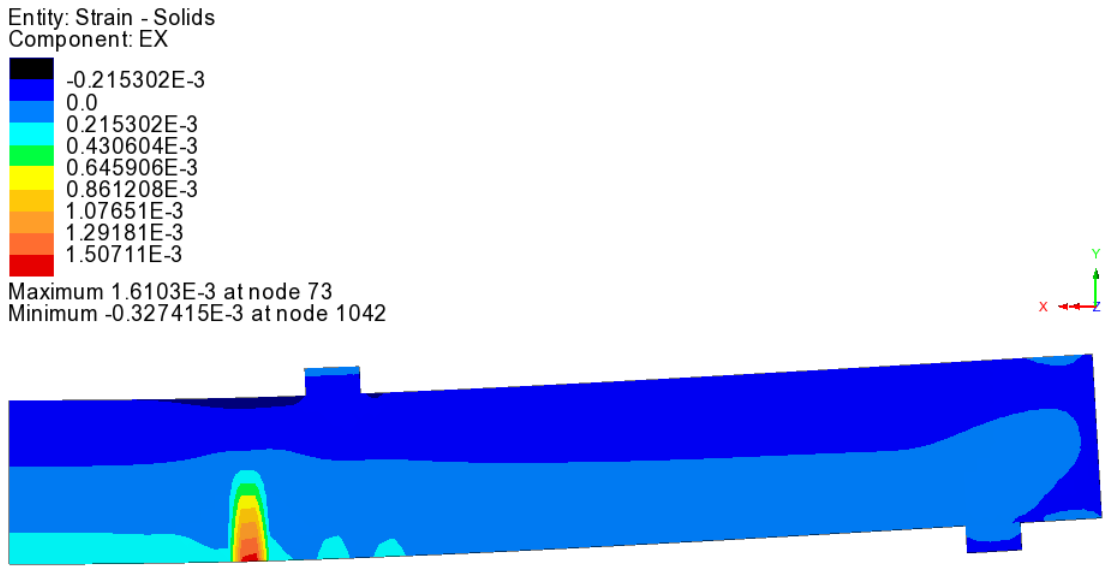

Figure G.3: Strain profile at stage b in Figure 7.15.

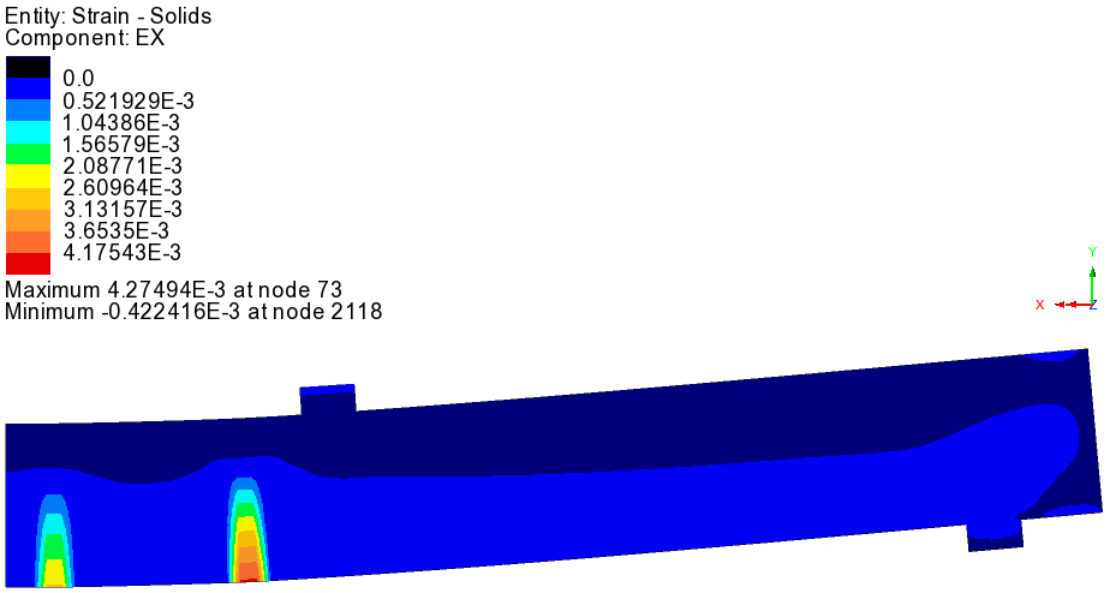

Figure G.4: Strain profile at stage c in Figure 7.15.

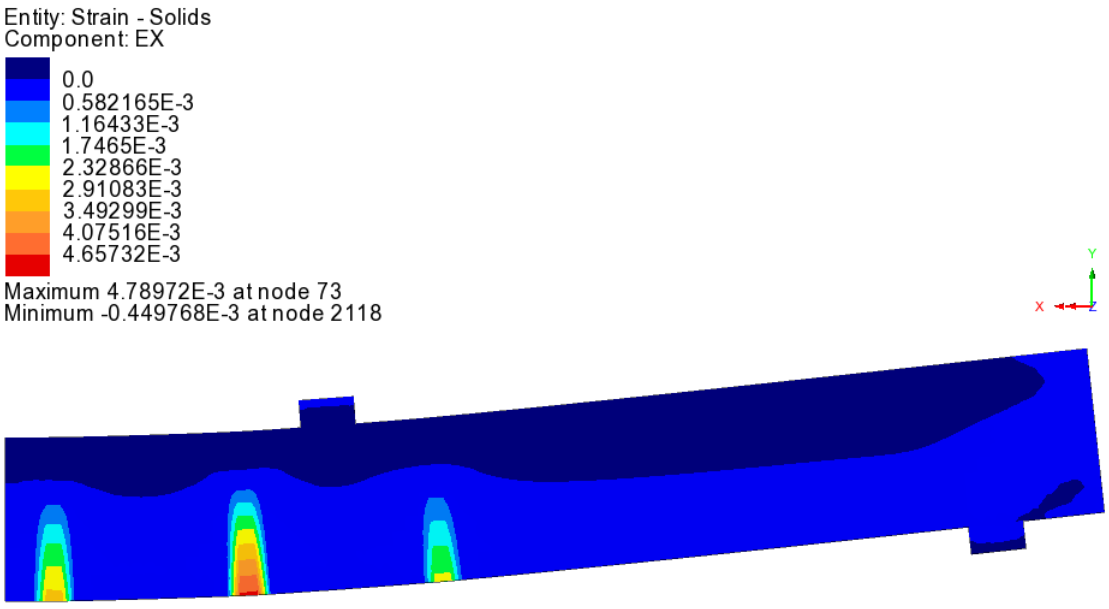

Figure G.5: Strain profile at stage d in Figure 7.15.

References

Abbas, M. Y. & Khan, M. I. (2016), 'Fiber-matrix interfacial behavior of hooked-end steel fiber-reinforced concrete', *Journal of Materials in Civil Engineering* **28**(11), 04016115.

Addessi, D., Marfia, S. & Sacco, E. (2002), 'A plastic nonlocal damage model', *Computer methods in applied mechanics and engineering* **191**(13-14), 1291–1310.

Ahmed, B., Voyiadjis, G. Z. & Park, T. (2021), 'A nonlocal damage model for concrete with three length scales', *Computational Mechanics* pp. 1–26.

Alam, S. Y. & Loukili, A. (2017), 'Transition from energy dissipation to crack openings during continuum–discontinuum fracture of concrete', *International Journal of Fracture* **206**(1), 49–66.

Alam, S. Y., Saliba, J. & Loukili, A. (2014), 'Fracture examination in concrete through combined digital image correlation and acoustic emission techniques', *Construction and Building Materials* **69**, 232–242.

Andrew, R. M. (2018), 'Global co2 emissions from cement production', *Earth System Science Data* **10**(1), 195–217.

Andrieux, S., Bamberger, Y. & Marigo, J. J. (1986), 'Un modéle de materiau microfissure pour les roches et les betons', *Journal de mécanique théorique et appliquée* **5**(3), 471–513.

Arslan, A., Ince, R. & Karihaloo, B. (2002), 'Improved lattice model for concrete fracture', *ournal of Engineering Mechanics* **128**(1), 57–65.

Bažant, Z. P. (1976), 'Instability, ductility, and size effect in strain-softening concrete', *Journal of the engineering mechanics division* **102**(2), 331–344.

Bažant, Z. P. & Gambarova, P. G. (1984), 'Crack shear in concrete: Crack band microflane model', *Journal of Structural Engineering* **110**(9), 2015–2035.

Bažant, Z. P. & Oh, B. H. (1983), 'Crack band theory for fracture of concrete', *Matériaux et construction,* **16**(3), 155–177.

Bažant, Z. P. & Oh, B. H. (1985), 'Microplane model for progressive fracture of concrete and rock', *Journal of Engineering Mechanics* **111**(4), 559–582.

Bažant, Z. P. & Planas, J. (1997), *Fracture and size effect in concrete and other quasibrittle materials*, CRC press.

Bažant, Z. P. & Tsubaki, T. (1980), 'Total strain theory and path-dependence of concrete', *ASCE Journal of the Engineering Mechanics Division* **106**(6), 1151–1173.

Balzano, B., Sweeney, J., Thompson, G., Tuinea-Bobe, C.-L. & Jefferson, A. (2021), 'Enhanced concrete crack closure with hybrid shape memory polymer tendons', *Engineering Structures* **226**, 111330.

Bao, G. & Song, Y. (1993), 'Crack bridging models for fiber composites with degraded interfaces', *Journal of the Mechanics and Physics of Solids* **41**(9), 1425–1444.

Barros, J. A. & Figueiras, J. A. (2001), 'Model for the analysis of steel fibre reinforced concrete slabs on grade', *Computers & Structures* **79**(1), 97–106.

Bažant, Z. P. & Prat, P. C. (1988), 'Microplane model for brittle-plastic material: I. theory', *Journal of Engineering Mechanics* **114**(10), 1672–1688.

Beghini, A., Bažant, Z. P., Zhou, Y., Gouirand, O. & Caner, F. C. (2007), 'Microplane model m5f for multiaxial behavior and fracture of fiber-reinforced concrete', *Journal of engineering mechanics* **133**(1), 66–75.

Belmokaddem, M., Mahi, A., Senhadji, Y. & Pekmezci, B. Y. (2020), 'Mechanical and physical properties and morphology of concrete containing plastic waste as aggregate', *Construction and Building Materials* **257**, 119559.

Belytschko, T. & Black, T. (1999), 'Elastic crack growth in finite elements with minimal remeshing', *International journal for numerical methods in engineering* **45**(5), 601–620.

Bentur, A. & Mindess, S. (1986), 'The effect of concrete strength on crack patterns', *Cement and Concrete Research* **16**(1), 59–66.

Benveniste, Y. (1987), 'A new approach to the application of mori-tanaka's theory in composite materials', *Mechanics of materials* **6**(2), 147–157.

Bernard, O., Ulm, F.-J. & Lemarchand, E. (2003), 'A multiscale micromechanics-hydration model for the early-age elastic properties of cement-based materials', *Cement and concrete research* **33**(9), 1293–1309.

Berton, S. & Bolander, J. E. (2006), 'Crack band model of fracture in irregular lattices', *Computer Methods in Applied Mechanics and Engineering* **195**(52), 7172–7181.

Böhm, H. J. (2021), ILSB Report / ILSB-Arbeitsbericht 206 (210430) - A short introduction to basic aspects of continuum micromechanics, Report, Institute

of Lightweight Design and Structural Biomechanics (ILSB), Vienna University of Technology.

Bhosale, A. B. & Prakash, S. S. (2020), 'Crack propagation analysis of synthetic vs. steel vs. hybrid fibre-reinforced concrete beams using digital image correlation technique', *International Journal of Concrete Structures and Materials* **14**(1), 1–19.

Bobiński, J. & Tejchman, J. (2016), 'A coupled constitutive model for fracture in plain concrete based on continuum theory with non-local softening and extended finite element method', *Finite Elements in Analysis and Design* **114**, 1–21.

Bolander, J., Choi, S. & Duddukuri, S. R. (2008), 'Fracture of fiber-reinforced cement composites: effects of fiber dispersion', *International journal of fracture* **154**(1-2), 73–86.

Bower, A. F. (2009), *Applied Mechanics of Solids*, CRC press.

Brekelmans, W. & De Vree, J. (1995), 'Reduction of mesh sensitivity in continuum damage mechanics', *Acta Mechanica* **110**(1), 49–56.

Brencich, A. & Gambarotta, L. (2001), 'Isotropic damage model with different tensile–compressive response for brittle materials', *International Journal of Solids and Structures* **38**(34-35), 5865–5892.

Budiansky, B. & O'Connell, R. J. (1976), 'Elastic moduli of a cracked solid', *International Journal of Solids and Structures* **12**(2), 81–97.

Camacho, G. T. & Ortiz, M. (1996), 'Computational modelling of impact damage in brittle materials', *International Journal of solids and structures* **33**(20-22), 2899–2938.

Camões, A. & Ferreira, R. (2010), 'Technological evolution of concrete: from ancient times to ultra high-performance concrete', *Structures and Architecture* pp. 1571–1578.

Caner, F., Bažant, Z. P. & Wendner, R. (2013), 'Microplane model m7f for fiber reinforced concrete', *Engineering fracture mechanics* **105**, 41–57.

Caner, F. C. & Bažant, Z. P. (2011), Microplane model m6f for fiber reinforced concrete. in: Proc., xi int. conf. on computational plasticity fundamentals nd applications, complas.

Caner, F. C. & Bažant, Z. P. (2013), 'Microplane model m7 for plain concrete. i: Formulation', *Journal of Engineering Mechanics* **139**(12), 1714–1723.

Carol, I., López, C. M. & Roa, O. (2001), 'Micromechanical analysis of quasi-brittle materials using fracture-based interface elements', *International Journal for Numerical Methods in Engineering* **52**(1-2), 193–215.

Carol, I., Prat, P. C. & Bažant, Z. P. (1992), 'New explicit microplane model for concrete: theoretical aspects and numerical implementation', *International Journal of Solids and Structures* **29**(9), 1173–1191.

Castañeda, P. P. & Willis, J. R. (1995), 'The effect of spatial distribution on the effective behavior of composite materials and cracked media', *Journal of the Mechanics and Physics of Solids* **43**(12), 1919–1951.

Cedolin, L. (1987), Fracture mechanics parameters and fracture process zone of concrete, *in* 'Fracture of Non-Metallic Materials', Springer, pp. 341–358.

Cedolin, L., Dei Poli, S. & Crutzen, Y. R. J. (1977), 'Triaxial stress-strain relationship for concrete', *ASCE Journal of the Engineering Mechanics Division* **103**(3), 423–439.

Cedolin, L. & Di Luzio, G. (2004), 'A nonlocal microplane model for fiber reinforced concrete', *6th RILEM symposium on fibre-reinforced concretes FRC-BEFIB* pp. 819–826.

Cervera, M., Chiumenti, M. & de Saracibar, C. A. (2004), 'Shear band localization via local j2 continuum damage mechanics', *Computer Methods in Applied Mechanics and Engineering* **193**(9-11), 849–880.

Chella Gifta, C. & Gopal, R. (2021), 'Modelling of strength and energy absorption capacity of hybrid fibre-reinforced concrete', *Magazine of Concrete Research* **73**(8), 410–419.

Chi, Y., Xu, L. & Yu, H. (2014), 'Constitutive modeling of steel-polypropylene hybrid fiber reinforced concrete using a non-associated plasticity and its numerical implementation', *Composite Structures* **111**, 497–509.

Choi, M. S., Kang, S.-T., Lee, B. Y., Koh, K.-T. & Ryu, G.-S. (2016), 'Improvement in predicting the post-cracking tensile behavior of ultra-high performance cementitious composites based on fiber orientation distribution', *Materials* **9**(10), 829.

Cicekli, U., Voyiadjis, G. Z. & Al-Rub, R. K. A. (2007), 'A plasticity and anisotropic damage model for plain concrete', *International Journal of plasticity* **23**(10-11), 1874–1900.

Comi, C. & Perego, U. (2001), 'Fracture energy based bi-dissipative damage model for concrete', *International journal of solids and structures* **38**(36-37), 6427–6454.

Cunha, V. M., Barros, J. & Sena-Cruz, J. (2011), 'An integrated approach for modelling the tensile behaviour of steel fibre reinforced self-compacting concrete', *Cement and Concrete Research* **41**(1), 64–76.

Cusatis, G., Pelessone, D. & Mencarelli, A. (2011), 'Lattice discrete particle

model (ldpm) for failure behavior of concrete. i: Theory.', *Cement and Concrete Composites* **33**(9), 881–890.

Davies, R., Jefferson, T. & Gardner, D. (2021), 'Development and testing of vascular networks for self-healing cementitious materials', *Journal of Materials in Civil Engineering* **33**(7), 04021164.

De Borst, R., Crisfield, M. A., Remmers, J. J. & Verhoosel, C. V. (2012), *Nonlinear finite element analysis of solids and structures*, John Wiley & Sons.

De Borst, R. & Verhoosel, C. V. (2017), *Damage, material instabilities, and failure*, John Wiley & Sons, pp. 1–50.

de Souza Neto, E. A., Peric, D. & Owen, D. R. (2008), *Computational methods for plasticity: theory and applications*, John Wiley & Sons, Torquay, UK.

Delatte, N. J. (2001), 'Lessons from roman cement and concrete', *Journal of professional issues in engineering education and practice* **127**(3), 109–115.

Delaunay, B. et al. (1934), 'Sur la sphere vide', *Izv. Akad. Nauk SSSR, Otdelenie Matematicheskii i Estestvennyka Nauk* **7**(793-800), 1–2.

Derucher, K. (1977), 'Microcracking of concrete', *Journal of the Washington Academy of Sciences* pp. 135–143.

Desmorat, R., Gatuingt, F. & Ragueneau, F. (2007), 'Nonlocal anisotropic damage model and related computational aspects for quasi-brittle materials', *Engineering Fracture Mechanics* **74**(10), 1539–1560.

Do, H. Q., Bishnoi, S. & Scrivener, K. L. (2020), 'Microstructural modelling of autogenous shrinkage in portland cement paste at early age', *Engineering Computations* .

Dragon, A. & Mróz, Z. (1979), 'A continuum model for plastic-brittle behaviour of rock and concrete', *International Journal of Engineering Science* **17**(2), 121–137.

Drucker, D. & Prager, W. (1952), 'Soil mechanics and plasticity analysis of limit design', *The Quarterly Journal of Mechanics and Applied Mathematics* **10**, 157–162.

Duan, Z., Li, B., Xiao, J. & Guo, W. (2021), 'Optimizing mix proportion of recycled aggregate concrete by readjusting the aggregate gradation', *Structural Concrete* **22**, E22–E32.

Durand, R. & da Silva, F. H. B. T. (2019), 'A coulomb-based model to simulate concrete cracking using cohesive elements', *International Journal of Fracture* **220**(1), 17–43.

Dutra, V. P., Maghous, S. & Campos Filho, A. (2013), 'A homogenization ap-

proach to macroscopic strength criterion of steel fiber reinforced concrete', *Cement and concrete research* **44**, 34–45.

Dutra, V. P., Maghous, S., Campos Filho, A. & Pacheco, A. (2010), 'A micromechanical approach to elastic and viscoelastic properties of fiber reinforced concrete', *Cement and concrete research* **40**(3), 460–472.

Dutta, S. & Kishen, J. C. (2019), 'Micromechanical damage model for plain concrete considering propagation of matrix microcracks', *Physical Mesomechanics* **22**(2), 96–106.

Eckardt, S. & Könke, C. (2008), 'Adaptive damage simulation of concrete using heterogeneous multiscale models', *Journal of Algorithms & Computational Technology* **2**(2), 275–298.

Eshelby, J. D. (1957), 'The determination of the elastic field of an ellipsoidal inclusion, and related problems', *Proceedings of the royal society of London. Series A. Mathematical and physical sciences* **241**(1226), 376–396.

Evans, R. & Marathe, M. (1968), 'Microcracking and stress-strain curves for concrete in tension', *Matériaux et Construction* **1**(1), 61–64.

Fanella, D. & Krajcinovic, D. (1985), 'Continuum damage mechanics of fiber reinforced concrete', *Journal of engineering mechanics* **111**(8), 995–1009.

Fantilli, A. P., Mihashi, H. & Vallini, P. (2009), 'Multiple cracking and strain hardening in fiber-reinforced concrete under uniaxial tension', *Cement and Concrete Research* **39**(12), 1217–1229.

Faria, R., Oliver, J. & Cervera, M. (1998), 'A strain-based plastic viscous-damage model for massive concrete structures', *International journal of solids and structures* **35**(14), 1533–1558.

Feenstra, P. H. & De Borst, R. (1995), 'A plasticity model and algorithm for mode-i cracking in concrete', *International Journal for Numerical Methods in Engineering* **38**(15), 2509–2529.

Feist, C. & Hofstetter, G. (2006), 'An embedded strong discontinuity model for cracking of plain concrete', *Computer Methods in Applied Mechanics and Engineering* **195**(52), 7115–7138.

Freeman, B. L., Bonilla-Villalba, P., Mihai, I. C., Alnaas, W. F. & Jefferson, A. D. (2020), 'A specialised finite element for simulating self-healing quasi-brittle materials', *Advanced Modeling and Simulation in Engineering Sciences* **7**(1), 1–24.

Fritsch, A. & Hellmich, C. (2007), 'Universal" microstructural patterns in cortical and trabecular, extracellular and extravascular bone materials: Micromechan-

icsbased prediction of anisotropic elasticity', *Journal of Theoretical Biology* **244**(4), 597–620.

Fuller, W. B. & Thompson, S. E. (1907), 'The laws of proportioning concrete', *Transactions of the American Society of Civil Engineers* **59**(2), 67–143.

Gagg, C. R. (2014), 'Cement and concrete as an engineering material: An historic appraisal and case study analysis', *Engineering Failure Analysis* **40**, 114–140.

Gambarotta, L. (2004), 'Friction-damage coupled model for brittle materials', *Engineering Fracture Mechanics* **71**(4-6), 829–836.

Gambarotta, L. & Lagomarsino, S. (1993), 'A microcrack damage model for brittle materials', *International Journal of Solids and Structures* **30**(2), 177–198.

Gitman, I., Askes, H. & Sluys, L. (2007), 'Representative volume: Existence and size determination', *Engineering fracture mechanics* **74**(16), 2518–2534.

Gitman, I. M. (2006), Representative volumes and multi-scale modelling of quasi-brittle materials, PhD thesis, Delft University of Technology.

Grassl, P. & Antonelli, A. (2019), '3d network modelling of fracture processes in fibre-reinforced geomaterials', *International Journal of Solids and Structures* **156-157**, 234–242.

Grassl, P. & Bolander, J. (2016), 'Three-dimensional network model for coupling of fracture and mass transport in quasi-brittle geomaterials', *Materials* **9**(9), 782.

Grassl, P., Grégoire, D., Rojas Solano, L. & Pijaudier-Cabot, G. (2012), 'Meso-scale modelling of the size effect on the fracture process zone of concrete', *International Journal of Solids and Structures* **49**(13), 1818–1827.

Grassl, P. & Jirásek, M. (2006), 'Plastic model with non-local damage applied to concrete', *nternational Journal for Numerical and Analytical Methods in Geomechanics* **30**(1), 71–90.

Grassl, P. & Jirásek, M. (2010), 'Meso-scale approach to modelling the fracture process zone of concrete subjected to uniaxial tension', *International Journal of Solids and Structures* **48**(7-8), 957–968.

Grassl, P., Lundgren, K. & Gylltoft, K. (2002), 'Concrete in compression: a plasticity theory with a novel hardening law', *International Journal of Solids and Structures* **39**(20), 5205–5223.

Green, P. J. & Sibson, R. (1978), 'Computing dirichlet tessellations in the plane', *The computer journal* **21**(2), 168–173.

Griffith, A. A. (1921), 'The phenomena of rupture and flow in solids', *Philosophical transactions of the royal society of london. Series A, containing papers of a mathematical or physical character* **221**(582-593), 163–198.

Griffith, A. A. (1924), The theory of rupture. in: Proceedings of the first international congress for applied mechanics.

Grzymski, F., Musiał, M. & Trapko, T. (2019), 'Mechanical properties of fibre reinforced concrete with recycled fibres', *Construction and Building Materials* **198**, 323–331.

Hameed, R., Sellier, A., Turatsinze, A. & Duprat, F. (2013), 'Metallic fiber-reinforced concrete behaviour: Experiments and constitutive law for finite element modeling', *Engineering Fracture Mechanics* **103**, 124–131.

Hartmaier, A. (2020), 'Data-oriented constitutive modeling of plasticity in metals', *Materials* **13**(7), 1600.

Hasegawa, T. & Bažant, Z. P. (1993), 'Nonlocal microplane concrete model with rate effect and load cycles. i: General formulation', *Journal of materials in civil engineering* **5**(3), 372–393.

Hazzard, J. F., Young, R. P. & Maxwell, S. C. (2000), 'Micromechanical modeling of cracking and failure in brittle rocks', *Journal of Geophysical Research: Solid Earth* **105**(B7), 16683–1669.

He, W., Wu, Y. F., Liew, K. M. & Wu, Z. (2006), 'A 2d total strain based constitutive model for predicting the behaviors of concrete structures', *International Journal of Engineering Science* **44**(18-19), 1280–1303.

Hearn, N. (1999), 'Effect of shrinkage and load-induced cracking on water permeability of concrete', *Materials Journal* **96**(2), 234–241.

Hellmich, C., Barthélémy, J. & Dormieux, L. (2004), 'Mineral–collagen interactions in elasticity of bone ultrastructure – a continuum micromechanics approach', *European Journal of Mechanics - A/Solids* **25**(5), 783–810.

Hill, R. (1965), 'A self-consistent mechanics of composite materials', *Journal of the Mechanics and Physics of Solids* **13**(4), 213–222.

Hofmeyer, H. & Van den Bos, A. A. (2008), 'Total strain fe model for reinforced concrete floors on piles', *The Structural Design of Tall and Special Buildings* **17**(4), 809–822.

Hofstetter, K., Hellmich, C. & Eberhardsteiner, J. (2005), 'Development and experimental validation of a continuum micromechanics model for the elasticity of wood', *European Journal of Mechanics - A/Solids* **24**(6), 1030–1053.

Hordijk, D. A. (1991), Local approach to fatigue of concrete., PhD thesis.

Horri, H' Hasegawa, A. N. F. (1989), Fracture process zone and bridging zone model and influencing factors in fracture of concrete. in: Shah s.p. and swartz, s.e. sem-rilem international conference. 1987. houston, texas, Springer-Verlag.

Hsu, T. T., Slate, F. O., Sturman, G. M. & Winter, G. (1963), Microcracking of

plain concrete and the shape of the stress-strain curve, *in* 'Journal Proceedings', Vol. 60, pp. 209–224.

Huang, B.-T., Weng, K.-F., Zhu, J.-X., Xiang, Y., Dai, J.-G. & Li, V. C. (2021), 'Engineered/strain-hardening cementitious composites (ecc/shcc) with an ultra-high compressive strength over 210 mpa', *Composites Communications* **26**, 100775.

Huang, X. & Karihaloo, B. L. (1992), 'Tension softening of quasi-brittle materials modelled by singly and doubly periodic arrays of coplanar penny-shaped cracks', *Mechanics of Materials* **13**(3), 257–275.

Imran, I. & Pantazopoulou, S. J. (2001), 'Plasticity model for concrete under triaxial compression', *Journal of engineering mechanics* **127**(3), 281–290.

Ingraffea, A. R. & de Borst, R. (2017), 'Computational fracture mechanics', *Encyclopedia of Computational Mechanics Second Edition* pp. 1–26.

Ingraffea, A. R. & Saouma, V. (1985), *Numerical modeling of discrete crack propagation in reinforced and plain concrete*, Springer, Dordrecht, pp. 171–225.

Jackson, M. D., Chae, S. R., Mulcahy, S. R., Meral, C., Taylor, R., Li, P., Emwas, A.-H., Moon, J., Yoon, S., Vola, G. et al. (2013), 'Unlocking the secrets of al-tobermorite in roman seawater concrete', *American Mineralogist* **98**(10), 1669–1687.

Jahren, P. & Sui, T. (2018), *History Of Concrete: A Very Old And Modern Material*, World Scientific Publishing Company.

Jansen, D. C. & Shah, S. P. (1997), 'Effect of length on compressive strain softening of concrete', *Journal of Engineering Mechanics* **123**(1), 25–35.

Janson, J. & Hult, J. (1977), 'Fracture mechanics and damage mechanics a combined approach', *J. mechanique appliquee* **1**(1), 69–84.

Jefferson, A. D. (2002), 'Local plastic surfaces for cracking and crushing in concrete', *Proceedings of the Institution of Mechanical Engineers, Part L: Journal of Materials: Design and Applications* **216**(4), 257–266.

Jefferson, A. D. (2003), 'Craft—-a plastic-damage-contact model for concrete. i. model theory and thermodynamic considerations', *International Journal of Solids and structures* **40**(22), 5973–5999.

Jefferson, A. D. & Bennett, T. (2007), 'Micro-mechanical damage and rough crack closure in cementitious composite materials', *International journal for numerical and analytical methods in geomechanics* **31**(2), 133–146.

Jefferson, A. D. & Bennett, T. (2010), 'A model for cementitious composite materials based on micro-mechanical solutions and damage-contact theory', *Computers & structures* **88**(23-24), 1361–1366.

Jefferson, A. D., Mihai, I. C., Tenchev, R., Alnaas, W. F., Cole, G. & Lyons, P. (2016), 'A plastic-damage-contact constitutive model for concrete with smoothed evolution functions', *Computers & Structures* **169**, 45–56.

Jiao, Y.-t., Wang, B. & Shen, Z.-z. (2019), 'A new 3d empirical plastic and damage model for simulating the failure of concrete structure', *International Journal of Concrete Structures and Materials* **13**(1), 1–18.

Jin, W. (2018), Computational modelling of the transition from damage to fracture in intrinsically anisotropic porous media., PhD thesis.

Jirásek, M. (2007), 'Nonlocal damage mechanics', *Revue européenne de génie civil* **11**(7-8), 993–1021.

Jirásek, M. & Bauer, M. (2012), 'Numerical aspects of the crack band approach', *Computers & structures* **110**, 60–78.

Joseph, C. (2008), Experimental and numerical study of the fracture and self-healing of cementitious materials, PhD thesis, Cardiff University, Cardiff.

Ju, J. W. & Sun, L. Z. (2001), 'Effective elastoplastic behavior of metal matrix composites containing randomly located aligned spheroidal inhomogeneities. part i: micromechanics-based formulation', *International Journal of Solids and Structures* **38**(2), 183–201.

Kachanov, M. (1958), 'On the time to rupture under creep conditions', *Izv. Acad. Nauk SSSR, OTN* **8**, 26–31.

Kachanov, M. (1987), 'Elastic solids with many cracks: a simple method of analysis', *International Journal of Solids and Structures* **23**(1), 23–43.

Kaneko, K. (1995), 'A plastic constitutive model for anisotropic hardening metals', *European journal of mechanics. A. Solids* **14**(5), 679–696.

Karavelić, E., Nikolić, M., Ibrahimbegovic, A. & Kurtović, A. (2019), 'Concrete meso-scale model with full set of 3d failure modes with random distribution of aggregate and cement phase. part i: Formulation and numerical implementation', *Computer Methods in Applied Mechanics and Engineering* **344**, 1051–1072.

Karihaloo, B. L. (1995), *Fracture mechanics and structural concrete*, Longman Scientific & Technical, Essex, England.

Karihaloo, B. L. & Fu, D. (1989), 'A damage-based constitutive law for plain concrete in tension', *European Journal of Mechanics A - Solids* **8**, 373–384.

Karihaloo, B. L., Fu, D. & Huang, X. (1991), 'Modelling of tension softening in quasi-brittle materials by an array of circular holes with edge cracks', *Mechanics of Materials* **11**(2), 123–134.

Karihaloo, B. L. & Wang, J. (2000), 'Mechanics of fibre-reinforced cementitious composites', *Computers & Structures* **76**(1-3), 19–34.

Karihaloo, B. L., Wang, J. & Grzybowski, M. (1996), 'Doubly periodic arrays of bridged cracks and short fibre-reinforced cementitious composites', *Journal of the Mechanics and Physics of Solids* **44**(10), 1565–1586.

Kholmyansky, M. (2002), 'Mechanical resistance of steel fiber reinforced concrete to axial load', *Journal of materials in civil engineering* **14**(4), 311–319.

Königsberger, M., Hlobil, M., Delsaute, B., Staquet, S., Hellmich, C. & Pichler, B. (2018), 'Hydrate failure in itz governs concrete strength: A micro-to-macro validated engineering mechanics model', *Cement and Concrete Research* **103**, 77–94.

Königsberger, M., Pichler, B. & Hellmich, C. (2020), 'Multiscale poro-elasticity of densifying calcium-silicate hydrates in cement paste: An experimentally validated continuum micromechanics approach', *International Journal of Engineering Science* **147**, 103196.

Kotsovos, M. D. & Newman, J. B. (1979), 'A mathematical description of the deformational behaviour of concrete under complex loading', *Magazine of Concrete Research* **31**(107), 77–90.

Kozicki, J. & Tejchman, J. (2008), 'Modelling of fracture process in concrete using a novel lattice model', *Granular Matter* **10**(5), 377–388.

Kupfer, H. (1973), 'Das verhalten des betons unter mehrachsiger kurzzeitbelastung unter besonderer berucksichtigung der zweiachsigen beanspruchung (the behavior of the concrete under short-term multi-axis loading with special consideration of the two-axis loading)', *Deutscher Ausschuss für Stahlbeton* **229**(1).

Kupfer, H., Hilsdorf, H. K. & Rusch, H. (1969), Behavior of concrete under biaxial stresses, *in* 'Journal proceedings', Vol. 66, pp. 656–666.

Kwon, S., Nishiwaki, T., Kikuta, T. & Mihashi, H. (2014), 'Development of ultra-high-performance hybrid fiber-reinforced cement-based composites', *ACI Materials Journal* **111**(3), 309.

Lakavath, C., Bhosale, A. & Prakash, S. S. (2020), Experimental investigation on crack-arresting mechanism of steel fibre-reinforced concrete prism specimens using dic and ae techniques, *in* 'Advances in Structural Engineering', Springer, pp. 51–65.

Landis, E. N., Kravchuk, R. & Loshkov, D. (2019), 'Experimental investigations of internal energy dissipation during fracture of fiber-reinforced ultra-high-performance concrete', *Frontiers of Structural and Civil Engineering* **13**(1), 190–200.

Landis, E. N. & Shah, S. P. (1995), 'The influence of microcracking on the mechanical behavior of cement based materials', *Advanced Cement Based Materials* **2**(3), 105–118.

Lange-Kornbak, D. & Karihaloo, B. L. (1997), 'Tension softening of fibre-reinforced cementitious composites', *Cement and Concrete Composites* **19**(4), 315–328.

Lawler, J., Wilhelm, T., Zampini, D. & Shah, S. (2003), 'Fracture processes of hybrid fiber-reinforced mortar', *Materials and Structures* **36**(3), 197–208.

Leckie, F. A. & Onat, E. T. (1981), *Tensorial nature of damage measuring internal variables*, Springer, Berlin, Heidelberg, pp. 140–155.

Lee, J. & Fenves, G. L. (1998), 'Plastic-damage model for cyclic loading of concrete structures', *Journal of engineering mechanics* **124**(8), 892–900.

Li, F. (1998), Fracture characterization of fiber-reinforced concrete in direct uniaxial tension, PhD thesis, Hong Kong University of Science and Technology, Hong Kong.

Li, F. & Li, Z. (2001), 'Continuum damage mechanics based modeling of fiber reinforced concrete in tension', *International journal of solids and structures* **38**(5), 777–793.

Li, V. C. (2019), *Engineered Cementitious Composites (ECC): Bendable Concrete for Sustainable and Resilient Infrastructure*, Springer-Verlag GmbH, Germany.

Li, V. C. & Huang, J. (1990), 'Relation of concrete fracture toughness to its internal structure', *Engineering Fracture Mechanics* **35**(1-3), 39–46.

Li, V. C. & Maalej, M. (1996), 'Toughening in cement based composites. part i: Cement, mortar, and concrete', *Cement and Concrete Composites* **18**(4), 223–237.

Li, V. C., Stang, H. & Krenchel, H. (1993), 'Micromechanics of crack bridging', *Materials and Structures* **26**(8), 486–494.

Li, V. C., Wang, Y. & Backer, S. (1991), 'A micromechanical model of tension-softening and bridging toughening of short random fiber reinforced brittle matrix composites', *Journal of the Mechanics and Physics of Solids* **39**(5), 607–625.

Li, Z. (1996), 'Micro crack characterization in concrete under uniaxial tension', *Magazine of concrete research* **48**(176), 219–228.

Li, Z. & Shah, S. P. (1994), 'Localization of microcracking in concrete under uniaxial tension', *Materials Journal* **91**(4), 372–381.

Lin, Z. & Li, V. C. (1997), 'Crack bridging in fiber reinforced cementitious com-

posites with slip-hardening interfaces', *Journal of the Mechanics and Physics of Solids* **45**(5), 763–787.

Logan, D. L. (2016), *A first course in the finite element method*, Cengage Learning.

López, C. M., Carol, I. & Aguado, A. (2008), 'Meso-structural study of concrete fracture using interface elements. i: numerical model and tensile behavior', *Materials and structures* **41**(3), 583–599.

Lubarda, V. A., Krajcinovic, D. & Mastilovic, S. (1994), 'Damage model for brittle elastic solids with unequal tensile and compressive strengths', *Engineering Fracture Mechanics* **49**(5), 681–697.

Lubliner, J., Oliver, J., Oller, S. & Onate, E. (1989), 'A plastic-damage model for concrete', *International Journal of solids and structures* **25**(3), 299–326.

Magalhães, M. d. S., Toledo Filho, R. D. & Fairbairn, E. d. M. R. (2014), 'Influence of local raw materials on the mechanical behaviour and fracture process of pva-shcc', *Materials Research* **17**(1), 146–156.

Maji, A. & Shah, S. P. (1988), 'Process zone and acoustic-emission measurements in concrete', *Experimental mechanics* **28**(1), 27–33.

Marfia, S., Rinaldi, Z. & Sacco, E. (2004), 'Softening behavior of reinforced concrete beams under cyclic loading', *International Journal of Solids and Structures* **41**(11-12), 3293–3316.

Markou, G. & Roeloffze, W. (2021), 'Finite element modelling of plain and reinforced concrete specimens with the kotsovos and pavlovic material model, smeared crack approach and fine meshes', *International Journal of Damage Mechanics* **30**(6), 845–871.

Marković, I. (2006), High-performance hybrid-fibre concrete: development and utilisation, PhD thesis.

Massarwa, E., Aboudi, J., Galbusera, F., Wilke, H. J. & Haj-Ali, R. (2017), 'A nonlinear micromechanical model for progressive damage of vertebral trabecular bones', *Journal of Mechanics of Materials and Structures* **12**(4), 407–424.

Mathern, A. & Yang, J. (2021), 'A practical finite element modeling strategy to capture cracking and crushing behavior of reinforced concrete structures', *Materials* **14**, 506.

Mazars, J. (1986), 'A description of micro-and macroscale damage of concrete structures', *Engineering Fracture Mechanics* **25**(5-6), 729–737.

Mazars, J. & Pijaudier-Cabot, G. (1989), 'Continuum damage theory—application to concrete', *Journal of engineering mechanics,* **115**(2), 345–365.

Mehta, P. K. & Monteiro, P. J. M. (2006), *Concrete: microstructure, properties, and materials*, third edn, McGraw-Hill.

Meng, Y., Chengkui, H. & Jizhong, W. (2006), 'Characteristics of stress-strain curve of high strength steel fiber reinforced concrete under uniaxial tension', *Journal of Wuhan University of Technology-Mater. Sci. Ed.* **21**(3), 132–137.

Mihai, I. (2012), Micromechanical constitutive models for cementitious composite materials, PhD thesis, Cardiff University, Cardiff.

Mihai, I. C. & Jefferson, A. D. (2011), 'A numerical model for cementitious composite materials with an exterior point eshelby microcrack initiation criterion', *International Journal of Solids and Structures* **48**, 3312–3325.

Mihai, I. C. & Jefferson, A. D. (2013*a*), 'A multi-asperity plastic-contact crack plane model for geomaterials', *International Journal for Numerical and Analytical Methods in Geomechanics* **37**(11), 1492–1509.

Mihai, I. C. & Jefferson, A. D. (2013*b*), 'Smoothed contact in a micromechanical model for cement bound materials', *Computers & Structures* **118**, 115–125.

Mihai, I. C. & Jefferson, A. D. (2015), 'The simulation of crack opening–closing and aggregate interlock behaviour in finite element concrete models', *International Journal for Numerical Methods in Engineering* **104**(1), 48–78.

Mihai, I. C. & Jefferson, A. D. (2017), 'A micromechanics based constitutive model for fibre reinforced cementitious composites', *International Journal of Solids and Structures* **110-111**, 152–169.

Mihai, I. C., Jefferson, A. D. & Lyons, P. (2016), 'A plastic-damage constitutive model for the finite element analysis of fibre reinforced concrete', *Engineering Fracture Mechanics* **159**, 35–62.

Mindess, S. (1991), The fracture process zone in concrete, *in* 'Toughening Mechanisms in Quasi-brittle Materials', Springer, pp. 271–286.

Mobasher, B., Castro-Montero, A. & Shah, S. (1990), 'A study of fracture in fiber-reinforced cement-based composites using laser holographic interferometry', *Experimental Mechanics* **30**(3), 286–294.

Moreno, D. M., Trono, W., Jen, G., Ostertag, C. & Billington, S. L. (2014), 'Tension stiffening in reinforced high performance fiber reinforced cement-based composites', *Cement and Concrete Composites* **50**, 36–46.

Moës, N., Dolbow, J. E. & Sukumar, N. (2017), *Extended Finite Element Methods*, John Wiley & Sons, pp. 1–21.

Mura, T. (1987), *Micromechanics of Defects in Solids*, second, revised edn, Martinus Nijoff Publishers.

Naaman, A. (2008), Development and evolution of tensile strain-hardening frc

composites, *in* 'Fiber Reinforced Concrete: Design and Applications, Proceedings of International Symposium, BEFIB', pp. 1–28.

Naaman, A. E. (2011), Half a century of progress leading to ultra-high performance fiber reinforced concrete: part 1-overall review, *in* 'Proceedings of the 2nd International RILEM Conference', pp. 17–26.

Nelson, P. K., Li, V. C. & Kamada, T. (2002), 'Fracture toughness of microfiber reinforced cement composites', *Journal of Materials in Civil Engineering* **14**(5), 384–391.

Nemat-Nasser, S. & Hori, M. (1999), *Micromechanics: Overall properties of heterogeneous materials*, North-Holland.

Nemati, K. M. & Monteiro, P. J. (1997), 'A new method to observe three-dimensional fractures in concrete using liquid metal porosimetry technique', *Cement and concrete research* **27**(9), 1333–1341.

Nemati, K. M., Monteiro, P. J. & Cook, N. G. (1998), 'A new method for studying stress-induced microcracks in concrete', *Journal of materials in civil engineering* **10**(3), 128–134.

Neville, A. B. & Brooks, A. M. (2010), *Concrete Technology*, second edn, Prentice Hall.

Newman, J, B. (1979), Concrete under complex stress, *in* 'Developments in concrete technology-1', Springer, London.

Ngo, D. & Scordelis, A. C. (1967), 'Finite element analysis of reinforced concrete beams', *ACI Journal* **64**(3), 152–163.

Nguyen, G. D. & Bui, H. H. (2019), 'A thermodynamics- and mechanism-based framework for constitutive models with evolving thickness of localisation band', *International Journal of Solids and Structures* **187**, 100–120.

Nguyen, V. P., Stroeven, M. & Sluys, L. (2012), 'Multiscale failure modeling of concrete: Micromechanical modeling, discontinuous homogenization and parallel computations.', *Computer Methods in Applied Mechanics and Engineering* **201**, 139–156.

Nikolić, M., Karavelić, E., Ibrahimbegovic, A. & Miščević, P. (2018), 'Lattice element models and their peculiarities', *Archives of Computational Methods in Engineering* **25**(3), 753–784.

Oliver, J., Huespe, A., Blanco, S. & Hirnyj, S. (2005), On a finite element with embedded discontinuities for numerical modeling of fracture, *in* '11th International Conference on Fracture', Citeseer, pp. 1229–1234.

Ortiz, M. (1985), 'A constitutive theory for the inelastic behavior of concrete', *Mechanics of materials* **4**(1), 67–93.

Ortiz, M. (1988), 'Microcrack coalescence and macroscopic crack growth initiation in brittle solids', *International Journal of Solids and Structures* **24**(3), 231–250.

Otero, F., Martinez, X., Oller, S. & Salomón, O. (2015), 'An efficient multi-scale method for non-linear analysis of composite structures', *Composite Structures* **131**, 707–719.

Otsuka, K. & Date, H. (2000), 'Fracture process zone in concrete tension specimen', *Engineering Fracture Mechanics* **65**(2-3), 111–131.

Owen, D. R. J. & Hinton, E. (1980), *Finite elements in plasticity, theory and practice*, Pineridge Press, Swansea.

Palaniswamy, R. & Shah, S. P. (1974), 'Fracture and stress-strain relationship of concrete under triaxial compression', *Journal of the Structural Division* **100**(5), 901–916.

Park, K., Paulino, G. H. & Roesler, J. R. (2009), 'A unified potential-based cohesive model of mixed-mode fracture', *Journal of the Mechanics and Physics of Solids* **57**(6), 891–908.

Park, M. S. & Kwon, Y. W. (2013), 'Elastoplastic micromechanics model for multiscale analysis of metal matrix composite structures', *Computers & Structures* **123**, 28–38.

Peerlings, R. H. J., De Borst, R., Brekelmans, W. A. M. & De Vree, J. H. P. (1996), 'Gradient enhanced damage for quasi-brittle materials', *International Journal for numerical methods in engineering* **39**(19), 3391–3403.

Peerlings, R. H. J., De Borst, R., Brekelmans, W. A. M. & Geers, M. G. (1998), 'Gradient-enhanced damage modelling of concrete fracture', *Mechanics of Cohesive-frictional Materials: An International Journal on Experiments, Modelling and Computation of Materials and Structures* **3**(4), 323–342.

Peng, X. & Meyer, C. (2000), 'A continuum damage mechanics model for concrete reinforced with randomly distributed short fibers', *Computers & Structures* **78**(4), 505–515.

Pensée, V. & Kondo, D. (2003), 'Micromechanics of anisotropic brittle damage: comparative analysis between a stress based and a strain based formulation', *Mechanics of materials* **35**(8), 747–761.

Pensée, V., Kondo, D. & Dormieux, L. (2002), 'Micromechanical analysis of anisotropic damage in brittle materials', *Journal of Engineering Mechanics* **128**(8), 889–897.

Petersson, P.-E. (1981), Crack growth and development of fracture zones in plain concrete and similar materials, Technical report.

Pichler, B., Hellmich, C. & Eberhardsteiner, J. (2009), 'Spherical and acicular

representation of hydrates in a micromechanical model for cement paste: prediction of early-age elasticity and strength', *Acta Mechanica* **203**(3), 137–162.

Pichler, B., Hellmich, C. & Mang, H. A. (2007), 'A combined fracture-micromechanics model for tensile', *International Journal for Numerical and Analytical Methods in Geomechanics* **31**(2), 111–132.

Pijaudier-Cabot, G. & Bažant, Z. P. (1987), 'Nonlocal damage theory', *Journal of engineering mechanics* **113**(10), 1512–1533.

Pijaudier-Cabot, G., Bažant, Z. P. & Tabbara, M. (1988), 'Comparison of various models for strain-softening', *Engineering computations* .

Piscesa, B., Attard, M., Samani, A. & Tangaramvong, S. (2017), 'Plasticity constitutive model for stress-strain relationship of confined concrete.', *ACI Structural Journal* **114**(2).

Poliotti, M. & Bairán, J.-M. (2019), 'A new concrete plastic-damage model with an evolutive dilatancy parameter', *Engineering structures* **189**, 541–549.

Puri, S. & Weiss, J. (2006), 'Assessment of localized damage in concrete under compression using acoustic emission', *Journal of materials in civil engineering* **18**(3), 325–333.

Qing, H. & Mishnaevsky, L. (2010), '3d multiscale micromechanical model of wood: From annual rings to microfibrils', *International Journal of Solids and Structures* **47**(9), 1253–1267.

Qiu, Y. (1999), An investigation into the microplane constitutive model for concrete., PhD thesis, University of Sheffield.

Reinhardt, H. W. (1984), 'Fracture mechanics of an elastic softening material like concrete', *HERON, 29 (2), 1984* .

Rezakhani, R., Zhou, X. & Cusatis, G. (2017), 'Adaptive multiscale homogenization of the lattice discrete particle model for the analysis of damage and fracture in concrete', *International Journal of Solids and Structures* **125**, 50–67.

Rodrigues, E. A., Manzoli, O. L., Bitencourt Jr, L. A., Bittencourt, T. N. & Sánchez, M. (2018), 'An adaptive concurrent multiscale model for concrete based on coupling finite elements', *Computer Methods in Applied Mechanics and Engineering* **328**, 26–46.

Schlangen, E. & Van Mier, J. G. M. (1992), 'Experimental and numerical analysis of micromechanisms of fracture of cement-based composites', *Cement and concrete composites* **14**(2), 105–118.

Sedighi-Gilani, M. & Navi, P. (2006), 'Experimental observations and micromechanical modeling of successive-damaging phenomenon in wood cells' tensile behavio', *Wood Science and Technology* **41**(1), 69–85.

Seupel, A., Hütter, G. & Kuna, M. (2018), 'An efficient fe-implementation of implicit gradient-enhanced damage models to simulate ductile failure', *Engineering Fracture Mechanics* **199**, 41–60.

Shah, S. P., Swartz, S. E. & C, O. (1995), *Fracture Mechanics of Concrete*, John Wiley & Sons, New York.

Shah, S. & Sankar, R. (1987), 'Internal cracking and strain softening response of concrete under uniaxial compression', *Materials Journal* **84**(3), 200–212.

Sharma, M. & Bishnoi, S. (2020), 'Influence of properties of interfacial transition zone on elastic modulus of concrete: Evidence from micromechanical modelling', *Construction and Building Materials* **246**, 118381.

Simo, J. C., Oliver, J. & Armero, F. (1993), 'An analysis of strong discontinuities induced by strain-softening in rate-independent inelastic solids', *Computational mechanics* **12**(5), 277–296.

Simone, A., Wells, G. N. & Sluys, L. J. (2003), 'From continuous to discontinuous failure in a gradient-enhanced continuum damage model', *Computer Methods in Applied Mechanics and Engineering* **192**(41-42), 4581–4607.

Singh, H. (2017), *Steel fiber reinforced concrete: behavior, modelling and design*, Springer Science+Business Media, Singapore.

Skarżyński, Ł. & Tejchman, J. (2013), 'Experimental investigations of fracture process using dic in plain and reinforced concrete beams under bending', *Strain* **49**(6), 521–543.

Slate, F. & Hover, K. (1984), Microcracking in concrete, *in* 'Fracture mechanics of concrete: Material characterization and testing', Springer, pp. 137–159.

Slate, F. O. & Olsefski, S. (1963), X-rays for study of internal structure and microcracking of concrete, *in* 'Journal Proceedings', Vol. 60, pp. 575–588.

Slobbe, A., Hendriks, M. & Rots, J. (2013), 'Systematic assessment of directional mesh bias with periodic boundary conditions: Applied to the crack band model', *Engineering Fracture Mechanics* **109**, 186–208.
URL: *https://www.sciencedirect.com/science/article/pii/S0013794413002361*

Spagnoli, A. (2009), 'A micromechanical lattice model to describe the fracture behaviour of engineered cementitious composites', *Computational Materials Science* **46**(1), 7–14.

Stroud, A. H. (1971), 'Approximate calculation of multiple integrals'.

Struble, L. J., Stutzman, P. E. & Fuller Jr, E. R. (1989), 'Microstructural aspects of the fracture of hardened cement paste', *Journal of the American Ceramic Society* **72**(12), 2295–2299.

Sun, H., Gao, Y., Zheng, X., Chen, Y., Jiang, Z. & Zhang, Z. (2019), 'Meso-scale

simulation of concrete uniaxial behavior based on numerical modeling of ct images', *Materials* **12**(20), 3403.

Sun, L. Z. & Ju, J. W. (2001), 'Effective elastoplastic behavior of metal matrix composites containing randomly located aligned spheroidal inhomogeneities. part ii: applications', *International Journal of Solids and Structures* **38**(2), 203–225.

Swamy, R. (1980), Prospects of fibre reinforcement in structural applications, *in* 'Advances in Cement-Matrix Composites, Proceedings, Symposium L, Materials Research Society Generai Meeting, Boston, MA', pp. 159–69.

Taylor, G. I. (1938), 'Plastic strain in metals', *Journal of the Institute of Metals* **62**, 307–324.

Thomas, C., De Brito, J., Cimentada, A. & Sainz-Aja, J. (2020), 'Macro-and micro-properties of multi-recycled aggregate concrete', *Journal of Cleaner Production* **245**, 118843.

Toro, S., Sánchez, P. J., Blanco, P. J., De Souza Neto, E. A., Huespe, A. E. & Feijóo, R. A. (2016), 'Multiscale formulation for material failure accounting for cohesive cracks at the macro and micro scales', *International Journal of Plasticity* **76**, 75–110.

Torrenti, J., Benaija, E. & Boulay, C. (1993), 'Influence of boundary conditions on strain softening in concrete compression test', *Journal of engineering mechanics* **119**(12), 2369–2384.

Torrenti, J., Desrues, J., Benaija, E. & Boulay, C. (1991), 'Stereophotogrammetry and localization in concrete under compression', *Journal of engineering mechanics* **117**(7), 1455–1465.

Trainor, K. J., Foust, B. W. & Landis, E. N. (2013), 'Measurement of energy dissipation mechanisms in fracture of fiber-reinforced ultrahigh-strength cement-based composites', *Journal of engineering mechanics* **139**(7), 771–779.

Tresca, H. (1868), 'Mémoire sur l'écoulement des corps solides', *Mémoires presentés a L'Institut des Sciences, Lettres et Arts, par divers savants èt lus dans ses assemblées : Sciences, Mathématiques et Physiques* **18**, 733–799.

Unger, J. & Eckardt, S. (2011), 'Multiscale modeling of concrete', *Archives of Computational Methods in Engineering* **18**(3), 341–393.

Van Mier, J. (1991), 'Mode i fracture of concrete: discontinuous crack growth and crack interface grain bridging', *Cement and Concrete Research* **21**(1), 1–15.

Van Mier, J. G. (1997), *Fracture processes of concrete*, CRC press.

Van Mier, J. G. M. (1984), Strain-softening of concrete under multiaxial loading conditions, PhD thesis.

Van Mier, J. G. M. (2013), *Concrete Fracture: A Multiscale Approach*, CRC Press, Boca Raton, Florida.

van Zijl, G. P., Slowik, V., Toledo Filho, R. D., Wittmann, F. H. & Mihashi, H. (2016), 'Comparative testing of crack formation in strain-hardening cement-based composites (shcc)', *Materials and Structures* **49**(4), 1175–1189.

Vecchio, F. & DeRoo, A. (1995), 'Smeared-crack modeling of concrete tension splitting', *Journal of engineering mechanics* **121**(6), 702–708.

von Mises, R. (1913), 'Mechanik der festen körper im plastische-deformablen zustand', *Nachrichten von der Gesellschaft der Wissenschaften zu Göttingen – Mathematisch-Physikalische Klasse* .

Vonk, R. A. (1992), Softening of concrete loaded in compression, PhD thesis.

Voyiadjis, G. Z., Taqieddin, Z. N. & Kattan, P. I. (2008), 'Anisotropic damage–plasticity model for concrete', *International journal of plasticity* **24**(10), 1946–1965.

Wang, F. (2013), The birth and use of concrete and reinforced concrete, *in* 'Advances in Manufacturing Science and Engineering', Vol. 712 of *Advanced Materials Research*, Trans Tech Publications Ltd, pp. 955–960.

Wang, J., Fang, J. & Karihaloo, B. L. (2000*a*), 'Asymptotic bounds on overall moduli of cracked bodies', *International Journal of Solids and Structures* **37**(43), 6221–6237.

Wang, J., Fang, J. & Karihaloo, B. L. (2000*b*), 'Asymptotics of multiple crack interactions and prediction of effective modulus.', *International Journal of Solids and Structures* **37**(31), 4261–4273.

Wang, J. & Karihaloo, B. L. (2000), 'Material instability in the tensile response of short-fibre-reinforced quasi-brittle composites', *Archives of Mechanics* **52**(4), 839–855.

Wang, S. & Li, V. C. (2007), 'Engineered cementitious composites with high-volume fly ash', *ACI Materials journal* **104**(3), 233.

Wang, W., Wang, J. & Kim, M.-S. (2001), 'An algebraic condition for the separation of two ellipsoids', *Computer aided geometric design* **18**(6), 531–539.

Wang, Y., Li, V. C. & Backer, S. (1988), 'Modelling of fibre pull-out from a cement matrix', *International Journal of Cement Composites and Lightweight Concrete* **10**(3), 143–149.

Wille, K., Kim, D. J. & Naaman, A. E. (2011), 'Strain-hardening uhp-frc with low fiber contents', *Materials and structures* **44**(3), 583–598.

William, K. & Warnke, E. (1975), Constitutive model for the triaxial behavior of concrete. in: International association of bridge and structural engineers,

seminar on concrete structure subjected to triaxial stresses. may 1974. iabse proceedings.

Withers, P., Stobbs, W. & Pedersen, O. (1989), 'The application of the eshelby method of internal stress determination to short fibre metal matrix composites', *Acta Metallurgica* **37**(11), 3061–3084.

Xenos, D. & Grassl, P. (2016), 'Modelling the failure of reinforced concrete with nonlocal and crack band approaches using the damage-plasticity model cdpm2', *Finite Elements in Analysis and Design* **117-118**, 11–20.

Xu, X. P. & Needleman, A. (1994), 'Numerical simulations of fast crack growth in brittle solids', *Journal of the Mechanics and Physics of Solids* **42**(9), 1397–1434.

Yan, Z. G., Zhang, Y., Woody Ju, J., Chen, Q. & Zhu, H. (2019), 'An equivalent elastoplastic damage model based on micromechanics for hybrid fiber-reinforced composites under uniaxial tension', *International Journal of Damage Mechanics* **28**(1), 79–117.

Yang, E. H., Wang, S., Yang, Y. & Li, V. C. (2008), 'Fiber-bridging constitutive law of engineered cementitious composites', *JCI Journal of Advanced Concrete Technology* **6**(1), 1–13.

Yip, M., Mohle, J. & Bolander, J. E. (2005), 'Automated modeling of three-dimensional structural components using irregular lattices', *Computer-Aided Civil and Infrastructure Engineering* **20**(6), 393–407.

Zhan, Y. & Meschke, G. (2017), 'Adaptive crack modeling with interface solid elements for plain and fiber reinforced concrete structures', *Materials* **10**(7), 771.

Zhang, Y., Ju, J. W., Zhu, H., Chen, Q., Guo, Q. & Yan, Z. (2019), 'A novel damage model based on micromechanics for hybrid fiber reinforced cementitious composites under uniaxial compression', *International Journal of Damage Mechanics* **28**(7), 1095–1132.

Zhao, L. Y., Shao, J. F. & Zhu, Q. Z. (2018), 'Analysis of localized cracking in quasi-brittle materials with a micro-mechanics based friction-damage approach', *Journal of the Mechanics and Physics of Solids* **119**, 163–187.

Zhou, R., Lu, Y., Wang, L.-G. & Chen, H.-M. (2021), 'Mesoscale modelling of size effect on the evolution of fracture process zone in concrete', *Engineering Fracture Mechanics* **245**, 107559.

Zhu, H., Yu, K. & Li, V. C. (2021), 'Sprayable engineered cementitious composites (ecc) using calcined clay limestone cement (lc3) and pp fiber', *Cement and Concrete Composites* **115**, 103868.

Zhu, Q. Z., Kondo, D. & Shao, J. F. (2008), 'Micromechanical analysis of coupling

between anisotropic damage and friction in quasi brittle materials: role of the homogenization scheme', *International Journal of Solids and Structures* **45**(5), 1385–1405.

Zhu, Q. Z., Kondo, D. & Shao, J. F. (2009), 'Homogenization-based analysis of anisotropic damage in brittle materials with unilateral effect and interactions between microcracks', *International Journal for Numerical and Analytical Methods in Geomechanics* **33**(6), 749–772.

Zhu, Q. Z. & Shao, J. F. (2015), 'A refined micromechanical damage–friction model with strength prediction for rock-like materials under compression', *International Journal of Solids and Structures* pp. 60–61.

Zhu, Q. Z., Zhao, L. Y. & Shao, J. F. (2016), 'Analytical and numerical analysis of frictional damage in quasi brittle materials.', *Journal of the Mechanics and Physics of Solids* **92**, 137–163.

Zienkiewicz, O., Taylor, R. & Fox, D. (2014), *The Finite Element Method for Solid and Structural Mechanics*, Elsevier Ltd.